Application of Virtual Design Tools to Tube Launched Projectile Systems

A thesis submitted in fulfilment of the requirements for the degree of Doctor of Philosophy

Christos Tsangalis
B.Eng(Aero) Hons

School of Aerospace, Mechanical and Manufacturing Engineering
Science, Engineering and Technology Portfolio
RMIT University
August 2008

Dedication

Prior to my father losing his battle with leukaemia in 1986, he began construction of a model aircraft for the enjoyment of his children. However, due to physical and mental restrictions imposed by illness, the model aircraft project was never completed. With the submission of this thesis, the culmination of an honours degree in Aerospace Engineering and post graduate research, I now complete that aircraft project in honour of my late father.

Declaration

I certify that except where due acknowledgement has been made, the work is that of the author alone; the work has not been submitted previously, in whole or in part, to qualify for any other academic awards; the content of the thesis is the result of work which has been carried out since the official commencement date of the approved research program; and, any editorial work, paid or unpaid, carried out by a third party is acknowledged.

Christos Tsangalis

Acknowledgements

To my Principal Supervisor, Professor Pavel Trivailo, I would like to pass on my sincere gratitude for his guidance, encouragement, efficiency and intellectual input. I greatly appreciated and admired his level of organisation, the manner in which he efficiently and methodically dealt with problems and his genuine concern for his students. I also extend my gratitude to RMIT University for providing the necessary facilities, resources and support staff required for the completion of this work.

I would like to gratefully acknowledge my co-supervisor, Dr Neil McLachlan, for his tireless efforts throughout every aspect of the project including modelling, manufacturing, analysis and writing. I thank him for his imaginative and innovative approach to research and his ability to tackle problems with passion and enthusiasm. I also acknowledge the many conversations conducted both professional and personal usually over lunch and a latte… Thanks Neil. Much appreciated.

I would like to extend great thanks to DSTO for their funding and support throughout the life of the project. Instrumental to this was my External Supervisor Dr Vinod Puri whose vision and guidance helped formulate the topic for this research. I would like to offer my sincere thanks for his technical direction and the time spent both proof reading and correcting my drafts. I would also like to thank DSTO for providing the necessary equipment, staff and facilities required to undertake the experimental work for prototype validation.

I would like to thank my family. To my mother who selflessly devoted her life to raising three young children. It is solely due to her that I have been granted these opportunities in life. To my brother Dimitri, whose academic pursuits and dedication to his goals served as inspiration to me completing this work. And to my sister Anastasia, for instilling colour in all our lives…

I would like to acknowledge my friends Asimenia, Michael, Kirk and Scotty for their support and guidance throughout the years we studied Aerospace Engineering together and for the many years we will continue to be friends. To my friend Alex, whose friendship and support transcended beyond anything I could ever put down on paper. And finally, to Theodora, whose love was unconditional…

List of Publications

Adams, R., Tsangalis, C., McLachlan, N., Tomas, J. A. and Bil, C. (2005). "Design Improvement of Components and Structures". *ANSA META International, Congress.* Thessaloniki, Greece.

Tsangalis, C., McLachlan, N. and Trivailo, P. (2004). "Historical Analysis of 16th Century Cannon using Modern Techniques of Explicit Finite Element Analysis", *Proceedings – Land Warfare Conference 2004, Melbourne, September 27– 30, 2004*. DSTO of Australia, SA, Australia.

Tsangalis, C., McLachlan, N. and Trivailo, P. (2005). "Virtual Design Processes for Weapon Systems". *Congress Proceedings – Eleventh Australian International Aerospace Congress.* Melbourne, March 13-17, 2005. The institution of Engineers, Australia.

Tsangalis, C., McLachlan, N. and Trivailo, P. (2006). "Fluid-Structure Interaction Modelling of Propellant Combustion." Australian and New Zealand Industrial and Applied Mathematics Journal 47: C388-C403.

Table of Contents

List of Figures

List of Tables

List of Abbreviations

APFSDS	Armour Piercing Fin Stabilised Discarding Sabot
CAD	Computer Aided Design
CFD	Computational Fluid Dynamics
EOS	Equation of State
FE	Finite Element
FEA	Finite Element Analysis
FSI	Fluid Structure Interaction
HVFSDS	High Velocity Fin Stabilised Discarding Sabot
IB	Interior Ballistics
JWL	Jones-Wilkins-Lee
KE	Kinetic Energy
Mk	Mark
TNT	Trinitrotoluene
VDP	Virtual Design Process
VDT	Virtual Design Tool

Nomenclature

A	=	JWL Material Constant	-
A_s	=	Bore Cross Sectional Area	mm^2
B	=	JWL Material Constant	-
$B`$	=	Burn Rate Coefficient	$mm.s^{-1}$
C	=	Charge Weight	*Tonne*
C_v	=	Average Heat Capacity	$mJ.K^{-1}$
c	=	Material Sound Speed	$mm.s^{-1}$
D	=	Diameter of Grain	*mm*
d	=	Distance form a Control Point (Influence Function)	*mm*
E	=	Young's Modulus	*MPa*
e	=	Specific internal energy per unit mass	$mJ.tonne^{-1}$
g_c	=	Unit Conversion Factor	-
L	=	Length of Grain	*mm*
M_E	=	Effective Mass	*tonne*
N	=	Number of Grain Perforations	-
n	=	Burn Rate Exponent	*For MPa*
n'	=	Mass of Gas	*tonne*
$\check{n}$	=	Number of moles of the gas	-
P	=	Pressure of Gas	*MPa*
P_A	=	Average Pressure	*MPa*
P_B	=	Projectile Base Pressure	*MPa*
R	=	Gas Constant	$mJ.t^{-1}.K^{-1}$
r	=	Grain Perforation Radius	*Mm*
R_1	=	JWL Material Constant	-
R_2	=	JWL Material Constant	-
R'	=	Projectile Radius	*Mm*
S	=	Projectile Travel	*Mm*
s	=	Pseudo Support (Influence Function)	-
T	=	Absolute Temperature of the Gas	*K*

T_0	=	Flame Temperature	K
V	=	Volume of Gas	mm^3
V_{C0}	=	Initial Chamber Volume	mm^3
V_p	=	Projectile Velocity	$mm.s^{-1}$
V_T	=	Total Volume	mm^3
$V`$	=	Relative Volume of Gaseous Detonation Products proportional to the change in Density	mm^3
w	=	Weight of Gas	$tonne$
W_s	=	Projectile Weight	$tonne$
x	=	Linear Recession of Grain	mm
Z	=	Fraction of Charge Burnt	-
β	=	Heat-Loss Adjustment Factor	-
Δt	=	Time Step	s
Δx	=	Element Length	mm
γ	=	Specific Heat Ratio	-
η	=	Gas Covolume	$mm^3.t^{-1}$
λ	=	Force Constant	$mJ.t^{-1}$
v	=	Poisson's Ratio	-
ρ	=	Overall material density	$tonne.mm^{-3}$
ρ_0	=	Reference density	$tonne.mm^{-3}$
ρ_s	=	Solid Propellant Density	$tonne.mm^{-3}$
$\sigma_{1,2,3}$	=	Principle Stresses	MPa
σ_y	=	Yield Stress	MPa
σ_{vm}	=	Von Mises Stress	MPa
ω	=	JWL Material Constant	-

Summary

With the current advances in computing power and software technology, the application of Virtual Design Tools (VDT) provides a significant means for reducing product development cycles and minimising production costs. Supported by experimental validation, a Virtual Design Process (VDP) incorporating VDTs could potentially be used to perform the entire design process from conception through to design for manufacture.

The emergence of Virtual Design Processes is evident in the literature across a large range of engineering applications including industrial design [1, 2], agricultural applications [3, 4] and manufacturing [5, 6].

VDTs have also been applied to the design and manufacture of components/products for defence applications. These include the use of implicit 2D axisymmetric finite element models to study sabot/projectile interactions of Kinetic Energy (KE) projectiles [7-10]. Fluid structure interaction modelling has been used to study the effects of landmine detonation and fragmentation on the hull of a Grizzly armoured vehicle [11]. Optimisation analyses have been performed on 5.56mm M249 barrels with the objective of reducing weight [12].

However, no evidence exists of a VDP which incorporates disciplines of structural mechanics, fluid dynamics and product optimisation to systematically develop advanced and novel weapons concepts. This thesis therefore presents a methodology which integrates Finite Element Analysis (FEA), Fluid-Structure Interaction (FSI) modelling and Shape Optimisation for the design and development of Tube Launched Projectile Systems. The resulting VDP provides the basis for designing weapon systems without the need for continual prototyping and physical testing.

The VDP was first demonstrated through a historical case study of 16th Century Cannons. While the weapon itself was redundant, it provided a means by which the VDP could be used to thoroughly analyse and refine a primitive design.

Methods of finite element analysis were first used to identify the nature of stresses inherent of the original cannon when fired. Implicit FE methods were able to provide information of static stresses in the barrel and breech. It was evident, however, that explicit FE methods were far more suitable for the analysis of tube launched weapons. These allowed the dynamic interaction of barrel and munitions to be studied over the entire Interior Ballistic (IB) cycle as the projectile was accelerated down the barrel.

FSI modelling was then introduced to analyse the impact of propellant performance on barrel/munition interaction. In attempting to perform FSI modelling on the cannon system, the lack of a material model to accurately describe propellant combustion in the FE environment was identified. Instead, a detonation using the JWL EOS was simulated inside the cannon chamber. The analysis demonstrated the potential for FSI to integrate the properties of the propellant and structural system into a single analysis.

Shape Optimisation was then applied to the cannon system to reach two design objectives. In the first instance, a mass reduction was performed on the cannon which interestingly revealed a design representative of a modern gun barrel. The second Shape Optimisation objective involved shifting the natural frequencies of the cannon system to control muzzle vibrations. Such techniques would be very useful in refining the accuracy of modern gun systems.

Subsequent to the 16th Century Cannon case study, an interior ballistic model proposed by Krier and Adams 1979 [13] was integrated into the MSC. Dytran Explicit Solver through a user subroutine. FSI modelling was then able to be used to study the structural behaviour of components subject to the dynamics of propellant combustion. A simulation was performed in which a projectile was accelerated down a barrel according to a set of known system parameters.

The VDP was then applied to the design and development of stacked kinetic energy rounds. More specifically, the design of a stacked High Velocity, Fin Stabilised, Discarding Sabot (HVFSDS) round was undertaken. The availability of a gun system with multiple rounds placed in a single barrel was considered to significantly increase the rate of fire of the weapon and hence increase its lethality.

Explicit finite element methods were used to develop a wide variety of design ideas. Both push and traction type sabots were assessed in this application, with the push type proving to be a more robust solution. Once the design concepts had been established, detailed explicit FE methods and Shape Optimisation were used to refine the design.

The use of the developed VDP resulted in a design for a stacked HVFSDS round which was consequently manufactured and subjected to physical testing. Experimental results were able to provide justification to both the design concept and the methodology employed in its development. Subsequent to testing, the VDP was again used to further refine the design.

The developed VDP was therefore successfully able to integrate disciplines of structural mechanics, fluid dynamics and optimisation in providing a framework for designing novel concepts for tube lunched weapons systems. The VDP provided a quick and inexpensive means by which designs could be analysed and modified subject to a variety of conditions. This also meant that the design could be significantly developed before the timely and costly tasks of prototype manufacture and testing were required.

1 Introduction

With the current advances in computing power and software technology, the application of Virtual Design Tools (VDT) provides a significant means for reducing product development cycles and minimising production costs. Supported by experimental validation, a Virtual Design Process (VDP) incorporating VDTs could potentially be used to perform the entire design process from conception through to design for manufacture.

Virtual Design Processes' are currently being used extensively across a large range of engineering disciplines including industrial design [1, 2], agricultural applications [3, 4] and manufacturing [5, 6]. For example, Su and Qin 2003 [1] developed a virtual process for the design of worm gears incorporating numerical analysis, three dimensional simulation and finite element analysis.

VDTs have also been applied to the design and manufacture of components/products for defence applications. These include the use of implicit 2D axisymmetric finite element models to study sabot/projectile interactions of Kinetic Energy (KE) projectiles [7-10]. Fluid structure interaction modelling has been used to study the effects of landmine detonation and fragmentation on the hull of a Grizzly armoured vehicle [11]. Optimisation analyses have been performed on 5.56mm M249 barrels with the objective of reducing weight [12].

However, no evidence currently exists where the application of a Virtual Design Process (VDP) including disciplines of structural mechanics, fluid dynamics and product optimisation are systematically studied to develop advanced/novel weapons concepts. The work presented in this thesis looks into the potential application of a VDP for the design and development of Tube Launched Weapon Systems. The methodology used was based on the integration of VDTs including Finite Element Analysis (FEA), Fluid-Structure Interaction (FSI) modelling and Shape Optimisation into the VDP. This provided the basis for designing a weapon system without the need for continual prototyping and physical testing.

1.1 Scope of Study

This study focuses attention on the development of a systematic approach where desirable components of VDT are studied and integrated to form a dynamic VDP. The principle objectives of this study are to:

- Investigate the use of FEA, FSI and Shape Optimisation models for the design of tube launched weapons.

- Integrate the identified VDTs to develop a VDP which facilitates the design and development of advanced/novel tube launched weapons.

- Conduct detailed analyses to demonstrate the capability of the VDP.

- Validate the VDP through prototyping and experimentation.

The VDP is first demonstrated through a historical case study of 16th Century Cannons. While the weapon itself is redundant, it provides a means by which the VDP can be used to thoroughly analyse and refine a primitive design. The VDP is then applied to the design and development of stacked kinetic energy rounds. More specifically, the design of a stacked High Velocity, Fin Stabilised, Discarding Sabot (HVFSDS) Round is undertaken.

The VDP first uses FEA to determine the distribution of stresses in the structural system during the Interior Ballistic (IB) phase. FEA can then be used to efficiently develop and assess a large range of design ideas and concepts before any detailed design is performed. Both implicit and explicit FEA techniques are assessed in this application.

FSI modelling is then introduced to analyse the impact of propellant behaviour on barrel/munition interaction. The resultant design tool would therefore be capable of simulating the whole tube launched weapon system in a single integrated model.

Shape Optimisation techniques are then used to refine the design. Design objectives relating to mass reduction, stress distribution, vibrational properties and reaction forces will be attempted subject to specified constraints.

The resultant VDP, developed as a part of this thesis, would provide a holistic framework for the assessment, design and visualisation of barrel and munition interaction, including propellant performance. The integration of the engineering disciplines allows the effect of changing one variable in the analysis to be seen over the entire system.

A basic outline of the thesis is given below:

- Chapter 2 presents a literature review containing the application of VDTs and VDPs across a range of engineering disciplines. A review of basic tube launched weapons concepts is also presented.
- Chapter 3 contains a description of VDTs methods and their implications in the VDP.
- Chapter 4 outlines the case study of 16th Century Cannon. The analysis of cannons is used to assess the application of the VDP in the development of tube launched weapons.
- Chapter 5 describes the incorporation of a simple interior ballistic model into the explicit FE environment. This allows the combustion behaviour of propellant to be included directly into FSI simulations of tube launched weapon systems.
- Chapter 6 considers the application of the VDP to the design and development of stacked HVFSDS kinetic energy rounds.
- Chapter 7 details how explicit FEA and Shape Optimisation techniques are used to refine the HVFSDS stacked round design concept.
- Chapter 8 describes the experimental validation and subsequent design refinement performed on the HVFSDS round concept.
- Chapter 9 presents conclusions.

2 Review of Literature

A review of current Virtual Design Processes across a broad range of engineering disciplines is presented in this chapter. Applications of the relevant VDTs, including FEA, FSI and Shape Optimisation are then studied individually. The review highlights the benefits of adopting virtual design processes against traditional design and development methods.

A basic review of tube launched weapons is also presented in order to introduce the appropriate terminology and concepts relating to these systems. This review focuses on issues relating to gun interior ballistics and other gun related processes which are complex and highly non-linear.

2.1 Virtual Design Processes

Virtual Design Tools exist which can be used to efficiently analyse and develop a whole range of engineering components. Advances in these areas have allowed designers to combine such tools to formulate processes from which design and testing can be undertaken in a purely virtual environment.

For example, as introduced in Chapter 1, Su and Qin 2003 [1] developed an integrated approach in designing optimised worm gearing. The process consisted of three modules including numerical analysis, three dimensional simulation and finite element analysis. It was the first time that the integration of multiple techniques into the whole design process of worm gearing had been presented in the literature.

Lye, et al., 2004 [2] successfully developed an intelligent design methodology for the virtual modelling, testing and analysis of protective packaging buffers. The methodology employed the use of genetic algorithms, finite element models and proprietary design routines. The developed process was capable of determining the optimal buffer design given the properties of the product for which it was to protect. Various case studies considering common consumer electrical appliances were used to validate the design methodology.

Altintas and Cao 2005 [6] present a virtual design and optimisation process for machine tool spindles. An integrated digital model of the spindle, tool holder, tool and cutting process was developed to improve the design of spindles for specific machining application. As a result, the process allowed the virtual testing of spindles under simulated cutting forces. The dynamic behaviour of the spindle, contact loads experienced by the bearings, mode shapes and dynamic deflections along the spindle shaft can all be predicted and optimised before physically building and testing the spindles.

Li, et al., 2002 [14] developed a virtual design method for brush shaped cleaning elements for sugarcane harvesters, again incorporating finite element methods. It was found that the factors affecting the design of the cleaning element were numerous and complex and difficult to analyse and design. Furthermore, it was acknowledged that if the design parameters were to be obtained through experiment, this would prove to be time consuming, laborious and costly.

A virtual design method was therefore developed in which finite element models were used to assess the influence of various design parameters. Orthogonal experiment analysis and regression analysis were conducted to determine the overall effect on results caused by changes of different parameter groups, thus obtaining the optimal design parameters of the cleaning element. In conclusion, Li, et al., 2002 [14] stated that "*This method economizes material, labor and time. It is the correct way of high efficiency and speed to reduce the development period and to increase the quality of the product"*.

Other researches have also investigated the application of VDPs to agricultural machinery. Queiroz, et al., 2001 [3] used virtual prototyping to construct a 3D simulation model for analysing the dynamic behaviour of a bean harvester. Similarly, Kim, et al., 2001 [4] used virtual prototyping to develop an automatic transplanter consisting of a pick-up system, a planting system and a feeding system. The kinematic characteristics of the pick-up and planting system were able to be simulated and improved. Virtual prototyping was also applied by Choi, et al., 2001 [15] to design an automatic pick up mechanism for plug-seedlings.

Yan, et al., 2004 [5] developed a three-dimensional functional virtual prototype of a vacuum packer. The virtual model was used for designing the rotational motions of the driving motors and predicting the power requirement of these motors. The development of key components including the vacuum packer, the pressing board and tape holder, were conducted for improving the packing quality of the automatic vacuum packer. The simulated prototype was able to match the real prototype with a 92.6% success rate.

Luo, et al., 2001 [16] developed a virtual process for optimum tooling design for resin transfer moulding. A systematic approach was introduced based upon a virtual manufacturing (simulation) model, coupled with a neural network-genetic algorithm optimisation procedure. Simulation models were able to predict the resin flow patterns and processing efficiency of particular tooling designs which were then optimised with genetic algorithms.

Similarly, Yeh and Vance 1997 [17] incorporated finite element modelling into a virtual design space. However, in this case MSC. Nastran data was introduced into Virtual Reality (VR) which allowed the designer to manipulate design variables and view the changes in a 3D virtual environment. The VR technology permitted natural head and hand motions to interact with the design and design variables. The authors argued that this allowed the attention of the designer to be dedicated to the design task rather than concentrating on interacting with the application program.

Whyte, et al., 2000 [18] investigated the use of VR in building design. Three different modelling approaches, including the library based, straightforward translation and database approaches, for VR applications in house building were explored. It was found that different modelling approaches were more appropriate for different tasks.

The development of VDPs can also facilitate in the design of large, multi-component systems, where individual designers are spread across numerous locations. Frameworks for interactive product design have been developed which allow designers to collectively undertake a common design goal within a virtual environment. Virtual design and simulation tools allow the communication of design changes to all parties as the design is developed.

For example, Hindman and Ousterhout 1998 [19] developed a World Wide Web-based Virtual Design System (VDS) for sheet metal forming design and manufacture. The system allows quick access to necessary information for the successful creation of a part and can run simulations of actual manufacturing processes. Completed designs are then forwarded directly to the manufacturing facility to quickly begin construction.

Kan, et al., 2001 [20] present an Internet-based VR collaborative environment called Virtual Reality-based Collaborative Environment (VRCE). VRCE was created to shorten product development cycles for teams in small to medium scale industries that need to design products collaboratively from geographically distributed locations.

Similarly, Lau, et al., 2003 [21] propose an Interactive Design Visualisation System (IDVS) to facilitate interactive product design. The system provides an interactive environment for communicating design concepts and sharing production data in real-time. The IDVS incorporates the concept of virtual product design, concurrent engineering, design visualisation and job allocation to streamline the design of modern industrial products.

In summary, the virtual design process may be used to efficiently explore and assess novel and advanced tube launched weapons concepts. However, on a larger scale involving the design of more complex weapon systems, the virtual design process can provide an environment within which multiple designers can perform individual tasks in geographically diverse locations in order to achieve a common design goal.

2.2 Virtual Design Tools

2.2.1 The Finite Element Method

The FE method provides a means by which a numerical solution can be obtained for a specific problem [22]. This is accomplished by breaking down large and complex structures into sets of elements which are connected by nodes to form a mesh. Describing the behaviour of each element mathematically results in a set of simultaneous algebraic equations that can be processed using a computer. Analyses can be performed using known environmental constraints, load/boundary conditions and relevant material/structural properties.

Structural FE analysis utilises Lagrangian formulation where the Euler equations are solved assuming a Lagrangian frame of reference. This results in a system where the mesh moves according to the flow of material. These methods fail where material flow becomes highly distorted resulting in irregular meshes.

When applying such techniques to highly transient dynamic phenomena, the process becomes far more computationally strenuous. In these cases, time marching integration schemes, generally referred to as explicit solvers are employed due to their superior non-linear problem solving capabilities. Explicit techniques differ from those of standard static and dynamic solvers, as no iteration or tangent stiffness matrices are required [23]. Instead, the explicit procedure integrates through time utilising many small time increments.

Advances in FEA have allowed for the behaviour of entire structures to be considered without having to make assumptions about the nature of interactions between multiple components [24]. This eliminates the requirement to approximate boundary conditions representing the interactions of adjacent structures in order to analyse a single component.

In order to produce a realistic FE model, a good understanding of FE methods and general engineering principles is necessary. A mesh that adequately covers the component to be analysed is required in addition to applied boundary conditions and loads [24] which represent the real system.

The application of FEA to the design and development of engineering components is widespread with many examples in the literature. They cover a wide range of areas including automotive engineering [25-27], manufacturing [28-30], structures [31-33] and biomechanics [34-37].

2.2.1.1 Stress Analysis

Stress analysis is the fundamental and most commonly used applications of the FE method. FE modelling is able to consider both non-linear geometries and material properties in the analysis of stress for any given component. With respect to tube launched weapons, the FE method has been used to calculate stresses for arbitrarily complicated projectile/barrel configurations allowing all components and interactions to be treated simultaneously [7-10].

The Von Mises Stress Criteria combines the orthogonal stress components created under multi-axial loading and calculates an effective stress. The effective stress values can then be compared against simple material properties derived from uniaxial tests, such as yield and ultimate stresses of the material. The Von Mises Stress can be expressed as:

$$\sigma_{vm} = \sqrt{\frac{1}{2}\sqrt{(\sigma_1 - \sigma_2)^2 + (\sigma_2 - \sigma_3)^2 + (\sigma_3 - \sigma_1)^2}} \quad [38] \qquad \textbf{Equation 2.1}$$

Where:

σ_{vm} = Von Mises Stress

σ_1, σ_2 and σ_3 = Principal Stress Components

Plastic yielding is predicted to occur when the Von Mises Stress is equal to or beyond the yield of the material [9]. The yield stress, stress at which plastic deformation begins, is usually a good limiting value to use during design. Any significant plastic deformation during in-bore travel will affect both the muzzle velocity and terminal ballistics of the projectile [38]. Drysdale and Burns 1988 [24] suggest that an elastic analysis be performed in the first instance. If this reveals stresses above the yield of the material, an elastic-plastic solution is then required.

Other factors such as temperature and strain rates may impact the stress behaviour of some materials. In ballistics applications, the projectile is exposed to high flame temperatures for only a few milliseconds and therefore temperature effects during in-bore travel are considered to be negligible [38].

Similarly, extremely high strain rates, like those endured during impacts, may significantly raise the static yield strength of some materials. However, strain rates associated with interior ballistics are only moderate and therefore any strengthening effect of the metals is negligible [38]. This notion is supported by Rabern and Parker 1995 [10] who state that the materials generally used in these applications show little variation in properties for the associated strain rates. Drysdale and Burns 1988 suggest, however, that the use of titanium may warrant the consideration of strain rate effects due to this material's sensitive nature to strain rate.

It is obvious that as projectiles are not used repeatedly, fatigue considerations are not necessary in the analysis. However, the analyst must appreciate that in addition to surviving the interior ballistic phase, the projectile must also be able to perform a desired function at the target. Therefore, any plastic deformations endured must not compromise the terminal ballistic phase [24].

Various examples of stress analysis applied to tube launched weapon systems exist in the literature. The majority of these are limited to implicit analysis employing 2D axisymmetric models. For example, Drysdale 1981 [38] used a 2D axisymmetric finite element model to design sabots for two different penetrator materials. He showed that it was necessary to decide on penetrator material and configuration initially in order to be able to design a minimum weight sabot.

Pflegl, et al., 1981 [8] performed a structural analysis of a Kinetic Energy (KE) projectile after witnessing the break up of a penetrator during cold temperature firing. They used a 2D axisymmetric model, created in NASTRAN, of a depleted uranium penetrator and an aluminium sabot in order to determine regions of high stress. Load cases representative of peak projectile base pressure were applied to the model in conjunction with peak inertial forces applied to the penetrator. This model was used to predict mechanisms by which the penetrator failed during launch. Accordingly, projectile design was modified in order to prevent similar failures.

Pflegl, et al., 1981 [8] also performed detailed finite element analysis on the lug profile used to transfer loads from the sabot to projectile. The interaction of these two components is crucial to the interior ballistic phase of the weapon and ensures that the penetrator is not deformed in a way which would affect its on target performance. The model was successful in calculating stresses and stress concentration factors for peak firing conditions.

Hollis 1994 [9] used finite element analysis to verify the structural integrity of a modified M86IP training round. In order to reduce the damage caused by such a round, Hollis 1994 [9] replaced the existing steel penetrator with a hollow aluminium equivalent. A 2D axisymmetric, quasi-static model was used to perform the stress analysis using the Von Mises Stress Criterion. Regions of unsatisfactorily high stress were found within the penetrator and the design was modified accordingly.

The survivability of saboted launch packages and the limitations of push and traction sabot designs were studied by Rabern and Parker 1995 [10]. They also used a 2D axisymmetric model however, the PRONTO2D explicit finite element code was used to perform dynamic simulations. They stated that the transient nature of the loading, the very high accelerations, multiple interfaces and system non-linearities warranted the use of a dynamic explicit solver. It was found that push type sabots were limited by corner failure on the rear of the penetrator. This affect could be alleviated by using soft aluminium inserts in the pusher to redistribute loads at the rear of the penetrator.

Rabern and Parker 1995 also considered traction sabots which were shown to outperform push type sabots. It was found that these designs were limited by shear loads in the sabot along the penetrator interface. Rabern and Parker 1995 were able to produce a model of the sabot penetrator system containing all the buttress grooves. This was an improvement on work performed by Pflegl, et al., 1981 [8] who only considered the behaviour of one groove, or lug.

Pathak and Jha 2001 [7] used an implicit 2D axisymmetric finite element model to study KE projectiles. A more rigorous contact definition was used to find a more realistic solution of the distribution of stresses at the sabot/projectile interface. Similar to Rabern and Parker 1995, this was an improvement on works conducted by Pflegl, et al., 1981 [8] and Hollis 1994 [9] who both omitted

contact related phenomena at the interface. Pathak and Jha 2001 [7] were able to provide better insight into the overall distribution of radial, axial, hoop and von mises stress in the projectile.

While the majority of previous authors used two dimensional axisymmetric models in the study of projectiles, there exist some significant limitations. Such models are unable to account for transverse forces due to transverse projectile or gun tube motion. 2D axisymmetric modelling is also insufficient when symmetry conditions are disrupted by the use of stiffeners, ribs or vanes in projectile design. Furthermore, the study of projectile "balloting" (transverse motion of the projectile inside the gun tube) or projectile interaction with a flexible gun tube is unsuitable for 2D axisymmetric conditions [24].

In order to proceed with the integrated design of novel tube launched weapon systems, a static 2D approach would limit the ability of the modeller to assess the dynamic behaviour of the system. A full 3D dynamic analysis considering all the relevant components and their interactions would be required. Such analyses could provide insight into projectile/barrel vibrations, either axisymmetric or bending, and stress waves arising from in-bore projectile impacts [24].

Eches, et al., 2002 [39] created a half 3D model of an entire weapon system including projectile, barrel, breech and cradle assembly. The model was used to consider the effect of interactions between the weapon and projectile on the mechanical behaviour of the weapon and muzzle exit conditions. Wilkerson, et al., 1996 [40] also used 3D tools to model complete gun systems including the breech, barrel, cradle, recoil system and mount. Such models were used to predict the effects of in-bore balloting on the accuracy of the weapon.

2.2.1.2 Structural Dynamics

The discipline of structural dynamics considers a structure's response to predicted dynamic loading. Dynamic responses are often vital in the design and development of sophisticated structures in order to avoid unwanted vibrations and resonances which can adversely affect performance.

Modal Analysis is a useful tool in determining a structures' likely response to a dynamic input or excitation. Modal analysis, can reveal information relating to the natural frequencies, mode shapes and inherent damping of a particular structure. The natural frequency refers to the frequency at which any input will result in an amplified response of the system. The mode shape refers to the vibrational pattern assumed by the structure for a given natural frequency while damping relates to the ability of the system to dissipate vibrational energy.

Various examples of the application of modal analysis to weapon systems exist in the literature. Gupta 1999 [41] used a three dimensional model of a hull-turret-gun assembly of an armoured vehicle to predict the lowest 30 modal frequencies using the ADINA transient finite element code. Good agreement of modal frequencies was found with comparison to experimental results for the low frequency modes. Cordes, et al., 2004 [42] performed a modal analysis on a 155mm projectile using the ABAQUS Standard implicit solver. Critical mode shapes during launch were identified and the maximum and minimum axial and radial projectile displacements were reported.

Livermore and Sadowski 2005 [12] performed an optimisation analysis in attempting to reduce the weight of a 5.56mm M249 barrel. The barrel was considered to be a periodically forced system governed by the rate of fire. Modal analysis was necessary to ensure that the natural frequencies of the system were significantly different to the rate of fire which would represent the period of the forcing function in this application [12]. This was required in order for the barrel to maintain its structural integrity and to guarantee that the accuracy of the weapon was not compromised due to an excessively vibrating barrel.

Alyanak, et al., 2005 [43] and Alyanak, et al., 2006 [44] performed normal mode analysis in GENESIS FEA software in the design and optimisation of a supercavitating torpedo. Again, the aim of the analysis was to ensure that the natural frequencies of the weapon structure did not overlap with any of the excitation frequencies of the system.

Yi, et al., 2004 [45] used a three-dimensional finite element model to perform vibrational analysis on Fin-Stabilised Sabot-Discarded Penetrators. The first twenty-eight orders of natural frequency for a given penetrator system were reported in order to identify which vibrational characteristics may

jeopardise launching security and fire precision. It was found that the bending modes were most dangerous when involving the penetrator tail, resulting in stress concentrations at the projectile tail/body interface.

Various authors have considered the dynamic loading experienced by projectiles during the ballistic cycle in order to improve sabot/penetrator design. Considering interior ballistics, severe dynamic axial loads are generally the result of pressures generated by propellant combustion. Considerable lateral loading can also occur when a round is fired from either a slightly bent or vibrating barrel.

Rabern 1992 [46] considered both axial and lateral impulsive loadings of a kinetic energy projectile when fired from a slightly bent launch tube. In assessing the phenomena, both experimental and numerical analyses were used. Experimentally, Rabern 1992 [46] utilised 5 X-ray units to produce radiographs of sabot/rod lateral deflections both inbore and outbore (during sabot separation). Numerically, Rabern 1992 [47] utilised the three-dimensional explicit finite element code DYNA3D to reproduce the lateral deflections obtained through experiment. In addition, numerical analysis allowed for the investigation of stress distributions experienced by the round during inbore travel and ejection.

Schmidt, et al., 1993 [48] studied the launch dynamics of kinetic energy projectiles in the hypervelocity range considering in-bore dynamics, muzzle blast, sabot discard and free flight aerodynamics. Allen 1995 [49] investigated the effects of launch tube non-straightness and asymmetric loading on the accuracy performance of kinetic energy projectiles. Issues relating to induced rigid body rotations and vibrations of the projectile were identified as possible factors affecting performance.

Shoji and Hino 2001 [50] explored the initiation of jump in long rod kinetic energy projectiles when fired from a vibrating barrel. The jump phenomena is responsible for the sight angle difference between the aiming point and the mean point of impact of the projectile [50]. This was achieved using a two-dimensional model of a projectile composed of one flexible rod and two rigid sabot segments connected with springs.

2.2.2 Shape Optimisation

The process of shape optimisation can also be performed in the FE environment. Powerful software packages, such as ReSHAPE [51], are commercially available in which design sensitivities are calculated directly from stiffness matrices used in static and modal FE analyses. The design sensitivities are used in gradient projection methods where design objectives and constraint functions are calculated iteratively after changes to the FE mesh. This enables rapid evaluation of optimisation and constraint functions and the application of shape changes directly to the FE mesh.

Design optimisation algorithms have been employed in the design engineering of many sophisticated products such as automotive components [52-54], biomechanical structures [55-57] and musical instruments [58].

In weapon applications, some literature exists in which components have been optimised for minimum weight or to shift natural frequencies. However, the optimisation processes used are not automated; rather, several different design iterations are assessed in order to find the optimum solution.

For example, Livermore and Sadowski 2005 [12] proposed a novel design concept to reduce the weight of a 5.56mm M249 barrel. Analysis of the design revealed that a significant reduction in weight could be achieved as compared to the existing system by implementing Stellite liner with a nickel boride coating. The use of these materials resulted in a barrel which was significantly less sensitive to heat, and therefore mass could be removed form the barrel as it was no longer required as a heat sink. The authors also investigated the natural frequencies of the barrel. This was to ensure that they did not coincide with the rate of fire of the weapon as this could lead to unwanted vibrations.

Authors such as Pflegl, et al., 1981 [8], Drysdale 1981 [38], Rabern and Parker 1995 [10] and Sorensen 2000 [59], have attempted to optimise the load transfer between the sabot/penetrator interface by more closely considering this interaction. However, no evidence exists of the development of an automated optimisation routine to more efficiently address such issues.

Alyanak, et al., 2005 [43] use the GENESIS finite element analysis software to optimise the design and performance of supercavitating torpedo. Detailed investigations on the effect of longitudinal and ring stiffeners on stresses, natural frequencies and global buckling were performed. However, the optimisation process again relied on the individual analysis of various design iterations in order to find the optimum solution.

2.2.3 Fluid-Structure Interaction

Fluid Structure Interaction (FSI) modelling combines both structural FE analyses, using Lagrangian formulation, with Computational Fluid Dynamics (CFD). CFD uses Eulerian formulation to describe the behaviour of a continuous fluid within a given domain. Elements are used to discretise the spatial domain, that is, the space in which the material is able to flow. The Euler Equations are then solved according to an Eulerian frame of reference such that material flows through a fixed mesh.

When performing FSI modelling, both Lagrangian and Eulerian meshes are defined within a problem. The external boundary of the Lagrangian mesh will act as a barrier to the flow of fluid. Therefore, while physically the Lagrangian and Eulerian meshes can overlap, fluid flow is not allowed in the overlapped region. FSI solvers calculate pressures generated by the fluids and then apply these to the surrounding structural system via coupling surfaces.

No literature could be sourced on the application of FSI modelling to tube launched weapon systems. The majority of authors have simplified the problem by applying loads generated by the combustion of propellant as boundary conditions directly on the structural components. Kloster 2001 [11] however used a coupled Lagrangian and Eulerian approach to study the effect of landmine detonation and fragmentation on the hull of the Grizzly armoured vehicle. The analysis was performed using Autodyn Explicit Analysis Software.

Other applications of FSI include the study of aeroelasticity [60] [61] [62] and the influence of water on flexible bodies [63] [64]. The study of impulsive loadings on underwater structures has been undertaken by McCoy and Sun 1997 [65] and Rabczuk, et al., 2007 [66].

Impact problems involving water using FSI modelling have been performed by Anghileri, et al., 2005 [67] and Lu, et al., 2000 [68]. FSI modelling is also used extensively in the medical field with applications in the modelling of blood flow, aneurysms and heart valves. Examples include [69], [70], [71], [72], [73], [74], [75], [76] and [77].

2.3 Interior Ballistics and FSI

Interior ballistics is the study of projectile motion inside the barrel. The interior ballistic process begins when the primer is ignited. The primer acts as a means of rapidly delivering a large amount of energy to ignite the propellant. As the solid propellant is burnt inside the reaction chamber, chemical energy is transformed to heat energy and kinetic energy. Hot gasses are produced which dramatically increase the pressure inside the chamber.

The projectile is designed to initially resist motion allowing significant pressure to build up in the chamber behind the projectile. The pressure required to move the projectile from its stationary position is referred to as the "shot start pressure". As the projectile travels down the barrel, the chamber volume is increased resulting in a decrease in pressure. Commonly there is an initial rapid pressure rise to a defined peak value followed by a gradual decrease in pressure as the projectile moves forward in the barrel.

Generally, chamber pressure at the muzzle varies from 10 – 30% of the recorded peak pressure. Muzzle pressure is an important parameter in weapon design as this pressure continues to work on the projectile for a short distance after exiting the barrel. This projectile is now in the intermediate ballistic phase which is vital to its range and accuracy.

In order to develop a realistic interior ballistics simulation using FSI, a material model for the combustion of propellant is required. No commercial FE Software currently possesses an established material model which is capable of representing gun propellant combustion. The majority of FE packages are able to model detonations via the use of the Jones-Wilkins-Lee (JWL) Equations of

State for explosive detonation products. However, this method is inappropriate in the study of combustion as the detonation process is significantly different, occurring in a much shorter time domain, and potentially catastrophic in the interior ballistics environment. LS-DYNA does provide an equation of state for propellant deflagration [78] but is directed at the modelling of combustion for airbag inflation

Various models exist in which the major parameters throughout the interior ballistic cycle are able to be predicted. Such parameters include chamber pressure, projectile base pressure and projectile velocity. Krier and Adams 1979 [13] propose a simple ballistic model which utilises the 'Nobel Abel Equation of State' in conjunction with a steady-state burning law to describe the recession rate of the burning propellant.

An equation of state (EOS) is a relationship between volume, pressure, quantity and temperature of a material in a given state [79]. There is no one EOS that can be derived for all materials. However, as we are dealing primarily with gasses, we can begin with the ideal gas equation which is given in Equation 2.2.

$$PV = \check{n}RT \qquad \textbf{Equation 2.2}$$

Where:

P = Pressure of the gas
V = Volume of the Gas
ň = Number of moles of the gas
T = Absolute Temperature of the Gas
R = Universal Ideal Gas Constant

The ideal gas equation is suitable for gasses at low pressure (up to 200atm) and nominal-to-high temperatures. As pressures rise above this threshold, the ideal gas equation begins to predict values further and further away from observed experimental data [79]. In the study of interior ballistics, it is not uncommon for pressures to be in the range of 5000atm at which the ideal gas equation is inadequate.

When considering interior ballistics theory, it is common practise to use an equation of state of the covolume type, namely the Noble Abel Equation of State which is given in Equation 2.3.

$$P(V- \eta w) = \check{n}RT \qquad \textbf{Equation 2.3}$$

Where

η = the covolume of the gas

w = weight of gas

Equation 2.3 only differs from the ideal gas equation in the volume expression. The covolume term compensates for the finite volume occupied by the gas molecules [80] as if they were compressed together with no space surrounding them. This therefore accounts for the high gas densities occurring in the gas chamber during combustion [80]. Figure 2.1 shows a comparison of the Nobel-Abel EOS and the Ideal Gas EOS for a mixture of gasses typical of those formed in both explosive and propellant reactions [79].

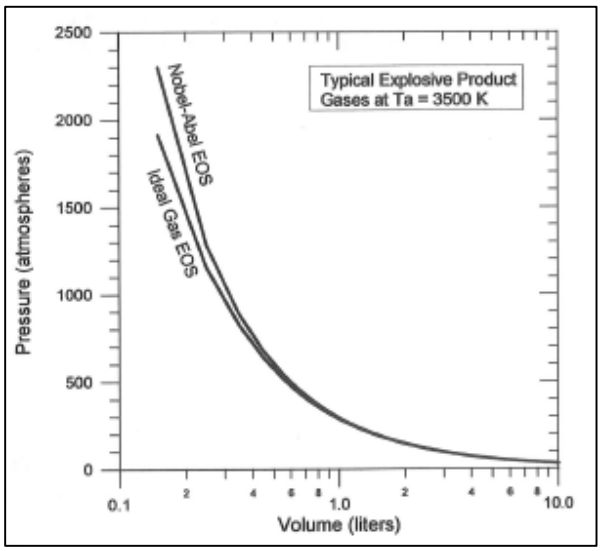

Figure 2.1: Comparison of the Nobel-Abel and Ideal Gas EOS's for a typical explosive or propellant product gas mixture [79]

Other authors have also utilised the Nobel-Abel Equation of State in ballistics applications. Papliski, Leciejewski et al. 2004 [81] discuss thermodynamical extensions to the Nobel-Abel Equation of State to describe properties of combustion products for given propellants. Johnston 2005 [80] uses the Nobel Abel Equation of State and derives additional thermodynamic functions for ballistics modelling using computational fluid dynamics solvers.

Examples of applications of interior ballistics models also exist in the literature. Rabern and Parker 1995 [10] used a simulation of interior ballistics to determine the launch conditions of various KE projectiles, considering the grain geometry of the propellant and the volume available in the breech. The pressure, velocity, acceleration and axial position of the projectile as well as the breech temperature were all calculated for many small time increments over the interior ballistic cycle.

The computational predictions of three standard interior ballistics codes widely used to predict the performance of modern interior ballistic systems were compared by Heiser 1999 [82]. The codes considered were a thermodynamic model with global parameters (IBHVG2), a 1-D gas-dynamic model (XKTC) and a 2-D gas-dynamic model (AMI). Significant differences in the predictions of the codes were found for high loading density charges.

Newill, et al., 2004 [83] performed a coupled analysis of projectile dynamics and interior ballistics using the DYNA3D and ARL-NGEN3 Codes. Results of interior ballistics were taken from the ARL-NGEN3 code and applied to the projectile using DYNA3D in order to assess the structural response. The analysis revealed the presence of significant pressure waves during the propellant burn which would pose significant challenges to the projectile designer. Such work identifies the need for coupled analysis of both structural and fluid dynamics when considering interior ballistics in the design of projectiles.

Earlier versions of the NGEN code were demonstrated by authors such as Nusca 1999 [84]. The advantages of the NGEN package over lumped parameter codes such as IBHVG2 which assume that grains and products of combustion constitute a well stirred mixture were identified. Nusca 1999 states that one-dimesional two-phase codes such as XNOVAKTC have also been used successfully in the past. The NGEN code however, was developed to accommodate charges which produce non-

uniformities in ballistic events (e.g. ignition, flame spreading, pressure wave generation) encompassing a multidimensional multiphase flow model.

Another example of a ballistic simulator is the Gamma Dynagun which was used by Ritchie, et al., 1999 [85] to predict the influence of the propelling charge on the performance of large calibre 120mm-tank ammunition. Pocock, et al., 2004 [86] use the FNGUN interior ballistics model of a 155mm gun system to compare the performance of non perfect propellant grains against perfect (designed) propellant grain geometries.

Dayan and Pila 2004 [87] developed a two-phase, two-dimensional transient interior ballistics model which was used with the PHOENICS CFD package. The model predicted the combustion modes generated by two different black powder configurations in the igniter. The results showed good agreement with experimentation.

Woodley 2004 [88] considered the influence of propellant constituents on molecular weight and the contribution of these towards attaining high muzzle velocities. The CTA1 interior ballistics code, a quasi-1D, multiphase flow model, was used to predict the internal ballistic performance of over fifty current and novel propellants. The CTA1 code was used again by Woodley, Henning et al. 2004 [89] in the comparison of various composite gun propellants. In this instance, the results of the CTA1 code were compared against the two dimensional FHIBS code which proved to be more accurate in this application.

As a first approximation and a means of developing an FSI capability in tube launched weapons applications, a high pressure gas can be initialised in the chamber and allowed to expand in order to accelerate the projectile. However, this method does not offer any insight into the effects of propellant combustion on the interior ballistic performance of the system. In order to further develop this type of analysis, a material model for the combustion of propellant will need to be created and incorporated into the FE environment as a subroutine.

The need for this development was highlighted above with the description of work performed by Newill, et al., 2004 [83]. This work used interior ballistics codes to identify interesting burn phenomena of the propellant, independent of the behaviour of the structural system. It was then necessary to manually apply the discovered burn phenomena to a Lagrangian Finite Element model of the projectile in order to assess its impact on design. The use of Fluid Structure Interaction Modelling including propellant burn, would allow for all these consideration to be included in the one dynamic analysis. That is, the behaviour of the combusting propellant could be considered simultaneously with the structural performance of the gun/projectile system.

The use of FSI in addition to shape optimisation and explicit finite element analysis can provide for a virtual design environment in which weapon prototypes can be developed. As a result, a significant level of design sophistication can be achieved prior to the need of prototype manufacture and testing.

2.4 Tube Launched Weapons: General Definitions

A tube launched weapon system can essentially be defined as a projectile launching device consisting of a projectile guiding tube which is connected to a reaction chamber [13]. The combustion of propellant, which begins in the reaction chamber, creates hot, high pressure gasses which propel the projectile down the tube or barrel.

2.4.1 Gun Barrels

A gun barrel is essentially a closed tube which provides support and orientation to the projectile as it is fired. A schematic of a typical gun barrel illustrating the basic components can be seen in Figure 2.2. A barrel is often defined in terms of calibres, where the calibre is the in-bore diameter of the gun. The length of the gun is then referenced as a multiple of calibres, for example, a fifty calibre gun has a length fifty times its bore diameter.

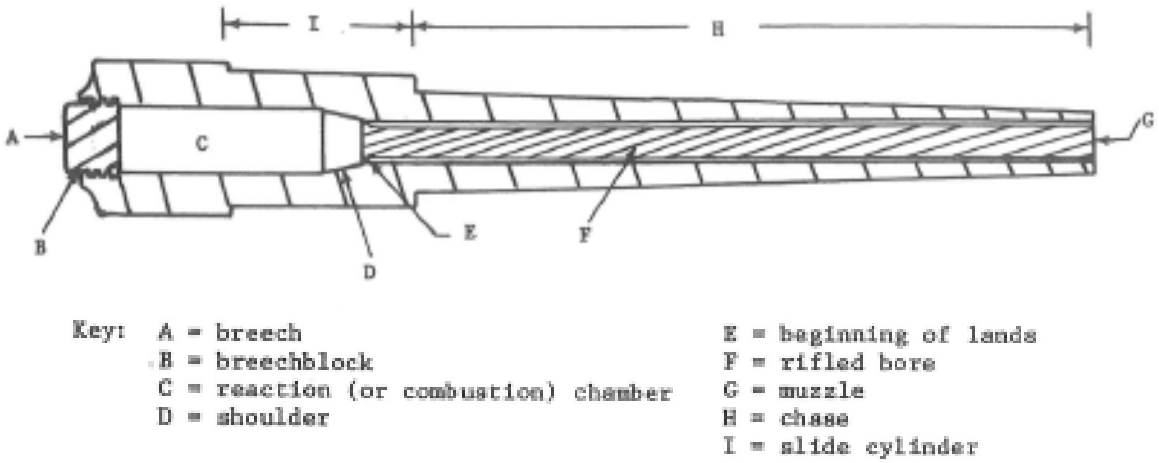

Figure 2.2: Gun Barrel Components [13]

The breech is the aft end of the gun barrel which is opened for projectile and propellant loading but is closed and seals the barrel when fired. The specific component or plug used to perform the opening and sealing is referred to as the breechblock [13].

Forward of the breechblock is the reaction chamber where propellant is loaded and ignited. The chamber diameter is usually larger than that of the barrel bore and therefore the front of the reaction chamber, known as the shoulder, is tapered. The larger diameter in this region allows more propellant to be packed for a given length. The tapering also accelerates the combustion gasses as they propel the projectile.

The diameter of the barrel beyond the shoulder is maintained right through to the front end of the barrel, or the muzzle. For rounds which are spin stabilised, the bore of the barrel must be rifled. Rifling involves engraving a set of spiral grooves into the bore surface [13]. As the projectile is fired, it engages the spiral grooves which force the projectile to spin at a specified rate based on the characteristic twist of the grooves. Twist is defined as calibre per turn which is the bore length taken for the rifling to make one complete turn.

Generally, small calibre gun barrels are rifled to impart spin to the projectile to ensure that the projectile stabilises during flight. Rifling is omitted for large calibre guns as the projectile is heavier and the environmental conditions have little effect during flight. Fin or cone stabilisation methods are therefore employed in these instances. Medium calibre rounds fired from smooth bore barrels are also generally fin or cone stabilised or more recent work has looked at lattice finned projectiles [90].

Temperature fluctuations are also very important to ensure the bore temperature remains below a critical value required for safe loading of projectiles. Cordes and Reinhardt 2004 [91] and Boisson 2004 [92] have considered this phenomenon in large calibre weapons providing information relating to temperature rises at specified fire rates.

2.4.2 Propellant

From the earliest days of firearms till about the 1880's, black powder which is formulated from potassium nitrate (saltpetre), sulphur and carbon [93] with an average ratio of 75:11:14 [94] was used. Black powder is still in use today as an igniter material in modern gun propelling charges [95]. Nitrocellulose, commonly referred to as smokeless powder, was discovered in 1845 by Schonbein [93] and forms the basis of most modern propellants.

The term smokeless is derived from the fact that the decomposition products of nitrocellulose-based propellants are entirely gaseous except for approximately half of a percent of water vapour. This is in stark contrast to black powder, where only approximately 43% of decomposition products are gaseous [96], the remaining 57% consisting of solid particles thus reducing the efficiency of the propellant.

The gasses which create the necessary pressure to accelerate the projectile are generated by the ignition of an explosive train termed the "propellant train" [97]. It consists of a primer, igniter and propellant. The propellant train is initiated by the primer which is a fast burning, high energy pyrotechnic formulation. Percussion primers are commonly used where the sensitive explosive is initiated by a mechanical energy source in the form of a firing pin [98].

The energy generated by the primer is transmitted and intensified by the igniter [97]. The igniter is defined as the principal energy source for initiating the propelling charge [98]. Igniter systems vary based on the gun systems. The igniter composition for small arms is very different to igniter systems for medium size and large calibre gun systems. The examples of Picolo tubes and Centre Core systems is mainly for medium calibre or large calibre gun systems, a full description of which can be found in [98].

The size and shape of propellant grains is vital in controlling the burning rate of gun propellants. As a result, propellants come in a variety of forms including flakes, strips, sheets, pellets and perforated grains [13]. Modern gun propellants generally utilise perforated grains due to their superior ability to manipulate the release of gases and burn time. Figure 2.3 contains a schematic of a perforated cylindrical grain identifying the key dimensional properties.

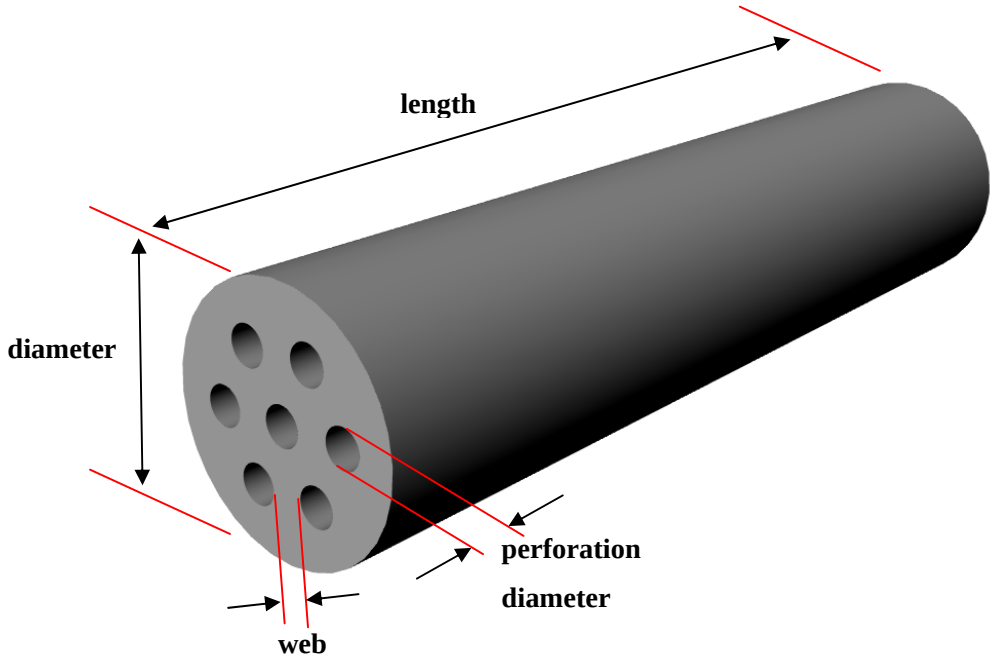

Figure 2.3: Perforated Propellant Grain-Physical Properties.

At a constant pressure, the evolution of gases from a burning propellant depends upon the amount of surface area exposed to the burning. The manner in which the burn proceeds will depend on whether the exposed surface area is increasing, decreasing or remaining constant. Based on this notion, propellant grains are designed to either be regressive, neutral or progressive. A regressive grain's surface area decreases with burning, a progressive grain's surface area increases and the neutral grain's surface area remains relatively unchanged throughout the burn cycle.

The burning rate of nitrocellulose propellants increases as a direct function of increased temperature and pressure [96]. A fine balance must therefore be achieved in designing a specific charge for a given gun such that material tolerances are not exceeded.

2.4.3 Rounds

The term round defines the entire launch package which is loaded into a gun. The round generally consists of the projectile, propellant, cartridge and primer. The propellant provides the energy to accelerate the projectile to the required muzzle velocity. The case used to house the propellant and ignition system is known as the cartridge. The primer is considered the ignition element and generally consists of a sensitive explosive mixture.

Rounds can be broadly classified into three different categories based on their assembly. The first category is termed Fixed Round and generally applies to small arms with calibres less than 20mm [97]. In a fixed round, the projectile is partially inserted into the top of the cartridge case above the propellant, thus creating a single unit [99]. The amount of propellant can not be adjusted for firing. The loading of this type of ammunition is completed in one single action.

The second category is termed Semi Fixed Round and consists of multiple parts. These include the projectile and a cartridge which contains the propellant charges and primer. The propellant uses a main charge which can have additional units of charge added to alter the trajectory of the projectile. The loading of this weapon is a two stage process where the projectile is loaded first followed by the cartridge [99].

The third category can be termed Separate Loading Round or Propellant Bag Charge and is generally used in large calibre guns. This round is composed of multiple parts, however, in this case the primer, propellant, projectile and fuse are all loaded separately [97]. The propellant is contained in a powder bag [99].

2.4.3.1 Projectiles

Projectile design is governed by the target it is to defeat and therefore a large degree of variability exists. Some of the broader projectile types include Fragmenting Projectiles, High Explosive Projectiles, Armour Piercing Projectiles, High Explosive Anti Tank Projectiles, Anti-Concrete Projectiles, Incendiary Projectiles and Mortar Projectiles. While a description of each is beyond the scope of this review, the reader is referred to the following references [97, 99].

Projectiles may also be broadly classed in terms of the stabilisation method they employ. Generally, there are two techniques used for primary stabilisation. These include spin-stabilisation and fin-stabilisation. The concept of spin-stabilisation was introduced in Section 2.4.1 in the description of rifled gun barrels. In essence, spinning a projectile relies on gyroscopic forces to provide directional stability.

3 Methods

3.1 Introduction

The analysis tools and techniques utilised throughout this research are presented in greater detail in this chapter. A detailed description of the underlying theory is beyond the scope of this document. Rather, the fundamental concepts of the methods used to achieve the research goals are presented.

3.2 Finite Element Analysis

The Finite Element Method provides a means by which a numerical solution can be obtained for a specific problem [22]. Large and complex geometries are discretised into elements which are connected by nodes to form a mesh. Studies can then be performed using known load/boundary conditions and material properties.

Most finite element analysis programs use implicit methods in performing linear static analyses and in some transient dynamic analyses. With respect to transient solutions, most implicit methods use Newmark schemes to integrate in time [23]. Accelerations are obtained by inverting the mass matrix.

When applying such techniques to highly transient dynamic phenomena, the process becomes far more computationally strenuous. In these cases, time marching integration schemes, generally referred to as explicit methods, are employed due to their superior non-linear problem solving capabilities.

The mass matrix generated using explicit methods is diagonal and therefore any inversion is trivial. Therefore, explicit methods are more efficient as they do not require matrix decompositions or matrix solutions. In addition, no iteration or tangent stiffness matrices are required. Instead, the explicit procedure integrates through time using the process illustrated in Figure 3.1 for each time step.

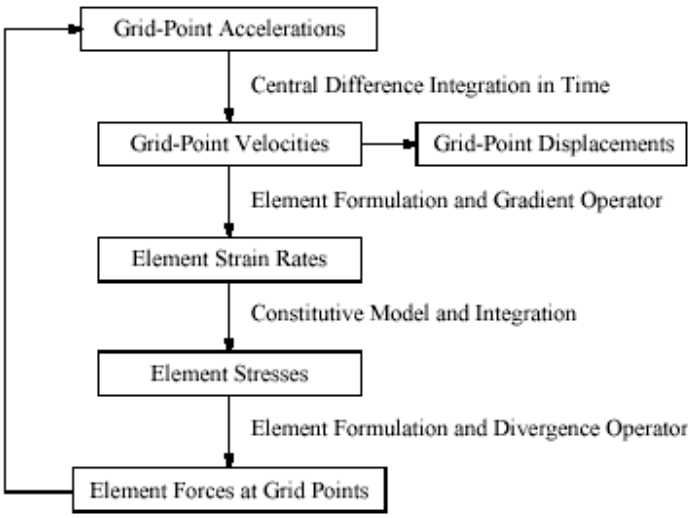

Figure 3.1 Explicit Solution Procedure for each Time Step [23]

One advantage of implicit methods is the fact that they are able to be made unconditionally stable regardless of the time step size. Explicit codes however, must ensure that the time step remains below the time taken for a stress wave to cross the smallest element in the mesh. In general, the time step is obtained using the following equation:

$$\Delta t < \Delta x/c \qquad \textbf{Equation 3.1}$$

where

Δt = Time Step

Δx = Element Size

c = Soundspeed

A stability factor is then applied to the smallest time step calculated from the entire mesh to ensure a stable time step for the cycle.

Due to the highly dynamic nature of the work undertaken as apart of this research, it was decided that explicit method of analysis would be the most appropriate. As a result, the MSC. Dytran explicit solver was selected for dynamic analyses. All pre and post processing was performed using MSC. Patran. The major computational aspects of MSC. Dytran utilised in this research are presented below.

3.2.1 Solvers

Two finite element solvers are contained within MSC. Dytran. These include a Lagrangian Finite Element Solver and an Eulerian Finite Volume Solver. Based on the given problem, a solver is chosen in order to provide an optimal numerical solution. While the Lagrangian method is most common for engineering applications, Eulerian solvers are often implemented for analyses of fluids or very large deformation problems. A basic description of each method follows.

3.2.1.1 Lagrangian

Lagrangian methods solve the Euler Equations assuming a Lagrangian frame of reference, where the computational mesh moves according to material flow as shown in Figure 3.2. Grid points are fixed to locations on the body being analysed. These grid points are then connected using elements of material in order to generate the mesh [23]. In essence, the Lagrangian solver is calculating the behaviour of elements of constant mass, with no material transported through element faces. Initially, the Lagrangian mesh should conform well to the geometry of the body, generally being of higher quality than an Eulerian grid.

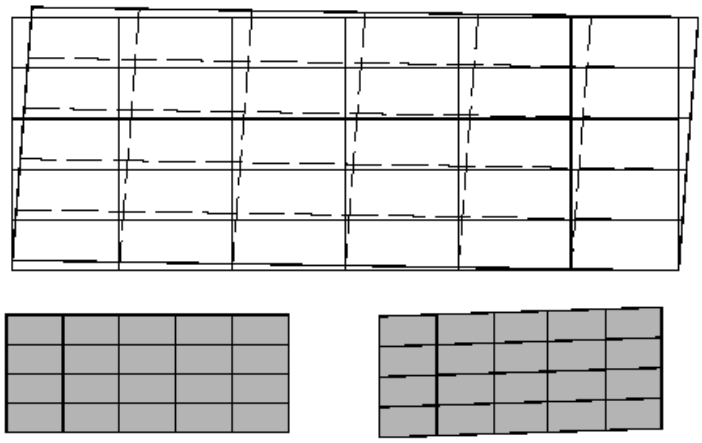

Figure 3.2: Lagrangian Mesh: Mesh moves according to material flow [23]

As the body undergoes deformation under applied loads and boundary conditions, the grid points move causing the elements to distort. The elements can assume virtually any shape, however, their performance is most accurate when they are close to cuboidal [100]. MSC. Dytran purposefully does not perform any checks on element shape, so as to not abort the solution due to one or two badly distorted elements. The onus is therefore on the user to ensure elements in critical regions remain stable and of suitable shape.

If the deformation of materials is well managed, with good mesh resolution in critical areas, the Lagrangian method should be able to provide an accurate solution. However, Lagrangian solvers are not suitable for large deformation problems or simulations involving fluids. As the flow becomes highly distorted so does the mesh resulting in low quality approximations which may even cause the solution to fail. Distorted Lagrangian meshes lead to artificial stiffness in the model where elements lock under certain modes of distortion. Eulerian solvers are therefore preferred in such instances.

3.2.1.2 Eulerian

Eulerian methods solve the Euler Equations according to an Eulerian frame of reference, where the mesh remains fixed. That is, elements are used to discretise the spatial domain, through which material is able to flow as shown in Figure 3.3. The grid points in Eulerian solvers remain fixed in space while the connected elements form partitions of that space. The material of a body flows through the fixed mesh, with mass, momentum and energy being transported from element to element depending on the direction and velocity of the flow [23]. In essence, the Eulerian solver calculates the motion of material through elements of constant volume.

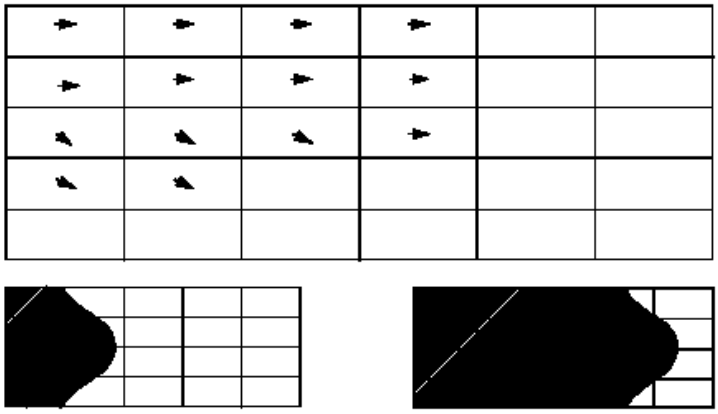

Figure 3.3: Eulerian Mesh: Mesh remains fixed while material flows through [23]

The definition of an Eulerian mesh in MSC. Dytran is conducted in exactly the same manner as that of a Lagrangian. The Eulerian mesh can be of an arbitrary shape and have an arbitrary numbering system [23]. However, the use of an Eulerian mesh is significantly different. Most importantly, the mesh must be constructed in such a way that it is large enough to accommodate the material after deformation. The mesh essentially forms a container, and material cannot leave the mesh unless specifically prescribed. A mesh that is too small can lead to unwanted stress wave reflections and pressure build ups.

Eulerian codes require the definition of elements throughout the entire spatial domain which may potentially be of interest. In contrast, Lagrangian codes allow better mesh resolution in critical areas, only requiring elements where material exists. As a result, Lagrangian solvers are usually less computationally extensive in run time and memory.

Both Eulerian and Lagrangian meshes can be used in the same simulation, where coupling surfaces are used to allow interaction of the meshes. A description of coupling and solver interaction will be given in the Fluid Structure Interaction section later in this chapter.

3.2.2 Material Models

The DMAT material model in MSC. Dytran was used for all elements throughout the research. The DMAT material entry provides a high degree of flexibility in defining material performance. Various combinations of material descriptions including Equations of State, Yield Models, Shear Models and Failure Models can be used to model the behaviour of materials. Below is a brief description of each of the constitutive models used.

3.2.2.1 Equation of State

The equation of state stipulates the bulk behaviour of the given material. Various forms of the equation exist in MSC. Dytran in order to represent a range of materials. These include polynomial equations, a gamma law gas equation or an explosive equation.

A Polynomial Equation of State was used to represent all Lagrangian elements. The equation relates pressure to the relative volume and specific internal energy using a cubic equation. The Polynomial Equation of State is given below for both Compression and Tension conditions.

In Compression ($\mu > 0$)

$$p = a_1\mu + a_2\mu^2 + a_3\mu^3 + (b_0 + b_1\mu + b_2\mu^2 + b_3\mu^3)\,\rho_0 e \qquad \textbf{Equation 3.2}$$

In Tension ($\mu \leq 0$)

$$p = a_1\mu + (b_0 + b_1\mu)\,\rho_0 e \qquad \textbf{Equation 3.3}$$

where

$\mu = \xi - 1$

$\xi = \rho / \rho_0$

ρ = overall material density

ρ_0 = reference density

e = specific internal energy per unit mass

The Gamma Law Equation of State was also used for the modelling of gasses. This equation defines pressure as a function of density, the specific internal energy and the ratio of specific heats for an ideal gas. The Gamma Law Equation of State is given below.

$$p = (\gamma - 1)\rho e \qquad \textbf{Equation 3.4}$$

where

ρ = overall material density

e = specific internal energy per unit mass

γ = ratio of specific heats (C_p/C_v)

MSC. Dytran also allows for a user defined equation of state. This capability was used in developing a material model for the combustion of propellant in order perform fluid structure interaction modelling.

The User Defined Equation of State was included into the analysis via the EXEOS Subroutine in MSC. Dytran. This subroutine can be used to calculate the pressure for Lagrangian or Eulerian elements according to a user specified model. It was necessary to write and compile the user defined model in FORTRAN 90 Programming Language in order to ensure compatibility with MSC. Dytran. A more thorough description of the subroutine is presented in Chapter 5.

3.2.2.2 Yield Models

A range of Yield models exist within MSC. Dytran which can be used to model elastic perfectly plastic behaviour, bilinear elastoplastic behaviour, piecewise linear behaviour or hydrodynamic behaviour. If no Yield model is stipulated, the material is considered to be fully elastic by MSC. Dytran.

For the analyses undertaken as apart of this research, a Von Mises criteria (YLDVM) was utilised for Lagrangian elements which resulted in bilinear elastoplastic behaviour. The Young's Modulus (E) and Yield Stress (σ_y) were defined explicitly for each material during the model set up. Yielding then occurred when the calculated Von Mises Stress (σ_{vm}) exceeded the Yield Stress. The expression for Von Mises Stress used in MSC. Dytran is given below with σ_1, σ_2 and σ_3 being the principal stresses.

$$\sigma_{vm} = \sqrt{\left[(\sigma_1 - \sigma_2)^2 + (\sigma_2 - \sigma_3)^2 + (\sigma_3 - \sigma_1)^2\right]/2} \qquad \textbf{Equation 3.5}$$

3.2.2.3 Failure Model

Various Failure models exist in MSC. Dytran. Failure may be defined by a maximum plastic strain or maximum stress limit. When the selected failure criterion is met, the material is no longer able to sustain its loading and effectively breaks. If no failure model is defined, the material possesses no failure criteria and will continue to distort according to the Yield Model.

The Maximum Plastic Strain Failure Model (FAILMPS) was utilised in this investigation where a maximum Von Mises effective plastic strain was explicitly defined for a material. Element failure occurred when the plastic strain exceeded the specified maximum (failure) value. That is, upon failure, all the stresses in the element were set to zero and the element could no longer carry a load. In the MSC. Dytran Output Controls, it could be stipulated that failed elements be removed from the mesh as the calculation proceeded.

3.2.3 Constraints and Loading

Constraint and Loading conditions are applied to models in order to simulate the operational conditions of the body under consideration. Constraints and Loading, both Lagrangian and Eulerian, will be described briefly in the sections below. Contacts, defining the interaction of Lagrangian parts, are also described.

3.2.3.1 Lagrangian Loading and Constraints

Lagrangian constraints prescribe the motion of a translational or rotational degree of freedom for a given node or set of nodes. The constraint is maintained throughout the entire analysis and is mandatory in defining both boundary and symmetry conditions.

Methods by which Lagrangian bodies can be loaded in MSC. Dytran include Concentrated Loads and Moments, Pressure Loads, Enforced Motion and Initial Conditions. Concentrated loads and moments are applied directly to nodes of Lagrangian elements. These loads can be constant throughout the simulation or can vary as a function of time using a table.

The majority of Lagrangian loading in this research was performed using Pressure Loads. These were best able to simulate the conditions imposed by the combusting propellant during the interior ballistic cycle. Pressure loads are applied to element faces and can be constant or vary with time.

Time dependent pressure profiles were generated using a table to define a piecewise linear graph of pressure versus time. MSC. Dytran varied the applied pressure throughout the simulation by interpolating data from this graph for each time step. Lagrangian loading was unnecessary when performing Fluid Structure Interaction modelling, as loads on Lagrangian bodies were generated by the interaction of Eulerian materials.

3.2.3.2 Eulerian Loading and Constraints

Eulerian Loading and Constraints in MSC. Dytran can be applied using several methods. These include specifying initial conditions for materials, defining flow barriers, applying body forces, activating pressure and flow boundaries or by coupling to Lagrangian meshes. If no boundary condition is prescribed for an exterior face of an Eulerian mesh, then MSC. Dytran automatically generates a barrier through which material is unable to flow.

The use of Initial Conditions was most prevalent to this research. It allowed the initial state of materials to be prescribed, allowing MSC. Dytran to determine the consequent behaviour of the system thereafter. The definitions of geometrical regions were used to identify the placement of materials within the Eulerian Mesh. Initial properties were also applied to these regions.

3.2.3.3 Contacts

In MSC. Dytran, the interaction of solid bodies, both rigid and deforming, can be prescribed using Contacts. Three types of contact surfaces exist in MSC. Dytran, which are General Contact and Separation, Single Surface and Discrete Grid Points.

In this study, the General Contact and Separation definition was used. It was capable of modelling the contact, separation and sliding of multiple Lagrangian bodies including friction. The contact surfaces were defined by specifying the element faces where contact was expected. It was necessary to define one as the slave surface and the other as the master, ensuring no initial penetration of the surfaces.

For each time step, each node in the slave surface is checked against the nearest master segment. If the grid point has penetrated the segment, then forces are applied normal to the master surface to prevent any further penetration. The magnitude of these forces is determined by the amount of penetration and the element properties possessed by the contacting bodies. To ensure a stable contact definition, the mesh density of the slave surface should be finer than that of the master.

Friction forces are also applied parallel to the contact surfaces. The magnitude of the force is the product of the normal force and user defined coefficients of friction. The friction forces are applied in the direction opposite to the relative motion of the surfaces.

3.2.4 Fluid Structure Interaction

Fluid structure Interaction modelling requires that both Lagrangian and Eulerian Meshes are able to interact. A coupling algorithm used in MSC. Dytran enables stresses in the Eulerian material to exert forces on the Lagrangian mesh causing it to distort. The interaction is achieved through the description of coupling surfaces on the Lagrangian mesh. General Coupling is the method most commonly used in MSC. Dytran and is described briefly below.

3.2.4.1 General Coupling

General Coupling in MSC. Dytran allows for both Eulerian and Lagrangian meshes to be used in the same calculation. In order to achieve the interaction of solvers, a coupling surface must be created on the Lagrangian body. It is this surface which allows the transfer of forces between the two solvers. The surface acts as a boundary to material flow in the Eulerian mesh. Stresses in the Eulerian elements which contact the boundary generate forces on the coupling surface which are transferred to the Lagrangian elements causing them to distort.

The one restriction on the definition of a coupling surface is that it must form a closed volume. As a result, some problems may require the inclusion of dummy Lagrangian elements in order to satisfy this condition. In addition, the closed volume formed by the coupling surface must intersect at least one Eulerian Element at the start of the calculation in order to be recognised by the Eulerian Mesh. Figure 3.4 contains an example of General Coupling in MSC. Dytran.

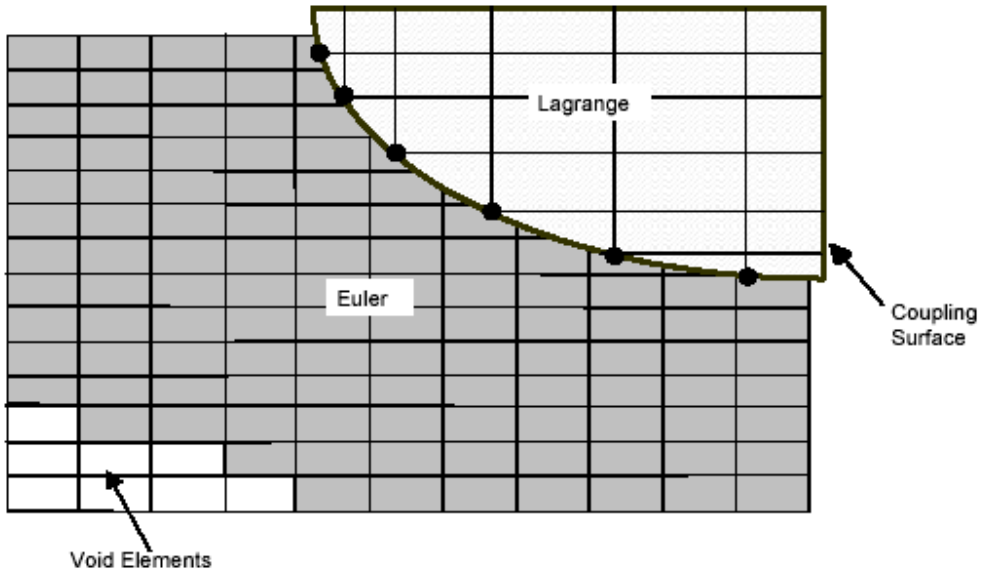

Figure 3.4: General Coupling in MSC. Dytran [23]

3.3 Shape Optimisation

The commercially available shape optimisation program ReSHAPE was used in this study as a part of the VDP. The program ReSHAPE uses sensitivity analyses based on the stiffness matrix of a linear finite element model to iteratively optimise shape for better performance. Raw sensitivity is defined as the differential of a performance parameter such as displacement or stress with respect to nodal coordinates. Mesh-geometry associativities, in the form of influence functions, are then applied to the raw sensitivity to ensure model smoothness is maintained. A brief description of the optimisation process used by ReSHAPE follows.

3.3.1 Raw Sensitivity

The sensitivity of a performance parameter, which could be displacement, stress, vibration mode etc, to the change of nodal coordinates is termed "Raw Sensitivity". For example, if π is the scalar value of a performance parameter and x is the vector of nodal co-ordinates, then the nodal or "raw" sensitivity can be defined as a row vector $d\pi/dx$ [101].

The raw sensitivity is often used as a preliminary analysis tool for identifying sensitive regions in complex structures. This is often useful for two reasons. Firstly, it avoids pointless attempts at trying to improve a structure which is inherently a bad design. And secondly, it allows for the more sensitive regions of a structure to be identified early for subsequent more detailed analyses.

While the raw sensitivity is useful for truss structures and as a preliminary analysis tool, its application to the detailed re-shaping of complex structures is almost pointless. It is incapable of retaining the original smoothness of a model as it is absent of any mesh-geometry associativity. That is, the changes derived for the model are directly proportional to the sensitivities $d\pi/dx$, possessing no sense of the original geometry.

It is therefore necessary to introduce a process which creates a best fit to nodal changes Δx to retain the smoothness of the model. This concept is known as smoothing and is discussed in the next section.

In order to demonstrate the use of Raw Sensitivity, an example was taken from the "Starting with ReSHAPE" Manual [102]. Figure 3.5 contains two images of a bracket which required its natural frequency be increased by 20% in order to avoid system resonances. An analysis of Raw Sensitivity was performed on the model to identify the most sensitive regions to changes in frequency.

The image on the left highlights some stiffeners which were originally included in the bracket in an attempt to alter the frequency. However, the plot of raw sensitivity demonstrates that these stiffeners are insensitive to changes in frequency and therefore only add unnecessary weight. It was pointless to include these stiffeners in the optimisation process and they were therefore removed prior to an attempt of improvement.

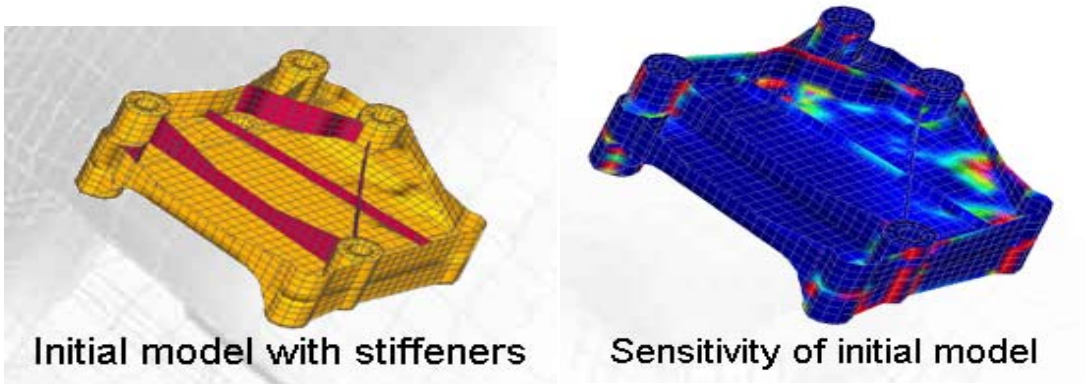

Figure 3.5: Raw Sensitivity Analysis of Bracket performed using ReSHAPE [102]

3.3.2 Smoothing

Previously, it was discussed that the concept of the raw sensitivity could be defined by the row vector $d\pi/dx$ and the shape change incorporated into the model was proportional to this row vector. To overcome any irregularity of shape generated by the above method it is necessary to introduce generalised co-ordinates q into the vector of nodal co-ordinates resulting in the relationship $x = x(q)$ known as mesh-geometry associativity [101].

In order to achieve a smooth change, it is firstly necessary to redefine the nodal sensitivities in terms of the generalised co-ordinates q as shown below:

$$\frac{d\pi}{dq} = \frac{d\pi}{dx} \cdot \frac{dx}{dq}$$

Equation 3.6

where:

$\frac{d\pi}{dx}$ = Raw Sensitivity

$\frac{dx}{dq}$ = Influence Matrix

The availability of the influence matrix is a necessity for reshaping a finite element model consisting of continuum elements as it provides the associativity between the finite element mesh and the related design [101].

Based on the fact that Δq is proportional to the sensitivity of the generalised co-ordinates $d\pi/dq$, the mesh change Δx can be calculated through the use of the influence matrix dx/dq as given below:

$$\Delta x = \left(\frac{dx}{dq} \right) \cdot \Delta q$$

Equation 3.7

This process forms the fundamentals applied to the concept of smoothing which provides a best fit to the nodal changes Δx. The process, however, is only correct theoretically for regular meshes and regular distributions of generalised co-ordinates. In practice, it is appreciated that meshes can be very irregular and that the design variables cannot be distributed regularly either. This restriction is overcome by enforcing the same best fit on both the nodal changes and on the changes of the generalised co-ordinates.

In ReSHAPE there exists three different processes that can be used to perform smoothing. These processes are FUNCTION, GEOMETRY and VECTOR. Only the FUNCTION process will be described below as it was the one utilised in this research.

3.3.2.1 Smoothing in ReSHAPE using Process(FUNCTION)

Using the 'Process(FUNCTION)' command in ReSHAPE introduces influence functions into the shape optimisation process. In ReSHAPE the influence function assumes the form:

$$\omega(x) = e^{-\left(\frac{d}{s}\right)^2}$$ **Equation 3.8**

where:

d = Distance form a control point

s = Pseudo support

This method of smoothing begins by calculating the raw sensitivities in the domain nodes i.e. nodes which are allowed to move. The influence function, as given above, is then used to calculate the influence matrix by assigning the influence function to a number of required design variables or 'control points'. These control points are selected by the user in regions where the optimisation is wanted.

The raw sensitivities are then transformed, by use of the influence matrix, into the control points using a similar method to that applied in redefining the nodal sensitivities into the generalized co-ordinate system as described previously. A best fit is then calculated to the control point's sensitivities and then transferred back to the nodes via the identity matrix.

The pseudo support 's' can be manipulated in such a way that the support of the influence function can be extended or reduced. That is, based on the value of the support the locality of the effect of the influence function can be determined i.e. the smaller the support, the more local the effect.

The advantage of using this technique is the fact that the influence function has unlimited support as opposed to using the other smoothing processes in ReSHAPE. Unlimited support allows for the model to assume any shape and generates a smooth transition of the shape between domain and non-domain regions. Multiple influence functions with overlapping domains are blended so that an appropriate overall relationship between the user defined control points and the model mesh is created.

4 Case Study: 16th Century Cannon

4.1 Introduction

In this chapter, the Virtual Design Process for tube launched weapon systems is introduced through a case study of a 16th Century Cannon. Methods of implicit and explicit finite element analysis are presented in addition to fluid structure interaction modelling. Shape optimisation analyses are also performed to achieve two different design objectives. While the study provides some useful insight into the behaviour of 16th century cannon, the main aim is to introduce and assess the use of VDT's in tube launched weapons applications. Aspects of this work were included in a paper entitled "Virtual Design Processes for Weapon Systems" which was presented at the *Eleventh Australian International Aerospace Congress,* Melbourne, March 13-17, 2005.

4.2 16th Century Cannon: Background

In times when the theory of internal ballistics and the stress and strain behaviour of thick walled tubes was virtually non existent [96], cannon makers relied on a process of trial and error to develop their artillery, building upon the strengths and weaknesses of earlier designs. Sixteenth century cannon founders had no means of measuring internal stresses and therefore the experience and bias of the founder dictated the design and manufacture of cannons.

An area of even greater uncertainty related to the metallurgy of bronze and the kinds of alloys that would produce the most effective cannon. Sixteenth century cannon founders were confident using a melt of 80-90 percent copper with the balance tin, in which 3 to 5 percent of impurities existed. Further complexities relating to the curing properties of bronze resulted in the concentration of tin varying through the material thickness. Only through strict manufacturing procedures and casting techniques could the founder hope to produce consistent and effective cannons.

4.2.1 Photoelastic Model Analysis of Cannons

In 1969, John Francis Guilmartin Jr. and a team from Princeton University attempted to demonstrate the relationship between internal stress and external design of a sixteenth century cannon using photoelastic model analysis [96]. Photoelastic model analysis creates optical fringes to illustrate stress behaviour, a concentration of fringes identifying regions of high stress.

A scale model of the breech of a Portuguese ten-pound half culverin (circa 1530, found in the collection of the Museu Militar, Lisbon) was machined from PL-4 resin. The model was plugged at a location where the cannonball would have sat in the loaded weapon. A pressure proportional to the relationship of peak firing pressure to the yield stress of the original cannon was then applied causing the resin to deform slightly [96].

The results of this analysis can be seen in Figure 4.1. High regions of stress are observed in the corners of the breech, and to a lesser degree at the location where the model was plugged. The main body of the barrel illustrates a gradual decrease in stress from the internal to external walls of the barrel. However, the analysis does not relate material and structural properties to actual values of stress.

Furthermore, the model must assume a totally homogenous material throughout which is not true in the case of cannons. Tests performed on sixteenth century cannon metal taken from different parts of the cannon showed significant variation in tin content from muzzle to breach. This is the result of the tendency of tin and copper, in a melt of molten bronze, to segregate as the molten metals cool, the tin migrating towards the last portions of the metal to solidify [96]. Therefore, the distribution of tin would depend on the orientation of the barrel when cast. This phenomena was generally exploited in order to provide for increased material strength and toughness in regions where required.

4.3 Implicit Finite Element Analysis of 16th Century Cannon

FEA was used to determine the Von Mises Stress distribution created in the cannon under firing conditions. Compared to the Photoelastic Model Analysis, FEA was able to provide a more realistic representation of cannon materials, hence providing further insight into the weapon's performance.

A quarter finite element model of the Portuguese ten-pound half culverin breech was created using the MSC. Patran pre-processor for analysis in the MSC. Nastran implicit solver. The model was constructed using the true dimensions of the original cannon, with a bore diameter of 120mm. The barrel was modelled using solid Lagrangian elements.

The blast pressure inside the cannon was simulated by applying a static pressure field representative of peak firing pressure. Similar to that assumed in the photoelastic model analysis, the pressure was applied to the internal walls of the barrel between the breech and hypothetical location of the cannonball. The pressure value used was adapted from experimental data obtained by Capt Thomas Jefferson Rodman on a large-bore (42 pounder) naval gun in the nineteenth century [103]. Based on this data, a maximum pressure of 69MPa was interpolated for the ten-pound cannon under consideration.

4.3.1 Homogenous Material Model

An elastic-plastic bronze material model was generated and applied to the barrel. For comparison to the analysis performed by Guilmartin 1974, a homogenous material definition was used in the first instance. A bronze alloy possessing 19% Tin was selected, the properties of which can be seen in Table 4.1. Through the application of symmetry conditions it was possible to utilise a quarter model of the breech for the analysis.

Table 4.1: Bronze Alloy Material Properties

	Bronze Alloys		
Property	19% Tin*	16% Tin*	10% Tin*
Density (*g/cc*)	8.64	8.64	8.64
Modulus of Elasticity (*GPa*)	100	100	100
Poisson Ratio	0.3	0.3	0.3
Stress-Yield (*MPa*)	207	172	138
Stress- Ultimate (*MPa*)	241	241	276

*Balance Copper

Note: Material data determined using www.matweb.com

Figure 4.1 illustrates the Von Mises Stress distribution generated by the FE analysis. The similarities of FEA results to those obtained by Guilmartin 1974 are immediately evident. Most obvious is the high concentrations of stress at the breech corner. For the alloy selected, a maximum stress of 174MPa was obtained. A gradual decrease in stress from internal to external walls of the barrel was also observed. In this region, values ranged between 128MPa at the internal wall to 13MPa externally. Similarly, a gradual decrease in stress was also evident through the wall of the breech. However, pressures were in the lower range of 0 – 70MPa due to the increased wall thickness at the breech.

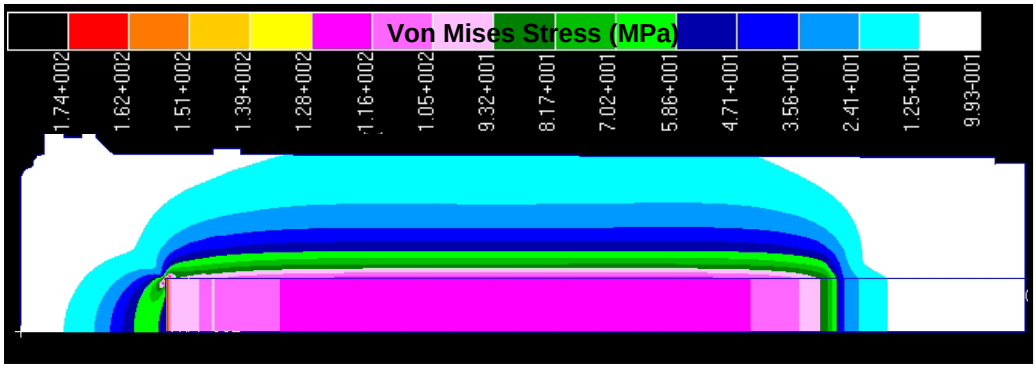

Photoelastic Analysis Result

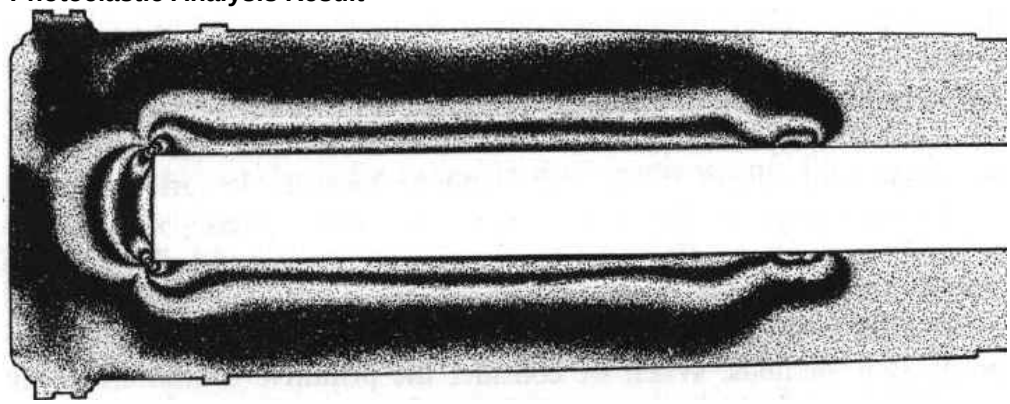

Figure 4.1: Comparison of internal stresses in sixteenth-century bronze cannon as shown by Finite Element and Photoelastic Analysis [96]

The maximum value of strain observed in the model was approximately 0.2% at the breech corner. A value of approximately 0.1% was sustained by the barrel at the internal wall. As the stress experienced by the model did not exceed the yield of the material, we would expect that the strain be elastic and recovered by the cannon after firing.

4.3.2 Non-Homogenous Material Model

A second simulation was performed using a non-homogenous material definition for the breech model to better simulate a real cannon. Knowledge of the curing properties of bronze assisted in the determination of the model.

The density and strength of bronze gunmetal increased as a function of the pressure under which it was cast. It was therefore assumed that the cannon was cast muzzle up, in order to maximise the pressure during casting at the breech. This method encouraged the tin to migrate towards the breech where the internal pressures of cannon operation were greatest. Extending this notion further, it was assumed that the external walls of the barrel would solidify prior to the internal walls. Therefore, it was expected that the tin content would be greater closer to the internal walls of the barrel compared to the external walls.

Three different material models were created, each possessing different properties based upon the tin content. Table 4.1 contains the properties for the alloys used. These alloys were applied to the model, as seen in Figure 4.2. The 19% Tin alloy was used at the breech (shown in red), the 16% Tin alloy was used at the internal wall (shown in pink) and the 10% Tin alloy was used at the external wall (shown in white).

The stress and strain results obtained for the non-homogenous material model exhibited similar patterns to those observed in Figure 4.1, however, the strain at the internal wall of the barrel had increased by up to 50% with a maximum value of 0.15%. This result highlights the sensitivity of the cannon to material properties rendering the assumption of a homogenous material model inadequate. The benefits of using finite element analysis in determining stress behaviour was also made obvious in this investigation.

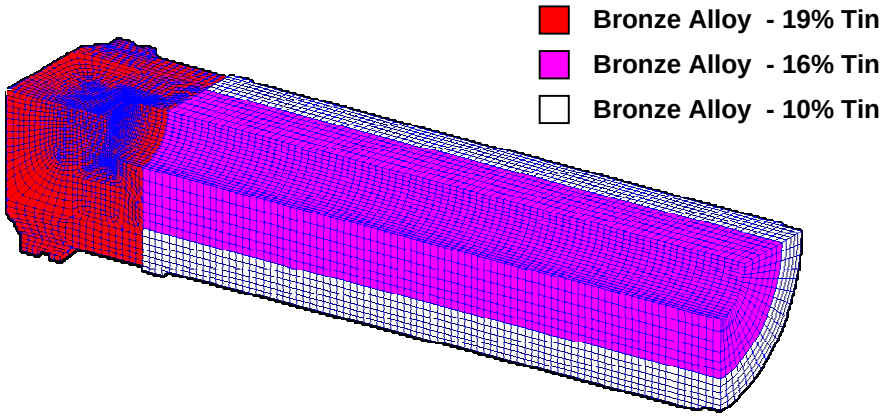

Figure 4.2: Non-Homogenous Material Distribution

4.4 Explicit Finite Element Analysis of 16th Century Cannon

The use of implicit analysis identified the stress behaviour endured by sixteenth century cannon for peak firing conditions. However, implicit methods are unable to account for the dynamic firing behaviour of tube launched weapon systems. They are also limited in their ability to determine the nature of interactions between multiple components. Both of these considerations are vital in the analysis and design of tube launched weapon systems.

Consequently, in order to further develop the analysis, explicit methods were applied to sixteenth century cannons. It was therefore possible to assess the interaction of multiple components (cannon and cannon ball) and develop time dependant data relating to each of these. The use of explicit methods also allowed performance parameters, such as muzzle velocities, to be assessed. Such parameters were unable to be determined using implicit solvers.

A firing simulation of a sixteenth century cannon was performed. A representative Spanish 42-pounder cannon was used so that load case data could be taken directly from the experimental Rodman data [103]. The major cannon dimensions are shown in Figure 4.3.

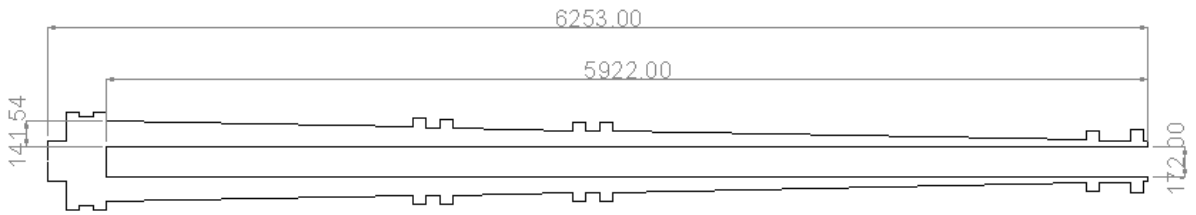

Figure 4.3: Spanish 42-pounder Cannon Dimensions (mm)

A finite element model of the Spanish 42-pounder cannon and ball was created using the MSC. Patran pre-processor for analysis in the MSC. Dytran explicit solver. The cannon and ball were modelled using Lagrangian solid elements defined by elastic-plastic material models. A non-homogenous bronze alloy, similar to that defined in Figure 4.2, was used to represent the cannon while the cannon ball was modelled using iron.

The blast pressure inside the cannon was simulated by applying a dynamic pressure field utilising pressure data from the Rodman results [103]. The pressure data used in the analysis can be seen in Figure 4.4. Pressures were applied to the internal walls of the barrel between the breech and dynamic location of the cannonball. Structural contacts employing friction were also used between the cannon barrel and ball.

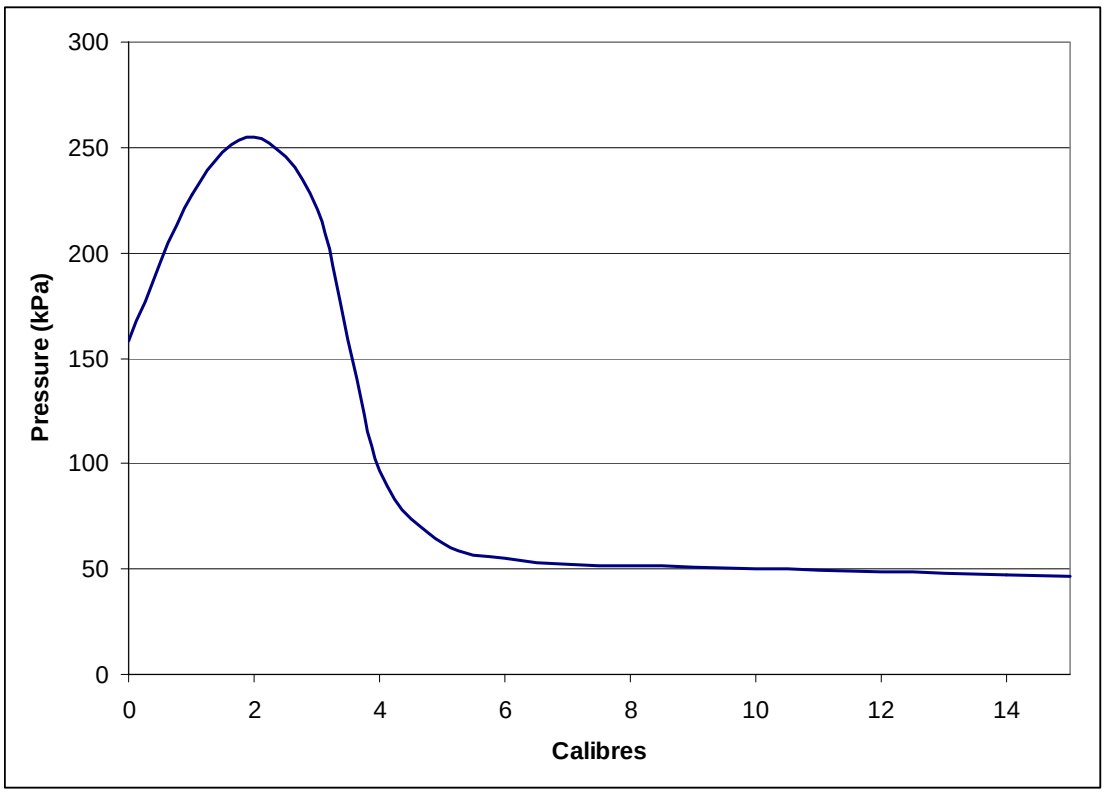

Figure 4.4: Spanish 42-pounder Cannon: Pressure Data

Figure 4.5 shows the Von Mises Stress results obtained from the dynamic simulation at different times. The results clearly illustrate the development of stress contours throughout the interior ballistic cycle. High stresses up to the material yield of 207MPa are noticed in the early stages of the simulation. As the cannonball proceeds down the barrel, the majority of high stresses are dissipated rendering values below 120MPa.

A rise in stress is again observed only when the cannonball is close to exit with values approaching 170MPa near the muzzle. It is assumed that this rise in stress is due to the decrease of material mass in this region. The stress is alleviated by the two reinforcement rings located at the muzzle however. The muzzle velocity calculated for the cannonball was 916m/s, which is within the range reported in historical documentation. Note the pressure wave propagating through the barrel ahead of the cannon ball which can be observed by regions of higher stress.

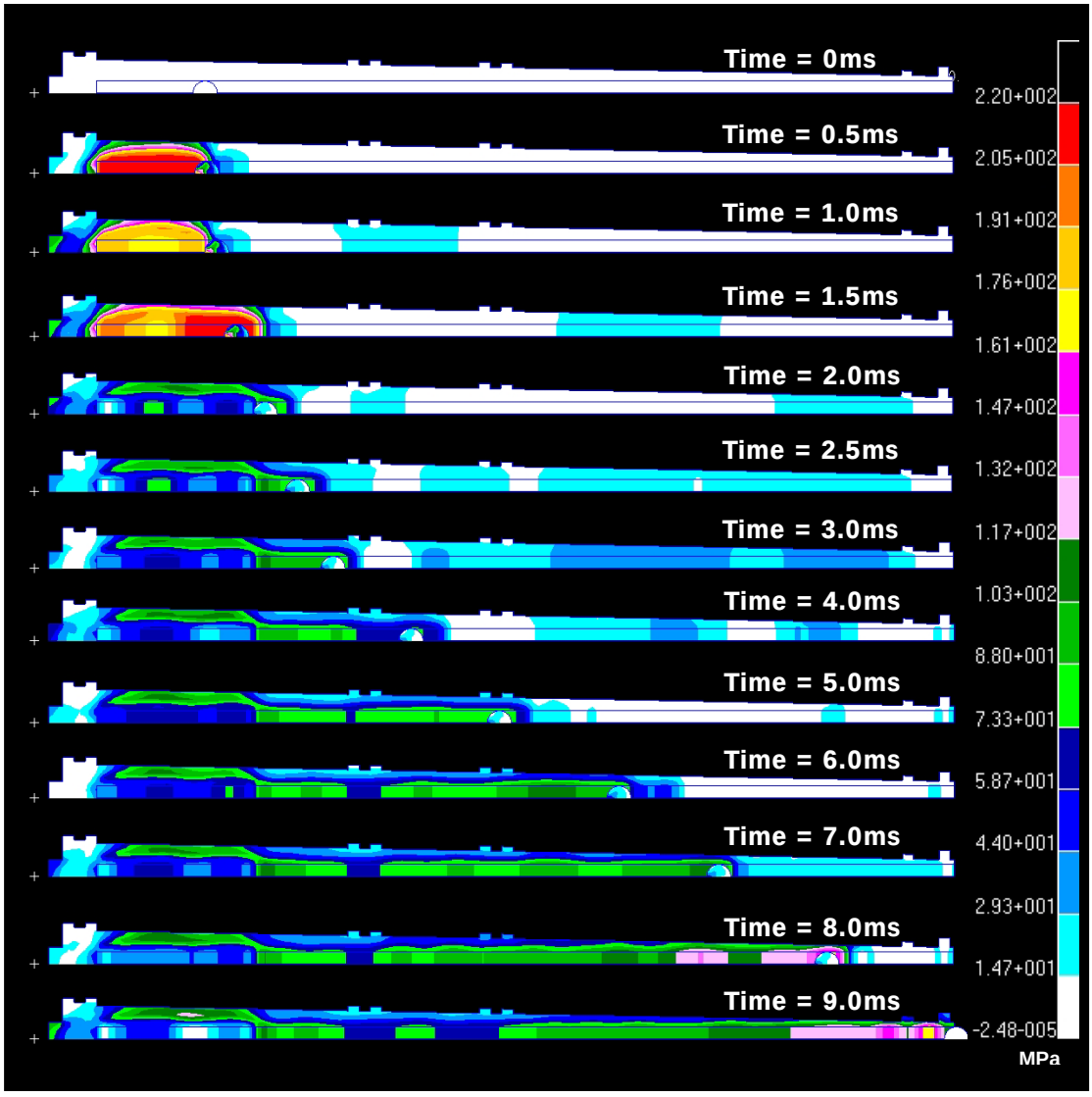

Figure 4.5: Spanish 42 pounder Cannon: Von Mises Stress Results from Explicit FEA

4.5 Fluid-Structure Interaction Modelling

The analyses presented above have assumed the behaviour of the combusting propellant. A dynamic pressure field, representative of firing conditions, was applied to the projectile and gun bodies as a boundary condition in order to simulate the interior ballistic environment. This enabled both implicit and explicit structural analyses to be performed on the cannon system in order to gain insight into its structural behaviour.

In this section, the sophistication of analysis is enhanced through the introduction of an Eulerian mesh to model the combusting medium. The interaction of Eulerian and Lagrangian elements is prescribed using the General Coupling capabilities of MSC. Dytran, as presented in Chapter 3.2.4. Hence, Fluid Structure Interaction (FSI) modelling was performed to further develop the virtual design process.

As presented in the literature review, the major limitation of current FSI techniques is the absence of a material model to simulate propellant burn. Most commercial finite element programs contain the Jones-Wilkins-Lee (JWL) Equations of State (EOS) for explosive detonation products. The detonation of propellant would be potentially catastrophic for any weapon system as the decomposition of material occurs at a rate of up to 10^5 times faster than that of combustion.

The JWL EOS as used by MSC. Dytran [23] is given below:

$$P = A\left(1-\frac{\omega\xi}{R_1}\right)e^{\frac{-R_1}{\xi}} + B\left(1-\frac{\omega\xi}{R_2}\right)e^{\frac{-R_2}{\xi}} + \omega\xi\rho_0 e \qquad \textbf{Equation 4.1}$$

where

$\xi = \rho/\rho_0$

ρ = overall material density

ρ_0 = reference density

e = specific internal energy per unit mass

A, B, R_1, R_2 and ω = JWL Material Constants associated with the material

JWL material constants can be obtained by correlating data from cylinder tests of detonations to simulations in hydrodynamic codes employing JWL material properties. Some difficulties, however, have been reported due to uncertainty in the chemical form of carbon in the detonation products [104].

As a first attempt of FSI modelling applied to tube launched weapon systems, the JWL EOS was used to simulate a detonation within the gun chamber. Applications may arise where a modern weapon system needs to be designed to sustain the extreme conditions associated with a detonation. It is appreciated, however, that a model of propellant combustion would need to be incorporated into the FE environment in order to develop tube launched weapon systems using FSI.

4.5.1 FSI applied to 16th Century Cannons

During the 16th century and until about the 1880's, the energy required by guns was supplied by black powder [93]. Describing the combustion of black powder is a difficult task and beyond the scope of this study. Black Powder is impossible to detonate. Black Powder on ignition decomposes Potassium Nitrate to produce nascent oxygen which helps in expediting the combustion process. When the gaseous pressure is not fumed off, it will rise and reaches a point where the container it is held in 'explodes'. There is a major difference in detonation and explosion as explosion is nothing more than a rapid expansion of high pressurised gas.

In order to conduct FSI modelling utilising the JWL EOS, it was decided that the detonation of Trinitrotoluene (TNT) inside a cannon would be simulated instead. TNT in its pure form is designated as 'high explosive' and TNT can detonate. This makes it appropriate for use with the JWL EOS. The following JWL EOS parameters, taken from [105], were used for the simulation:

$\rho_0 = 1.63e^{-9}$ *tonne.mm*$^{-3}$
e = 6.0e6 kj/m3
A=3.7377e8 kPa
B=3.7471e6 kPa
$R_1 = 4.15$

$R_2 = 0.9$

$\omega = 0.35$

The Lagrangian model of the Spanish 42-pounder cannon, presented in Section 4.4, was again used to perform fluid-structure interaction modelling. An Eulerian mesh possessing the JWL EOS was also included in this instance to simulate the detonation of propellant. Contacts between the Lagrangian cannon barrel and ball were imposed in conjunction with general coupling between Lagrangian and Eulerian elements. MSC. Dytran was again used to perform the analysis.

A material described by the JWL EOS requires that a point be selected at which the detonation begins. A detonation point was therefore selected on the internal barrel wall to represent the most likely location of the cannon fuse. A detonation velocity of 6.93e3m/s [105] was also defined.

Figure 4.6 contains a series of plots showing the pressure generated by the detonation of TNT as determined by FSI using MSC Dytran. The plots show a detonation wave emanating from the detonation point and traversing through the explosive.

The early motion of the cannon and ball can also be seen in the figure, as the chamber pressure begins to accelerate the cannonball. Interestingly, the plot at 6 milliseconds shows that the cannon chamber has undergone significant deformation and is unable to sustain the imposed detonation conditions. Consequently, the analysis was able to demonstrate that fluid structure interaction modelling could be used in the design of weapons systems where a risk of propellant detonation existed.

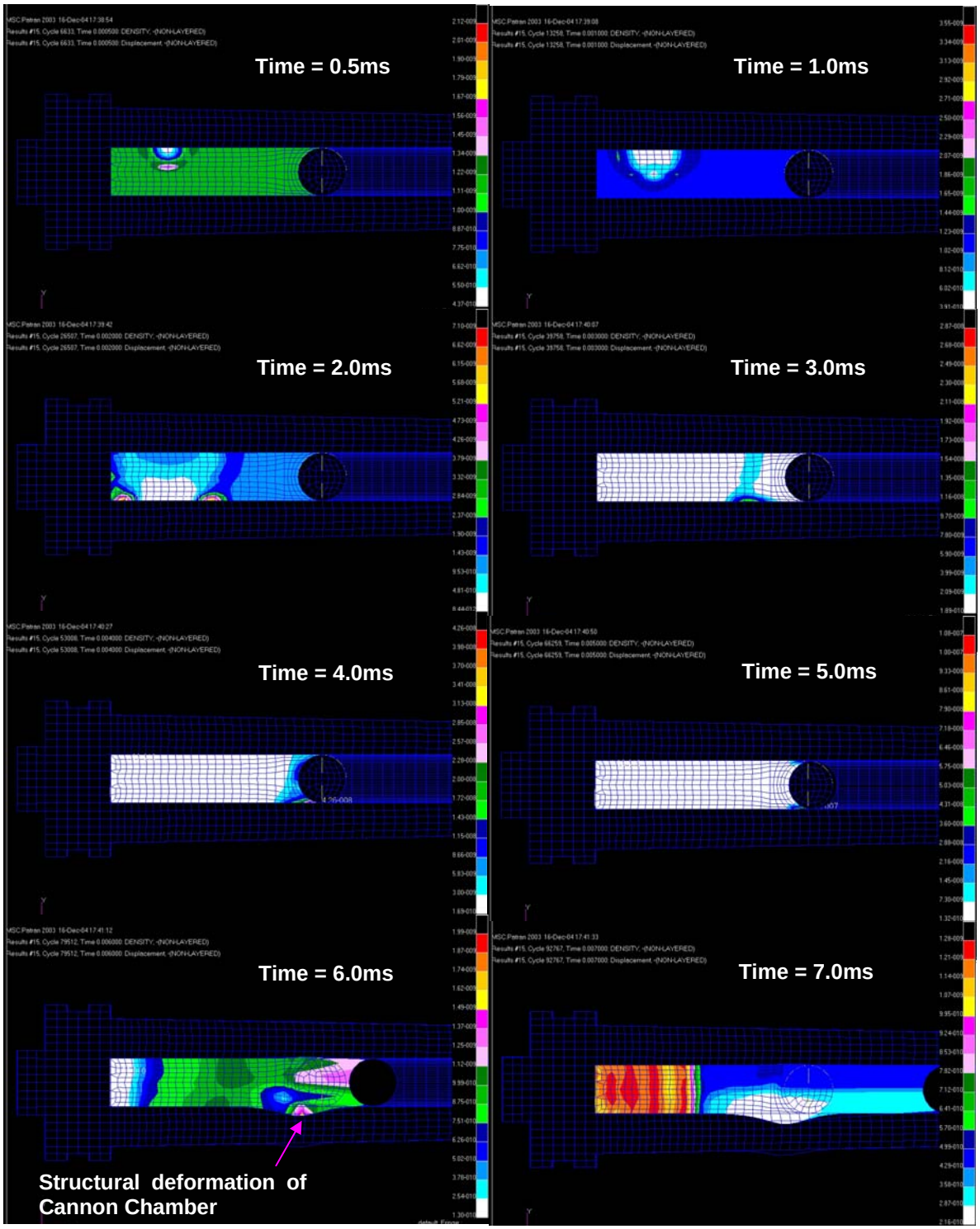

Figure 4.6: Fluid-Structure Interaction Modelling: TNT Detonation inside Cannon Chamber

4.6 Shape Optimisation: 16th Century Cannon

Weapon system performance parameters may be improved by shape optimisation. Optimisation may be carried out on structural properties, such as vibration and structural integrity, and correlated properties such as mass and mass distribution.

The shape optimization process utilised by the software program ReSHAPE was presented in Chapter 3. ReSHAPE was used to perform two individual optimisations on the Spanish 42-pounder Cannon. The first optimisation involved a mass reduction of the cannon. The second optimisation target was to alter the vibrational behaviour of the cannon by using shape changes to manipulate natural frequencies.

4.6.1 Mass Reduction

A reduction of mass was performed on the Spanish 42-pounder cannon using ReSHAPE. The MASS Objective [106] was prescribed in ReSHAPE with a target mass reduction of 15% for the cannon. A STRESS Constraint [106] was also imposed in order to maintain the maximum allowable stress of the material. That is, any shape changes endured by the cannon were restricted by the yield stress of the bronze alloy.

As discussed previously, ReSHAPE utilises the linear finite element method in performing optimisations. It was therefore necessary to generate a linear load case to best represent the dynamic results obtained for the cannon using explicit analysis. The peak pressure condition, taken from the experimental Rodman data [103] was used.

Figure 4.7 shows the results obtained for a 15% reduction of mass without exceeding material tolerances. Significant amounts of material have been removed through the centre section of the barrel and towards the muzzle. The reinforcing rings used by cannon founders were removed entirely from the middle section of the cannon. This result is supported by results shown in Figure 4.5, where stresses in the reinforcement rings remain quite low.

Very little material has been removed in the vicinity of the chamber and breech, where pressures of cannon operation are greatest. The profile is now substantially more similar to modern artillery barrels. Naturally, 16th Century cannon makers required large safety tolerances to account for material impurities and a lack of knowledge regarding stress and strain behaviour of metals.

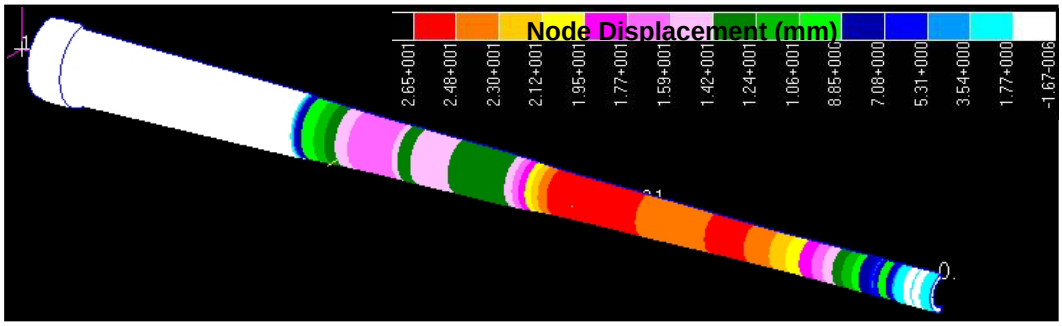

Figure 4.7: Design Optimisation: Cannon Mass Reduction

4.6.2 Barrel "Tuning"

Explicit analysis of the Spanish 42 pounder Cannon presented in Section 4.4 showed that pressure waves travelled through the cannon ahead of the cannon ball as seen in Figure 4.5. It was suggested that these waves were possibly the result of vibrational modes being excited in the cannon subsequent to firing. Although the accuracy of sixteenth century cannons was certainly limited by the flight dynamics of spherical projectiles, these vibrations would affect the precision of modern weapons. The following analysis was therefore undertaken to demonstrate the usefulness of these techniques for application to modern weapon systems.

Figure 4.8 illustrates the first two transverse modes obtained for the Spanish 42-pounder cannon from a modal analysis performed in MSC. Nastran. The first mode was found to have a frequency of approximately 21.5 Hz, while the second mode had a frequency of approximately 59.6Hz.

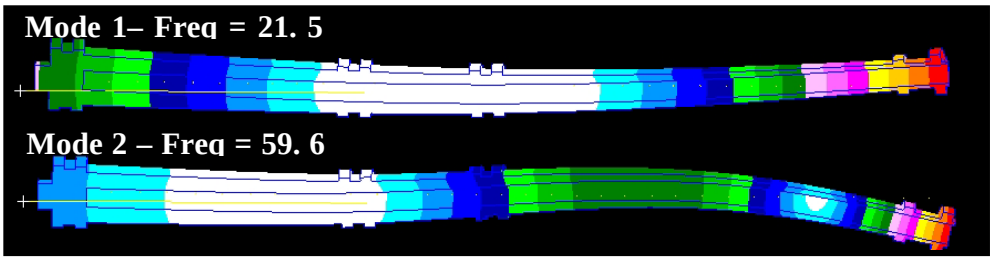

Figure 4.8: Spanish 42-pounder Cannon: Modal Analysis Results

ReSHAPE was used to perform an optimisation on the Spanish 42 pounder cannon. The objective of the optimisation was to shift the natural frequency of the first transverse mode to improve the cannon's accuracy. This would be achieved by ensuring that the mode had a phase angle of 180^0 at the time of muzzle exit of the cannon ball whilst maintaining stresses below the material yield. Since the cannonball took about 10msec to leave the barrel, this required that the frequency of this mode be around 40Hz.

Small decreases in the barrel length would linearly decrease the time taken for the cannonball to exit but increase the frequency by a power of two. This would make the tuning easier to achieve if shortening the barrel length was permissible in relation to other gun performance parameters.

Using ReSHAPE, the tuning objective was possible without exceeding the material yield stress or changing the barrel length. The FREQUENCY Objective [106] was prescribed in ReSHAPE with a target of increasing the first modal frequency by 50% for the cannon. A STRESS Constraint [106] was again imposed in order to maintain the maximum allowable stress of the material.

Figure 4.9 displays the results obtained for the analysis. Image A shows the shape changes incurred in tuning the lateral modes of the cannon to achieve a frequency of 40Hz for the first mode. Image B shows the minor corrections performed by ReSHAPE to ensure the stresses in the material were maintained below the yield stress.

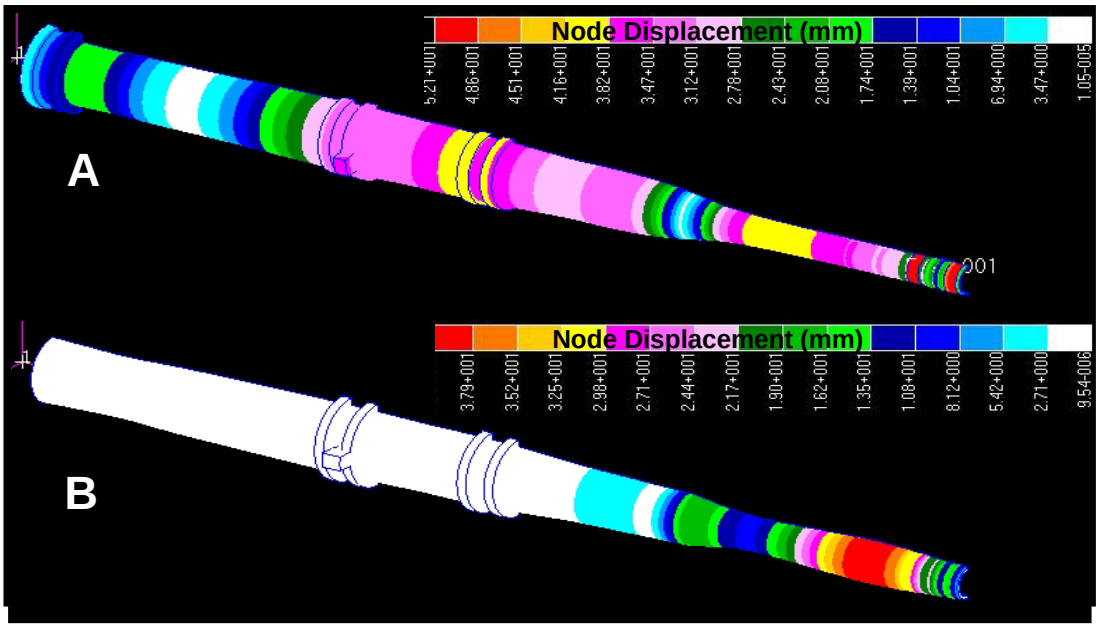

Figure 4.9: Design Optimisation: Cannon Barrel 'Tuning'

The use of shape optimisation to manipulate natural frequencies in the design of modern gun barrels would be invaluable where a high degree of firing precision was required. However, this design tool would also be useful in design and optimisation of other weapons components. For example, a vibrating barrel and projectile system may impose adverse friction conditions during the interior ballistic phase. Shape optimisation could be used to tune the vibrational behaviour of the system and hence achieve a desired performance.

4.7 Conclusions

The study of 16th century cannons presented in this chapter was used as a means of assessing the use of VDT's in tube launched weapons applications. Some interesting conclusions were able to be drawn which contributed to refining the VDP for future applications.

Implicit finite element methods were used to determine the stresses experienced by cannons using real material properties. The comparison of homogenous and non homogenous material definitions revealed significant variation in strain results for the cannon. It was found, however, that implicit methods were limited in their ability to fully describe the highly dynamic nature of the system under development. Assessing the dynamic interaction of barrel and munitions as well as determining vital performance parameters such as muzzle velocity would not be possible using these methods.

Explicit methods of finite element analysis were found to offer greater insight into the design. Time dependent Von Mises stress data were produced over the entire interior ballistic cycle of the cannon. Regions of high stress were identified in the chamber and muzzle regions. The analysis also revealed the development of system vibrations which travelled ahead of the cannon ball which could impact weapon accuracy in modern systems.

Fluid structure interaction modelling was also performed on the cannon system. In the absence of a material model to describe propellant combustion, a detonation using the JWL EOS was simulated inside the chamber. The analysis demonstrated the potential for FSI to integrate the properties of the propellant and structural system into the one analysis. A model of propellant combustion is incorporated in to the explicit finite element environment in the following chapter.

Shape optimisation analyses were also performed on the 16th century cannon. In the first case, the mass of the cannon was reduced to reveal an optimised structure which closely resembled a modern gun barrel. The second optimisation was able to tune the natural frequencies of the cannon in order to control vibrations during the interior ballistic phase. This process would be invaluable when refining the performance of modern gun systems.

5 Fluid-Structure Interaction Modelling and Interior Ballistics

5.1 Modelling Interior Ballistics

The controlled combustion of solid propellants has a variety of applications in engineering. For example, propellant combustion is vital to weapon system design, rocket motor design and gas generators used for airbag inflation and fire suppression. Much literature exists [107-109] in which the combustion behaviour of various propellants are simulated.

Due to inherent complexities associated with propellant ignition and combustion, the description of propellant burn and consequent impact on structural design is not well understood. This chapter investigates the impact of propellant burn on interior ballistics through the development of a computer simulated model. Given the characteristics of any propellant and structural system, a model of ballistics should be able to establish the energy release and corresponding pressure generated by the propellant on the system.

The Nobel-Abel Equation of State in conjunction with a steady-state burning law, which describes the recession rate of the burning propellant, was incorporated into a finite element environment through a user subroutine. Fluid-structure interaction modelling was then performed to consider the impact of evolving combustion gasses on the structural system. The derived model was able to consider a wide range of system parameters and analyse their effect on system performance. As revealed in Chapter 2, no evidence of this type of FSI modelling considering propellant combustion could be found in the literature.

5.1.1 The Ballistic Model

In any ballistic system, there exists a set of fixed and variable factors which ultimately affect performance. Fixed factors are generally related to the structural properties of the system and often these are difficult to manipulate without requiring a total redesign and manufacture of structural components. More conveniently, variable factors associated with the propellant can be modified to improve performance.

Propellant type, configuration and quantity can be varied in order to achieve a particular burn cycle and hence a desired performance. Various models exist in which structural and propellant properties are used to predict the performance of interior ballistic systems. One such model is proposed by Krier and Adams 1979 [13] in which the Nobel Abel Equation of State is used to establish the energy release and corresponding pressure generated by the combusting propellant.

The Nobel Abel Equation of State is of the covolume type and is generally used as a good first approximation in the formulation of interior ballistic problems. In simplest form, the Nobel Abel Equation of State is given by the following expression:

$$(P/n')(V - n'\eta) = RT_0 \qquad \textbf{Equation 5.1}$$

Where

n'= mass of gas *(tonnes)*

η = gas covolume $(mm^3.t^{-1})$

R = gas constant $(mJ.t^{-1}.K^{-1})$

In this study, a version of Krier and Adams 1979 ballistic model is incorporated into the finite element environment through a user subroutine. The resulting fluid-structure interaction model is able to simulate the fluid dynamics of the propellant and its impact on the structural system. Aspects of this work were refereed and published in the Australian and New Zealand Industrial and Applied Mathematics Journal [110].

The ballistic model proposed by Krier and Adams 1979 [13] considers the physical parameters of the propellant, barrel and round in order to generate approximations of interior ballistic performance. The model is developed through consideration of the following areas: 1) Equation of State, 2) Form Function Analysis, 3) Propellant Burning Rate Equation, 4) Variable Volume Considerations, 5) Pressure Considerations, 6) Projectile Motion and 7) Heat Loss Effects.

As the ignition process is quite complex, it was not treated with any detail in this investigation. Instead, the simulation assumed that simultaneous and uniform ignition of all propellant grains always occurred. The following equations and initial conditions were utilised in this investigation to construct the ballistic model. The equations are derived in Kreir and Adams 1979 [13].

Propellant Burning Rate Law:

$$\frac{dx}{dt} = B`P_A^n$$ **Equation 5.2**

Piston Acceleration:

$$\frac{dV_p}{dt} = \frac{P_B A_s}{W_s}$$ **Equation 5.3**

Piston Travel:

$$\frac{ds}{dt} = V_p = \int_0^t \left(\frac{dV_p}{d\tau} \right) dt$$ **Equation 5.4**

Total Chamber Volume (including propellant and gas volumes):

$$V_T(t) = V_{c0} + A_s S(t) - C\{(1/\rho_s) + Z[\eta - (1/\rho_s)]\}$$ **Equation 5.5**

Where

$$Z = \frac{2[cL + d]x - [L(1-n) + 4c]x^2 + 2(1-n)x^3}{Ld}$$

and $c = R + nr$

$d = R^2 - nr^2$

Average Gas Pressure (with heat loss):

$$P_A = \frac{\lambda CZ - (\gamma - 1)(1 + \beta)(M_E V_p^2 / 2)}{V_T(t)} \qquad \textbf{Equation 5.6}$$

where

$$M_E = W_s + (CZ / 3)$$

Pressure Conversion (base to average):

$$P_B : P_A = \left[1 + \frac{\gamma - 1}{2}\frac{V_p^2}{g_c \lambda}\right]^{\frac{-\gamma}{(\gamma-1)}} \qquad \textbf{Equation 5.7}$$

Initial Values:

$X(0) = X_0$ [a small number of order 10^{-3}inches] **Equation 5.8**

$V_p(0) = 0$ **Equation 5.9**

$S_p(0) = 0$ **Equation 5.10**

$V_T(0) = V_{c0} - (C / \rho_s)$ [approximate due to Equation 5.8] **Equation 5.11**

The ballistic model was solved by simultaneously integrating Equations 5.2-5.4, utilising Equations 5.5-5.7 and specified initial conditions (Equations 5.8-5.11). Note that Equation 5.3 was simplified for a smooth bore barrel as compared to [13] which considers a rifled barrel.

As described in Krier and Adams 1979 [13], the ballistic model presented above makes the following assumptions:

- The propellant gas flow is taken to be one-dimensional, inviscid and compressible.
- The propellant gas mixture is described by the Noble-Abel Equation of State.
- The steady state burning law can be used to describe the recession rate of the propellant grains.
- Average properties are used to describe all propellant grains in the propelling charge.
- At t=0, all propellant grains have been ignited uniformly, with all exposed surface areas of the grains having recessed by a small distance.
- All exposed surfaces recede at a uniform rate, implying that all grains shrink symmetrically.
- Decomposition of a unit mass of propellant always will liberate the same amount of energy, which heats product gasses to the same temperatures.
- Dissociation of the main constituents of the propellant gas mixture is not significant.
- Heat loss to the gun surface can be accounted for by applying an adjustment factor that reduces the amount of available energy.
- The round forms a perfect seal with the gun bore.
- Sliding friction losses between the round and gun bore are taken to be negligible.
- A special solution to the Lagrange problem is used to relate the average pressure to the projectile base pressure.

The above model was first solved using MATLAB in order to asses the influence of various parameters on system performance. The developed MATLAB model can be seen in Appendix A. The MATLAB model was then used to validate results produced using finite element analysis incorporating the Ballistic Model as a user subroutine. The results are presented below.

5.2 Combustion in a Constant Volume

5.2.1 MATLAB Analysis

The first simulation of the MATLAB Ballistic Model considered the combustion of granular multi-perforated propellant in a constant volume in order to investigate the resultant pressure rise. Other authors such as Pocock, et al., 2004 [86] and Ritchie, et al., 1999 [85] also considered the performance of perforated propellant grains using numerical methods.

As a constant volume was only considered to begin the investigation, terms relating to piston acceleration and travel were ignored. Table 5.1 contains a set of arbitrary parameters selected by the author to represent a modern granular perforated propellant for use in the analysis. The plot in Figure 5.1 shows the predicted pressure rise obtained for the simulation. A maximum pressure of 67MPa was recorded after 3 milliseconds.

Table 5.1: System Parameters for Constant Volume Simulation

Parameter	*Symbol*	*Value*	*Units*
Propellant Properties			
Length of Grain	L	6.13	*mm*
Diameter of Grain	D	3.12	*mm*
Number of Perforations	N	1	
Perforation Radius	r	0.255	*mm*
Solid propellant Density	ρ_s	1.45e-9	$tonne.mm^{-3}$
Charge Weight	C	0.00005	*tonne*
Specific Heat Ratio	γ	1.2582	
Force Constant	λ	9.41e11	$mJ.t^{-1}$
Gas Constant	R	364.5e6	$mJ.t^{-1}.K^{-1}$
Gas Covolume	η	1.06e9	$mm^3.t^{-1}$
Burn Rate Coefficient	$B`$	0.732	$mm.s^{-1}$
Burn Rate Exponent	n	0.952	*For MPa*
Structural Properties			
Constant Volume	V_T	2.759e5	mm^3

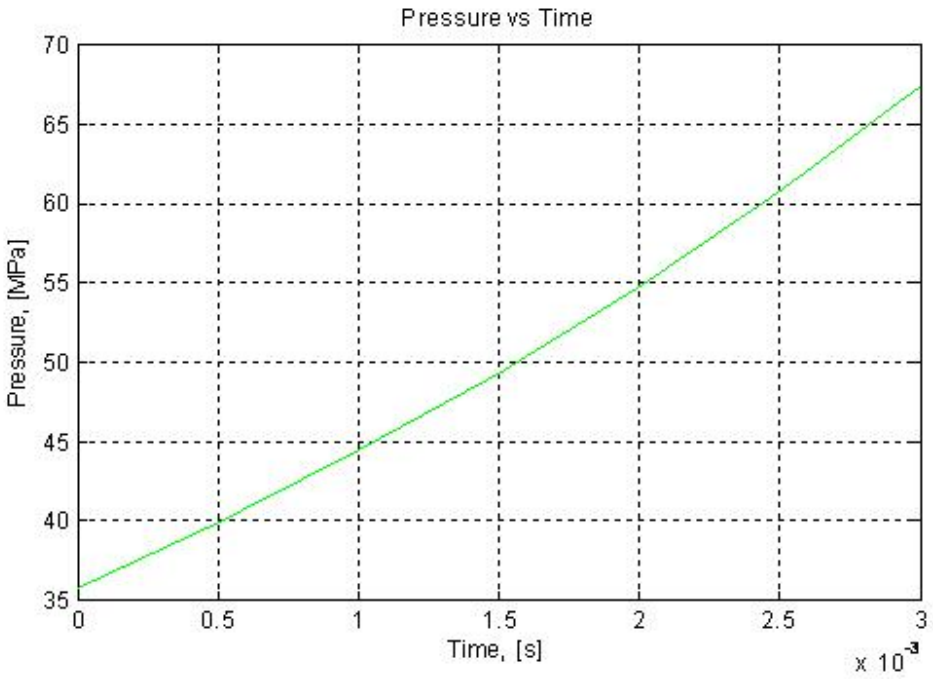

Figure 5.1: Pressure vs Time Relationship for Propellant Combustion in Closed Volume

5.2.2 Finite Element Analysis

In order to include the Ballistic Model in the finite element environment it was necessary to create a User Subroutine. As MSC. Dytran was used to perform the analysis, it was necessary to adapt the MATLAB code to FORTRAN 90 Language. When adapting the code, only statements relating directly to the propellant needed to be included as any structural properties were entered directly into MSC. Dytran. Therefore Equations 5.3, 5.4, 5.5 and 5.7 were omitted from the user subroutine. The expression for the Burn Fraction "Z" from Equation 5.5 was still necessary however.

Figure 5.2 illustrates the equations utilised in the main loop of the user subroutine. In the finite element analysis, the Ballistic Model was applied to each individual element, as opposed to the MATLAB simulation where it was computed over the entire volume. Information relating to element volume and mass (charge weight) were retrieved directly from MSC. Dytran throughout the simulation run and can be seen as RELV and XMASS in Figure 5.2 respectively. The NZ term represents the element numbers assigned by MSC. Dytran and the loop is constructed such that each equation is computed for all elements for each time step. The developed subroutine for the ballistic model can be seen in Appendix B.

```
*     Calculate Burn Fraction
************************************************
*
 Z(NZ)=((2*((c*L)+d)*x(NZ))-(((L*(1-N))+(4*c))*
     +    ((x(NZ))**2))+(2*(1-N)*((x(NZ))**3)))/(L*d)
*
*     Calculate New Pressure
************************************************
*
 PNEW(NZ)=(λ*XMASS(NZ)*Z(NZ))/(RELV-
     +    ((XMASS(NZ)/ρs)*(1-Z(NZ)))-(η*Z(NZ)*XMASS(NZ)))
*
*     Calculate Grain Recession
************************************************
*
 x(NZ)=x(NZ)+DLTH*B`*(PNEW(NZ))**n
```

Figure 5.2: Main Loop of User Subroutine

Note:

NZ = Element number assigned by MSC. Dytran.

XMASS = Mass (Charge Weight) of element.

RELV = Volume of Element

DLTH = Time Step Calculated by MSC. Dytran

PNEW = New Pressure calculated by MSC. Dytran

Finite element analysis was used to repeat the simulation conducted in MATLAB in Section 5.2.1. A simple cube mesh composed of solid Eulerian elements was constructed in the MSC. Patran pre-processor with the same volume as that used in the MATLAB analysis. No boundary conditions were required as MSC. Dytran automatically assumes that any external Eulerian mesh surfaces act as boundaries to the flow.

The results produced by MSC. Dytran for pressure in the constant volume were identical to those displayed in Figure 5.1. However, it would be expected that finite element analysis could further improve the accuracy of results in more complex problems. The time steps utilised in finite element solvers are generally orders of magnitudes smaller than those used when running MATLAB simulations resulting in more precise integration schemes.

It was also shown that in this case mesh density did not affect the simulation as identical results were produced using 1 element and 125 elements. In more advanced simulations, possibly incorporating expanding volumes or more eccentric geometries, mesh density would be a vital variable in accurately representing the flow of material. In such models, both the unburnt propellant and combustion gases would disperse unevenly throughout the chamber volume resulting in an irregular distribution of pressure.

5.3 Combustion in a Closed Box

It was envisaged that fluid structure interaction modelling could be used to assess the impact of propellant combustion on structural systems. MSC. Dytran would compute the pressures generated in the combusting medium, via the Ballistic Model subroutine, and then apply these to the surrounding structural system via coupling surfaces.

In order to develop this capability a simple model was created in which propellant would be combusted inside a closed aluminium box. A half model was utilised in the simulation to allow visual inspection of the pressures generated inside the box. The appropriate boundary conditions were applied to the symmetry plane.

The propellant was modelled using solid Eulerian elements and solid Lagrangian elements were used to model the box. To allow fluid-structure interaction it was necessary to overlap the two meshes and define a coupling surface on the external surfaces of the Lagrangian box. At the beginning of the simulation, the overlapped Eulerian mesh contained no material and was considered to be a void space as the coupling surface acted as a boundary to the flow. The overlapped mesh allowed for deformation in the Lagrangian mesh and the attached coupling surfaces without loss of coupling to the Eulerian elements. Figure 5.3 demonstrates the requirement of the overlapped mesh.

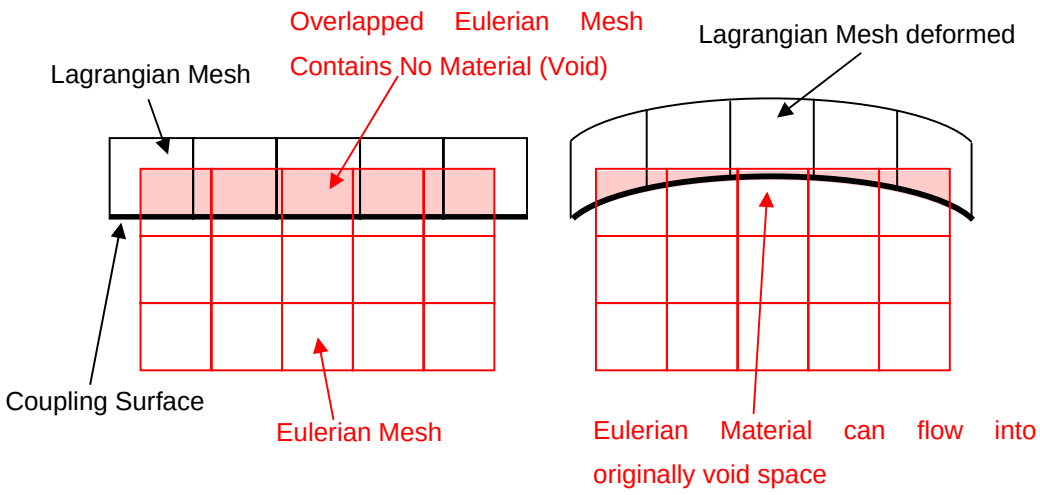

Figure 5.3 Eulerian/Lagrangian Mesh Coupling

Figure 5.4 contains the finite element model of the closed box simulation. Image A shows the Lagrangian box only, Image B includes the Eulerian mesh and highlights the overlapped region.

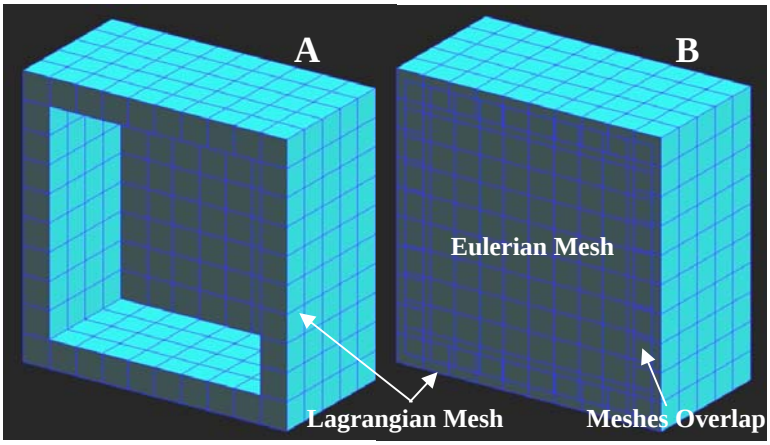

Figure 5.4: Finite Element Model of Closed Box Simulation

A – Lagrangian Box Only; B – Lagrangian and Eulerian Mesh with Overlapped Region

The system parameters from Table 5.1 were again utilised for the simulation. The box was modelled using aluminium with an Elastic Modulus of 70GPa, a Density of 2.8g/cc and a Yield Stress of 250MPa. The results of the simulation can be seen in Figure 5.5. Column A shows the pressures generated by the propellant, Column B illustrates the stresses in the Aluminium Box and Column C shows the deformation of the Aluminium Box.

The results in Figure 5.5 clearly demonstrate the pressure rise in the combusting propellant, the resultant stressing of the aluminium box beyond yield and the consequent deformation of the structure. Early in the simulation we notice pressure waves developing in the gas with four distinct regions of high pressure on the symmetry plane. This is followed by more erratic and turbulent conditions beyond 1msec except for the rear corners of the box where we see distinct pressure drops. These results offer significantly more insight compared to those produced by MATLAB, where an average pressure would be computed for the entire Eulerian mesh.

Results for the aluminium box presented in Columns B and C demonstrate the success of the fluid structure interaction modelling using the user defined subroutine. Pressures calculated in the Eulerian mesh were successfully transferred to the Lagrangian body causing it to deform. Column B shows that the Yield Stress of the material was reached within 0.5msecs as the box begins to plastically deform. Plastic deformation continues as more of the structure reaches its yield under the increasing pressure.

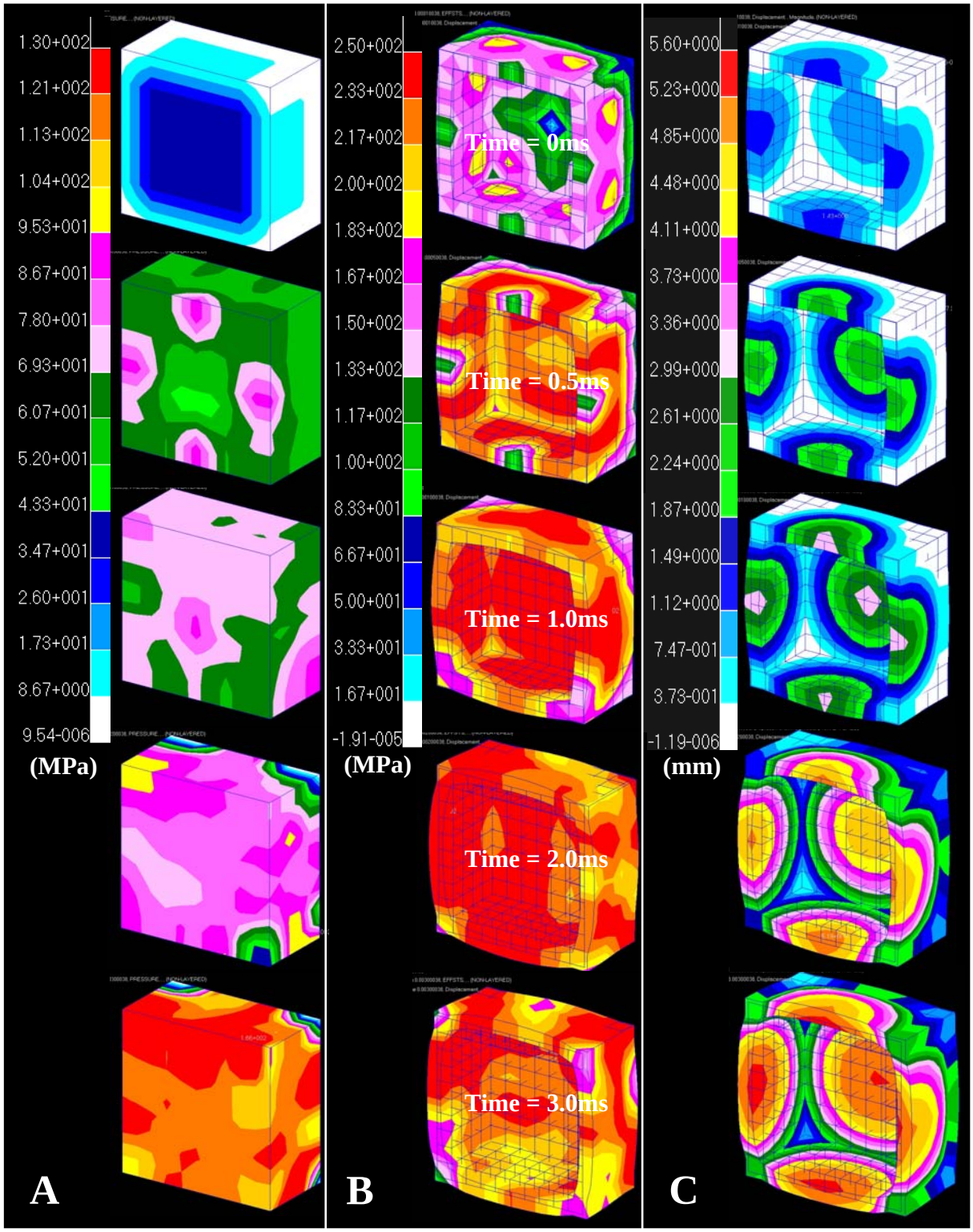

Figure 5.5: Fluid Structure Interaction Results for Closed Box Simulation

A – Gas Pressure (Eulerian Mesh shown only); B – Material Stress (Lagrangian Mesh shown only); and C – Material Deformation (Lagrangian Mesh shown only).

5.4 Combustion in an Expanding Volume

Fluid-structure interaction modelling enabled the combustion of propellant to expand a closed box through the use of coupling surfaces and overlapping meshes. However, the deformation in this model did not exceed the thickness of one Eulerian element. That is, each Eulerian element was at least partially filled by propellant at the beginning of the calculation. Then, as the Lagrangian body deformed, more of the partially filled Eulerian elements' volume was able to be occupied.

Modelling the combustion of propellant in large expanding volumes, where overlapping meshes will be many rows of elements thick, would require new and originally void Eulerian elements to be introduced into the analysis. These are filled by the gas/propellant mixture as coupling surfaces are displaced.

For example, Figure 5.6 contains a model of a projectile located inside a barrel, both modelled with Lagrangian elements. While the Eulerian elements are not shown in the figure, it is assumed that they would occupy the entire internal volume of the barrel. Overlapping of meshes would be required at the internal barrel wall in order to transfer stresses from the propellant to the Lagrangian elements. As the projectile is accelerated down the barrel and through the Eulerian mesh, more and more originally void Eulerian elements would be filled by the gas/propellant mixture. To perform such an analysis would require the dynamic specification of conditions on the newly introduced Eulerian elements equivalent to those possessed by immediately adjacent elements.

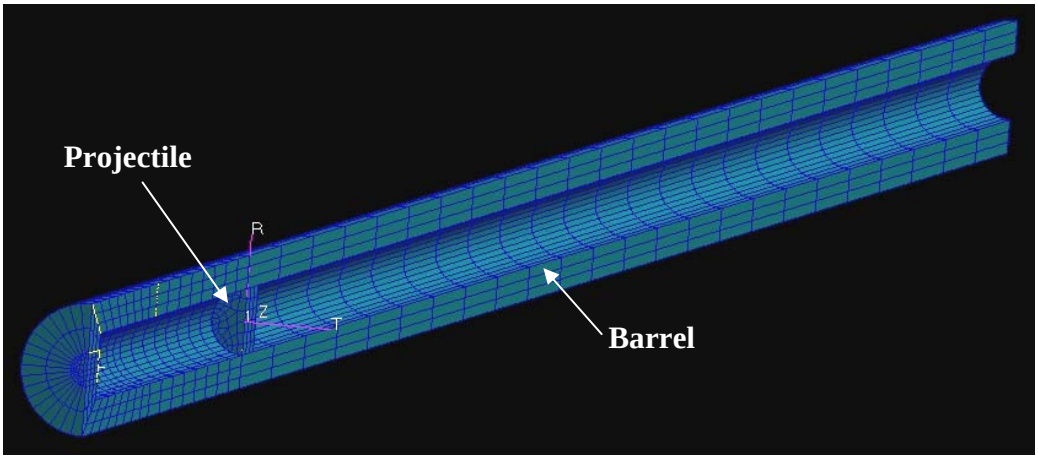

Figure 5.6: Barrel and projectile Finite Element Model

In order to achieve this behaviour, it was necessary to adjust the user subroutine containing the ballistic model. The revised Subroutine can be seen in Appendix C. All Eulerian elements containing propellant at the start of the calculation were assigned the Initial Condition as stipulated by Equation 5.8. Then, as new Eulerian elements were occupied by material, conditions of immediately adjacent elements were averaged and applied to the new elements.

To test the stability of the revised subroutine, a small amount of propellant, identical to that simulated in Section 5.2.2 was again modelled. However, the combustion in this instance was able to expand into a larger volume. The finite element model used for the simulation can be seen in Figure 5.7. The highlighted region on the left shows the elements which contained the propellant at the start of the calculation. All the other elements were designated as being void initially. The volume occupied by the propellant was 2.759e5 mm^3. The entire volume was a factor of 20 larger than the aforementioned value. The propellant properties in Table 5.1 were again used, with the Constant Volume value being ignored. In this demonstration, no Lagrangian bodies were necessary.

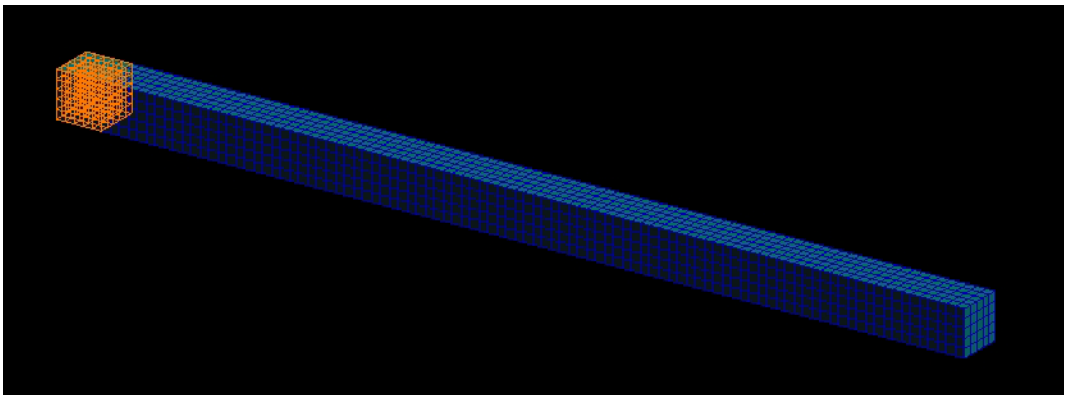

Figure 5.7: Finite Element Model of Combustion in an Expanding Volume

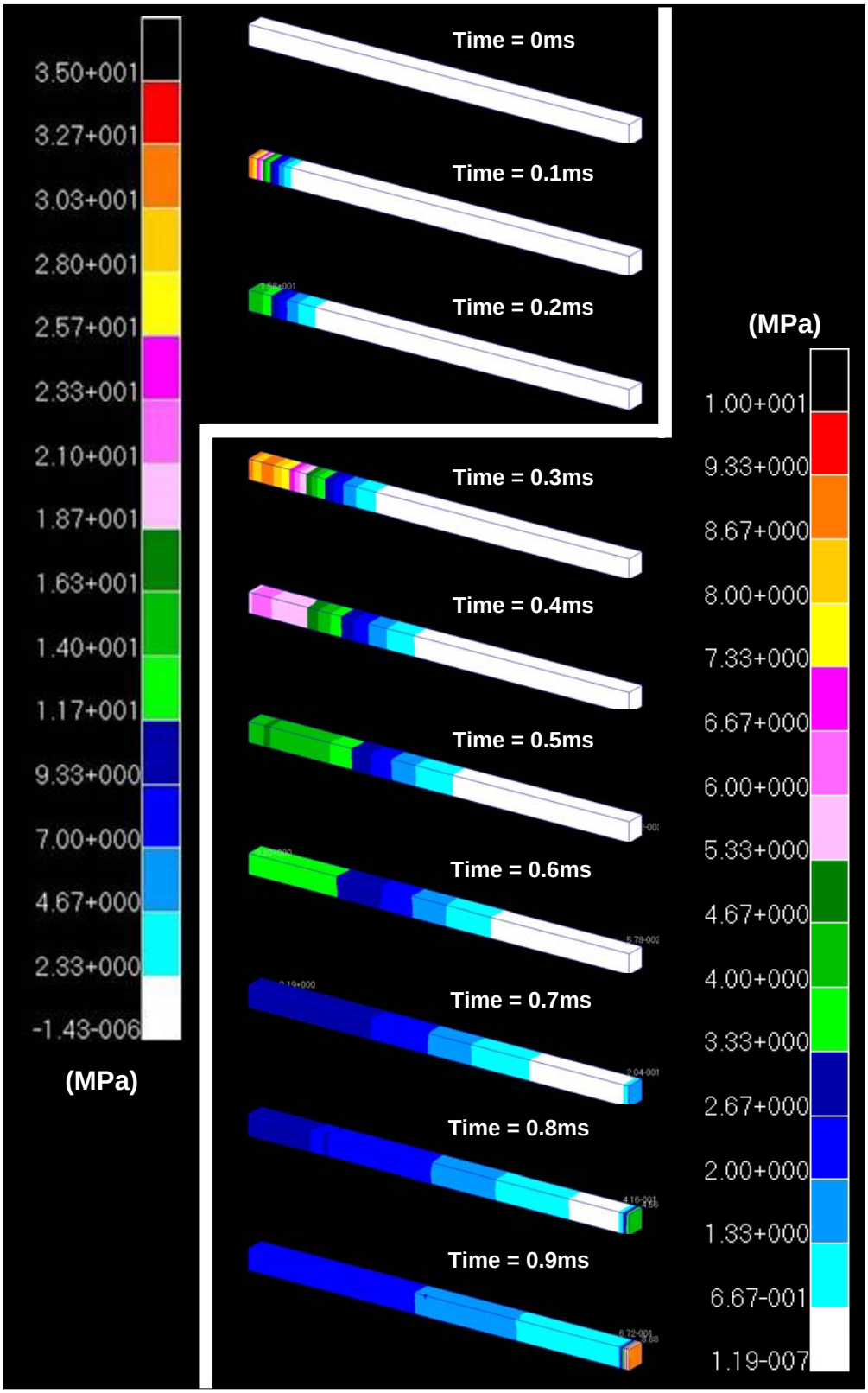

Figure 5.8: Pressure Results of Combustion in an Expanding Volume

Figure 5.8 contains the pressure results from the analysis using the revised subroutine. Early in the combustion, pressures reach a maximum of 35MPa. This value decreases rapidly however, as pressures are able to expand into the large volume. Well defined regions of decreasing pressure are shown to develop as time progresses, confirming the stability of the subroutine. Beyond 0.7msec, we notice a build up of pressure at the far right face of the Eulerian mesh. As no specific boundary condition was prescribed for any of the external Eulerian faces, each acts as a barrier to the flow. The results show the pressure wave striking the right face and being reflected in the opposite direction.

5.5 Combustion in an Expanding Volume with Projectile

The final analysis performed in this investigation again modelled the combustion of propellant in an expanded volume using the revised subroutine shown in Appendix C. However, in this instance, a projectile was included into the simulation and Fluid-Structure Interaction modelling was performed. The expanding volume represented the gun tube. In order to validate the accuracy of results, a similar analysis was performed using the developed MATLAB model and results were compared.

The same Eulerian mesh as that presented in Section 5.4 was used. A Lagrangian mesh for the projectile was also included and was located just in front of the propellant. A coupling surface was defined on all the external faces of the projectile. The motion of the projectile was constrained such that it could only travel down the length of the gun tube. Parameters in Table 5.1, ignoring the 'Constant Volume' value, were again used. Figure 5.9 contains the finite element model used for the analysis.

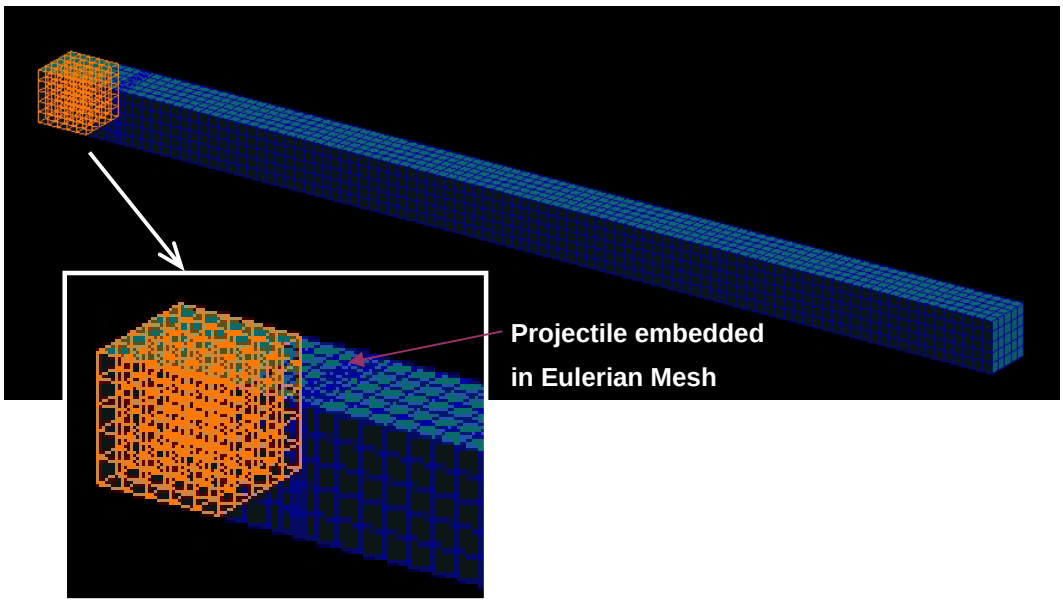

Figure 5.9: Finite Element Model of Combustion in an Expanding Volume with Projectile

The pressure results obtained for the analysis can be seen in Figure 5.10. A maximum pressure of 40MPa is generated by the propellant early in the simulation. Higher pressures, compared to those observed in the previous section, are maintained for a longer period as the propellant is forced to accelerate the weight of the projectile. Beyond 1.5ms, the average pressure of the system has decreased to below 10MPa as the projectile is displaced and the available volume for the combustion products continually increases.

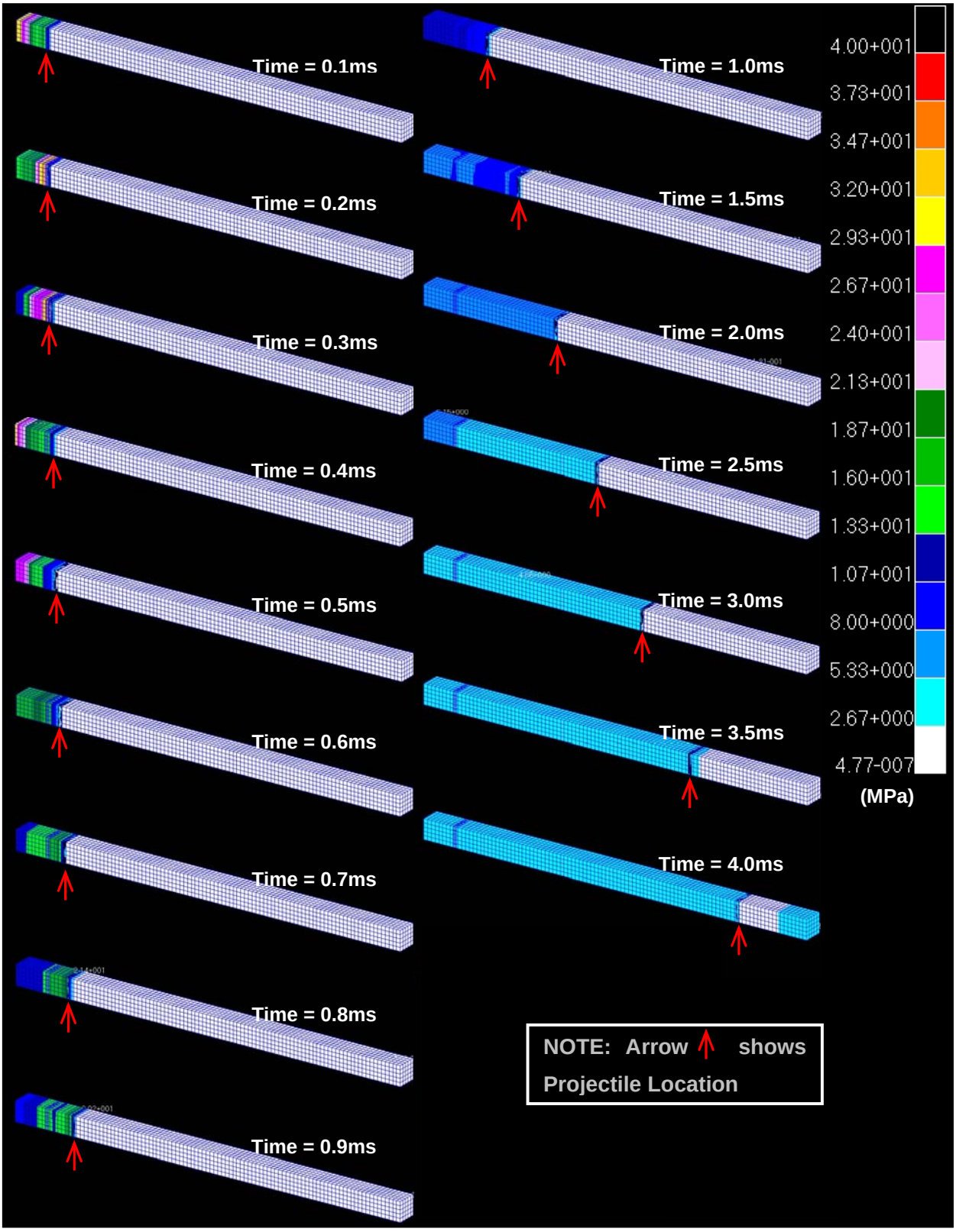

Figure 5.10: Pressure Results of Combustion in an Expanding Volume with Projectile

The same parameters used to create the finite element model above, were also used to solve the Ballistic Model in MATLAB. Figures 5.11, 5.12 and 5.13 compare the results of the two simulations.

Figure 5.11 contains the results of Average Pressure for the system, as given by Equation 5.6. A maximum average pressure of approximately 28MPa occurred at 0.2msec according to the MATLAB calculation. Results of finite element analysis shown in Figure 5.10, revealed a localised maximum pressure of approximately 40MPa. However, if the pressures were averaged across the entire chamber volume for the 0.2msec plot, where pressures ranged between 18-40MPa, then good agreement would be had between both analyses.

This result highlights the benefit of solving the Ballistic Model using finite elements. High values of localised pressure may affect the mechanical design of the weapon. Failing to recognise these potential phenomena could lead to designs which are not structurally suitable for the intended ballistic environment. In addition, the geometries considered as apart of this analysis were overly simplified, possessing only square cross sections. In designs exhibiting intricate geometries, the possibility for localised pressure increases would be far more significant. Such instances would definitely require the use of finite elements.

Considering the plot at 1msec in Figure 5.10, we notice that the pressure gradients have reduced significantly, showing an average pressure of approximately 10MPa. This result shows good agreement with MATLAB results (Figure 5.11), where a value of just below 10MPa was recorded. The trend of average pressures is very similar for both analyses all the way up to the end of the simulation (4msec), even though the finite element predictions appear to be slightly greater.

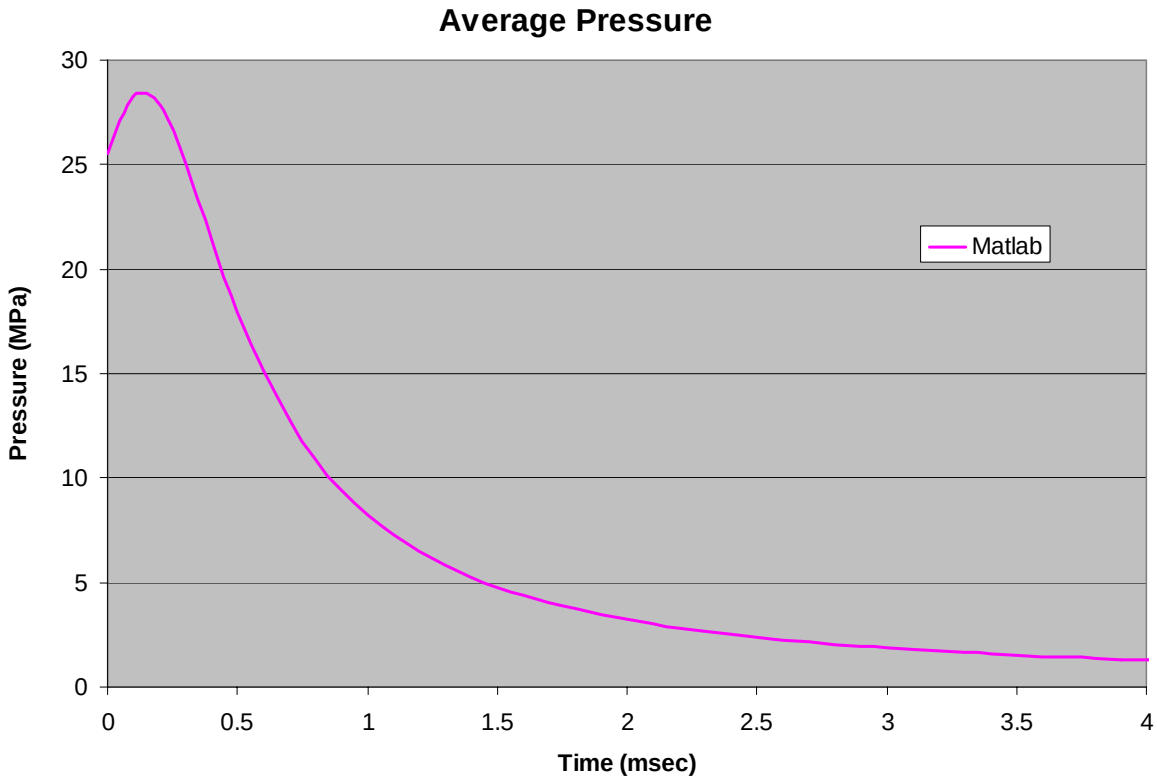

Figure 5.11 MATLAB Average Pressure Results of Combustion in an Expanding Volume with Projectile

Figures 5.12 and 5.13 compare the finite element and MATLAB results for the motion of the projectile. Considering the results of Projectile Displacement, shown in Figure 5.12, we notice excellent agreement in the early stages of the motion up to 2.5 milliseconds. Beyond this, the curves begin to diverge slightly, as the finite element result shows a greater displacement. This result would be expected, as the pressure results revealed that the finite element predictions were marginally higher.

This is further emphasised by the results of Projectile Velocity shown in Figure 5.13. Finite element analysis calculates a higher velocity for the later stages of the cycle, as compared to MATLAB. However, there was very good agreement in the first half of the cycle.

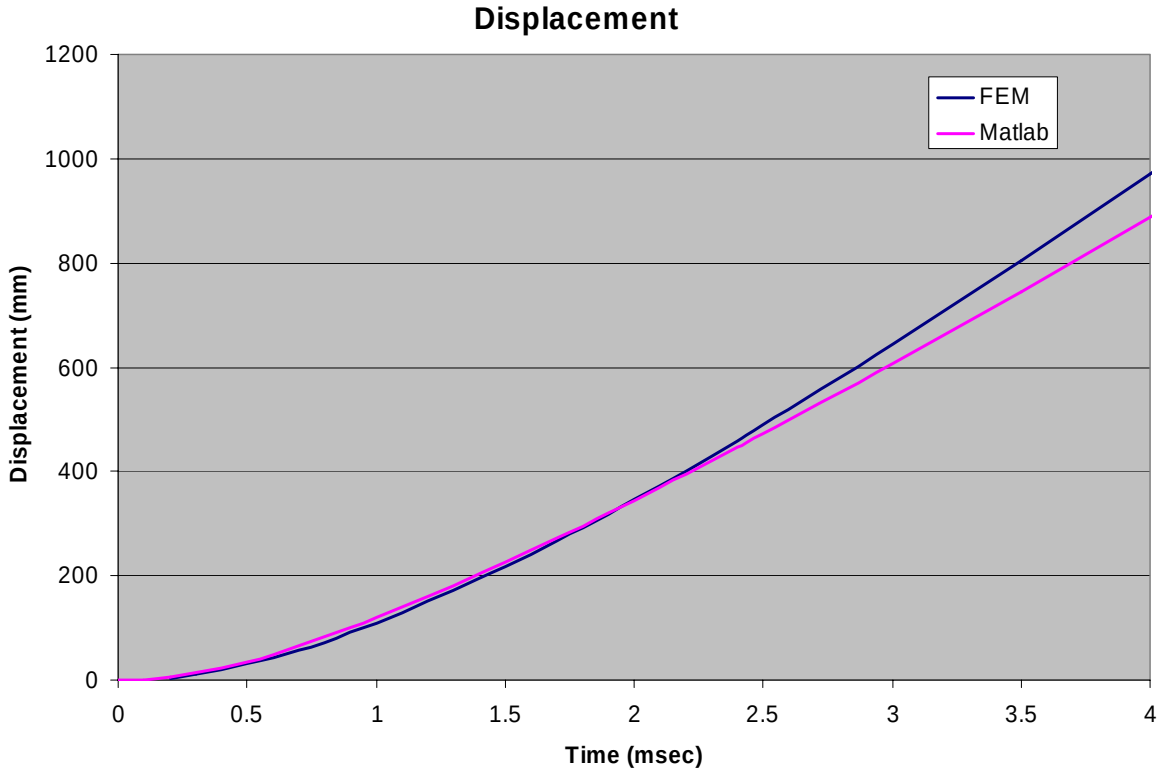

Figure 5.12 Displacement Results of Projectile

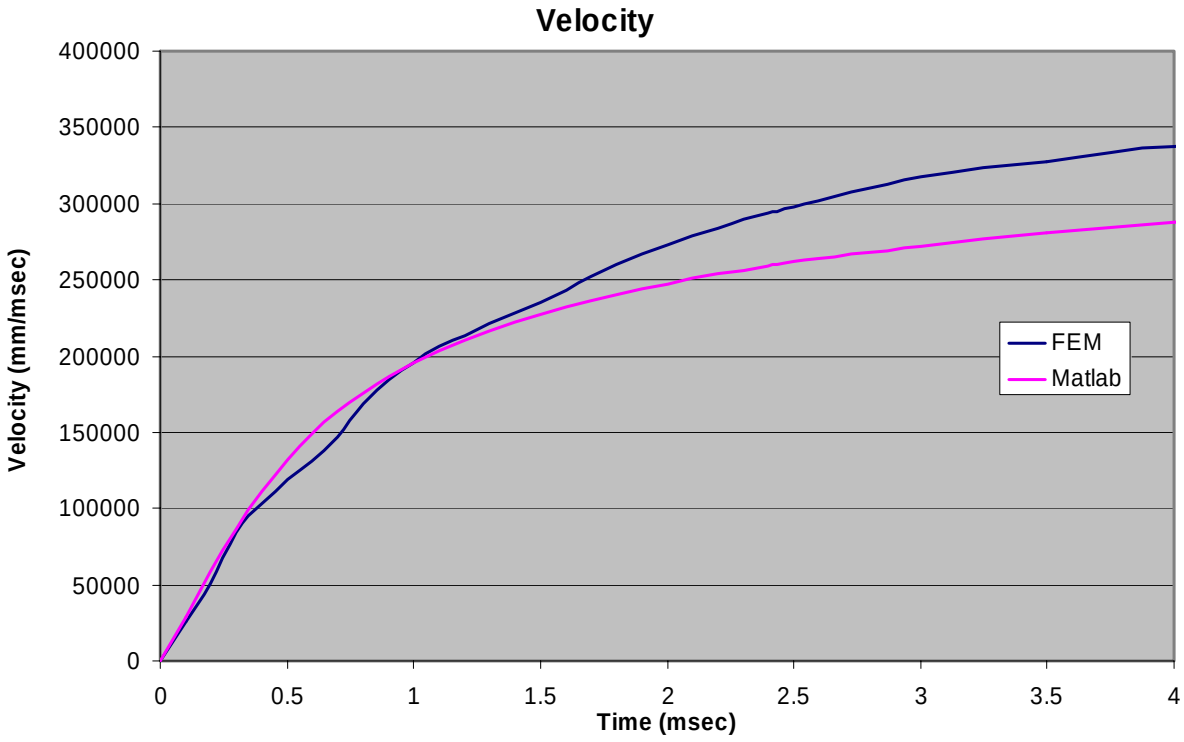

Figure 5.13 Velocity Results of Projectile

The analysis where propellant combustion was used to accelerate a projectile highlighted the benefits of using finite element methods in this application. The Ballistic Model solved in MATLAB was only able to calculate average pressures generated by the propellant and use these to predict the performance of a ballistic system. Solving the ballistic model using Fluid Structure Interaction modelling in the finite element environment allowed for greater insight into the behaviour of the propellant. Sharp pressure gradients were observed in the expanding chamber volume, where peak values significantly exceeded those predicted by MATLAB.

It was suggested that such results would be crucial in the mechanical design of gun and projectile components. The use of Fluid Structure Interaction modelling allows for considerations of mechanical design to be included directly in the modelling process. Therefore, the finite element tool developed in this investigation allows for impact of ballistics and propellant combustion to be used in the design of mechanical systems. Solving the Ballistic Model alone can only be used as an indication of ballistic performance. These averaged results must then be applied to components in a suitable analysis environment in order to attempt structural design.

5.6 Conclusion

In this Chapter, a Ballistic Model was integrated into the finite element environment to describe propellant burn. A User Subroutine defining the Nobel-Abel Equation of State was incorporated into the MSC. Dytran explicit solver. It enabled the use of propellant properties to determine the pressures generated during the interior ballistic cycle. Fluid-structure interaction modelling could then be used to study the structural behaviour of components subject to the dynamics of propellant combustion.

The performance of the subroutine was first validated against a MATLAB simulation of the Ballistic Model where propellant was combusted inside a closed volume. The investigation was then expanded to include the interaction of Lagrangian and Eulerian elements. A simulation was performed where the combustion of propellant was used to stress a closed Lagrangian box.

A revised subroutine was then developed to allow the combustion of propellant in an expanding volume. The challenge of this task was the dynamic introduction of new and originally void Eulerian elements into the analysis. This capability was then used to accelerate a projectile according to a set of known system parameters. This simulation was again validated against a MATLAB simulation of the Ballistic Model using the same parameters. A good agreement of results was observed, however, advantages of using the finite elements in this application were revealed.

The advantages of integrating a ballistic model into an explicit finite element solver are clearly demonstrated, however, some significant limitations still exist. For example, the current model was only stable while considering simple rectangular geometries as presented above. The process of dynamically allocating combustion properties into originally void Eulerian elements is complicated when considering more elaborate geometries. Further development of the subroutine would be required in order to design real tube launched weapons. However, the further development of such a model would require undertaking a significant body of work which is beyond the scope of this research.

6 Application of VDP for the Design and Development of Stacked Kinetic Energy Rounds

6.1 Introduction

In this chapter, novel concepts for developing a stacked Kinetic Energy Round (KE) are explored using the VDP. More specifically, studies were undertaken to develop a gun system containing multiple High Velocity Fin Stabilised Discarding Sabot (HVFSDS) Kinetic Energy rounds in a single barrel.

A number of options were considered with a view to develop solutions to the design problems. Valid ideas were first translated into a Computer Aided Design (CAD) environment in order to develop key design features and assess their suitability in the application. A judgement was then made as to whether or not the design should progress into the finite element environment for preliminary analysis.

As highlighted earlier, the use of implicit finite element methods was limited in its ability to fully explore the dynamic nature of tube launched weapon systems. Consequently explicit finite element methodology was used to develop stacked HVFDS rounds. This process allowed for any dynamic phenomena experienced during the interior ballistic cycle, which would impact both design and performance, to be identified early.

6.2 HVFSDS Kinetic Energy Rounds

HVFSDS KE rounds concepts were based on sub-calibre rounds where fin stabilised projectiles are encompassed by a lightweight, parasitic sabot structure. This allows the projectile to be fired from a larger calibre gun to achieve a very high muzzle velocity. After ejection from the barrel, aerodynamic loads act on the sabot and cause it to strip away from the projectile immediately leaving the sub caliber projectile to fly towards the intended target. The projectile was designed as a dense penetrator dart which is accelerated to very high velocities to maximize the kinetic energy delivered to the target.

The design of the HVFSDS KE round followed a similar pattern to that for the Armour Piercing Fin Stabilised Discarding Sabot (APFSDS) round currently developed by BOFOR firing at muzzle velocities of 1500m/s. The main objective of APFSDS round is to penetrate armoured vehicles and other high value material targets. Examples of APFSDS rounds can be seen in Figure 6.1.

Figure 6.1 Examples of APFSDS Rounds

The concept and application of APFSDS rounds have been well documented in the literature. They provide a firm background on the applications and major design considerations associated with such munitions. In this study, however, the challenge was to design high velocity rounds similar to APFSDS which could be loaded in multiple configuration in a single barrel and fired at a muzzle velocity of 1600m/s at corresponding pressures of approximately 500 MPa.

Guidos and Cooper 1999 [111] developed a methodology for analytically modelling KE projectile motion in free flight when subjected to an in-flight lateral impulse. The model was able to predict the resulting projectile translation and angular responses. Newill, et al., 1999 [112] asses the impact of changes to KE projectile design on performance using numerical analysis. They found that by changing the forward diameter of the sabot, the variability in yaw could be significantly reduced.

The separation characteristics of parasitic components for kinetic energy penetrators were considered by Hasslid 1999 [113]. An analytical methods approach provided an understanding of the different loads and constraints associated with the problem. A CFD-parametric study was performed to modify the dimensions of an improved nose cap.

Newill, et al., 2002 [114] considered the launch performance of two design candidates for the experimental XM1002 training projectile. Variability in launch characteristics were attributed to differences in transverse moments of inertia of the two designs. The authors concluded that a projectile possessing a lower moment of inertia was less able to resist path changes created by the imperfections of the gun tube.

Analysis into the development of practice rounds was also conducted by Worst 2004 [115] whose goal was to design a limited range practice round which could be safely fired on ranges. Worst 2004 was successfully able to use venturies as fins which were designed to choke at a certain mach number, thus limiting the range.

Apparent from the literature is that traditional gun systems allow for the firing of one APFSDS round from a single barrel. The time consuming tasks of cartridge ejection and munition reload are then required for the firing of successive rounds. The development of a high velocity stacked round concept aims to increase the lethality of a given weapon through dramatically increasing the rate of fire. A well designed system would allow subsequent rounds to be fired almost simultaneously, delivering numerous rounds to the target instantly.

The possibility of eliminating the cartridge ejection and reload mechanism provides further scope for developing a more sophisticated and efficient weapon system. Ultimately, the gun/projectile system could be designed to allow for a continuous feed of rounds into the chamber. This would result in a weapon system which could sustain a high rate of fire for an indefinite number of rounds.

6.2.1 Stacked Round Considerations

The development of a stacked HVFSDS round presents some challenging design requirements. High charge levels are required to achieve the specified muzzle velocities for the round.

The high propellant gas pressures generated from firing the first round would impart large rearward axial loads on the following rounds. The fracturing, compacting or moving of propellant grains in the second projectile propellant could cause a dramatic increase in rise-time and peak-pressure on ignition of the second round. Furthermore, any significant rearward movement of the aft projectiles may even result in sympathetic ignition of propellant. Such an event would obviously be catastrophic and undesirable.

The gas pressure generated by the combusting propellant must be effectively sealed from the following round's propellant charge. Any leakage of hot, high pressure gasses could again result in the premature ignition of subsequent rounds. Other concerns relating to excessive heat generation or flash instigating spontaneous firing of the second round propellant must also be considered.

Any gun system firing multiple rounds must make allowance for the following rounds to pass through the breech/cartridge and barrel unimpeded. Hence, any mechanism used to fix and seal forward rounds, must not interfere with the following rounds exit from the barrel.

6.2.2 Penetrator Design

As the penetrator relies on kinetic energy to defeat its target, a combination of high weight and velocity is required. Dense materials such as depleted uranium or tungsten are usually used to maximise weight [24]. The best penetration performance is achieved using a high length to diameter relationship for the penetrator where a ratio of 16:1 is common. Due to this configuration the dart is often referred to as a "long rod penetrator". As the penetrator needs to cover large distances, it is commonly fitted with fin stabilisation to achieve accuracy and is fired from a smoothbore barrel.

A significant amount of information is available in the literature in reference to KE penetrator design and performance. The influence of yaw angles on the performance of long rod penetrators has been studied by authors such as Bless, et al., 1999 [116], Hohler and Behner 1999 [117], Heider, et al., 2004 [118] and Lundberg, et al., 2004 [119]. Borrmann, et al., 1999 [120] demonstrated significant reduction in penetration performance of vibrating penetrators depending on the deflection phase of the penetrator at the time of impact.

A significant body of research has been undertaken to use tungsten as a penetrator material [121]. Xu, et al., 1999 [122] consider the penetration properties of torqued and non-torqued tungsten alloy rods. Transverse impact experiments were conducted by Chan, et al., 1999 [123] in order to asses the resistance of tungsten to transverse fracture.

Much work has also considered improving the structural integrity and penetration performance of tungsten rods using jacketing or sleeving materials. Examples of which can be found in Gee 2004 [124], Kaufmann, et al., 2004 [125], Leeming and Rigby 2002 [126] and Lanz and Kaufmann 2002 [127]. Other researchers have considered temperature influences on penetration performance [128] and penetration mechanisms at material interfaces [129].

6.2.3 Sabot Design

A sabot is a light weight carrier structure used both to position a subcalibre projectile inside a gun barrel and to transmit energy from the propellant to the projectile [97]. This allows for slender projectiles, with good aerodynamic profiles [24], to be launched from larger calibre guns for either higher terminal velocities or increased range. These improvements arise due to the increase in bore area created by the sabot on which the propellant gas pressure is able to act.

The associated increase in total projectile launch weight is minimal in comparison to the increase in performance. Sabot weight generally represents one-quarter to one half of the entire projectile weight for most modern kinetic energy projectiles [38]. Optimally however, the sabot mass should be kept to a minimum as it represents parasitic weight in terms of on target performance.

Most sabots used to launch modern high velocity KE projectiles are multi-segmented, arranged annularly about the penetrator to seal the bore. At muzzle exit, they are designed to separate into separate segments under aerodynamic loads.

In terms of in-bore structural requirements, the sabot must seal the bore of the gun against the hot, high pressure propellant gas as well as support the penetrator during in-bore travel. The force applied to the sabot by the propellant gas pressure must be transferred across the sabot/penetrator interface for the acceleration of the penetrator without causing any unwanted permanent deformations or fractures.

The way in which the gas pressure is transferred from sabot to projectile is a major concern in sabot design. Traditionally, sabots can be categorised as either push or traction type, each of which are shown in Figure 6.2.

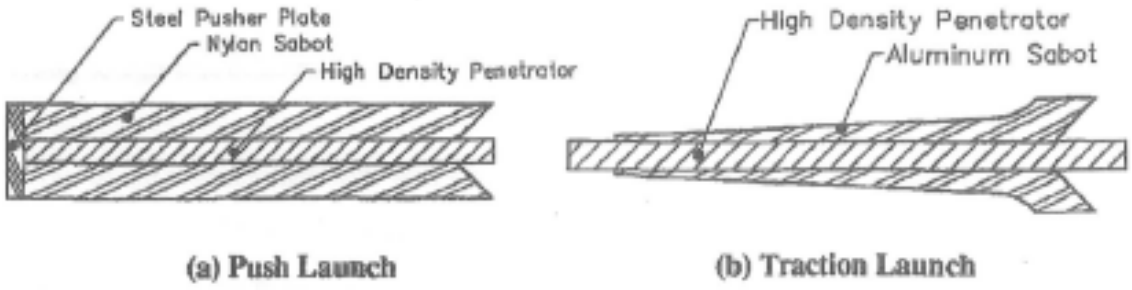

Figure 6.2. Push and Traction Type Sabot Systems [59]

The supporting length offered by the sabot greatly affects penetrator design [38]. The high accelerations experienced during launch result in large inertial loads. The unsupported regions of the penetrator are severely restricted due to allowable stress limits. Many factors may affect the stability of the unsupported penetrator length. These include transverse loads, eccentricity of the axis of the penetrator due to manufacturing tolerances and inertial loads [38].

In a push type sabot, the entire gas pressure is transferred to the penetrator at its base via a pusher plate. The entire penetrator length is unsupported and therefore these types of sabots are inappropriate for most applications. Traction sabots, however, use a series of lugs or teeth to grip the penetrator along a portion of its length and hence offer a more robust solution.

Rabern and Parker 1995 [10] found in their analysis of different launch packages that the traction sabot system, however, was much more expensive to manufacture [59] due to complex geometries as compared to the push type sabot.

All sabots must also provide means by which they are able to be discarded once having exited the barrel without disturbing the motion of the projectile. In general, high muzzle pressures experienced immediately upon exit from the gun tube act on the scoops or wings of the sabot [38]. This produces a lift force on the sabot segments and results in separation from the penetrator as shown in Figure 6.3. This process is vital in the projectile maintaining its accuracy as any non-symmetrical forces will cause it to change its trajectory.

Figure 6.3 Separation of Sabot from Penetrator under Aerodynamic Loading.
(Taken from http://www.army-technology.com/contractors/ammunition/apfsds.htm)

Predicting this pressure is extremely difficult due to intersecting shock waves from the penetrator and sabot petals [38]. Computational modelling of the sabot discard process was carried out by Sahu, et al., 1998 [130] in which the aerodynamic interference of the multibody system was simulated. It was necessary to consider 3D shock-shock interactions, shock-boundary layer interactions and highly viscous-dominated separated-flow regions. This kind of study is beyond the scope of this research as it would require detailed analysis of the intermediate ballistics phase which is not considered.

6.2.4 Design Requirements

The focus of this study is to design a sabot which is capable of performing its traditional role of supporting a sub-calibre projectile in addition to providing the necessary capability for firing axially stacked rounds. That is, the role of the sabot will also include providing the necessary gas sealing and axial restraint mechanisms necessary for the stacked round concept. While penetrator design is vital to the success of an HVFSDS round, it is not the major focus contained herein. Generally, tungsten penetrators are assumed with masses similar to that reported in the literature for APFSDS rounds.

Some basic design goals and constraints are stipulated below in order to guide the development of the stacked round concept. These include:

- Bore size = 60mm
- Barrel length = 70 calibers (4.2m)
- Muzzle velocity = 1600 m/s
- Minimum Rate of Fire = 10 rounds/second
- Minimum of 2 rounds per barrel

While high propellant gas pressures are required to accelerate the round to the required muzzle velocity, associated erosion effects also serve to reduce barrel and breech life. A peak firing pressure of 420MPa was selected initially as a compromise for these opposing issues. However, an overpressure situation of 30% (546MPa) is not uncommon in these types of weapons. Therefore, any structural design must allow for the gun system to still perform at these higher pressures.

A simple numerical model of interior ballistics, similar to that presented in Section 5.1.1, was used to estimate the average pressure expected in the firing of a 60mm APFSDS round. That is, considering properties of the gun, projectile and propellant, the model predicted the expected average pressure inside the gun barrel for the entire interior ballistic phase. This pressure data would be used initially in explicit finite element simulations to rapidly develop and assess design ideas. The predicted curve was slightly modified in order to reduce computation time during the design phase. The original and modified curves can be seen in Figure 6.4.

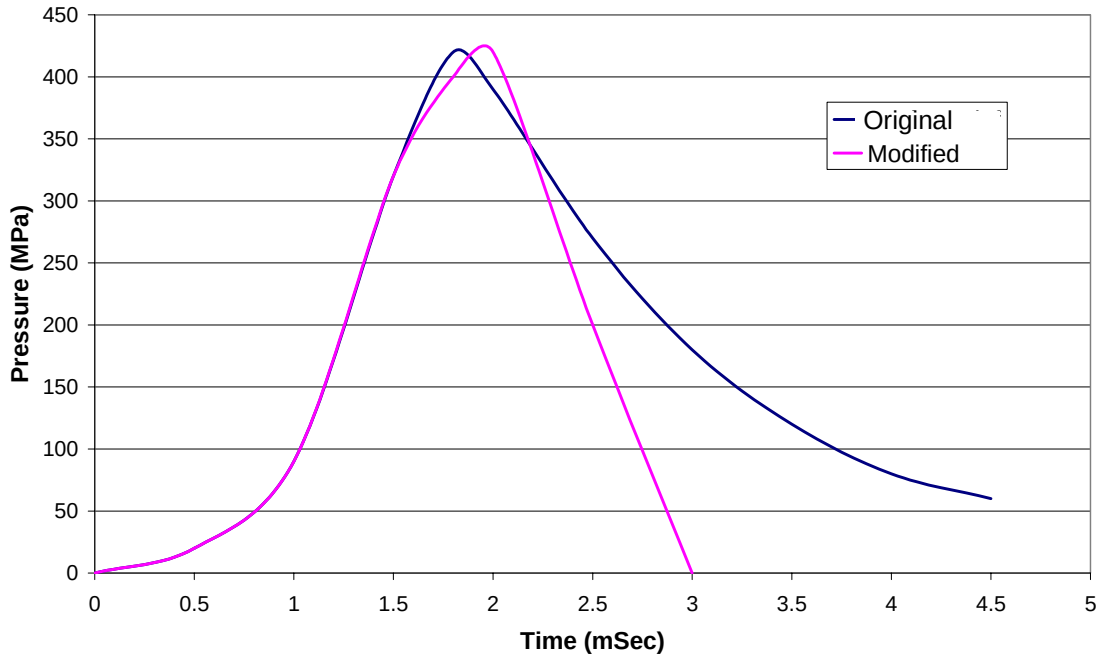

Figure 6.4: Modified Pressure Curve

The positive pressure phase remains relatively unchanged, with the maximum being shifted slightly forward to occur at 2msec. This allows results to be plotted more simply knowing that the maximum pressure condition occurs at exactly 2msec. The negative phase of the pressure curve has been shortened considerably in order to speed up computation time. This portion of the curve is deemed to be less important in the design of the gas sealing and restraint mechanism of the sabot. However, in order to determine the ejection performance of the round, the original negative phase would have to be used.

When proposing design concepts throughout this study, the analysis considers both rearward and forward load cases. The rearward load case considers the sealing and restraint behaviour of a saboted round, simulating the gas pressures generated as if the round in front had been fired. The forward load case refers to the pressures applied to the rear of the sabot as it is accelerated out of the barrel.

The same pressure curve is used in both cases, however it is applied in opposite directions and to different parts of the round depending on the design. Figure 6.5 demonstrates each load case. Using the modified pressure curve given in Figure 6.4, the event time required for computation for both the rearward and forward load cases can be reduced to 6msec for a given round. Depending on the complexity of the model, this may save several hours of computation for any given simulation.

Rearward Load Case (For Round Sealing and Axial Restraint)

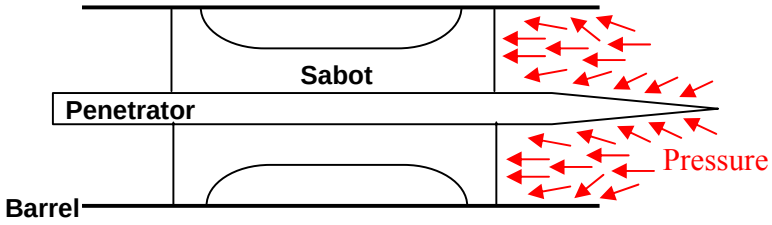

Forward Load Case (For Round Ejection from Barrel)

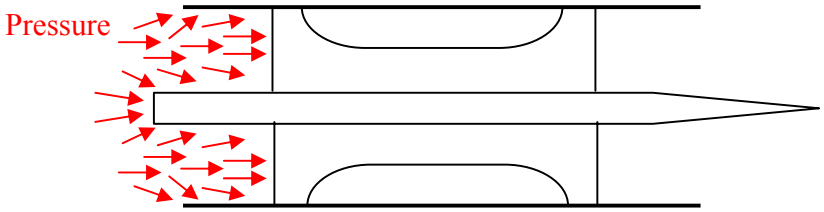

Figure 6.5: Forward and Rearward Load Case Definition

The total projectile mass is another vital consideration in achieving the design goals. As the peak firing pressure is limited, the total mass must also be limited in order to achieve the required muzzle velocity of 1600 m/s. A mass of about 1kg seems reasonable as a first approximation in order to achieve maximum on-target performance. This will act as a basic guide as the sabot design develops.

6.3 Stacked KE Round: Concept Development using Explicit FEA

Explicit FEA was used to explore a large range of novel concepts for achieving a stacked HVFSDS round. Many design ideas were able to be efficiently evaluated against the design goals in terms of their suitability in satisfying both design and performance requirements. In this section, a selection of concept developments is presented in order to demonstrate the process. Figure 6.6 contains a flow chart which outlines the major design ideas explored throughout the development process.

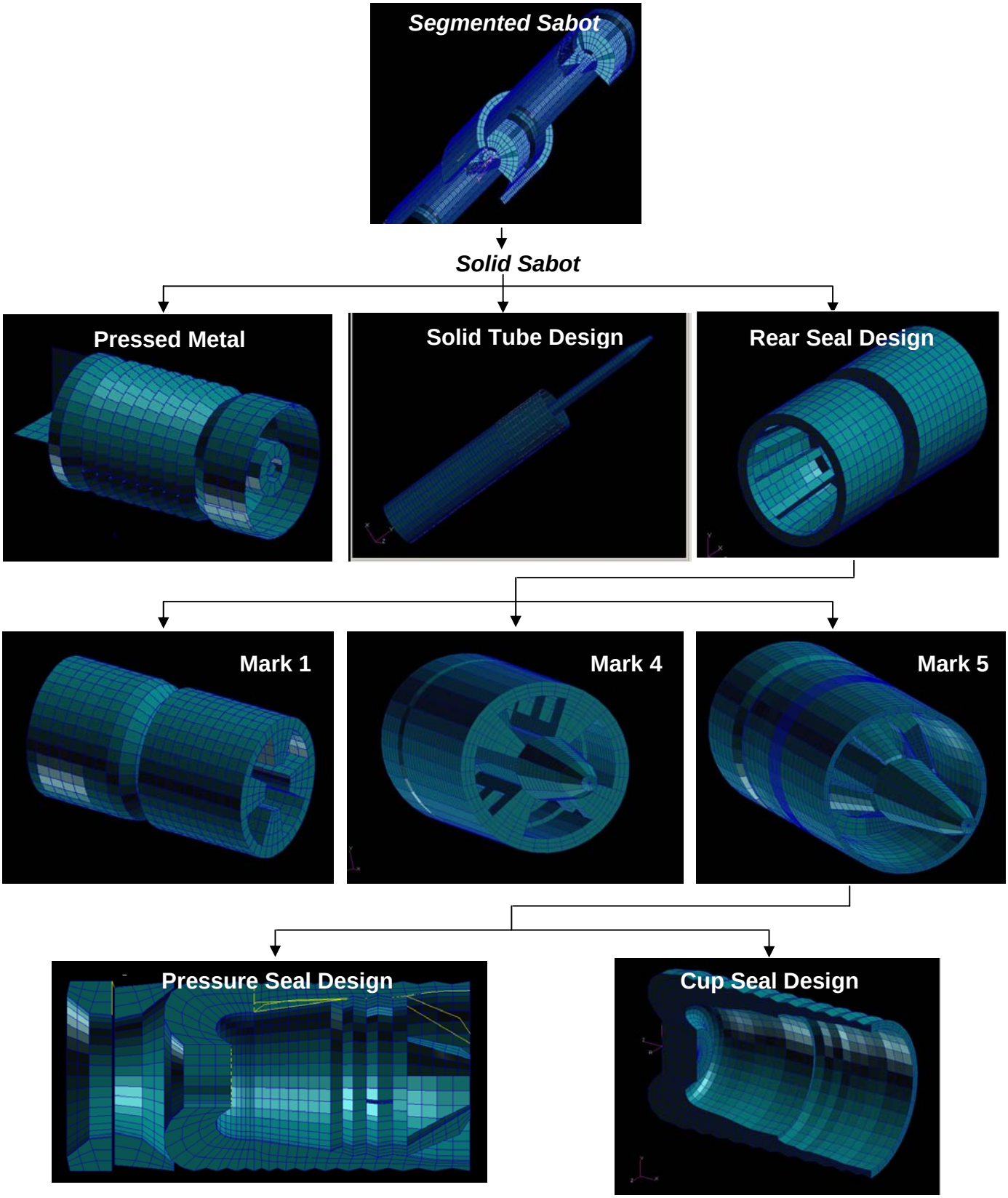

Figure 6.6: Conceptual Design Flow Chart

6.3.1 Segmented Sabot

The first design concept, termed Segmented Sabot, maintained some features of traditional sabot design. The design was based on a traction type sabot and was composed of four identical petals which would disengage from the penetrator under aerodynamic loading. However, in this design the sabot also acted as a cartridge which would both contain the propellant and provide means by which subsequent sabots could be attached via a clip.

A locking mechanism was incorporated into the front region of the sabot, intended to engage with a matching profile machined into the inner barrel wall. Figures 6.7 and 6.8 graphically illustrate the concept, with Figure 6.8 highlighting the locking mechanism of the sabot.

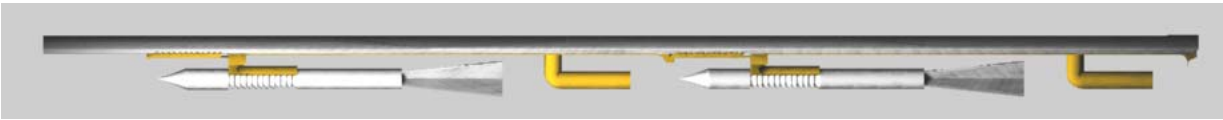

Figure 6.7: Segmented Sabot Design: Two Rounds located inside the Barrel (Quarter Model shown)

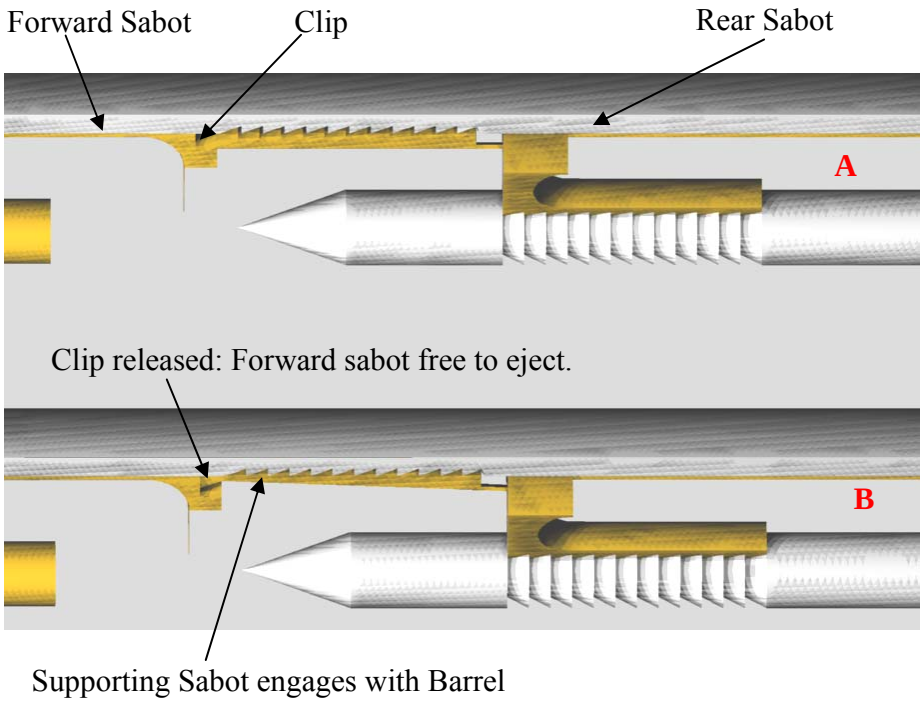

Figure 6.8: Detail of Segmented Sabot Locking Mechanism and Clip.

A) Second sabot shown locked to first; B) Second sabot released from first and locked to barrel.

This concept allows as many rounds as practical to be clipped together end to end to form a continuous cylinder which is inserted into the barrel. Due to the nature of the clip, the first round could not be released without the sabot of the second round engaging with the barrel. This creates both a breech for the fired round whilst also providing axial support for the supporting round to ensure its propellant is not compressed and prematurely ignited. The engagement of the supporting sabot with the barrel is also assisted by the blast pressures of the fired round which expand the sabot petals into the barrel.

When the second round is fired, its sabot disengages with the barrel insert. Disengagement may simply occur due to elastic relaxation of the sabot material after the first round clears the barrel. High friction surfaces on the barrel insert would ensure the sabot remains engaged while the pressure is high. Alternatively, the sabot could be designed to undergo plastic deformation during the firing of the first round. In this case, the locked section would be pushed clear of the barrel insert when the round is fired.

A finite element model was created in MSC. Patran in order to assess the dynamic behaviour of the Segmented Sabot design using MSC. Dytran. A large and complex sheet metal design employing four overlapping sabot sections was created, as seen in Figure 6.9. Shell elements were used for the entire model excluding the penetrator and penetrator support structure. These were modelled using solid brick elements.

Elastic-plastic material models were used to represent each component. The sabot was composed entirely of aluminium, while tungsten was used for the penetrator. The portion of the barrel containing the machined sabot profile was also modelled in order to assess the locking mechanism. A high tensile steel was used to model the barrel. A dynamic pressure field was applied to the system representing the firing of the front round. Various contact definitions employing friction were also imposed. These included contacts between individual sabot petals, between sabot and penetrator and between sabot and barrel.

The analysis demonstrated the ability of the design to expand under gas pressures and engage with the barrel insert. Concerns, however, arose due to the difficulty of maintaining a gas seal in the expanded sabot petals. The expansion revealed longitudinal gaps in the sabot which could only be sealed via the incorporation of overlapping petals. Further concerns related to the possible jamming of the overlapped petals during sabot discard after the round was ejected from the muzzle. While this configuration was a potential design solution, the increasing complexity associated with forming a gas seal suggested that a simpler solution was required.

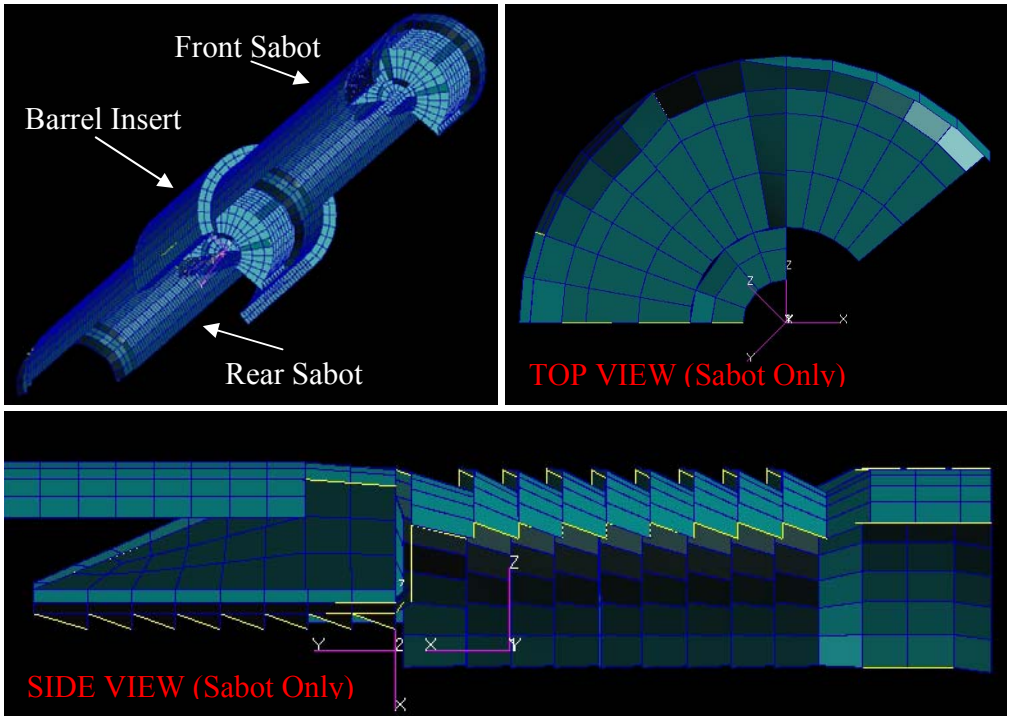

Figure 6.9: Segmented Sabot Design: Finite Element Model

6.3.2 Push Type Sabot Design

Based on the difficulties experienced in developing a traction type sabot, a new design approach was adopted. For design simplicity, it was decided that the penetrator should be deployed in front of a solid bulkhead, representing a push type sabot. It was suspected that such a system may provide for a more robust gas seal. However, the limited penetrator support offered by push type sabots would require close attention. As a result, various design prototypes emerged and are described below.

6.3.2.1 Pressed Metal Teeth

The Pressed Metal Teeth concept, shown in Figure 6.10, attempted to incorporate aspects of the Segmented Sabot into a push sabot design. As the entire penetrator was mounted in front of a pusher plate, problems with petal disengagement were no longer relevant.

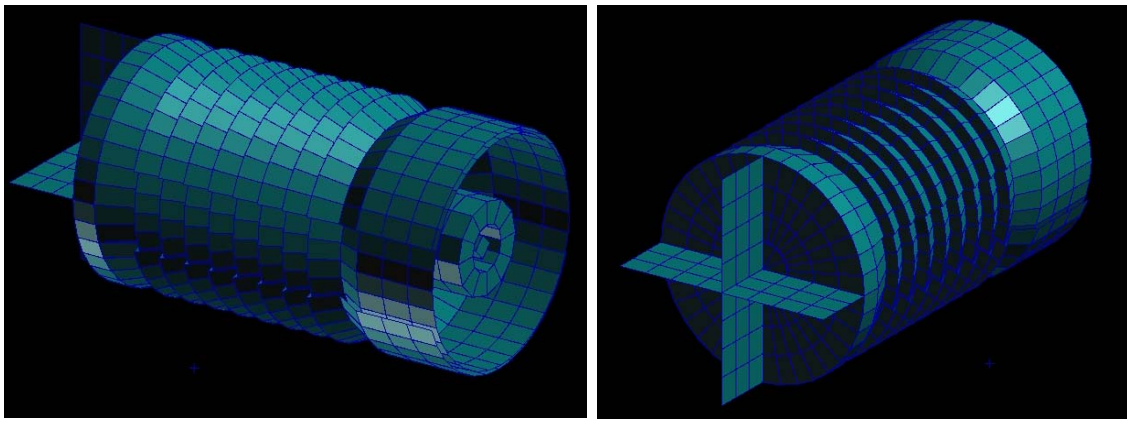

Figure 6.10: Pressed Metal Teeth Design: Finite Element Model

The concept was composed of two layers of teeth, modelled using shells, protruding in front of a solid bulkhead. Each layer was split in half enabling it to readily deform and engage with the barrel. The splits of each layer were rotated 90^{o} to prevent any gas leakage. Various combinations of teeth dimensions and material properties were explored to maximise the seal's effectiveness. The penetrator was mounted on a pin in front of the solid bulkhead.

The various configurations were again analysed using explicit finite element analysis. A dynamic pressure field was applied to the internal walls of the sabot in order to expand and engage the petals with the barrel. The sabot and penetrator were again modelled with aluminium and tungsten respectively, using elastic-plastic material models. Contact definitions were again used between components.

The investigation began by observing the behaviour of a single layer of teeth. The teeth were shown to engage smoothly with the barrel and prevented any rearward movement of the sabot. Figure 6.11 contains a plot of Von Mises Stress for the sabot in its locked position. Stress values were maintained well below that of the yield of the selected aluminium which was assumed to be 500MPa. However, in order to generate the necessary gas seal, the second layer of teeth was also necessary.

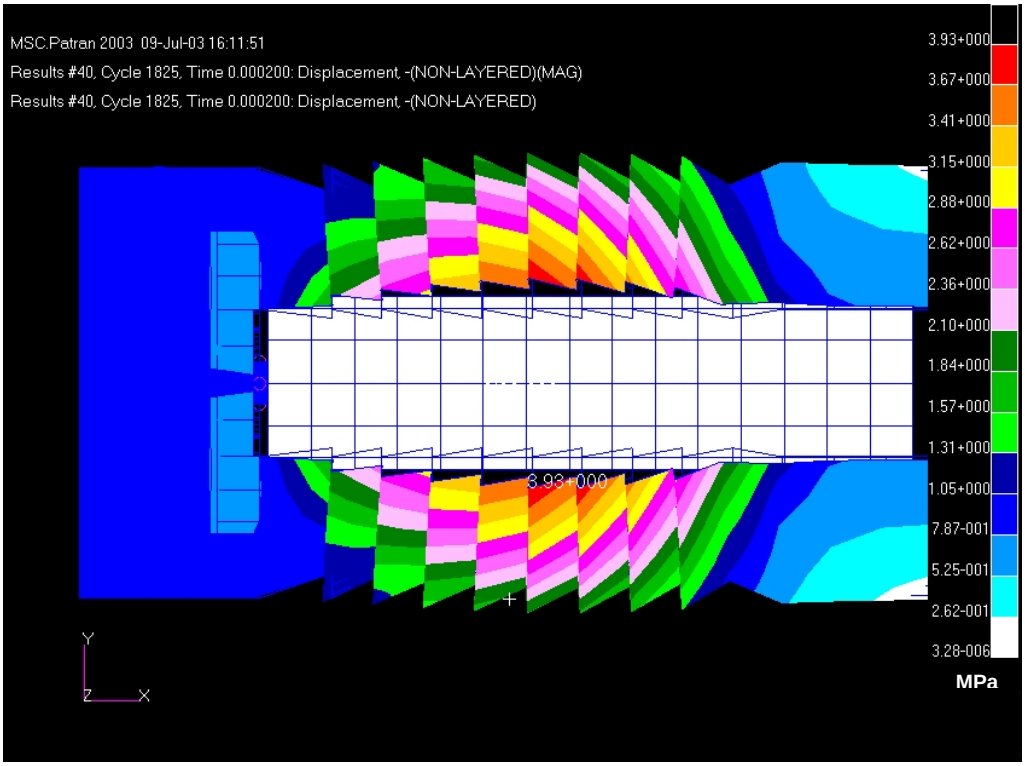

Figure 6.11: Pressed Metal Teeth Design: Stress Contours of Sabot in Locked Position

When the analysis was repeated using two layers of teeth, it was found that the model would become very unstable due to the overlapping layers of contacts between elements. After analysing different configurations, materials, and contact parameters it was found that the most likely cause of this instability was the buckling of the internal layer of teeth. Figure 6.12 illustrates the failure mode of this concept.

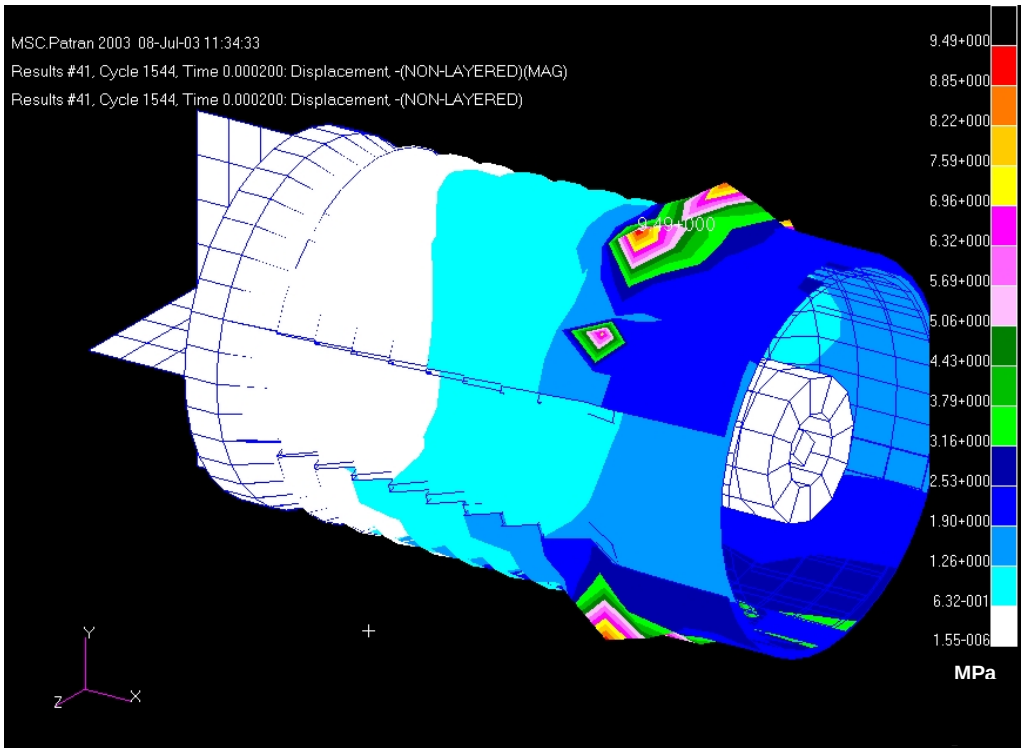

Figure 6.12: Pressed Metal Teeth Design: Model instability due to overlapping layers of teeth

This instability confirmed that a design concept composed of layers of overlapping teeth would be difficult to achieve. Therefore, the further development of this design was suspended in favour of the solid tube designs which are described in the next section.

6.3.3 Solid Tube Designs

The intention of the solid tube designs was to eliminate the requirement for sabot petals in order to improve and simplify the integrity of the gas seal. Essentially, the solid tube design relied on the expansion of a tube to seal against the barrel wall. The tube would also act as the cartridge and hence contain the propellant. Two mechanisms for generating the gas seal and preventing rearward motion of the sabot were investigated. The two mechanisms were termed “Plastic Deformation” and “Small Teeth” and are described in the sections below.

6.3.3.1 Plastic Deformation

The concept of Plastic Deformation relied solely on the friction generated between the two flat surfaces of the barrel and sabot when contacted under blast pressures. The generated friction would have to both provide axial restraint and gas sealing. Two main design approaches were investigated. In the first approach the bulkhead, or pusher plate, was located in the front half of the sabot. In the second approach, the bulkhead was shifted to the back of the sabot in order to maximise the area of deformable sabot. A schematic depicting these two approaches can be seen in Figure 6.13.

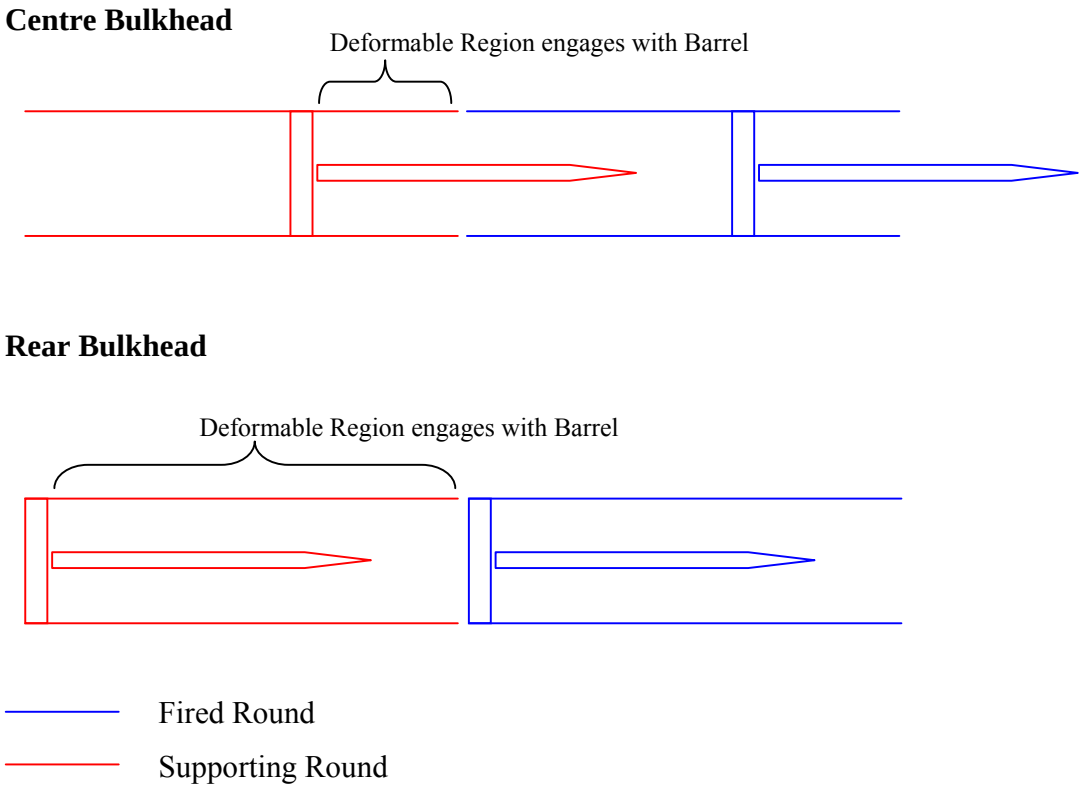

Figure 6.13: Solid Tube Design: Bulkhead Location Schematic

Figure 6.14 shows the finite element model created for the "Centre Bulkhead" design. A single tube of aluminium, modelled using shells, protrudes in front of the solid bulkhead. When subjected to the blast pressures of the fired round, it was expected that the aluminium would rapidly deform into the barrel. Friction between the components would then be relied upon to lock the sabot and create a gas seal. A titanium sheet was also used to reinforce the sabot at the bulkhead junction, where inertial effects would tend to stretch the aluminium tube. Similarly, a series of titanium wires were also used to reinforce the tube along its length, located at 20^{o} intervals around the circumference.

Titanium ribs, which can be seen on the right of Figure 6.14 (tube not shown), reinforce the bulkhead and also enable for some of the blast pressures to be transmitted to the aft rounds. It was assumed that either a pin or clip could be used to mount the penetrator in front of the bulkhead.

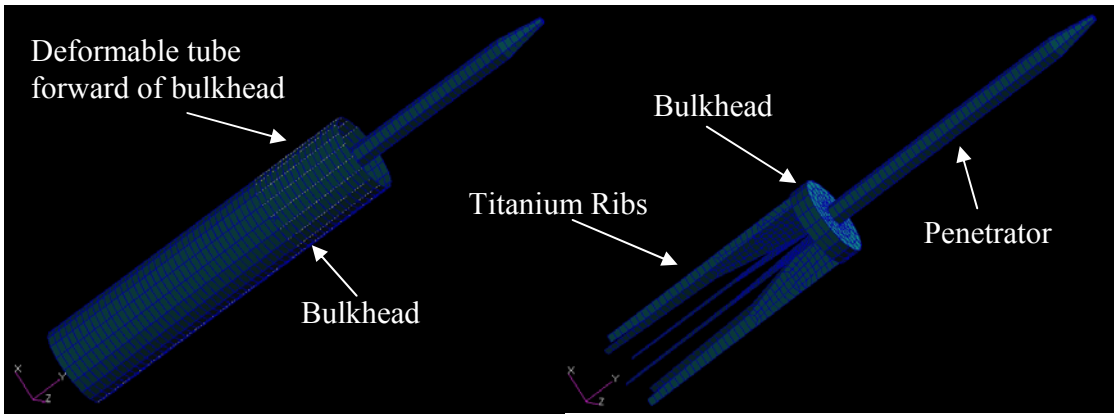

Figure 6.14: Solid Tube Design - Plastic Deformation (Centre Bulkhead): Finite Element Model

In the second approach the bulkhead was shifted to the rear of the sabot to allow for a greater area of deformable material as can be seen in Figure 6.15. The tube again utilised a high friction surface to prevent any rearward motion of the sabot. Similar to the centre bulkhead design, the tube was reinforced with titanium wire along its length at 20^{o} intervals around the circumference. A titanium sheet was again used at the bulkhead junction to counteract inertial effects.

The penetrator could again be located on either a pin or clipped to the front of the bulkhead. The bulkhead design in this instance was made more intricate in an attempt to minimise mass. A spherical rear section was therefore introduced. It was envisaged that this design would be better able to distribute stresses in this region. A forward deployed flat pusher plate, located in the centre of this spherical region, was used for penetrator mounting.

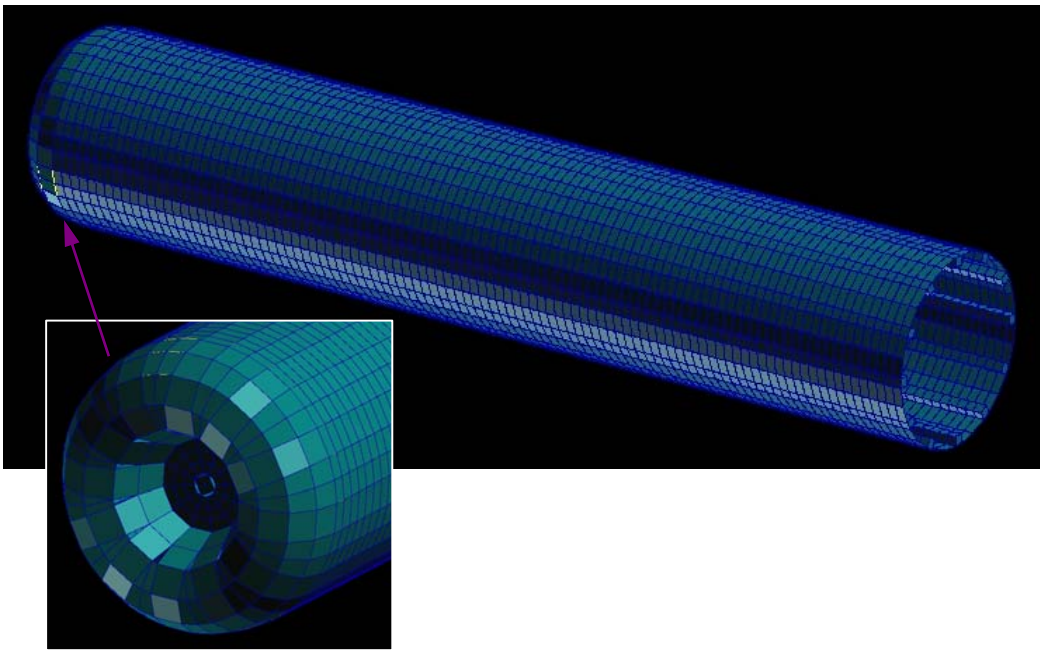

Figure 6.15: Solid Tube Design - Plastic Deformation (Rear Bulkhead): Finite Element Model

Both designs relied heavily on the assumed friction coefficients used to represent the contact between sabot and barrel. Depending on the magnitude of these values, various degrees of slippage were observed, hence not fully satisfying the axial restraint requirement.

In addition, problems were also encountered with the fired round again due friction. It was found that the friction generated at the sabot/barrel interface would cause the sabot to crumple as it travelled down the barrel for ejection. This crumpling may have the undesired effect of obstructing the penetrator from cleanly disengaging with the sabot once in the atmosphere. This was more severe in the rear bulkhead design as the deformable sabot region surrounded the entire length of the penetrator.

The use of a thin aluminium tube was found to only satisfy this limitation if the friction coefficient could be reduced in the forward direction. However, axial restraint requirements still necessitated a large friction coefficient in the rearward direction for the same sabot. An attempt at satisfying this condition was made by assuming the sabot could have small teeth machined around its surface. This design approach is discussed in more detail in the next section.

Supporting the sabot using aft rounds could also have been used to prevent backward motion during the early stages of the blast. Once significant pressure had been produced, frictional adhesion between the sabot and barrel could then resist the majority of the axial load. This configuration could minimise the required friction coefficient between sabot and barrel and hence alleviate the crumpling during sabot ejection. Temporary gas seals in the form of O-rings could be used to seal any low pressures prior to the onset of frictional contact.

Some interesting dynamic phenomena were observed in both bulkhead configurations. In the centre bulkhead design, it was found that as friction began to restrict rearward sabot motion, necking would occur in the bulkhead. This behaviour caused the sabot to deform away from the barrel. This observation was even more prevalent in the rear bulkhead design where necking resulted in the loss of frictional contact between the sabot and barrel causing the round to slip.

This finding led to the design proposition of a seal located behind the bulkhead. Such a design would use rearward deformations of the bulkhead to force the sabot to form a seal with the barrel.

6.3.3.2 Small Teeth

The small teeth concept attempted to address the requirement for a differential friction condition as described in the previous section. The design reverted back to using teeth, consistent with some of the earlier concepts, in order to lock the sabot. However, in this case, no matching teeth profile was modelled in the barrel; rather the teeth would contact a smooth surface. This concept was again assessed using both centre and rear bulkheads.

Figure 6.16 shows the small teeth concept utilising a centre bulkhead. A single tube of readily deformable aluminium possessing small pressed teeth protrudes in front of a solid bulkhead. Similar to previous designs, the tube is reinforced with titanium wire along its length at 20^{o} intervals around the circumference. A titanium sheet is also used to reinforce the structure near the bulkhead junction while titanium ribs reinforce the bulkhead. The penetrator is either located on a pin or clipped to the front of the bulkhead.

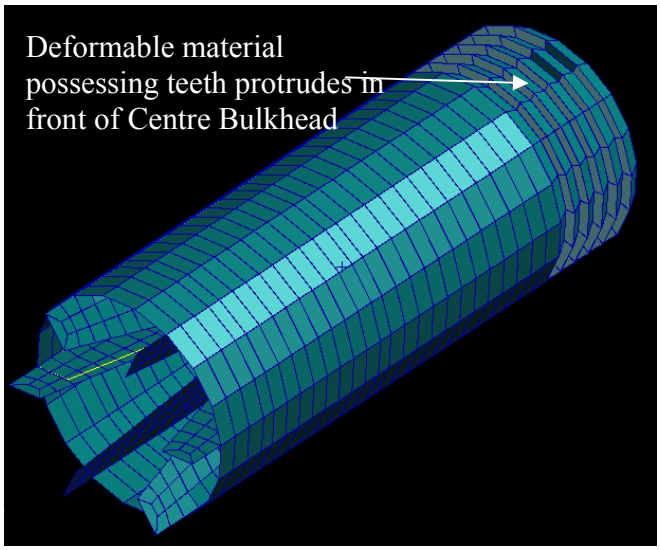

Figure 6.16: Solid Tube Design - Small Teeth (Centre Bulkhead): Finite Element Model

Figure 6.17 illustrates the rear bulkhead version of the small teeth concept. Again a single tube of readily deformable aluminium possessing small, machined teeth protrudes in front of a solid bulkhead. The tube is reinforced with titanium wire along its length at 20^{o} intervals around the circumference. The bulkhead junction is also reinforced with a titanium sheet. The bulkhead again adopts the spherical geometry as developed previously for the plastic deformation concept. The penetrator is either located on a pin or clipped to the front of the bulkhead.

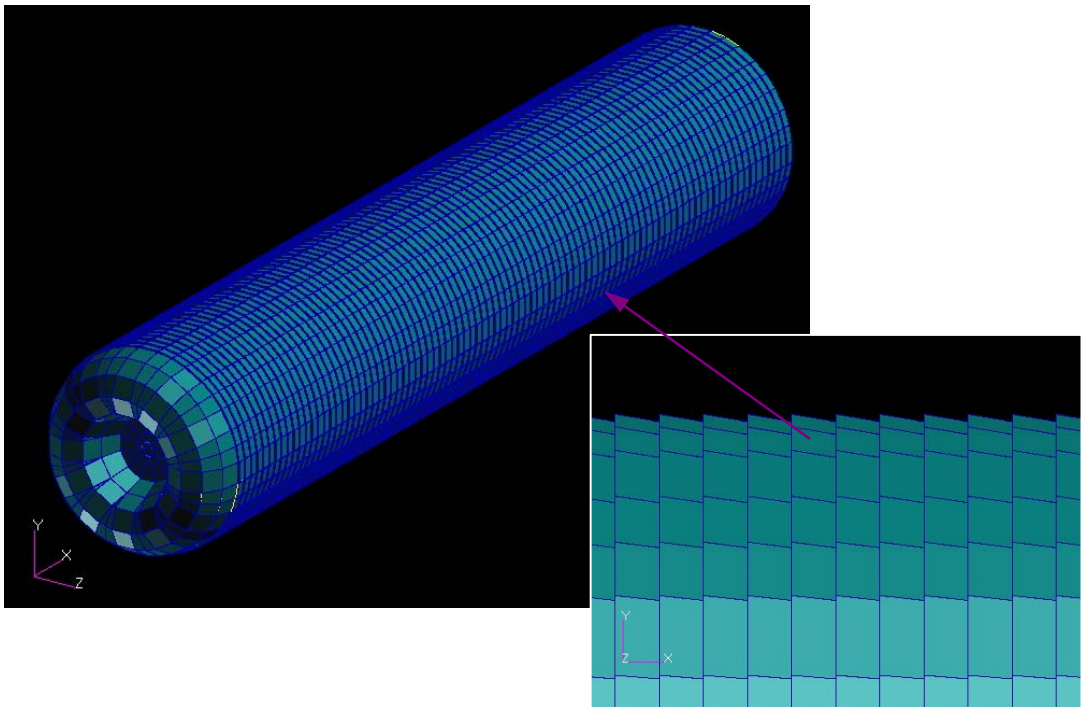

Figure 6.17: Solid Tube Design - Small Teeth (Rear Bulkhead): Finite Element Model

The inclusion of teeth on the contact surface of the sabot was intended to concentrate the contact force between sabot and barrel. This would serve to increase both seal effectiveness and axial restraint. As with the previous 'plastic deformation' concept, the centre bulkhead configuration suffered from longitudinal stretching and necking of the sabot away from the barrel. It was also observed that the teeth profile increased the radial stiffness of the sabot. As a result, the contact force between the sabot and barrel was reduced, causing the sabot to progressively slip as blast pressures increased.

The rear bulkhead configuration also suffered from increased radial stiffness of the tube resulting in a decreased contact force. The tube was found to expand first near the bulkhead with the onset of blast pressures. However, it was found that the teeth in this region failed due to shear when engaging with the barrel, causing the sabot to slip. This behaviour caused the model to become unstable due to highly distorted elements, causing the solution to terminate prior to simulating the entire blast. The use of stronger metals was explored however they further prevented the sabot from expanding and contacting the barrel.

The loss of some teeth may not create a problem in a real system. The use of more sophisticated material models, describing material failure, would have enabled a more realistic attempt at modelling this behaviour. However, modelling instability and sabot slip lead to the development of a new concept termed 'Rear Seal Design' and is discussed in the next section.

6.3.4 Rear Seal Designs

The Rear Seal Design relied on buckling forces to lock and seal the sabot. These forces were generated by allowing the front section of the sabot to be rapidly accelerated onto a more massive rear section. During backward acceleration, a buckling zone was designed to be forced outwards into the barrel to both lock and seal the sabot. However, during forward acceleration, the buckled zone would be forced to neck and pull away from the barrel. This alleviated any concerns of jamming the round as experienced in previous designs.

Several iterations of the Rear Seal concept were developed in order to improve the functionality of the buckle zone. It would be impractical to introduce all the design variations considered and therefore only some of the later design iterations are presented in the following.

6.3.4.1 Rear Seal Design: Mark 5

Rear Seal Design Mk5 consisted of a sabot constructed of three parts. These included a deformable cup, penetrator mounting structure and the rear seal ring as shown in Figure 6.18. The sabot cup was capable of rapid expansion into the barrel to generate a low pressure gas seal. A taper was included in the front sabot lip to allow for greater deformation and sealing. As pressures increased, it was expected that the rear seal ring would force the trailing edge of the cup to contact the barrel. This mechanism would then provide the majority of axial support and gas sealing.

The internal penetrator mounting structure was threaded into the main sabot cup. The new internal structure was capable of supporting the penetrator, both during sealing and ejection, while not restricting the action of the cup in producing a low pressure gas seal. The sabot was modelled using an aluminium alloy with a yield stress of 550MPa.

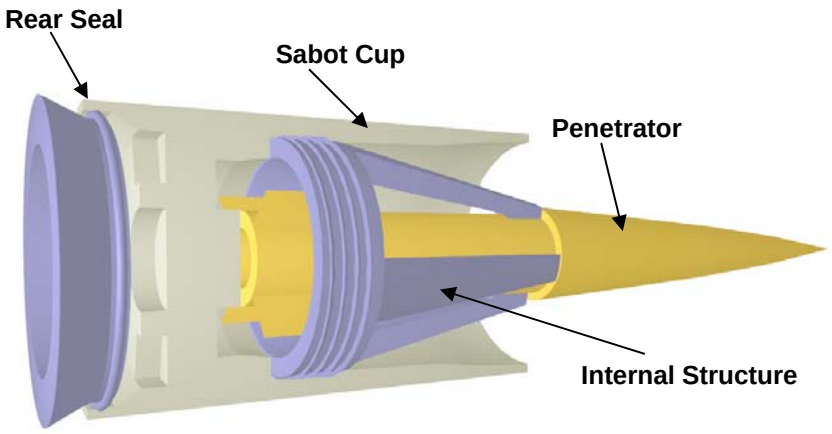

Figure 6.18: Rear Seal Design Mk5: CAD Model

Using the FE Model Shown in Figure 6.19, it was found that the sabot leading edge rapidly deformed against the barrel at low gas pressures. At maximum pressure, the leading edge had achieved a radial displacement of up to 0.2mm, indicating good contact with the barrel. At the conclusion of the rearward load case, the leading edge had returned to its original geometry implying that no plastic strain was sustained.

Plots of Von Mises Stress for maximum pressure in the forward and rearward load cases are shown in Figures 6.20 and 6.21 respectively. These plots reveal well-distributed stresses around the circumference of the sabot cup. This result implies that the contact forces between the sabot and barrel are consistent around the circumference which is vital to securing a gas seal. The plots also indicate that some yielding of the sabot cup may be taking place as regions of Von Mises stress in excess of the material yield stress (550MPa) are evident. However, as these regions are relatively small and are occurring in compression, it is not expected that they would significantly impact on the design.

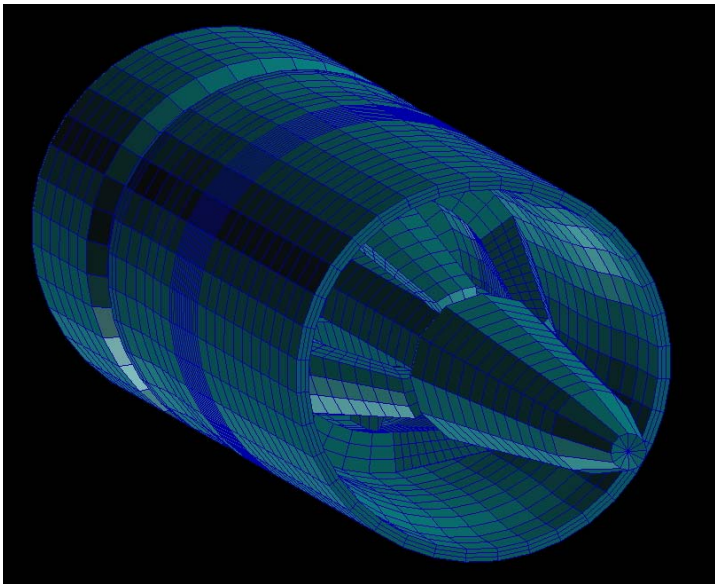

Figure 6.19: Rear Seal Design Mk5: Finite Element Model

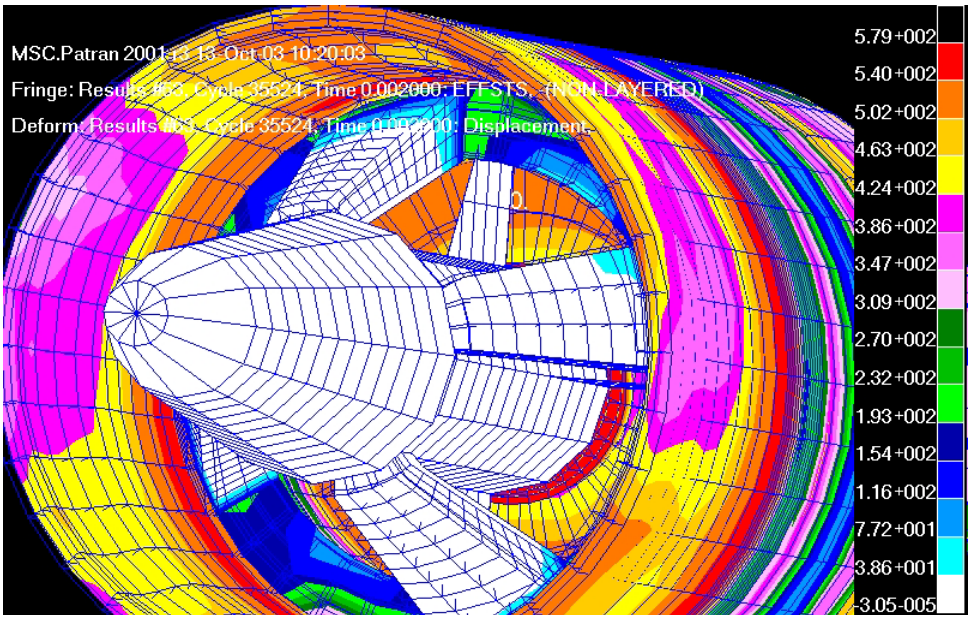

Figure 6.20: Rear Seal Design Mk5: Stress Results at Maximum Rearward Pressure (Units in MPa).

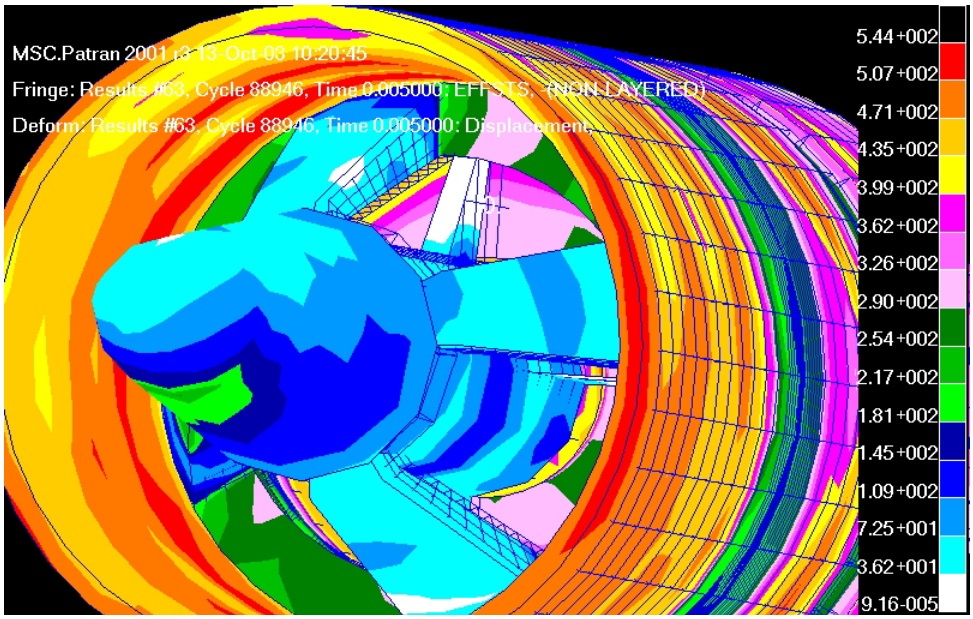

Figure 6.21: Rear Seal Design Mk5: Stress Results at Maximum Forward Pressure (Units in MPa).

To further investigate the impact of contact forces and the potential yielding of the sabot into the barrel, plots of average contact forces were generated using MSC. Patran. Average contact forces were obtained for a series of circumferential bands measured from the leading edge of the sabot. Figure 6.22 contains a schematic demonstrating the designation of these bands and the results are shown in Figure 6.23.

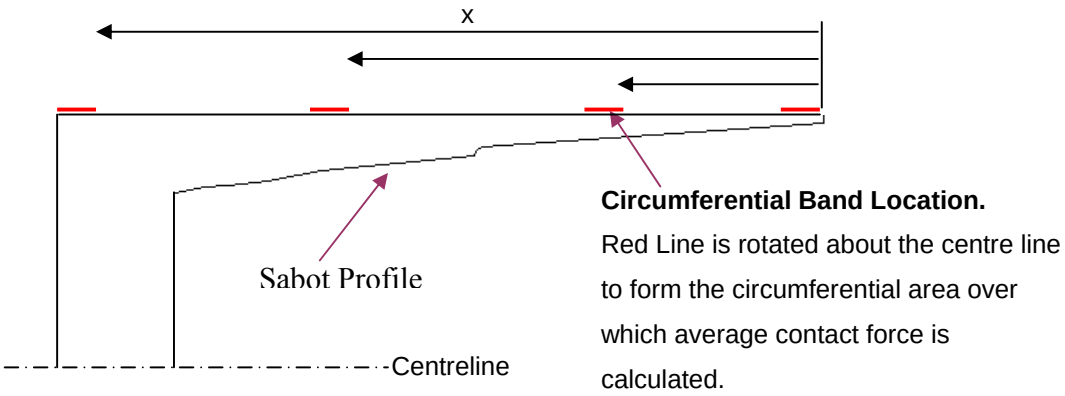

Figure 6.22: Contact Force Area Designation

The plot in Figure 6.23 indicates high contact forces for the rearward load case (0-3msec) with the greatest forces being experienced at the leading edge.

When considering the forward load case (3-6msec), the sabot again experiences significant friction with the greatest contact forces appearing close to the trailing edge. Contact forces at the front of the sabot appear more erratic suggesting that either the sabot was deflecting back and forth in the barrel during ejection, or a vibrational mode had been set up in the system. Modal behaviour is considered more closely is the next chapter.

The design of the trailing edge in Mk5 meant that during the forward load case, blast pressures were deforming this edge, causing it to contact the barrel and hence generate unwanted friction. It was evident that achieving the required muzzle velocity with this design would be difficult.

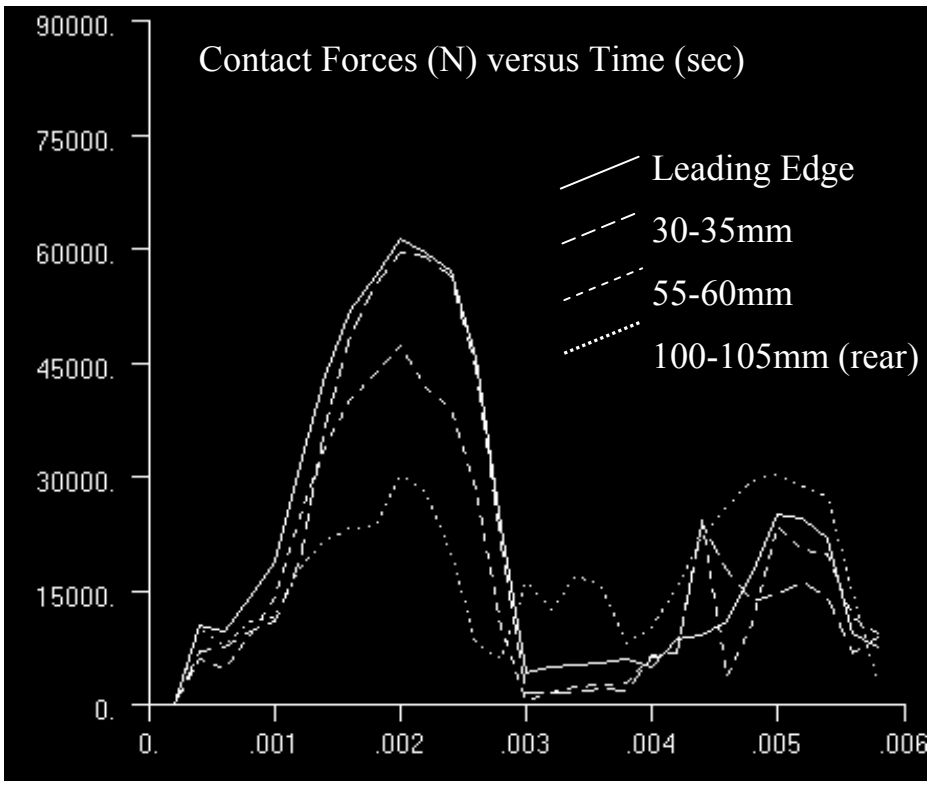

Figure 6.23: Rear Seal Design Mk5: Contact Force Results

Note: Distances indicate longitudinal location of circumferential bands measured from the leading edge.

A variant of Rear Seal Design Mk5 was developed in which the trailing edge geometry was curved away from the barrel. This increased the outside surface area of the trailing edge relative to the inside surface and was intended to force the trailing edge away from the barrel during launch. It was found that this was successful in minimising the contact forces on the trailing edge during ejection resulting in a significant increase in muzzle velocity. While successful, the design was judged to be too sensitive to operational conditions and susceptible to damage.

6.3.4.2 Rear Seal Design: Mark 6

Rear Seal Design Mk6 possessed a similar design ideology to that of the previous design utilising the same internal structure for penetrator support. However, the problems associated with the trailing edge were addressed through adopting a 'reversed' rear seal design. In this case, the seal was achieved through using a solid rear sabot section to deform a ring into the barrel. Figure 6.24 illustrates the reverse rear seal design concept.

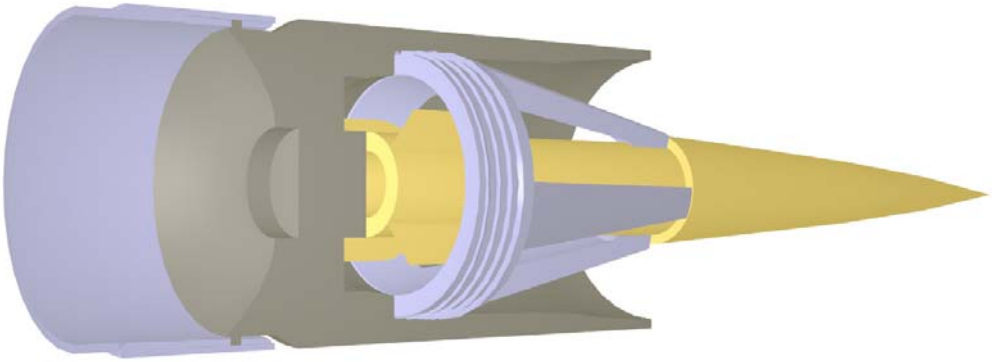

Figure 6.24: Rear Seal Design Mk6: CAD Model

The deformation plots shown in Figure 6.25 illustrate the dynamic action of the sabot during sealing and ejection. The design was effective in both the rearward and forward loading cases. For rearward loading (0-3msec), the sabot was successfully able to expand the rear ring which provided sufficient axial restraint and gas sealing. The forward loading case (3-6msec) showed that the sabot was free to accelerate down the barrel and achieve the specified muzzle velocity.

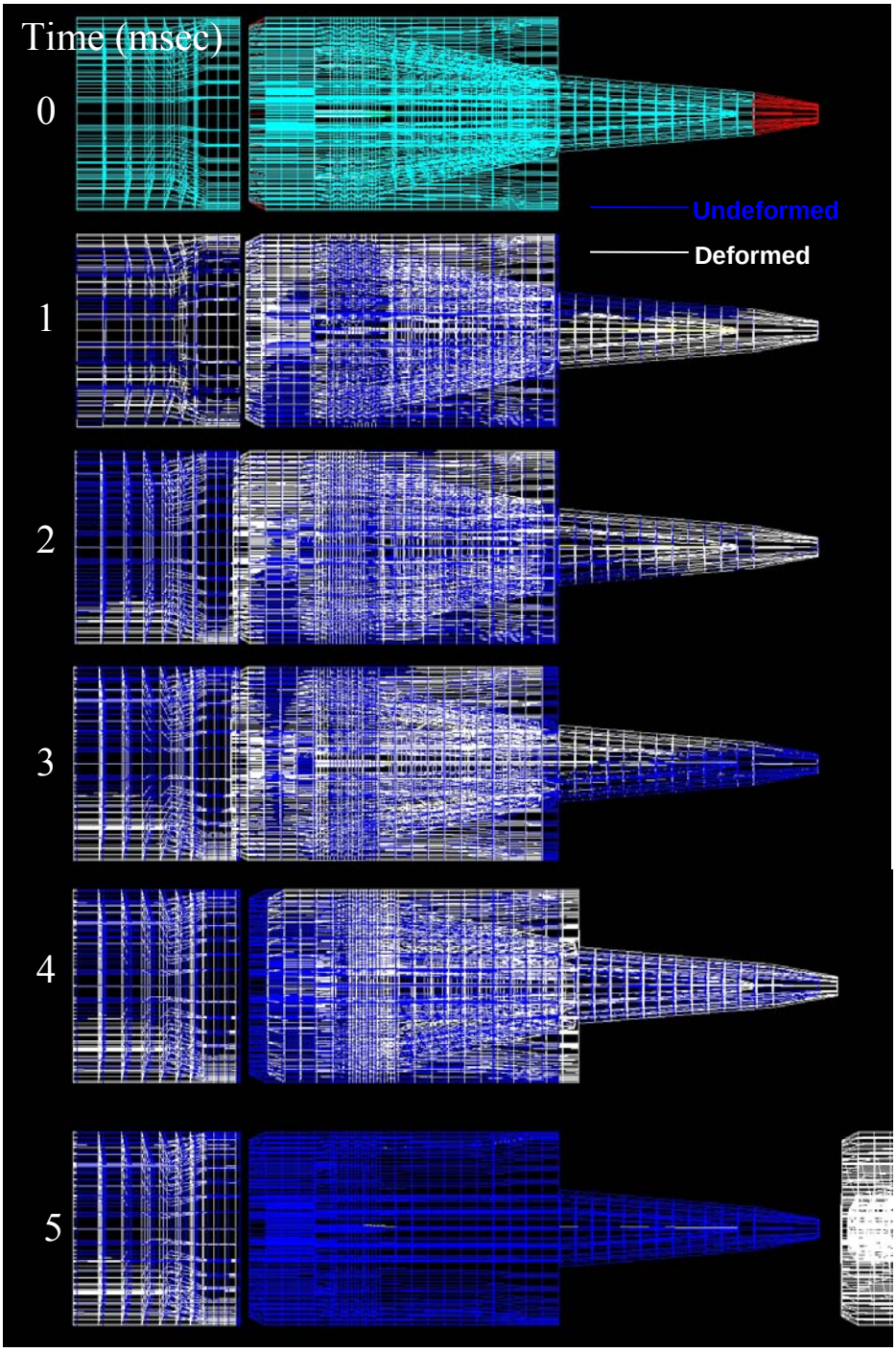

Figure 6.25: Rear Seal Design Mk6: Deformation Results

A comparison of Contact Results for Designs Mk5 and Mk6 can be viewed in Figure 6.26. Mk6 has maintained the sealing effectiveness of Mk5 during rearward loading (0-3msec) which is evident through the similarity of white and yellow curves in this domain. However, in the forward load case the reversed rear seal (dotted yellow curve) exhibits zero contact forces as would be expected. The spikes in the curve during ejection can again be attributed to the sabot either deflecting or vibrating against the barrel.

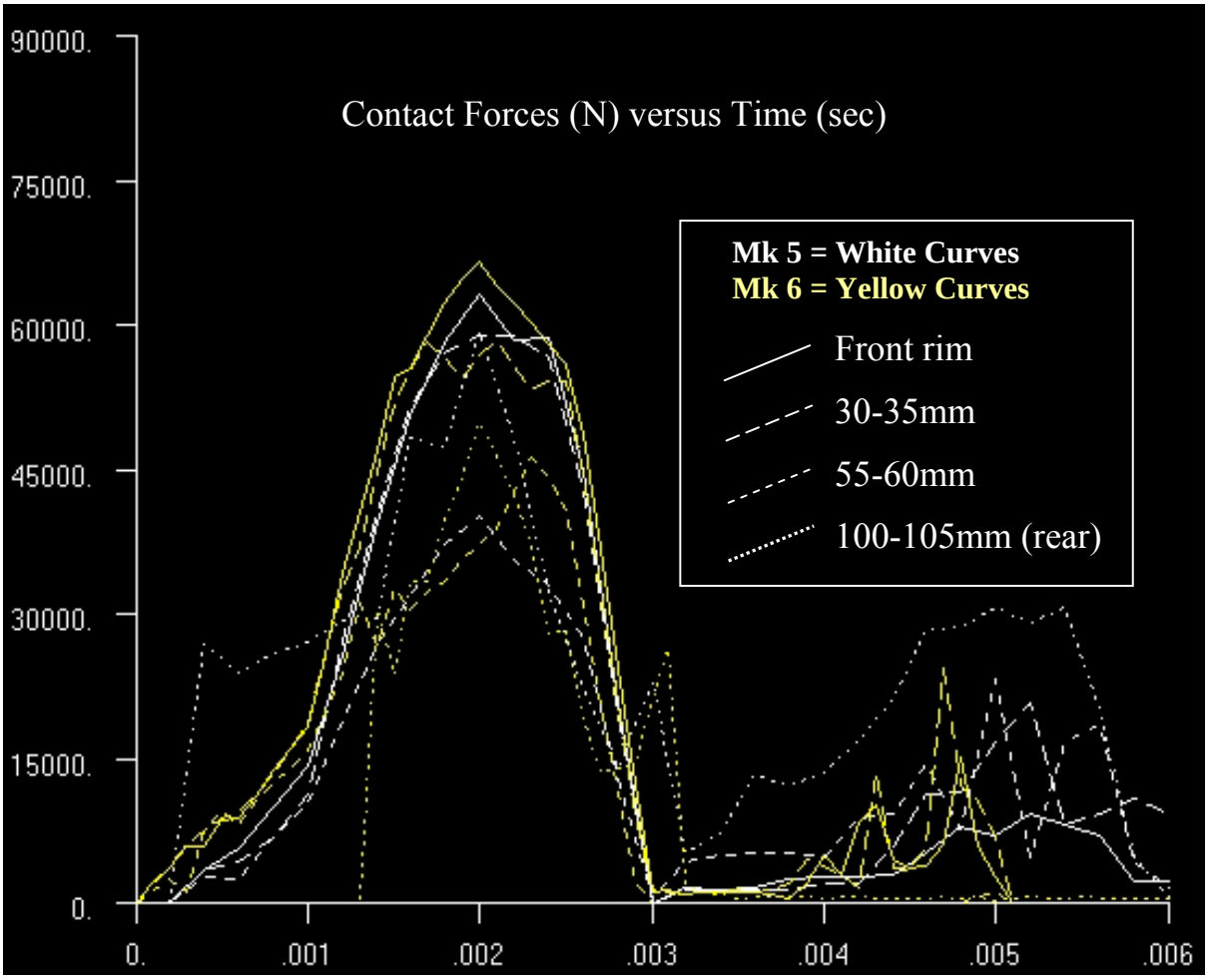

Figure 6.26: Contact Force Results: Comparison of Designs Mk5 and Mk6

Note: Distances indicate longitudinal location of circumferential bands measured from the leading edge.

Further development of the contact behaviour between the sabot and barrel was still required to ensure the design's gas sealing ability. Large concerns, however, were had in terms of the amount of compressive pressure imparted to the propellant of the aft round. It was feared that the action of the rear seal was creating significant pressure in this region which increased the risk of premature propellant ignition of the aft round. As a result, the rear seal concept was eliminated.

6.3.5 Cup Seal Design

The goal of the Cup Seal Design Concept was to eliminate the requirement of inertial forces, generated by the rearward motion of the sabot, to force a seal. Figure 6.27 contains the finite element model of the Cup Seal Design which solely relied on the friction created by the expansion of the sabot into the barrel for both gas sealing and axial restraint. Teeth were incorporated into the external sabot profile so that the magnitude of contact forces could be concentrated at the teeth for a more efficient gas seal. The penetrator mounting structure was also shifted forward in this design. This allowed for greater bulkhead thickness and strength and reduced the size and mass of the penetrator mount.

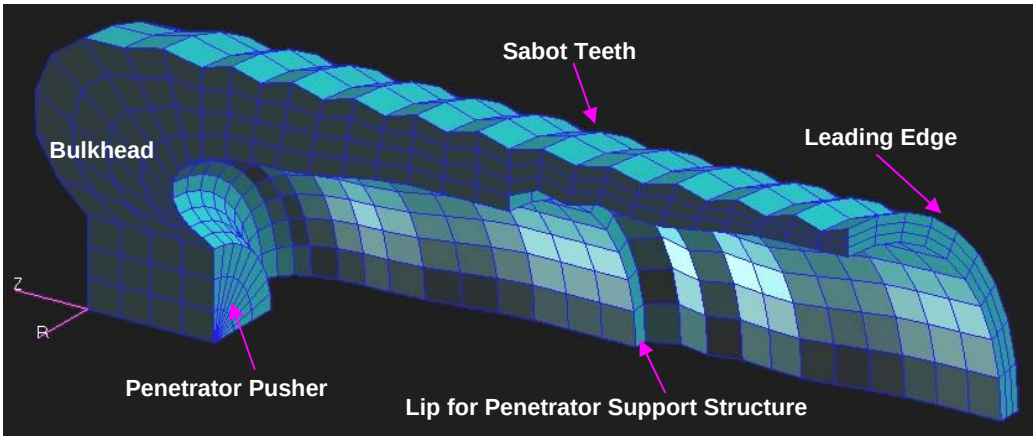

Figure 6.27: Finite Element Model of Cup Seal Design – Penetrator Mount not shown. (Quarter Model)

The rear section of the sabot evolved from the early Solid Tube Designs presented in Section 6.3.3 where the rear bulkhead configuration utilised a similar spherical geometry. The internal profile of the sabot was thinnest at the leading edge and progressively became more massive towards the bulkhead. Previous analyses showed longitudinal stretching of the sabot in this region due to inertial effects, hence the bulk of material in this region. The thin material at the leading edge of the cup provided for rapid expansion into the barrel to begin the sealing and restraint mechanisms early in the blast cycle. The internal profile of the cup also contained a lip on which the penetrator support structure (not shown in Figure 6.27) was located.

The finite element model of the cup seal design was set up in MSC. Patran for analysis in the MSC. Dytran explicit solver. Elastic-plastic material models were used for both the sabot and barrel. The sabot was modelled assuming 7000 series aluminium with an elastic modulus of 70GPa, a density of 2.8g/cc and a yield stress in the region of 500MPa. The material used for the barrel was high tensile steel with an elastic modulus of 205GPa, a density of 7.8g/cc and a yield stress of approximately 1500MPa. A friction coefficient of 0.2 was used in the contact definition between the sabot and barrel.

The analysis showed that the cup was readily able to expand and contact the barrel in the early stages of the blast. However, the radial expansion of the cup was accompanied by severe longitudinal stretching which compromised the structural integrity of the sabot.

Results of this analysis, in addition to those observed throughout the concept development phase, suggested that an alternative to aluminium was necessary. The low strength of aluminium appeared to be incapable of sustaining the inertia of the massive tungsten projectile during the rearward load case.

The aluminium was therefore replaced with a titanium alloy. It was hoped that the high strength of titanium could alleviate the severity of this stretching while still providing enough radial expansion for axial restraint and gas sealing. The selected titanium had an elastic modulus of 113GPa, a density of 4.5g/cc and a yield stress of approximately 1000MPa. An elastic-plastic material model was again used for the simulation. The value used for the friction coefficient between the sabot and barrel was again assumed to be 0.2.

Figure 6.28 illustrates the displacement results obtained for the titanium cup seal design. Very little movement was noticed in the rearward loading case (0-3 msec). Fears of the increased stiffness of titanium affecting the radial flexibility of the sabot were alleviated by this result as good axial restraint was achieved. Furthermore, the structural integrity of the teeth was maintained as opposed to previous aluminium designs, therefore not compromising seal effectiveness. Beyond 3msec the plots show the sabot in forward motion without any significant friction.

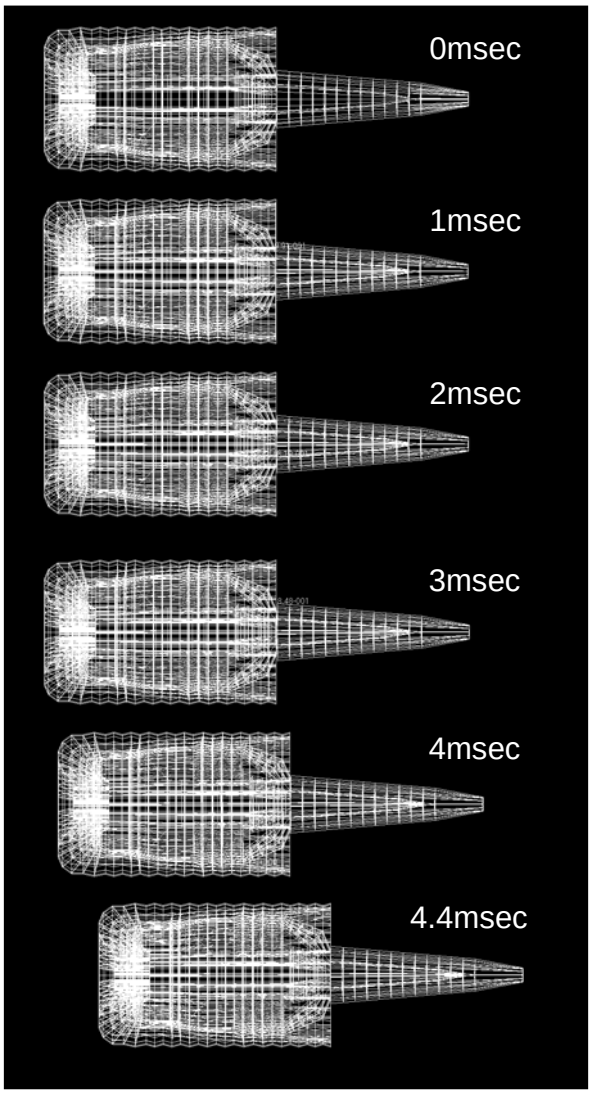

Figure 6.28: Titanium Cup Seal Design: Displacement Results

Considering the plots in Figures 6.29 and 6.30 we notice significantly higher stresses in the titanium cup at 2msec (maximum pressure) as compared to those for aluminium. However, the majority of stresses in all regions are maintained below the titanium yield stress such that no significant plastic deformation was apparent. From the plots, it is also obvious that the problem of longitudinal stretching was eliminated through the use of titanium.

The plot of plastic strain at 3msec (No Pressure) shows very little residual strain in the structure after rearward loading. This is again vital for sabot ejection as unwanted friction may compromise the ability of the round to achieve the required muzzle velocity.

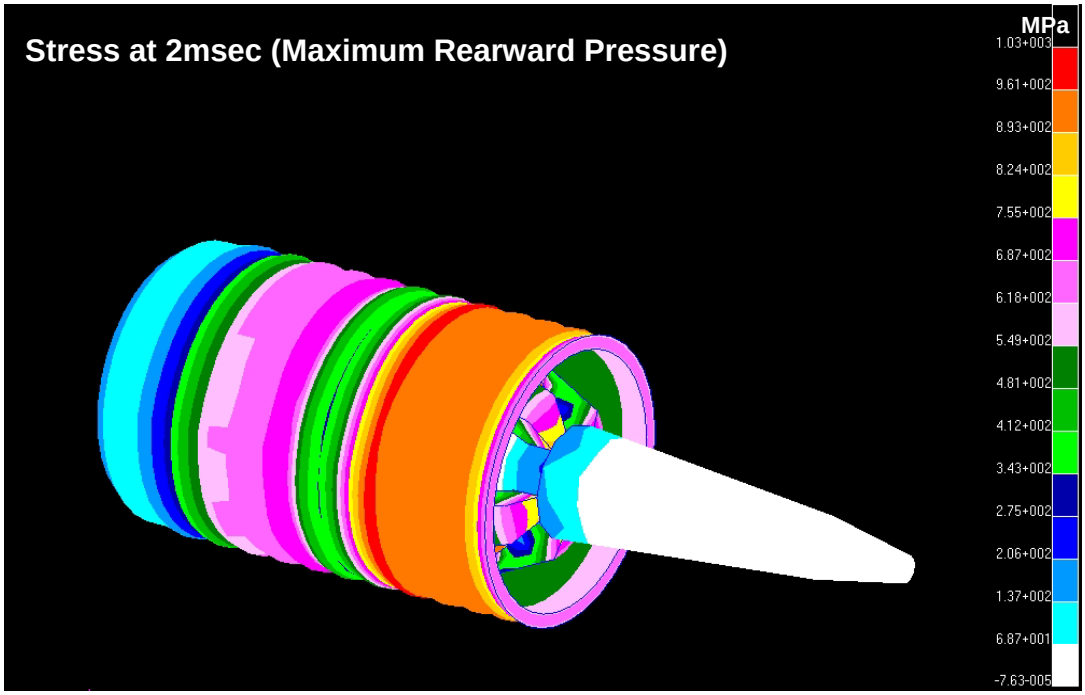

Figure 6.29: Titanium Cup Seal Design: Stress Results at Maximum Rearward Pressure

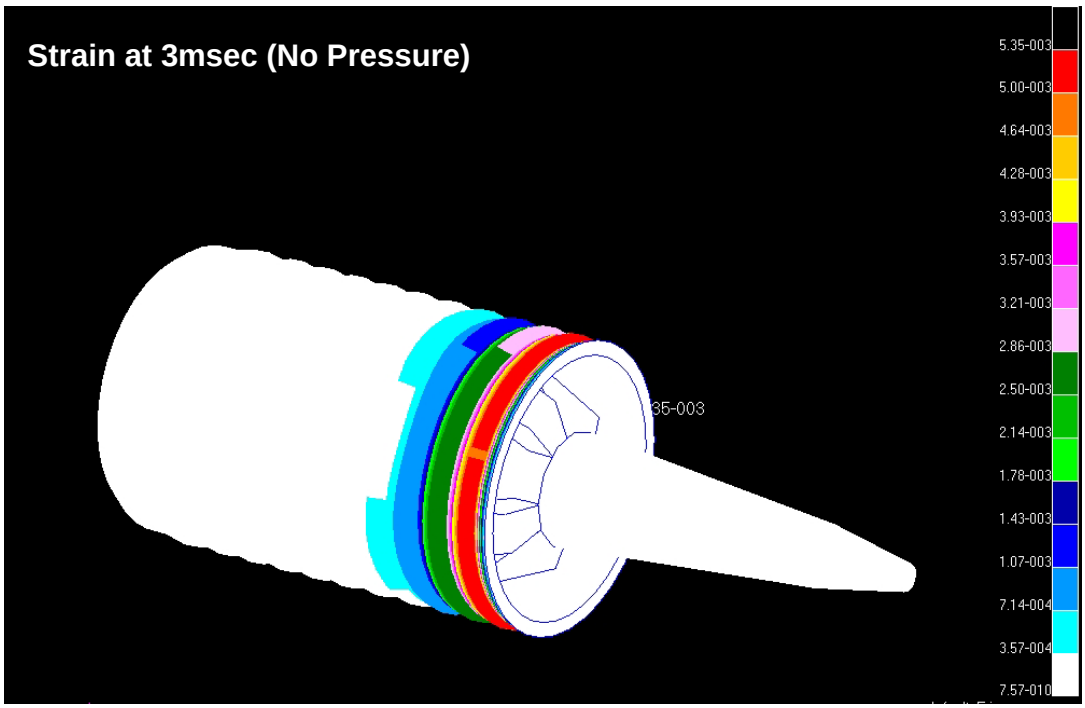

Figure 6.30: Titanium Cup Seal Design: Strain Results after Rearward Load Case

6.4 Conclusion

VDP was applied for the design and development of a stacked round concept for HVFSDS rounds in which explicit finite element methods were used to assess a wide variety of design concepts in an efficient manner.

Initially, a discussion of the major design criteria and parameters were presented in order to provide the necessary framework from which to proceed the design. Consequently, many design iterations were developed and assessed against specified design requirements. It was found early that the use of a traction type sabot possessing multiple petals would complicate the gas seal mechanism. A push type sabot solution was therefore sought.

The Cup Seal Sabot evolved from many push type sabot configurations. The design relied on friction created by the expansion of the sabot into the barrel for both gas sealing and axial restraint.

7 Design Development

7.1 Introduction

In this chapter, the capability of explicit FEA in addition to Shape Optimisation methods is demonstrated in order to further refine the stacked HVFSDS design concept.

Detailed explicit finite element analysis is conducted to consider the barrel teeth interactions of the Cup Seal Design more closely using a refined mesh. This was necessary in order to ensure that the contact pressure between sabot and barrel exceeded that of the combustion pressure at all times throughout the interior ballistic cycle. This condition ensured the integrity of the gas seal and eliminated the risk of premature ignition of supporting rounds.

Previous analyses of barrel and sabot interactions also revealed some interesting phenomena regarding system vibrations. It was observed in the contact plots presented in Figures 6.23 and 6.26 that some periodic contact forces were generated in the fired sabot as it travelled through the barrel. It was considered that these may have been the result of either the sabot deflecting back and forth against the barrel as it exited, or the result of system vibrations being set up. This behaviour is also considered more closely in this chapter.

Shape Optimisation tasks are also carried out on the cup seal design concept for HVFSDS rounds. The objective was to streamline the total mass and amplify the contact forces with the barrel.

7.2 Refined Explicit FEA - Analysis of Barrel/Teeth Interactions

Explicit FEA is used to refine the Cup Seal Design by further investigating the interaction of the sabot teeth with the barrel. Various design options were explored to achieve the best sealing and restraint performance. A detailed analysis was therefore undertaken in order to determine the best configuration. Much attention was placed on the elastic-plastic behaviour of the materials. That is, in order to achieve the best performance, should all components remain elastic throughout the blast cycle? Or would it be beneficial to allow a controllable degree of plastic deformation in either the sabot or barrel to improve performance?

Detailed finite element models were produced in MSC. Patran. The mesh in the front portion of the sabot/barrel was refined to assess any damage sustained by either the teeth or barrel during the blast cycle. A friction coefficient of 0.2 was assumed between components in this study. The finite element model constructed for the analysis can be seen in Figure 7.1.

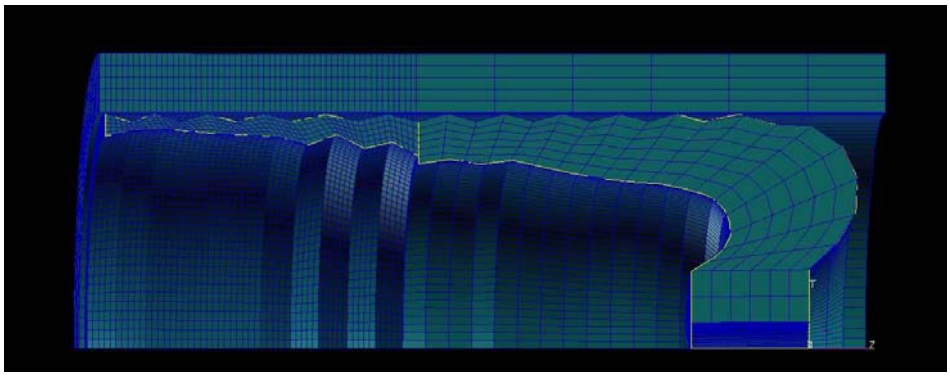

Figure 7.1: Cup Seal Design: Refined Sabot/Barrel Quarter Finite Element Model for Teeth Analysis

Two principal modes of interaction between the barrel and sabot were explored. The first proposal was to use a soft replaceable insert in the barrel that would yield around the teeth to assist in restraining rearward motion. This would require that the insert be loaded and ejected with each set of rounds. The second proposal was to use a barrel harder than the sabot in order to maximize contact forces and remove the need for replaceable barrel inserts. The use of the hard barrel may have resulted in the plastic deformation of some sabot teeth.

Prior to the analysis, some basic design improvements were applied to the sabot teeth. That is, the outer profile of the sabot was adjusted in order to reduce the possibility of stress concentrations in the valleys between the teeth. This was simply achieved by reducing the distance between the teeth located close to the sabot leading edge and filleting the profile between teeth.

It must also be noted that non-axisymmetric motion might be important in restraining the sabot during the early motion of the cup. The use of a quarter model in this analysis therefore may not have revealed the full dynamic behaviour of the system. However, the quarter model was appropriate in closely analysing the teeth interactions as was the specific goal of this study. Table 7.1 contains the material properties used in the simulations.

Table 7.1 – Material Properties

	High Tensile Steel	Titanium Alloy	Aluminium Alloy
Density (g/cm^3)	7.85	4.50	2.70
Modulus of Elasticity (GPa)	205	113	72
Poisson's Ratio	0.3	0.3	0.3
Yield Strength (MPa)	1515	1000	520

7.2.1 Soft Barrel Insert Design Option

The first design option included a soft barrel insert which would yield around sabot teeth to form a seal. It was envisaged that this behaviour would improve the axial restraint mechanism of the system. There was some concern related to the ability of the sabot to release from its locked position once fired.

The interaction between a titanium sabot and an aluminium barrel insert was simulated using the quarter model shown in Figure 7.1. Figures 7.2 – 7.5 contain plots of plastic strain on the sabot and barrel at maximum pressure.

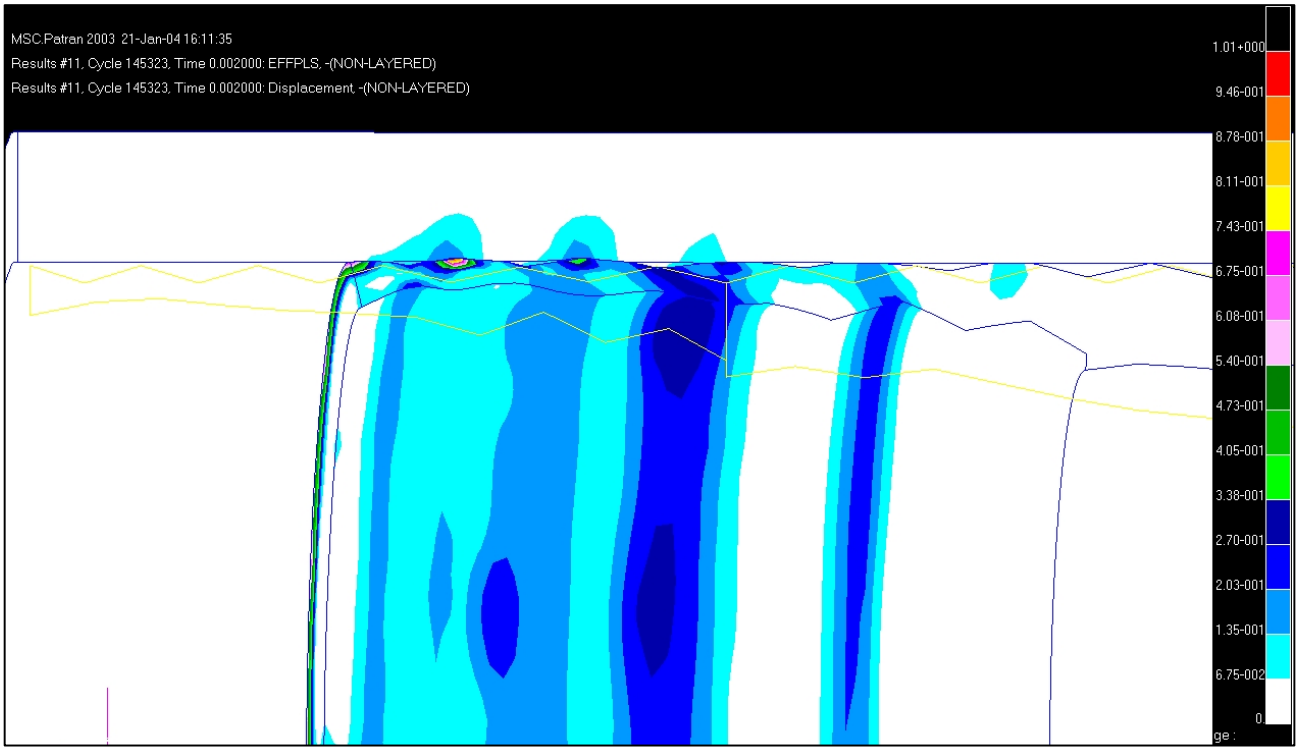

Figure 7.2: Plastic Strain at 2msec – Maximum Pressure

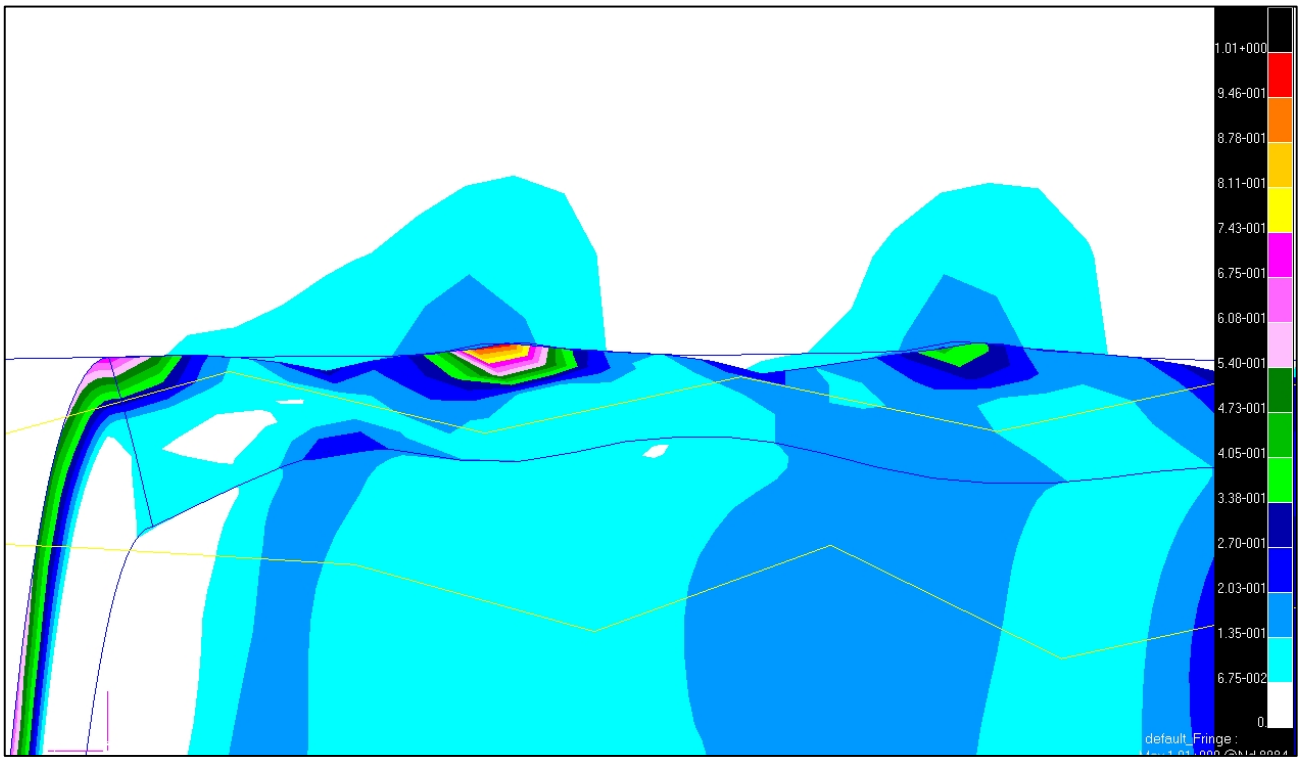

Figure 7.3: Plastic Strain at 2msec – Maximum Pressure (Magnified view of front Teeth)

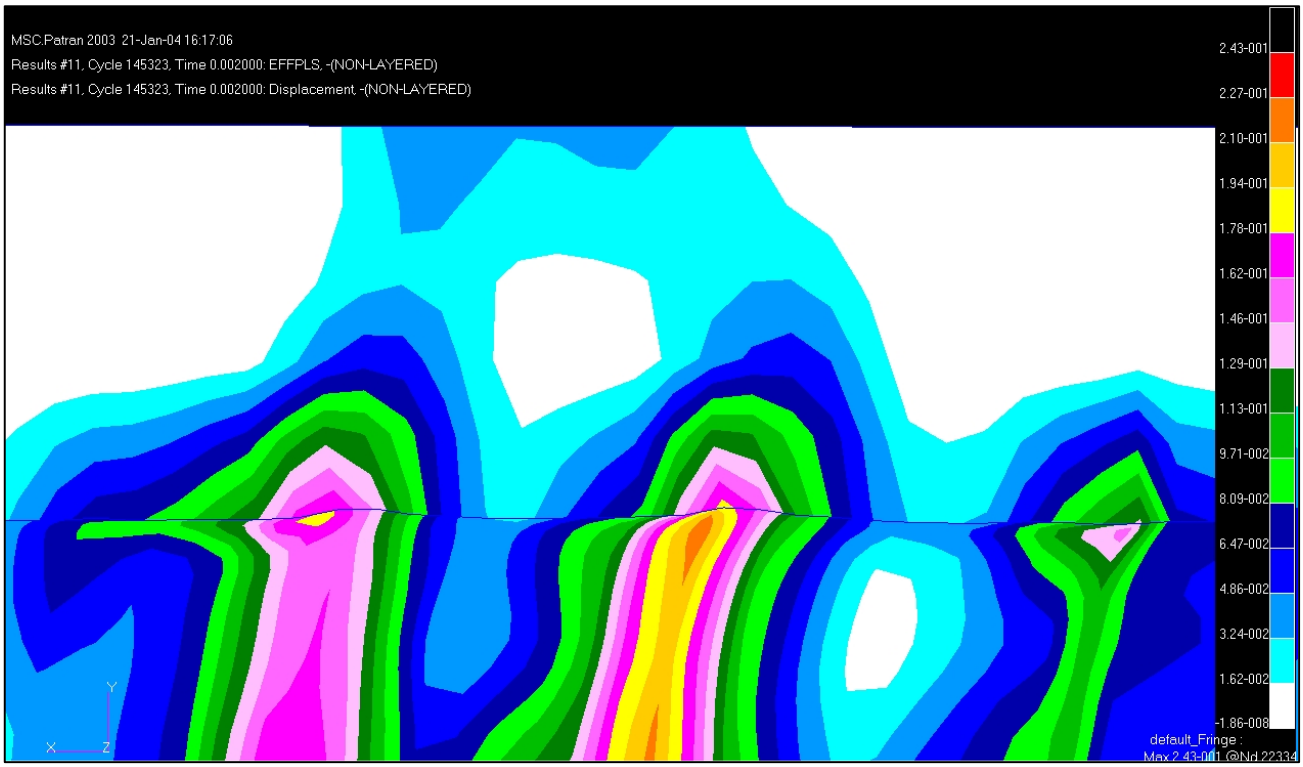

Figure 7.4: Plastic Strain at 2msec – Maximum Pressure (Magnified view – Barrel Only)

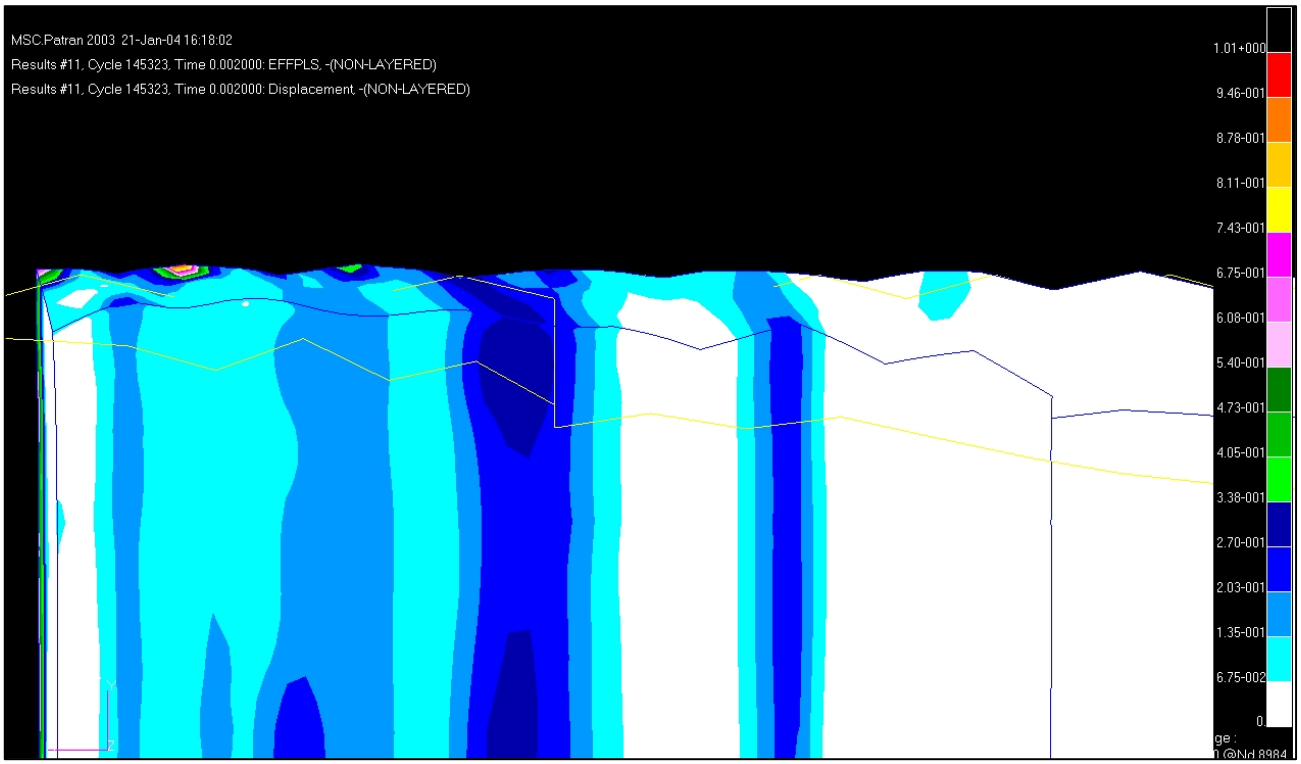

Figure 7.5: Plastic Strain at 2msec – Maximum Pressure (Sabot Only)

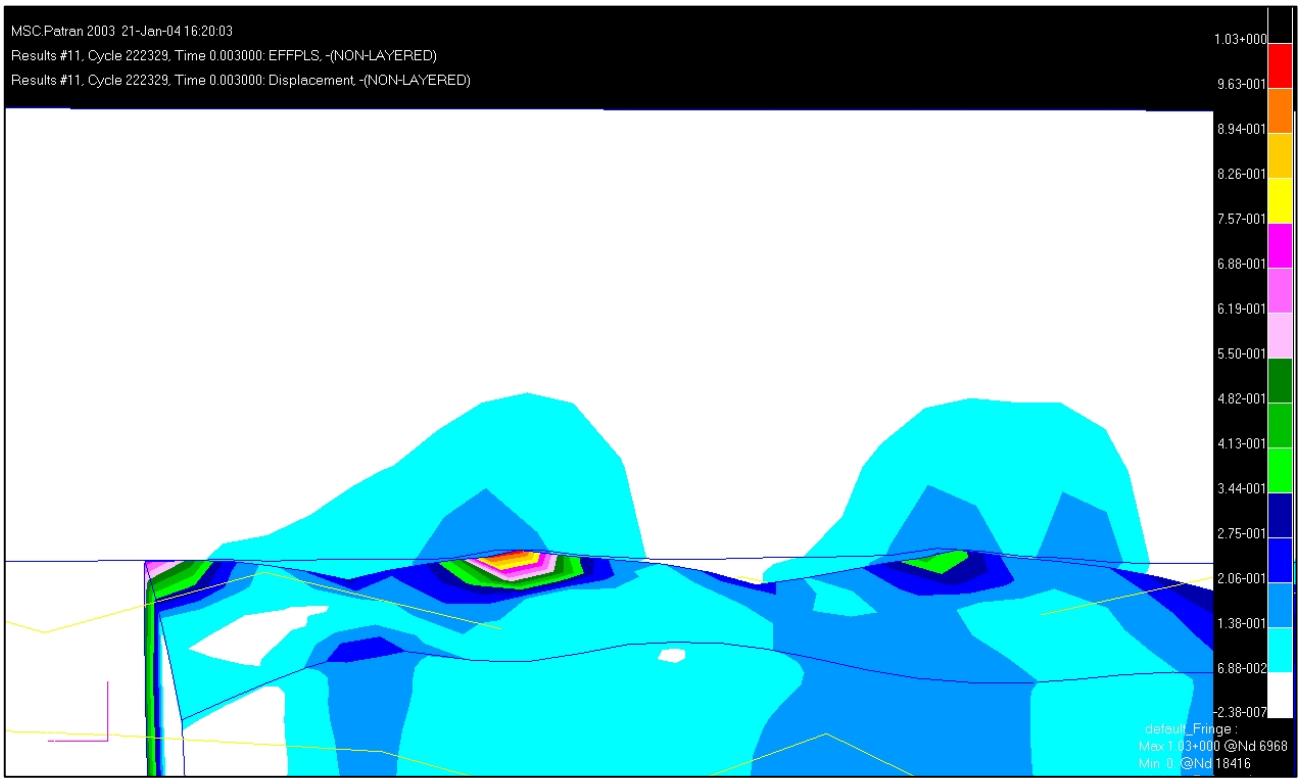

Figure 7.6: Plastic Strain at 3msec – No Pressure

The plots indicate that deformation of the sabot at maximum load imparts plastic strain onto the teeth and barrel. The aluminium barrel insert was shown to yield by 0.5mm under the force of the 2nd to 4th row of teeth. Figure 7.5 clearly illustrates the plastic deformation of teeth at maximum load where the ridges of the original model have flattened against the barrel. Figure 7.6 shows that the sabot partially recovers its original geometry at zero pressure (Time =3ms).

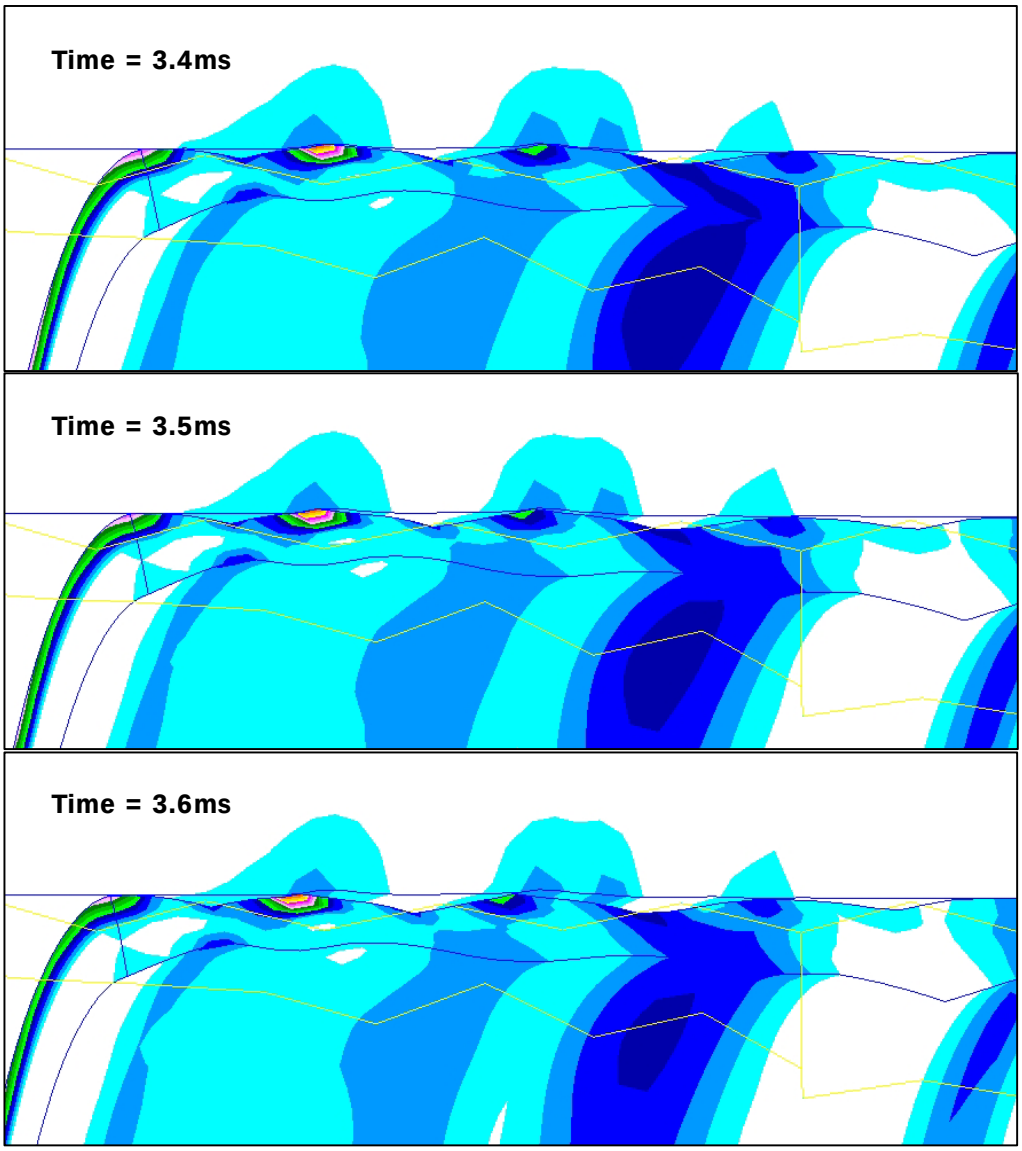

Figure 7.7: Sabot shown releasing from barrel under forward pressure

Figure 7.7 shows the forward movement of the sabot in the early stages of the forward load case. The coloured contours illustrate the residual strain in the system, however, the sabot was able to disengage with the barrel and begin forward motion. This result eliminated fears of potentially jamming the round due to plastic deformation. It was unknown however, if these permanent deformations in the barrel insert would adversely affect the firing and acceleration of subsequent rounds.

The use of a soft barrel insert increased the restraining forces on the cup as only negligible rearward motion was observed. These inserts could act as cartridges in which multiple rounds are stacked and loaded into the barrel as one piece. Further studies could be undertaken using different materials in order to optimise the degree of plastic deformation for best performance.

Such a system would have the advantage of ensuring identical contact conditions between the sabot and constraining wall regardless of barrel conditions. That is, the required friction coefficient could easily be maintained for consistent performance. This would be difficult to achieve in a barrel as residues build up after numerous firings. The major disadvantage of this option is the need to remove the cartridge after each set of rounds is fired.

7.2.2 Hard Barrel Design Option

This design option utilised a hard barrel so as to not undergo any permanent plastic deformation during the sealing phase. While the hard barrel option could be developed using a barrel insert as above, the intention of this design was to eliminate the requirement of a removable insert. That is, the sabot would seal against the barrel wall itself. As a result, a constant feed of rounds into the chamber could be possible in this case as no ejection of components was necessary. Combustible cartridge cases would be used in this instance.

Maintaining consistent friction conditions inside the barrel may be an issue with this design. As stated above, the build up of residues after numerous firings may serve to alter contact conditions. A more strict maintenance routine would be required in order to ensure the necessary friction conditions remained consistent.

The sabot was again modelled using the titanium alloy, while high tensile steel was used for the barrel. However, the use of a hard barrel resulted in the sabot not being sufficiently restrained as significant rearward movement occurred up to maximum pressure.

It was also found that the sliding of the cup when in contact with the barrel caused the excitation of vibrational modes. This behaviour reduced the axial restraint of the cup as parts of its surface periodically moved out of contact with the barrel. The stress plots shown in Figure 7.8 clearly demonstrate the development of modal vibration as periodic regions of high stress are evident in a series of circumferential bands down the barrel. The development of higher order modes from 0.4-0.5 milliseconds was noticed.

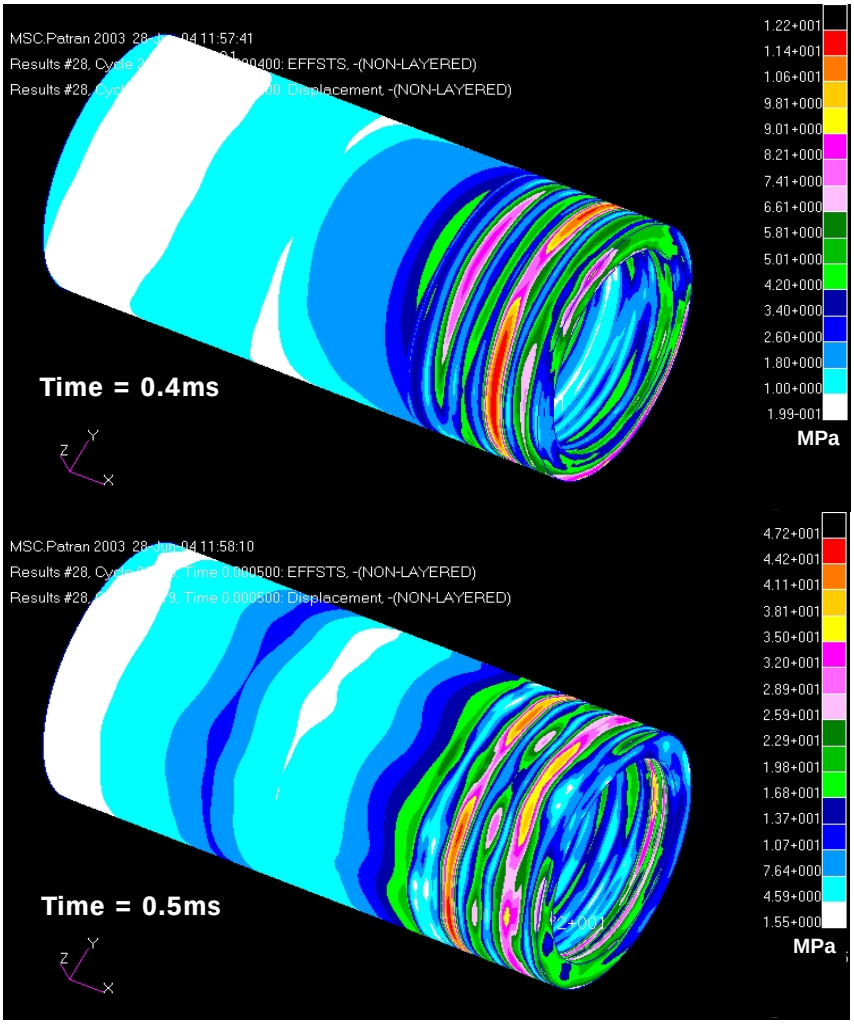

Figure 7.8: Barrel Stress Contours illustrate modal development

Where insufficient rearward restraint of the sabot occurs, a supporting structure could be included and utilise the strength of the penetrators to distribute load to the breach of the barrel. The supporting tube would provide significant support to the sabot during the early stages of the blast. As blast pressures increase, friction forces between the sabot and barrel would then take over the majority of the load. From previous analyses, this seems to occur after about 1 millisecond. Furthermore, the support structure could also be utilised to house the primer and firing electronics.

7.3 Shape Optimisation: Cup Seal Design

In order to improve the Cup Seal design, two design objectives were sought using ReSHAPE. These included mass optimisation and increased radial flexibility of the sabot. The use of titanium significantly increased the parasitic weight of the sabot due to its greater density as compared to aluminium. Sabot weight needed to be kept to a minimum so as to not adversely affect the achievable muzzle velocity for the round. Due to titanium's superior strength, it was expected that the mass of the cup seal design could be reduced significantly.

As the optimisation process utilises linear static finite element methods, it was necessary to develop linear load cases to best represent the dynamic results obtained through explicit analysis. In order to achieve this linearisation, careful attention was given in defining boundary conditions and applied loads to ensure an accurate representation of the dynamic results was obtained.

This notion was further complicated where structural contacts possessing friction were used. Friction forces were applied in static load cases as point loads with care taken to achieve an overall force balance in the model. Any modification of shape during the optimisation process would affect the magnitude of contact forces. This required that a new dynamic analysis of the optimised structure be carried out to redefine contact forces and boundary conditions prior to further optimisation runs.

The maximum rearward pressure condition (546MPa) at 2msec, obtained from explicit analysis, was linearised for the optimisation. The model had to include the friction restraining forces between the sabot teeth and the barrel. As stated previously, the friction forces were applied as point loads to the sabot teeth, as the barrel itself is not considered in the optimisation. The friction forces were

determined by evaluating the distribution of contact (normal) forces obtained through explicit analysis and multiplying them by the assumed friction coefficient of 0.2.

The leading edge of the sabot was constrained in the linear elastic model and the friction forces were scaled so that a reasonable force balance was achieved. However, by employing this method the stresses about the constrained leading edge of the sabot could only be approximated. The nodes at the top of the sabot teeth were also constrained in the vertical direction assuming they were in contact with the barrel. Figure 7.9 contains a free body diagram showing the boundary conditions used to linearise the results of explicit analysis.

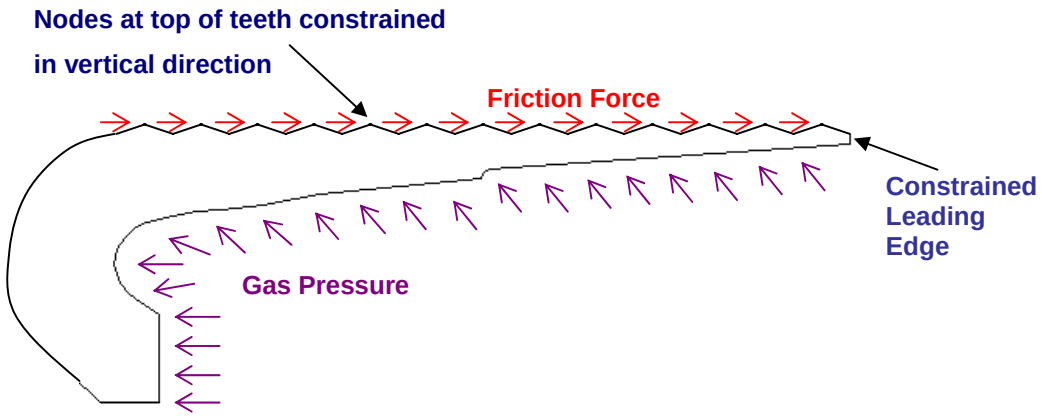

Figure 7.9: Boundary Condition/Applied Loads for Linear Analysis – Maximum Pressure Rearward Load Case

Given the same loads and boundary conditions, multiple objectives can be specified in ReSHAPE for a single simulation. This is achieved by essentially splitting the problem into two or more tasks based on the amount of objectives. Once the sensitive regions have been determined (Raw Sensitivity) an improvement process is applied to achieve the first objective. Once completed, the first objective is transformed into a constraint on the new model, and the raw sensitivity and improvement process is performed to satisfy the second objective [102]. This process is continued until all objectives have been addressed.

In the case of the sabot, the mass reduction was performed first using the MASS Objective [106] in ReSHAPE. Once performed, the MASS of the new model was transformed into a constraint, stipulating that any further optimisation could not increase the current mass of the sabot. Increasing the radial flexibility of sabot was then performed using the REACTION Objective [106]. This objective can be used to increase the reaction force on a constrained node in any direction. In this case, ReSHAPE was requested to increase the vertical reaction force on the constrained nodes at the top of each of the teeth.

Figure 7.10 illustrates the optimised design produced by ReSHAPE. A STRESS Constraint [106] was also imposed in order to maintain the maximum allowable stress of the material. That is, any shape changed performed by the software could not result in the sabot experiencing stresses greater than the yield of titanium. This was necessary to ensure that the problem of longitudinal stretching was not reintroduced into the design. Furthermore, any plastic deformation sustained during the sealing phase may have an adverse effect on round ejection (forward load case) and terminal ballistics.

The contours shown in Figure 7.10 represent the magnitude of shape change incurred by the mesh. A significant reduction of mass was obtained at the leading edge of the sabot and aft of the restraining lip of the penetrator support structure. Some mass had also been removed from the spherical bulkhead at the rear of the sabot.

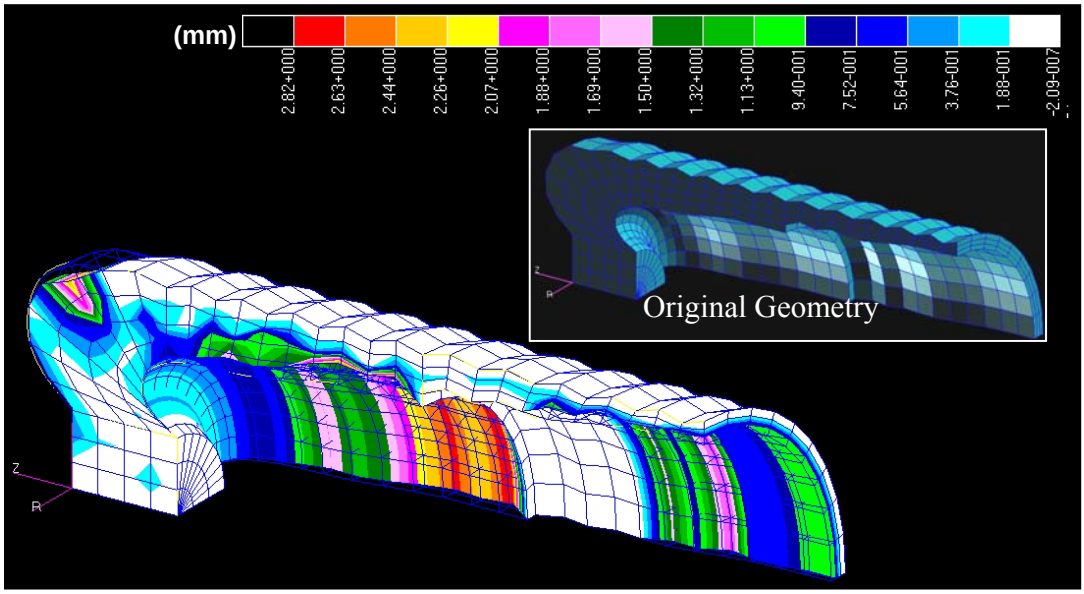

Figure 7.10: Cup Seal Design – Results of Optimised Shape for Mass Reduction

Figure 7.11 contains the optimised finite element model created by ReSHAPE. The optimised model was resubmitted into DYTRAN in order to assess its dynamic performance and ensure the yield stress constraints were satisfied by the optimisation. Figures 7.12 and 7.13 show the stress and plastic strain of the sabot at maximum rearward pressure.

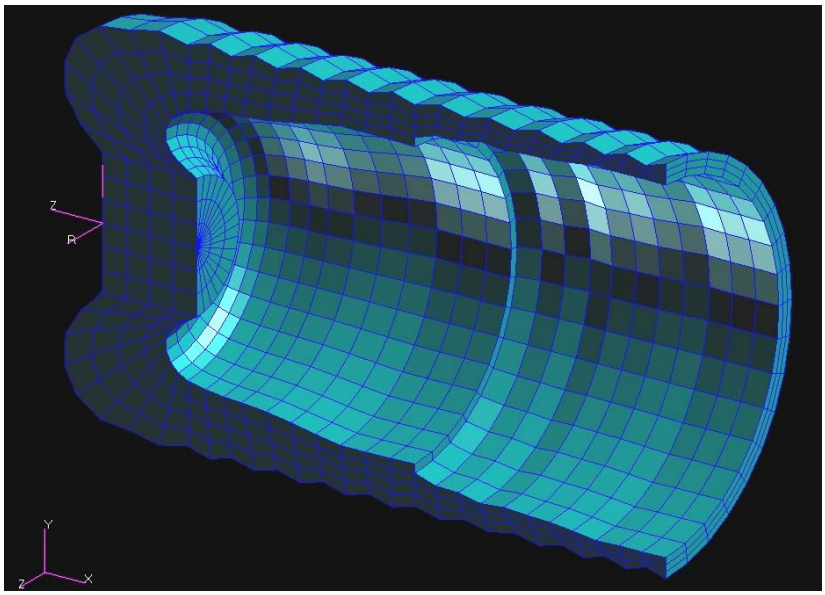

Figure 7.11: Cup Seal Design – Optimised Shape

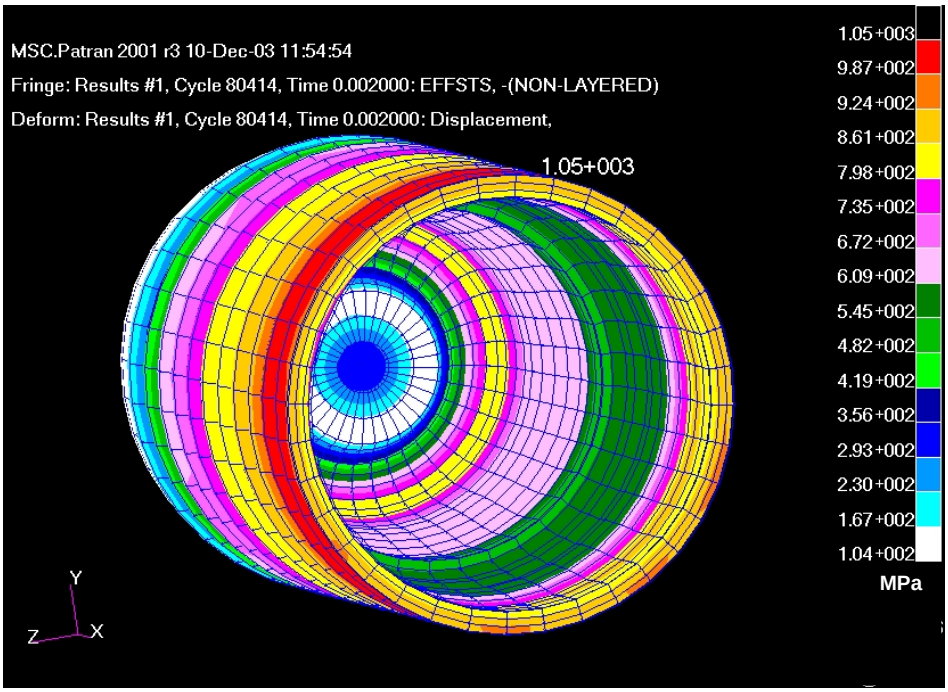

Figure 7.12: Optimised Cup Seal Design – Von Mises Stress Results (Max. Rearward Pressure - 546MPa)

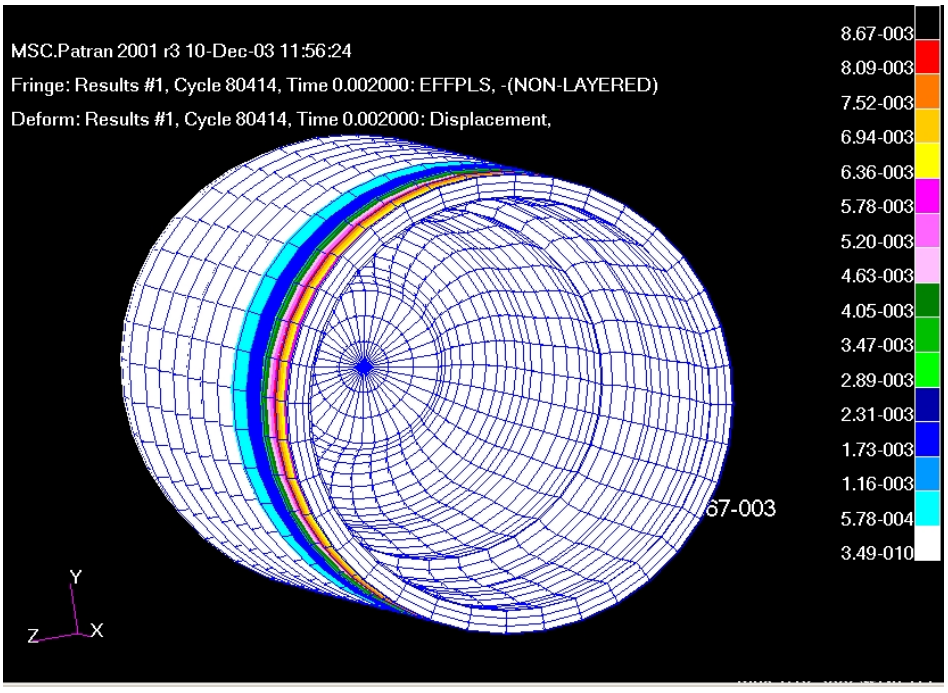

Figure 7.13: Optimised Cup Seal Design – Plastic Strain Results (Max. Rearward Pressure - 546MPa)

Figures 7.12 and 7.13 clearly indicate that the optimisation process was successful in maintaining stresses within the tolerances of the material. Some high stresses, close to titanium yield, are apparent near the leading edge of the sabot. This result is reinforced by the plot of plastic strain, where minor strains of up to 0.9% are apparent. This degree of strain should not be a problem in the real system and is ignored at this stage.

The plot in Figure 7.14 compares the contact force results obtained for the original and optimised titanium cup seal designs. The contact forces generated for the optimised design (red curves) showed significant improvement as compared to the original. Again, this optimisation was aimed at improving both the effectiveness of the gas seal and axial restraint.

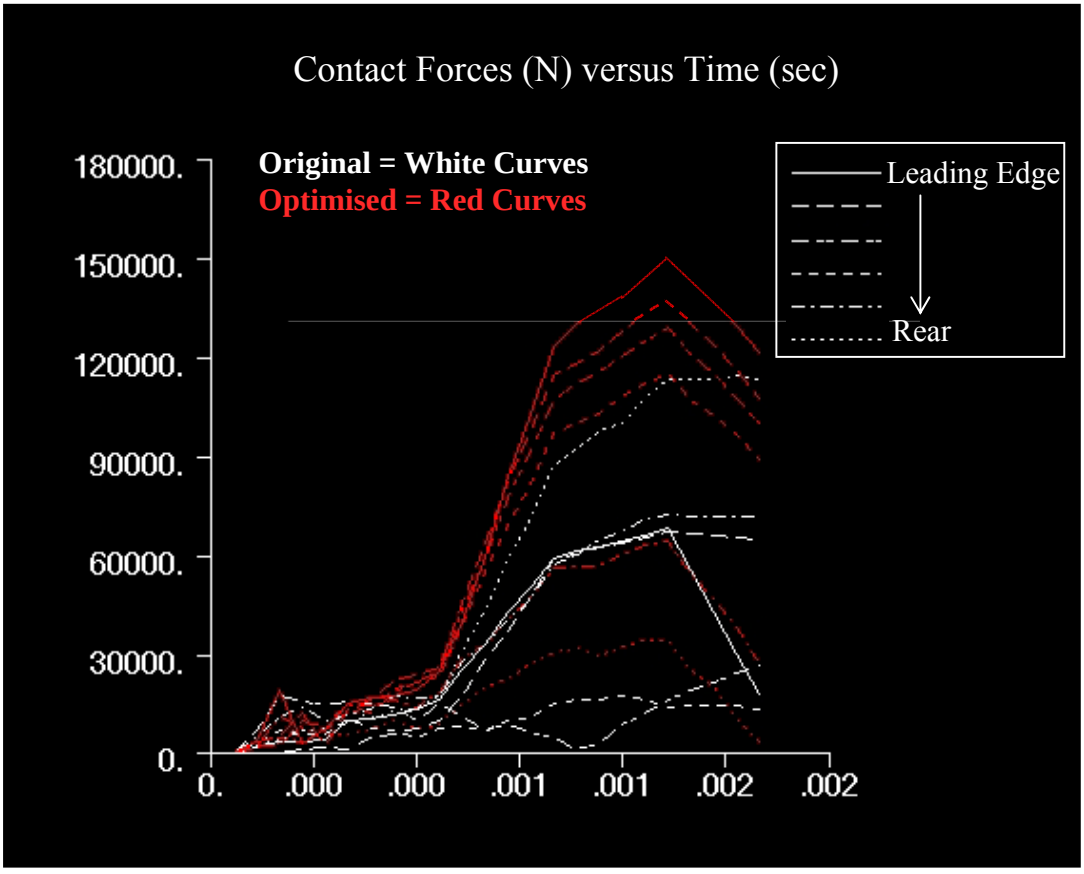

Figure 7.14: Optimised Cup Seal Design – Contact Force Results

Note: Solid to Dotted Lines- Leading Edge to Rear of Sabot at 15mm intervals

7.4 Conclusion

A detailed investigation of the barrel/teeth interaction of the stacked round concept was undertaken in order to address some design issues relating to hard and soft barrel inserts.

In addition to explicit finite element analysis, shape optimisation techniques using ReSHAPE were included into the development process to improve the design. The method by which dynamic load cases could be linearised and used to perform the optimisation was first presented. A successful reduction in mass and increase of contact forces was achieved for the cup seal design whilst remaining within material yield tolerances.

The design was considered appropriate for the construction of a prototype in order to conduct preliminary testing of the axial restraint and gas sealing mechanisms. The outcomes of prototype testing would help to decide some of the more complex design issues. The process of experimentation would also serve to validate the VDP.

8 Design Validation and Refinement

8.1 Introduction

In order to validate the design developed using VDP, an experiment was devised in which the gas sealing and axial restraint mechanisms of the developed HVFSDS stacked round could be tested. That is, the performance of the stacked HVFSDS round was tested in the rearward load case. As discussed in Section 6.2.1, these criteria were essential in developing an axially stacked round as they mitigate against the premature ignition or irregular combustion of the sealing rounds' propellant.

Validation of the prototype was conducted in a test chamber designed and manufactured by the Defence and Science Technology Organisation (DSTO) of Australia. The chamber was able to replicate the conditions which would be present in the barrel of a real gun system. The test exposed the round to the combustion of a propellant charge equivalent to that expected in the real system. A series of pressure transducers were used to record pressures both in front of and behind the round, in order to assess the integrity of the pressure seal.

8.2 The Design Concept

Figure 8.1 illustrates the Design Concept which was submitted for physical testing in April 2004. The figure shows a cartridge arrangement containing three stacked rounds loaded into the barrel. The concept, however, was not limited to three rounds such that any number of rounds could be loaded and fired based on gun geometry and capacity. A mock penetrator, built into the breech of the gun, was used to locate the final round in the barrel.

The concept required that each sabot act as a breech and gas seal for the firing of forward rounds. The cup sabot was designed to expand elastically under blast pressures and seal against the barrel insert. The teeth on the sabot outer profile were used to concentrate the contact force between sabot and barrel insert to ensure the most effective gas seal. It was argued that a flat outer profile would distribute contact forces over a larger surface, hence reducing the average contact force and compromise the seal.

Friction generated between sabot teeth and barrel insert were expected to generate significant forces and thus axially restrain the sabot inside the barrel. This behaviour was vital in ensuring that the propellants of proceeding rounds were not compressed and prematurely ignited. Once the fired round was ejected, the sealing sabot was free to elastically return to its original geometry, hence disengaging with the barrel in preparation for firing.

A supporting rod was included into the design to restrain any axial displacement of the round early in the blast cycle. Results of finite element analysis presented in Section 7.2 revealed that depending on the combination of sabot and barrel material, some initial axial support may be required. It was shown that with harder barrel inserts, the sabot tends to slip until maximum gas pressure, at which point frictional forces on the cup began to take over.

It was therefore decided that some form of axial support would be required initially, prior to the expansion of the cup to the barrel walls. The supporting rod used the penetrators to transfer loads to aft sabots and through to the breech of the gun barrel. While a sabot possessing an interference fit could provide initial restraint, eliminating the requirement for a supporting rod, concerns relating to the ease of round loading and ejection warranted against its use. The inclusion of a supporting rod could be further utilised to contain the propellant primer and/or firing electronics.

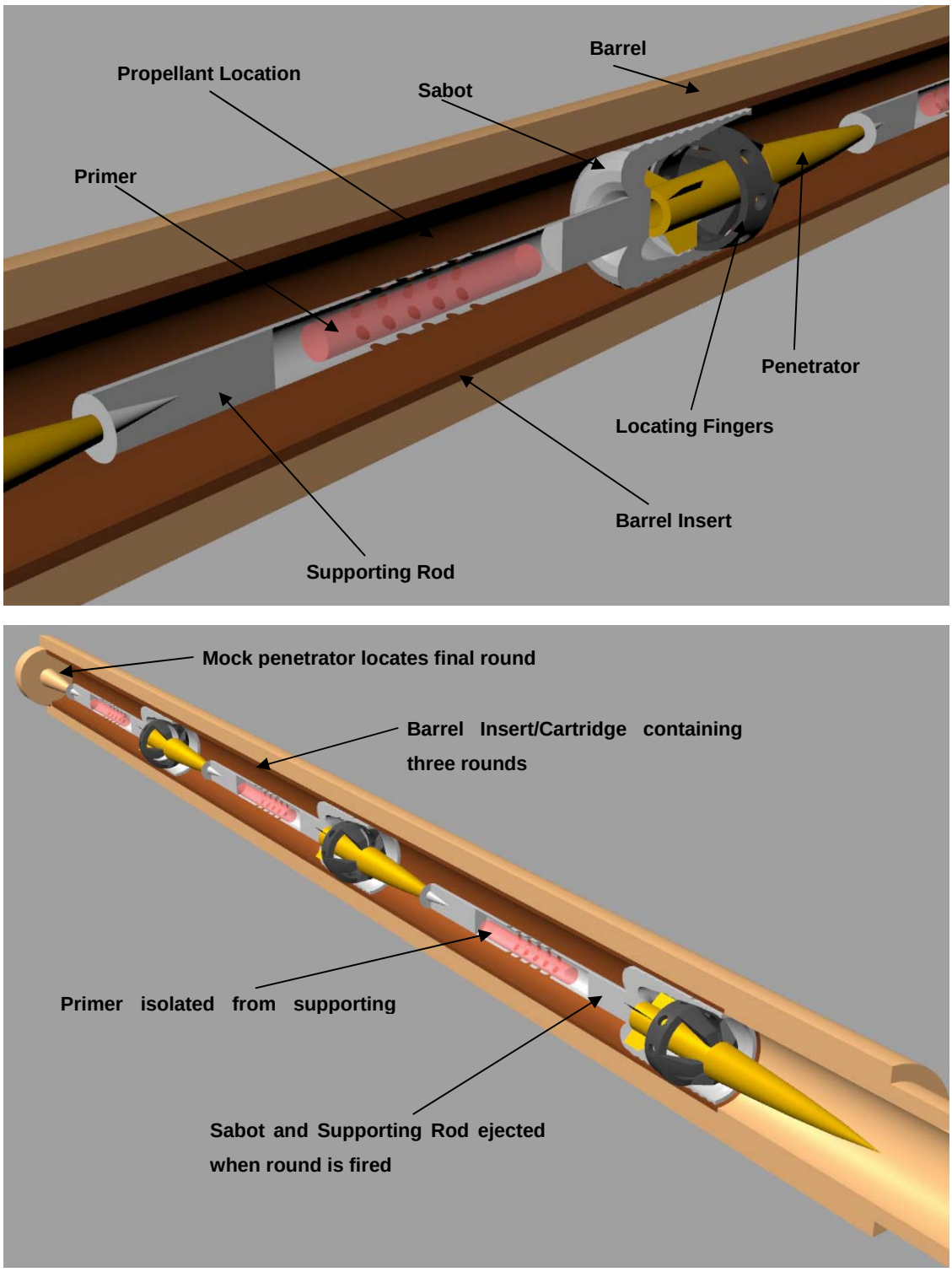

Figure 8.1: Design Concept submitted for Physical Testing of Rearward Load Case

The penetrator mounting structure, referred to as "locating fingers", was designed to better distribute loads to the penetrator during launch. It has been shown in the literature that push type sabots are generally limited in terms of the support they are able to afford the penetrator during launch [10]. That is, experiments have shown that the base of the penetrator can be compressed by inertial loads at large accelerations. For this reason, traction type sabots are preferred in traditional systems. In the case of axially stacking rounds, it was shown in Chapter 6 that traction sabots complicated the sealing mechanism, hence a push type sabot was developed.

The locating fingers were designed to be separate from the main sabot cup. As both the sabot and fingers possessed intricate geometries, manufacturing was made simpler by having separate components. Greater flexibility was also available in terms of material selection and finger/penetrator interaction independent of the sabot cup design. That is, the design of the sabot cup could proceed independent of the locating fingers.

The contact surface between sabot and locating fingers was designed to translate any rearward pressure on the locating fingers to radial force on the sabot to enhance contact with the barrel. A schematic of this action is shown in Figure 8.2. Furthermore, holes in the locating finger band (See Figure 8.1) were incorporated to vent gas pressures to sabot walls to again assist with the expansion of the cup.

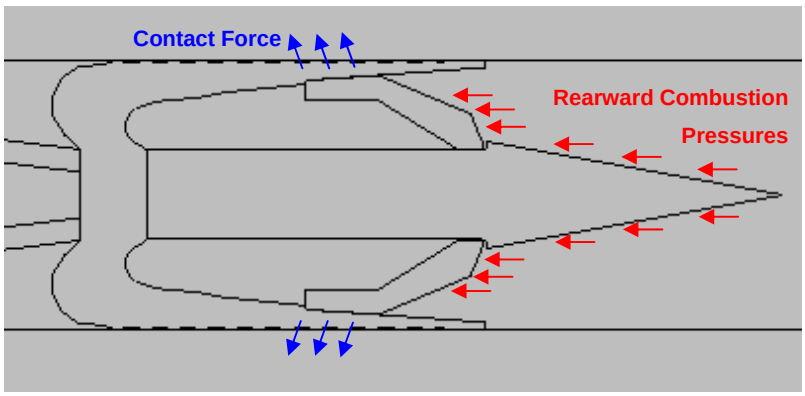

Figure 8.2: Rearward Pressure translated through Sabot/Finger interface to increase Contact Force with the Barrel.

The finger design was also important in terms of its ability to secure and release the penetrator under inertial loads. For example, when fired, the weight of the penetrator forces the fingers to grip the penetrator while traveling the length of the barrel. Upon entering the atmosphere, the fingers release from the penetrator as this inertia load is eliminated.

Sabot disengagement with the penetrator occurs under aerodynamic loads once the round has exited the muzzle. Unlike traditional sabot design, where separation usually involves the splitting of a petal arrangement, a solid sabot must cleanly disengage off the back of the penetrator. Due to concerns associated with clean disengagement, it was envisaged that separation may be designed to occur while the round is still inside the barrel. This could be achieved by designing a barrel tip which vents blast pressures to the atmosphere prior to round ejection.

8.3 Prototype Manufacture

Based on the design process conducted as apart of Chapter 7, three design options were proposed for physical testing. These included:

- Titanium Sabot with Soft Barrel Insert.
- Titanium Sabot with Hard Barrel Insert and Supporting Rod.
- Aluminium Sabot with Hard Barrel Insert.

Studies in Chapter 7 revealed that a titanium sabot used in conjunction with a soft barrel insert was able to axially restrain the cup. This configuration was tested without the use of the supporting rod. However, some reservations were still had as to the impact of a plastically deformed barrel insert on the firing of subsequent rounds. While the testing would be able to identify the amount of plastic deformation endured in this configuration, it was unable to assess its impact on the firing of subsequent rounds.

The titanium sabot with the hard barrel insert was shown to still act as an effective gas seal using finite element analysis. However, large slippage was observed up to maximum pressure and therefore a supporting rod was used to test this configuration. The benefit of this design was that no removable barrel insert would be necessary in the real gun system.

Due to the inclusion of the supporting rod, it was also decided to test an aluminium version of the design. It was hoped that the use of the rod would eliminate the longitudinal stretching of the sabot which was a major concern in previous aluminium designs. Aluminium could offer some significant advantages over titanium in this application. These include cost, weight and ease of manufacture.

For manufacturing purposes, it was necessary to prepare 2D drawings of the cross sections of each component. As the components were all axisymmetric, 2D drawings were sufficient in order for the manufacturer to create the necessary tool paths.

A mock supporting rod also needed to be designed and implemented for the physical testing. Due to size restrictions of the test chamber, the rod concept illustrated in Figure 8.1 was unable to be tested. Rather, an alternative support was designed and manufactured to satisfy test requirements.

The components which were manufactured to test the design are listed below:

- **Part 1:** Sabot Cups (9 off) – 6 Titanium (Ti-10V-2Fe-3Al) and 3 Aluminum (Al7075-T6). 1 titanium cup included 3 rubber ‘O’ rings located on alternate ridges at the trailing end of the cup. (Figure 8.3)
- **Part 2:** Projectile Support Fingers (9 off) – 5 Titanium (Ti-10V-2Fe-3Al) and 4 Aluminum (Al7075-T6) (1 Extra Aluminium due to manufacturing difficulties). (Figure 8.4)
- **Part 3:** Projectiles (9 off) – All in Mild Steel. (Figure 8.5)
- **Part 4:** Chamber Inserts (3 off) – 2 in 4140 High Tensile Steel and 1 in Mild Steel. (Figure 8.7)
- **Part 5:** Supporting Rod and Spacer Disk (1 off) – All in 4140 High tensile steel. (Figure 8.8)

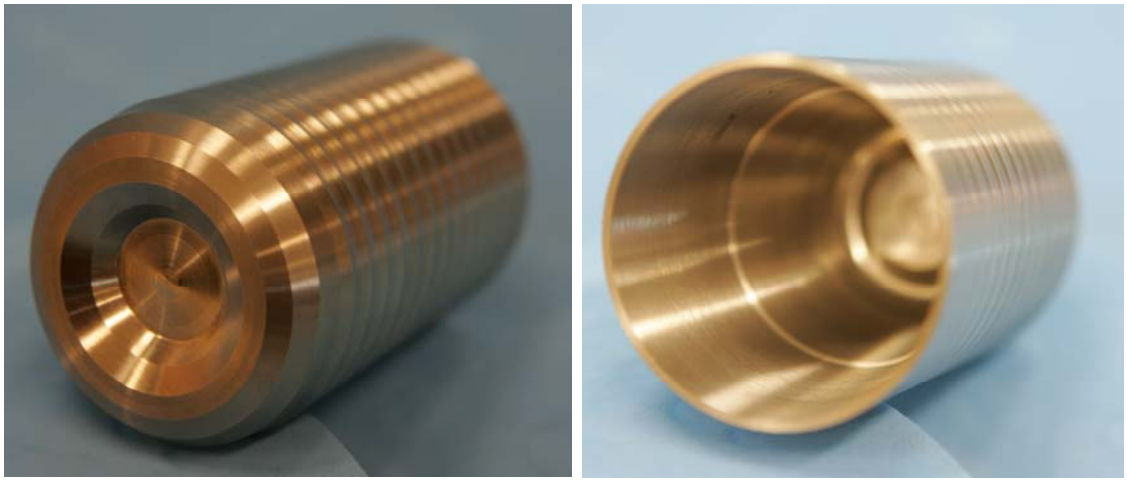

Figure 8.3 : Part 1 – Sabot Cup

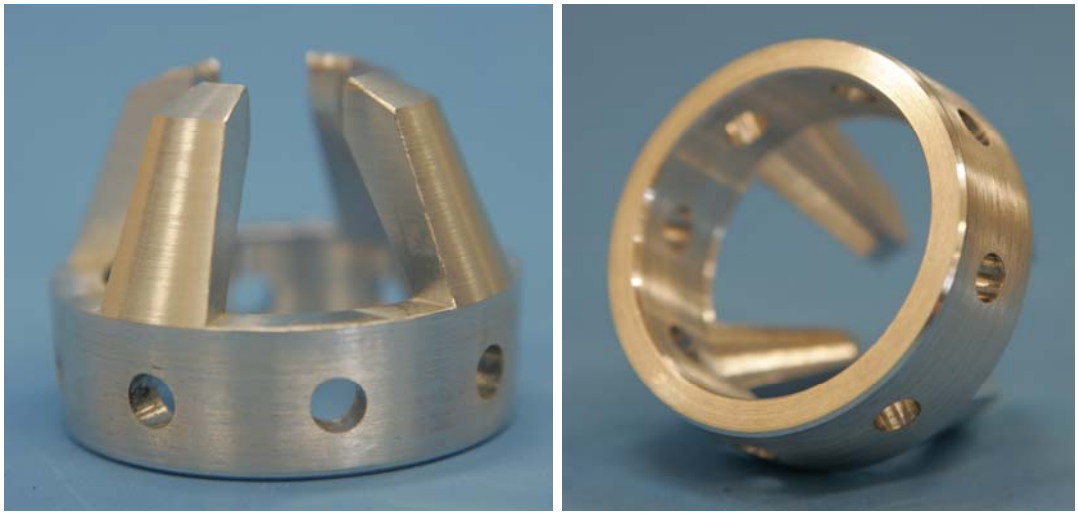

Figure 8.4: Part 2 – Projectile Locating Fingers

Figure 8.5: Part 3 – Mock Penetrator

Figure 8.6: Parts 1, 2, 3 Assembly

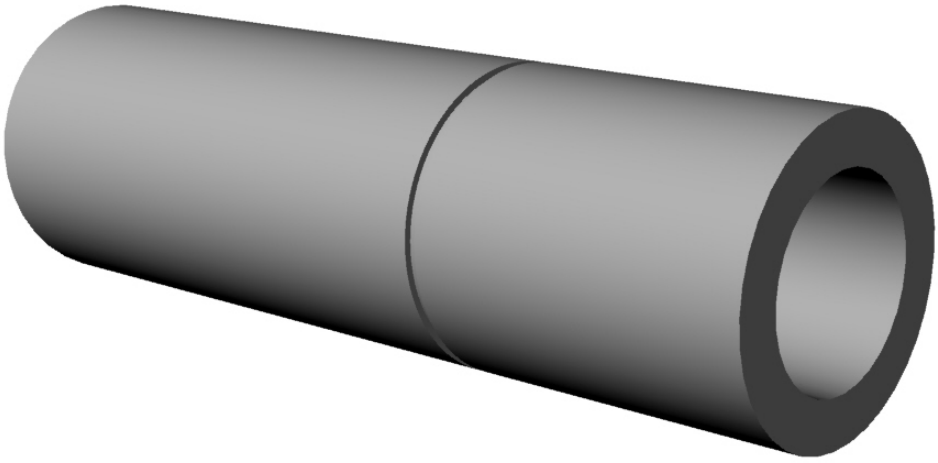

Figure 8.7: Part 4 – Chamber Insert (CAD Drawing)

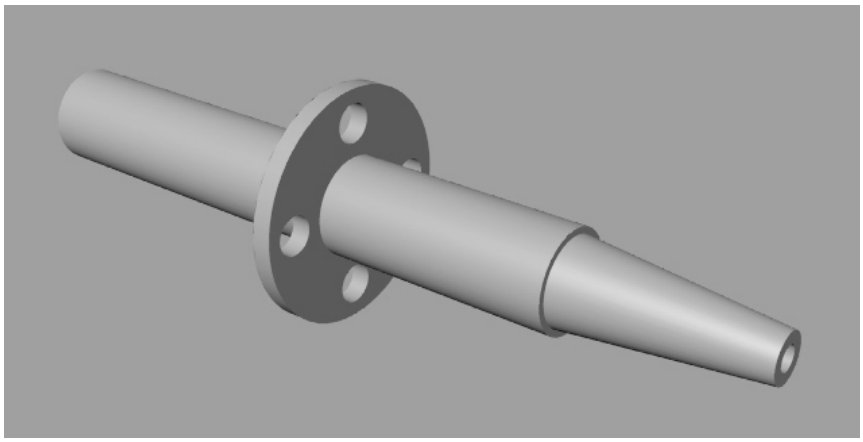

Figure 8.8: Part 5 – Supporting Rod and Spacer Disk (CAD Drawing)

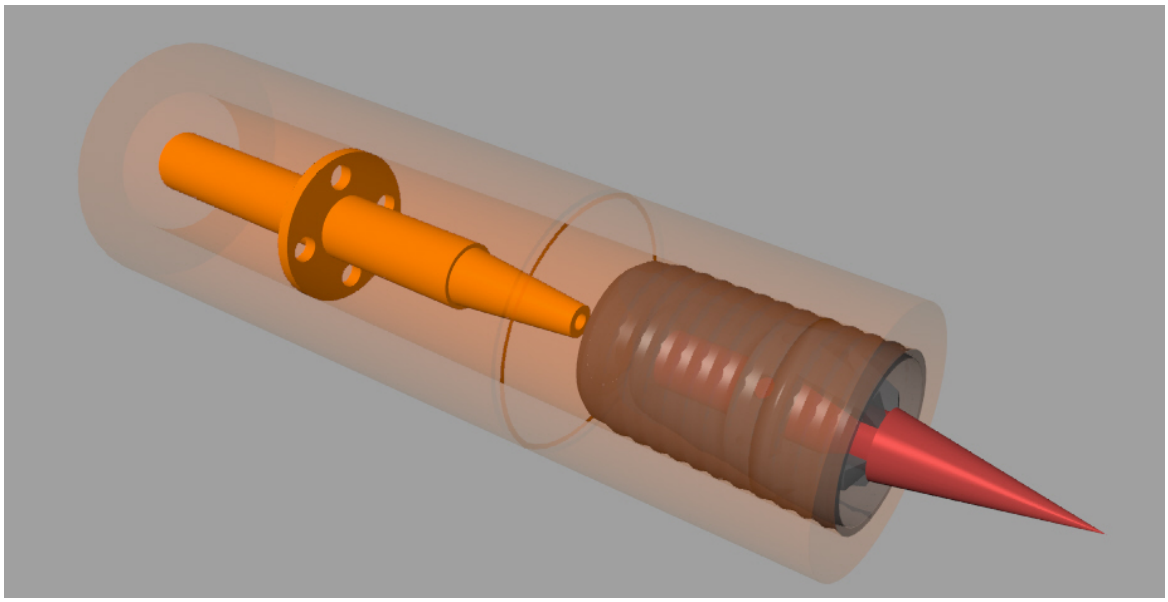

Figure 8.9: Test Assembly – CAD Drawing

The test assembly, including the supporting rod is shown in Figure 8.9. The clearance between the sabot cup and the insert was nominally 0.01mm in radius. The insert was not finely honed as this was expected to reduce the friction coefficient. Some setbacks were encountered during the manufacturing process due to the difficulty of machining titanium components. The increased time for manufacturing meant that only three chamber inserts were able to be completed. Ideally, a separate chamber insert should have been manufactured for each test. As a result, it was necessary to reuse the inserts where possible.

8.4 Prototype Testing

An experiment was devised to test the effectiveness of the gas seal of the proposed concept under specified performance conditions. The ability of the round to act as a breech and hence provide axial support was also tested. The testing took place on the week commencing 29th March 2004. The following data was extracted from the tests:

- Blast profile
- Gas Seal Effectiveness (Pressure recorded behind seal)
- Temperature Profile
- Concept Performance
- Structural Integrity

8.4.1 Experimental Set Up

Figure 8.10 contains a schematic of the Test Chamber designed and manufactured by DSTO. The rig was essentially a pressure vessel designed to replicate the rearward loading condition experienced by the sealing projectile. As seen in the figure, the round was housed in an interchangeable test sleeve. The interchangeable sleeve offered great flexibility in terms of the different designs and sealing mechanisms that could be tested. That is, a specific test sleeve could be manufactured for each of the designs considered.

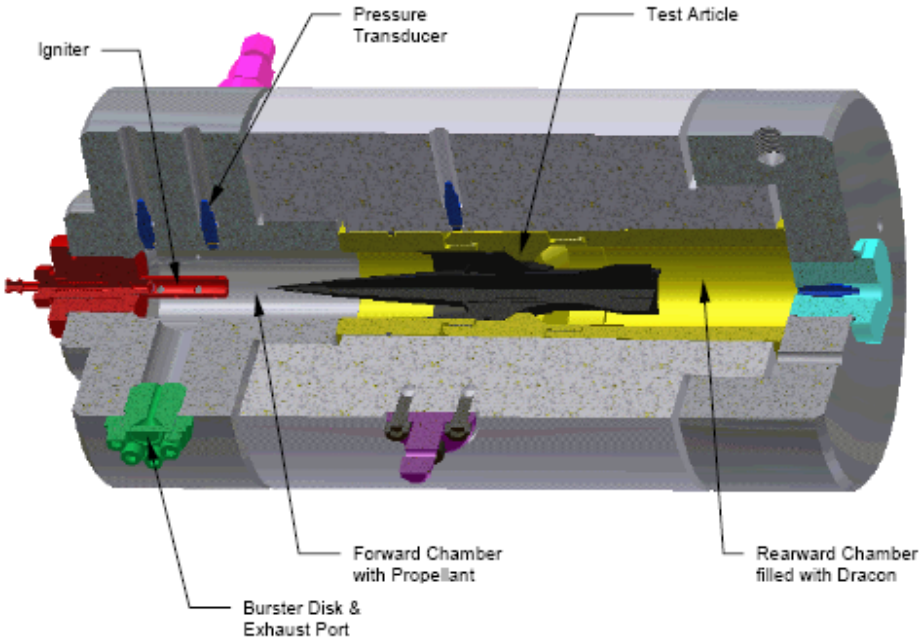

Figure 8.10: Schematic of Test Chamber developed by DSTO.

The pressure time environment in front of the test article was controlled by the propellant, a burster disk and exhaust port. The propellant was loaded into the forward chamber which also contained the ignition system. Two pressure transducers were used to record the pressure generated by the propellant. Another pressure sensor was located in the rearward chamber in order to record any pressure rise behind the round and hence determine the efficiency of the seal. A pressure transducer was also located adjacent to the test article but was not used for all tests. The schematic in Figure 8.11 shows the location and designation of each of the pressure transducers.

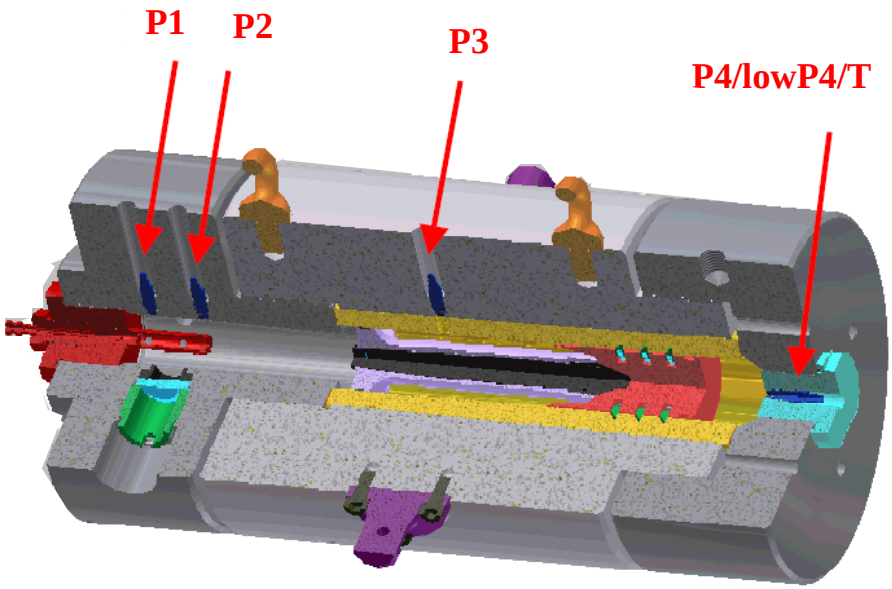

Figure 8.11: Pressure Transducer Layout and Designation

The data was sampled using a digital data acquisition system. The pressure transducers in the forward chamber were rated to the expected maximum pressure to be generated by the propellant, including a safety margin. The pressure transducer in the rear chamber was rated for lower pressures for better resolution in order to check for any gas leakage.

A series of burster disks were designed to burst at different peak gun pressures. Upon bursting, the high pressure gas was able to be vented through the exhaust port. Different combinations of bursting disks and amount of propellant allowed for a range of peak firing pressures to be generated. Peak pressures ranged between 100MPa to 540MPa. A pressure relief valve was also included into the design to allow the test rig to be vented in the event of the burster disk failing to burst.

The rise time in the test chamber was steeper and more severe than that expected of the real gun system as volume expansion was not possible in the chamber until the burster disk was activated. It was unclear whether this difference in rise time would adversely affect the dynamic sealing action of the design. However, it was decided that the testing would still provide useful insight into the rounds behaviour and was therefore conducted.

After each test, a visual inspection of the test articles was undertaken to assess the structural integrity of the prototype. In doing so, signs of any material plastic strain or fracture were identified and recorded. In addition, Dacron fibres were placed in the rearward chamber behind the projectile in order to check for flashover. That is, any charring of the Dacron would suggest that combustion flames were not appropriately sealed.

The test rig, as seen in Figure 8.12, was used in the vertical firing position with a percussion primer assembly for ignition.

Figure 8.12: Test Rig Set-Up in Vertical Firing Position.

8.4.2 Results

Testing of the design concept commenced in the afternoon of Wednesday 31st March 2004. Unfortunately, only four test shots were conducted due to damage sustained by a thread on the end cap of the test rig. The full set of results obtained for testing, including photographs and measurements recorded from the transducers, were unable to be published as apart of this document due to classification restrictions. However, basic performance results and observations are described below for each test.

8.4.2.1 Test Number 1

Date: 31st March 2004, 13:00hrs

Description: Test Rig Qualification of Titanium Cup and Supporting Rod using Hard Barrel Insert at 250MPa Nominal Peak Pressure.

Objective: Verify the performance of the Titanium cup and Supporting rod using the Hard Barrel Insert (4140 Steel) with a pressure pulse width representative to that of the gun system.

Test Piece Observations:

- The supporting rod was destroyed by the blast and the titanium cup slipped back to the rear of the test section.
- High temperatures were generated by the compression of the supporting rod. This caused parts of the titanium cup to melt and adhere to the wall of the chamber insert.
- No test pieces were able to be recovered from the test as all were severely damaged and welded to the inside of the insert.
- The maximum peak chamber pressure achieved was only 110MPa due to the rapidly increasing volume within the chamber.

- Failure of the supporting rod was suspected to have occurred due a mistake in manufacturing (Mild Steel used for Supporting Rod instead of the prescribed High Tensile Steel. A new supporting rod was consequently manufactured).

8.4.2.2 Test Number 2

Date: 1st April 2004, 11:00hrs

Description: Test Rig Qualification of Titanium Cup Variant (with 'O' rings) and New Supporting Rod using Hard Barrel Insert at 450MPa Nominal Peak Pressure.

Objective: Verify the performance of the Titanium Cup Variant which uses three 'O' rings to seal initial gas pressures, a new Supporting Rod and Hard Barrel Insert (4140 Steel) subjected to a maximum peak pressure of 450MPa with a pressure pulse width representative to that of the gun system.

Test Piece Observations:

- The peak recorded nominal pressure was approximately 450MPa as expected.
- No pressure was recorded behind the seal.
- No charring was observed on the Dacron fibers.
- No damage was observed on the cup, penetrator or supporting fingers.
- No carbon was observed on the outer wall of the cup.
- The insert was grooved at the position of the cup ridges except for where the 'O' rings were located.
- The supporting rod had slight grooves stamped into its surfaces at the contact locations with the sabot and test rig.
- The penetrator remained positioned in the cup.
- The cup had to be dislodged with some light hammer blows after the test.

8.4.2.3 Test Number 3

Date: 1st April 2004, 13:30hrs

Description: Test Rig Qualification of Titanium Cup with No Supporting Rod using Hard Barrel Insert at 450MPa Nominal Peak Pressure.

Objective: Verify the performance of the Titanium Cup without a support structure using a Case Hardened Steel Insert (4340 Steel) subjected to a maximum peak pressure of 450MPa with a pressure pulse width representative to that of the gun system.

Test Piece Observations:

- The peak recorded nominal pressure was approximately 425MPa.
- No significant pressure was recorded behind the seal.
- No charring was observed on the Dacron fibres.
- The cup slid back significantly inside the insert.
- No damage was observed on the cup, penetrator or supporting fingers apart from some grinding of cup teeth between the 2nd and 6th teeth from the front. The removal of material increased toward the front until the 2nd ridge was entirely removed.
- No carbon observed on the outer wall of the cup.
- The cup was easily removed from the insert after the test.

Note: Case Hardened Steel Insert (4340 Steel) was provided by DSTO.

8.4.2.4 Test Number 4

Date: 1st April 2004, 14:30hrs

Description: Test Rig Qualification of Titanium Cup with New Supporting Rod using Hard Barrel Insert at 450MPa Nominal Peak Pressure.

Objective: Verify the performance of the Titanium Cup with the New Supporting Rod using a Case Hardened Steel Insert (4340 Steel) subjected to a maximum peak pressure of 450MPa with a pressure pulse width representative to that of the gun system.

Test Piece Observations:

- The peak recorded nominal pressure was approximately 477MPa.
- No significant pressure was recorded behind the seal.
- No charring was observed on the Dacron fibers.
- No damage was observed on the cup, penetrator or supporting fingers apart from minor damage to some forward teeth on the cup.
- No carbon was observed on the outer wall of the cup.
- The insert was marked at the position of the cup ridges.
- The penetrator shifted out of position inside the sabot.
- The cup was easily removed from the insert after the test.

8.4.3 Discussion

The physical testing was successful in providing design validation for both the concept and Virtual Design Process used in the development. Unfortunately, problems with the test rig prevented two design options from being tested. These were Aluminium Sabots with Hard Barrel Inserts and Titanium Sabots with Soft Barrel Inserts (mild steel insert). However, the obtained results for the Titanium Sabots using Hard Barrel Inserts provided enough confidence such that design development and refinement could continue.

The titanium sabots were shown to perform as effective pressure seals as no pressure was recorded behind the round in any of the tests. Test 1 suffered a catastrophic failure from what was identified to be an error in material selection during manufacturing. The supporting rod used for the test was manufactured from a mild steel instead of the prescribed 4140 High Tensile Steel. This meant that combustion pressures were able to compress the rod which generated a large amount of heat destroying both the rod and round.

Upon inspection of the test pieces after Test 1, the round had slid to the rear of the chamber insert, entirely compressing the rod and becoming welded to the insert. The increase in chamber volume resulting from the slippage of the round meant that the peak chamber pressure only reached 110Mpa instead of the 250Mpa expected. Subsequent to the failure, a new supporting rod was manufactured using the prescribed high tensile steel.

The titanium sabot variant incorporating ‘O’ rings was tested in Test 2 using a hard barrel insert and the new support structure. The designated peak pressure for the test was 450Mpa, which was successfully achieved. The round performed well in this configuration showing no recorded pressure behind the seal and no charring of the Dacron fibres. In addition, the external sabot face was inspected for any sign of carbon deposits, which would suggest that some flame (flashover) penetrated around the sabot cup. Nothing of this nature was prevalent.

No significant damage was observed on any of the test pieces including the new supporting rod as a result of Test 2. Some grooves were noticed inside the chamber insert at locations where the sabot teeth sealed against the insert. This result suggested that in the real system, a harder barrel material would be required to avoid being severely damaged by numerous firings. This would not be a problem in the case of using interchangeable inserts for the sealing surface. The sabot was able to be easily removed from the test insert using some light hammer blows after the test.

Test 3 considered the performance of a titanium sabot using a hard barrel insert without a supporting rod. While this configuration was not explicitly proposed in the test plan, it was decided that this test could provide further justification to the results obtained using explicit finite element analysis. According to results of finite element analysis, the titanium sabot should experience significant rearward slippage until maximum pressure is achieved.

The peak pressure recorded in Test 3 was 425MPa, slightly below the prescribed 450MPa. The titanium sabot was tested with a case hardened steel insert (4340 Steel), which was supplied by DSTO. As with the previous test, no pressure was recorded behind the seal along with no charring of the Dacron fibres or any sign of carbon on the sabot outer profile.

However, as predicted, the sabot slid back significantly inside the insert, reinforcing the requirement for a supporting rod in this configuration. The resultant increase in chamber volume was the most likely cause of the chamber pressure not quite reaching the prescribed maximum. While no significant damage was observed on the test pieces, some grinding of sabot teeth, between the 2^{nd} and 6^{th} ridges from the front, resulted from this movement. The removal of material appeared to increase toward the leading edge until the 2^{nd} ridge was entirely removed. While the slippage did not compromise the behaviour of the seal, propellant compression would be a major concern in this instance. The sabot was able to be easily removed from the insert after the test.

Finally, Test 4 considered the behaviour of the titanium sabot using a case hardened barrel insert and a supporting rod. In this instance, the peak firing pressure slightly overshot the prescribed 450MPa, reaching a maximum of 477MPa. Again, as with previous tests, no pressure was recorded behind the seal along with no charring of the Dacron fibres or any sign of carbon on the sabot outer profile.

No damage was observed on the cup, penetrator or supporting fingers apart from minor damage to some forward teeth on the cup. However, in this case, the penetrator was jolted out of position by the test and was no longer resting on the pusher plate. It was the first time this phenomenon had been observed in the tests, with both the penetrator and locating fingers remaining stationary in previous firings. Rather than further complicating the design, it was proposed that the penetrator could simply utilise some mild adhesive to hold it in position during the sealing phase. The round was again easily removed from the chamber insert, suggesting elastic behaviour of the sabot as predicted in the modelling.

Inspection of the internal wall of the chamber insert again revealed some minor grooving at the contact locations of the sabot teeth. As previously mentioned, a harder barrel material would be required in the real system in order to avoid this damage. It was predicted that the use of aluminium sabots would eliminate this behaviour, however, these were unable to be tested due to damage sustained by the test rig.

Overall, the tests showed good agreement with the results obtained using explicit finite element analysis. The ability of the sabot to deform and create a robust seal whilst remaining in the elastic region was well predicted by finite element methods. In practise, the cup sabots were able to efficiently seal the blast pressure of the propellant and subsequently be easily removed from the inserts after the tests. This finding suggested that the rounds would be free to be fired in the forward load case after having performed the seal.

Careful consideration of the available design options led to the decision that a hard barrel design, eliminating the requirement for an interchangeable insert, would be the best solution. The testing results reinforced the expectation that the sabot was unlikely to be retained by friction alone using a hard barrel design. The design of a supporting structure would therefore be required and is presented in the next section.

8.5 Design Refinement

8.5.1 Design of an Integrated Supporting Rod

The use of a supporting rod aimed at taking advantage of penetrator strength in order to transfer loads to aft rounds and into the breech of the gun barrel. This transfer of load would offer support to the sealing sabot in the initial stages of the blast. Friction generated from the expansion of the sabot cup into the barrel would then be expected to take over the majority of the rearward load and perform the gas seal.

The supporting rod took the form of a hollow tube, which could be used to house the primer and firing electronics. The support would therefore require a series of periodic holes drilled down its length in order to vent the hot, high pressure products generated by the primer. To guarantee against premature ignition, it was necessary to design a support that did not yield under the applied load. This ensured that the primer or propellant of the sealing round was not compressed and ignited prematurely.

The rigid support would also allow for greater flexibility in terms of material selection. Previously, much effort was exhausted in trying to produce aluminium designs as they were lighter, cheaper and more machineable than titanium. It was found that an aluminium sabot was capable of generating sufficient contact pressure to create a gas seal, however, the cup would yield close to the bulkhead when subjected to pressures greater than 500MPa. Eventually, the design switched to titanium to avoid the longitudinal stretching. Using a support structure to distribute some of the axial load to the gun breech may allow the design to revert back to using aluminium sabot cups.

It was also decided that a hard barrel insert would be the most feasible in a real gun system. This would eliminate the requirement for a removable insert, which requires the cumbersome tasks of loading and ejection with each set of rounds. Therefore, in this current investigation, the hardness of the barrel material was maintained well in excess of that of the sabot. The use of an aluminium sabot complemented this requirement.

The sabot cup profile remained relatively unchanged. Some curvature was introduced to the tips of the sabot teeth in order to reduce stress concentrations in the barrel. It was shown in physical testing that the sabot ridges would generate grooves in the barrel wall. As the new design philosophy eliminates the requirement for a removable insert, the internal barrel wall should not sustain any form of permanent deformation. The use of 'blunt' teeth and aluminium should alleviate this concern. Close attention was paid to ensure this modification did not adversely affect the contact force between the sabot and barrel such that the seal was compromised.

The rear bulkhead section of the sabot also underwent some minor modifications in order to reduce mass and allow for the attachment of the rigid support. It was assumed that the support would be manufactured as a separate component and threaded into the back of the sabot. Appropriate adjustments to the sabot were therefore made to allow for this attachment.

Figure 8.13 contains an image of the new concept and in Figure 8.14 the details of the sabot design incorporating the rigid support are shown. It is proposed that for assembly the support should be first loaded with the primer tube, and then threaded onto the rear section of the sabot cup. The aft end of the support possesses an identical geometry to that of the penetrator tip so as to effectively distribute load through the penetrators to the gun breech. The penetrator and mounting fingers remain unchanged from previous designs.

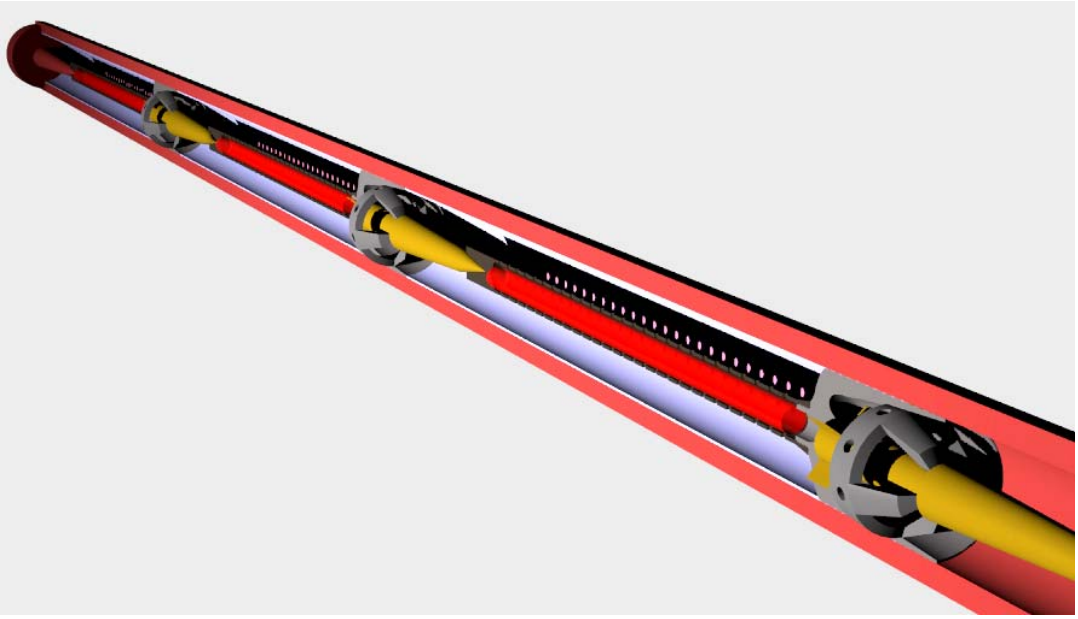

Figure 8.13: Design Concept of Sabot with Integrated Support Structure

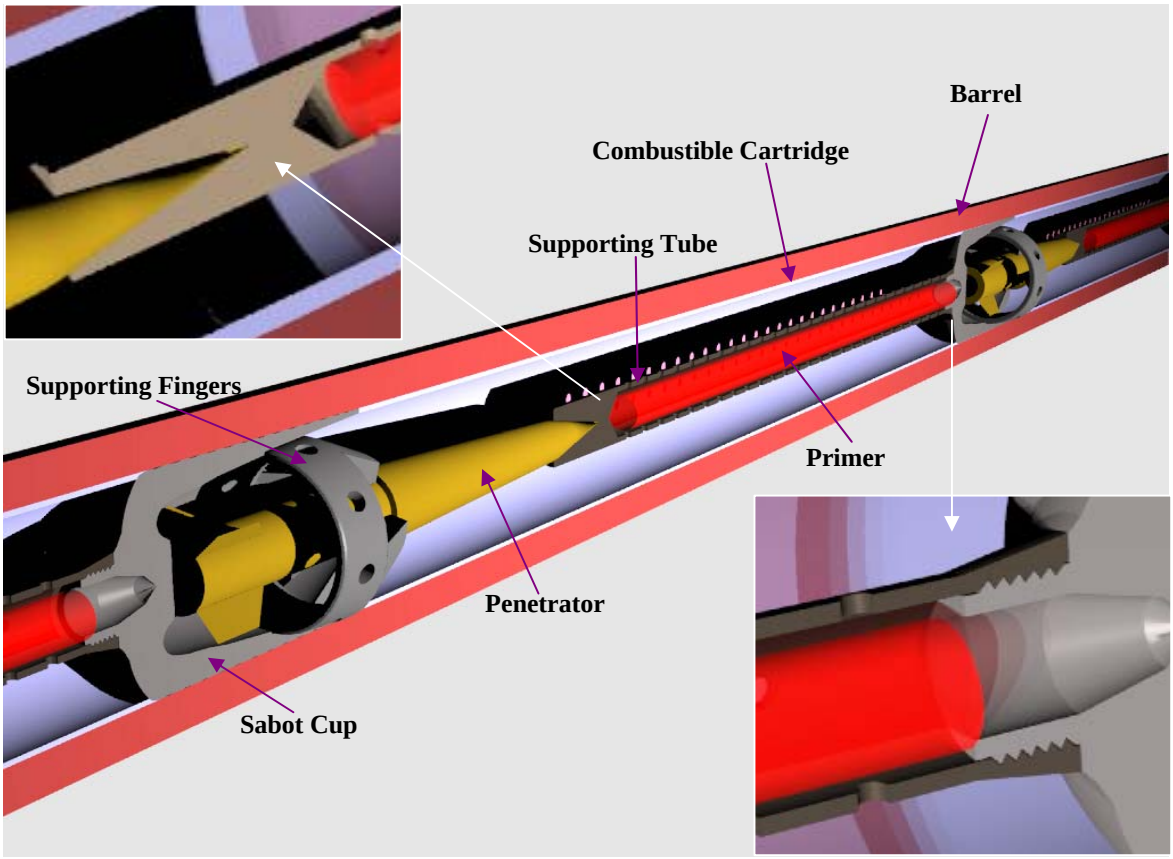

Figure 8.14: Sabot Design with Integrated Support Structure

8.5.1.1 Explicit Finite Element Analysis

Detailed finite element models of the integrated sabot/support were produced in order to develop the supporting rod design. The sabot, penetrator locating fingers and supporting rod were all modelled using aluminium. The penetrators were modelled using tungsten, while high tensile steel was used to model the barrel. Elastic plastic material models were again used for the analysis with material properties shown in Table 8.1. A failure model was included in this instance for the aluminium constitutive model, utilising a maximum plastic strain failure criteria.

Table 8.1 – Material Properties

	High Tensile Steel (Barrel)	Aluminium Alloy (Sabot & Rod)	Tungsten Alloy (Penetrator)
Density (g/cm^3)	7.85	2.83	19.3
Modulus of Elasticity (GPa)	206	71	400
Poisson's Ratio	0.3	0.3	0.28
Yield Strength (MPa)	1100	532	750
Elongation at break	-	7.8%	-

A quarter finite element model of the sabot and rigid support was used to simulate both the forward and rearward load cases. Figure 8.15 illustrates the finite element model constructed for the analysis (barrel, locating fingers and penetrator not shown). In order to simplify the modelling process, the threaded connection between the sabot and support was not included in the simulation. Rather, the components were considered as a single part using a continuous mesh.

A contact was defined between the sabot and barrel with assumed coefficients of friction of 0.2. A contact was also placed between the rear of the supporting rod and the aft penetrator tip. This contact was important in assessing the stresses imparted to the aft penetrator from the blast. It was also important to determine whether or not any yielding occurred at this interface, which could potentially result in the support jamming onto the aft penetrator.

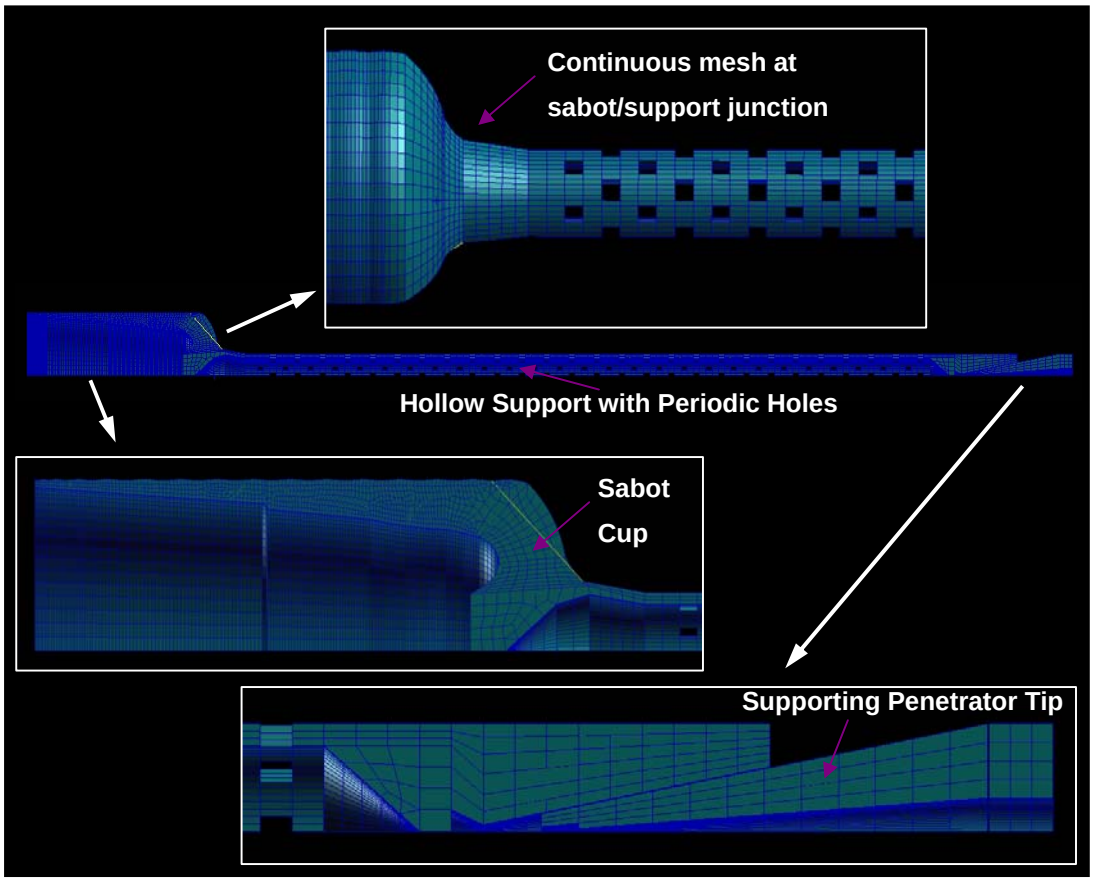

Figure 8.15: Quarter Finite Element Model of the Sabot and Integrated Support Structure

Figure 8.16 illustrates the contours of Von Mises stress experienced by the model at different times throughout the rearward load case. Note that the maximum pressure of 540MPa occurred at 2ms. Beyond 3ms, the forward load case was applied to the back of the sabot to accelerate it out the barrel.

For the first fractions of a millisecond, a stress wave can be seen travelling through the structure until it strikes the aft penetrator at approximately 0.3ms. At that time, the aft penetrator experienced a sharp rise in stress with values approaching 470MPa. This value was still well below the yield stress of the tungsten alloy and did not result in any permanent deformations. This stress rapidly dissipated with the maximum reduced to 50MPa by 0.4ms.

After the stress wave had travelled through the structure, a series of standing waves began to develop in the rigid support. The stress plots between 0.4-1.4ms clearly demonstrate the growth of longitudinal vibrations, as regularly spaced regions of high stress are evident down the support. Higher order modes begin to dominate as time progresses, which can be seen by the increase in the amount of high-pressure regions along the support.

High stresses are observed in the sabot teeth with values approaching 500MPa by 1msec, close to the yield stress of the material. By this stage, it can be confidently assumed that the contact between the sabot and barrel is providing the majority of the restraint as stresses remain consistently low on the aft penetrator.

The stresses on the sabot ridges appear to gradually increase as the blast pressure reaches its maximum at 2msec. At this time, the last two ridges experience the highest stresses with values exceeding 750MPa. While these values are beyond the aluminium yield stress, we would not expect this behaviour to be catastrophic as the yielding is occurring in compression and is obviously constrained by the geometry of the barrel. Even at maximum pressure, very little increase in stress is observed in the supporting aft penetrator tip.

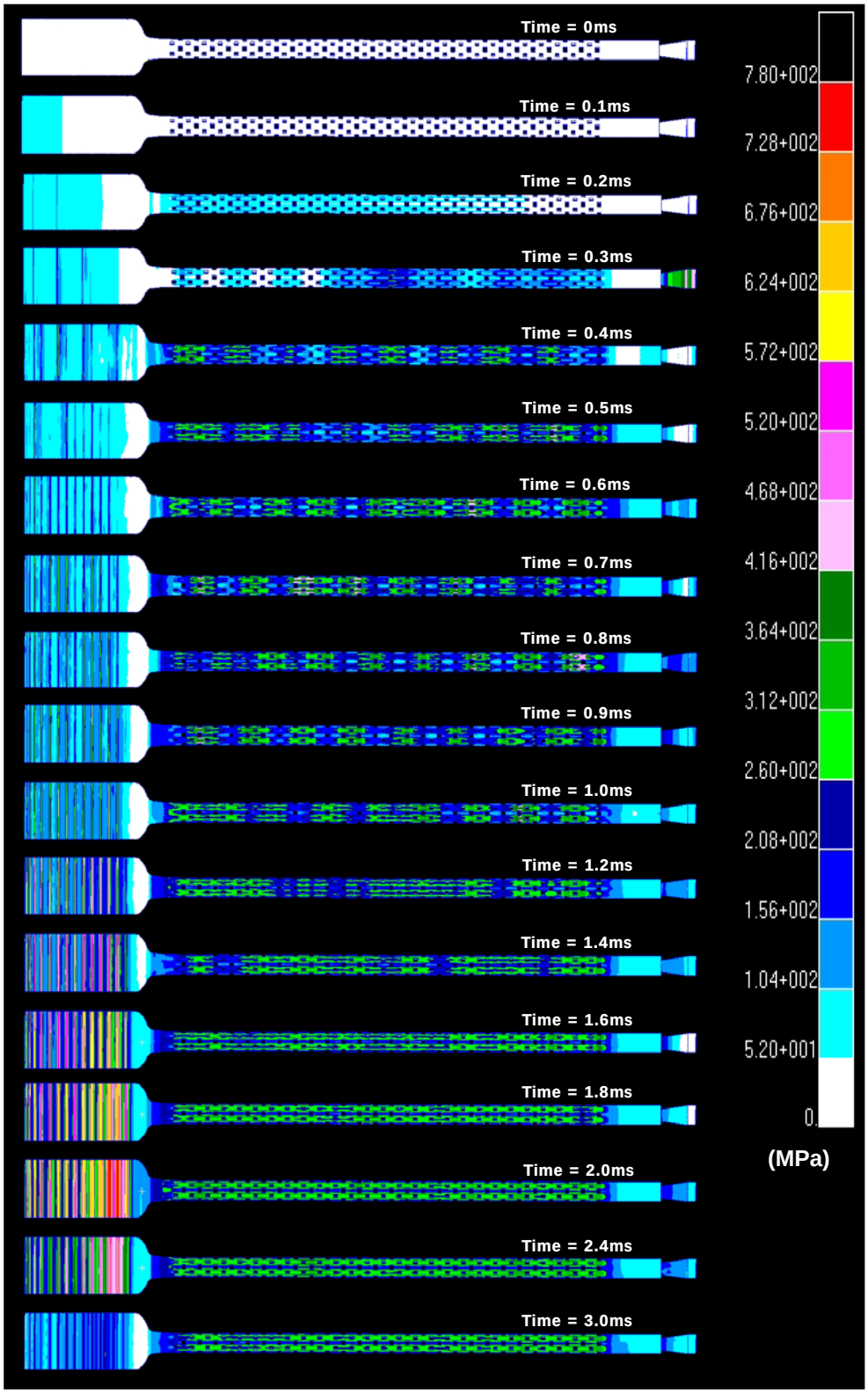

Figure 8.16: Sabot and Integrated Support Structure: Von Mises Stress Results

Figure 8.17 shows the plastic strain endured by the model at maximum rearward pressure. Most encouraging is the fact that no plastic strain is observed in the supporting rod. It was feared that any deformation in this region might serve to compress and hence ignite the primer prematurely. Considering the sabot cup, plastic strains on the ridges average approximately 2% with maximums approaching 4% at the rear ridges. Some compression of the sabot teeth should not significantly impact the ejection of the sabot during the forward load case and was therefore not a concern.

After maximum pressure, stresses in the round reduced gradually until the rearward blast pressure had ceased at 3msec. Residual stresses in the supporting rod reached values of up to 300MPa, however no significant plastic deformation was observed.

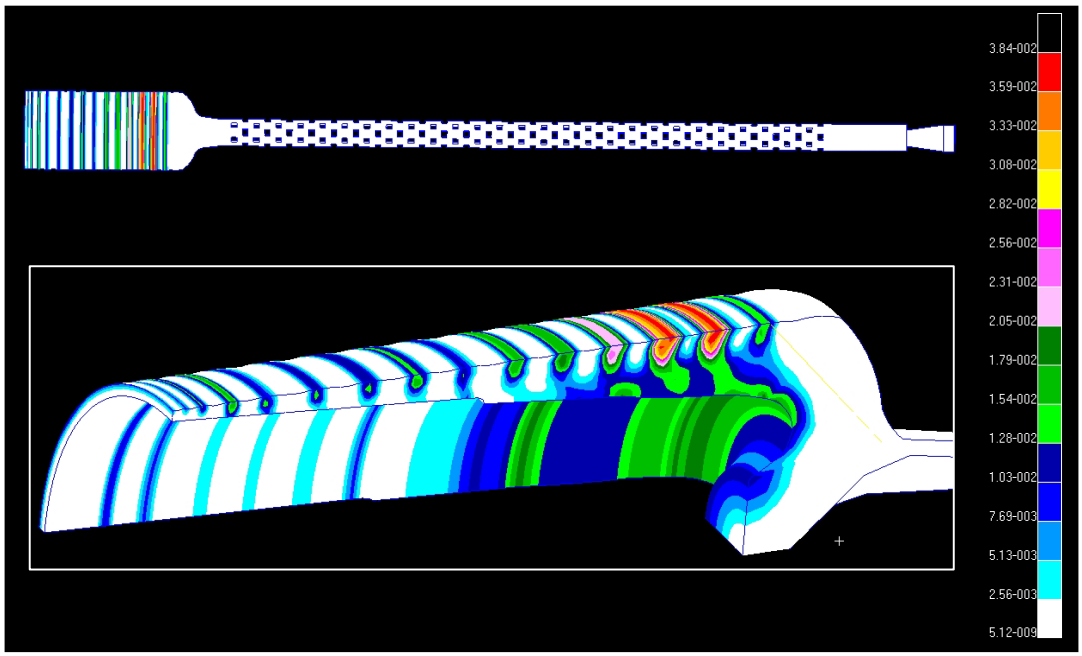

Figure 8.17: Sabot and Integrated Support Structure: Plastic Strain at Maximum Rearward Pressure (2msec)

After 3msec, the forward load case was applied to the rear of the sabot cup and supporting rod to simulate the ejection of the round. The simulation confirmed that the sabot was free to move forward under firing pressures, eliminating any concern of the yielded teeth jamming the sabot in the barrel.

An interesting feature of the forward motion was observed in the structural behaviour of the supporting rod. Figure 8.18 illustrates the plastic strain possessed by the model at 4.1msec (1.1msec of forward pressure). The plot shows plastic strains, created by inertial loads, close to the maximum allowable plastic strain in the supporting rod just rear of the sabot cup.

The result suggests that the supporting rod will break away from the sabot cup during firing. This should result in an increased muzzle velocity for the sabot cup and penetrator due to the decreased weight. That is, energy that would otherwise be used in accelerating the supporting rod to the desired muzzle velocity could instead be expended on the sabot cup and penetrator.

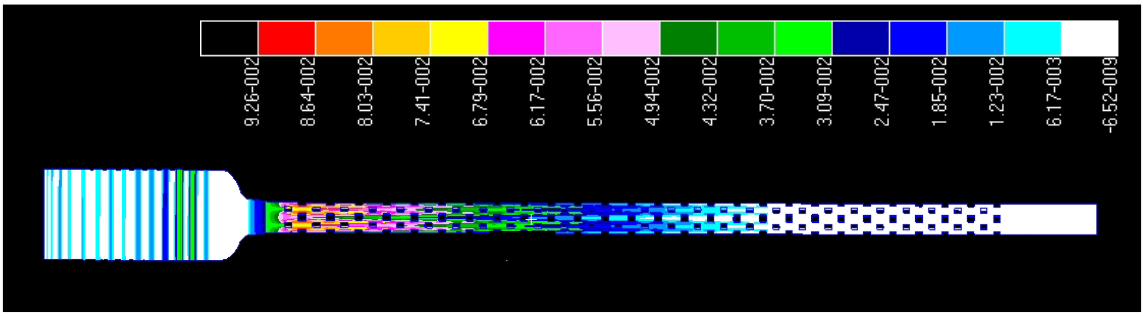

Figure 8.18: Sabot and Integrated Support Structure: Plastic Strain at 4.1msec (1.1msec of forward pressure)

8.5.1.2 Sabot Weight Reduction

Further inspection of Figure 8.17 revealed a large region of the sabot cup bulkhead which experienced no plastic strain. It was apparent that the extra support offered by the supporting rod could be further utilised to reduce the mass of the bulkhead. Shape optimisation using ReSHAPE was again performed to reduce the mass of the bulkhead. Figure 8.19 compares the original and reduced mass profiles.

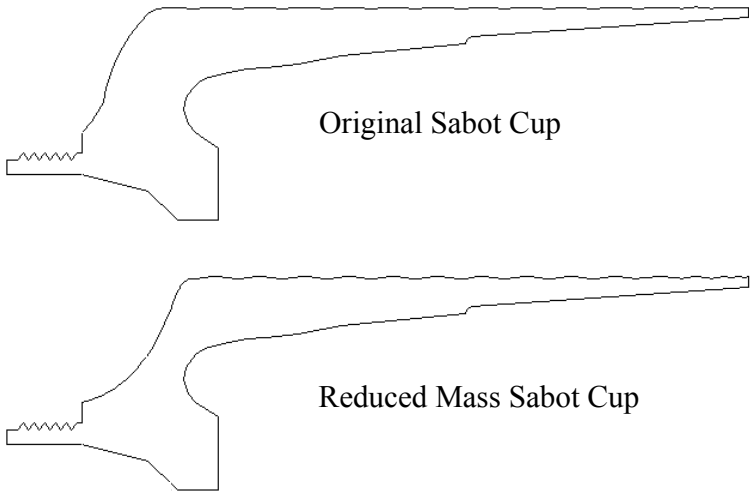

Figure 8.19: 2D Profiles of Original and Reduced Mass Sabot Cups

Figures 8.20 and 8.21 show Von Mises stress and plastic strain results obtained for this modified cup at maximum rearward pressure (2 msec). Plastic strains of between 1 and 1.6% can now be observed in the bulkhead region. However, these values are still well below the break elongation of 7.8% reported for this alloy.

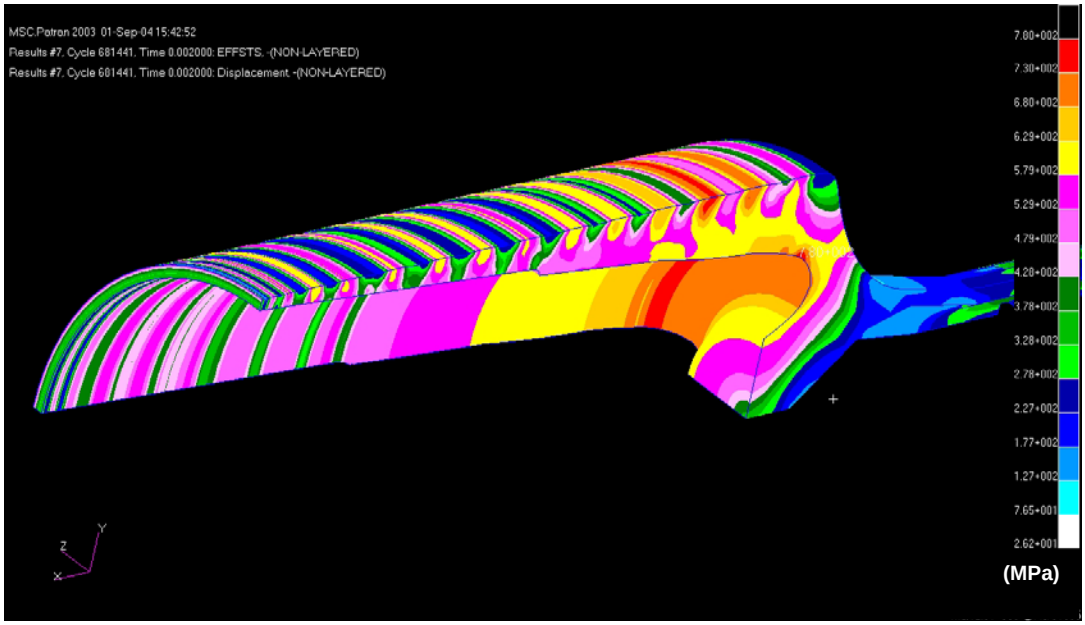

Figure 8.20: Reduced Mass Sabot Cup: Von Mises Stress Results at Maximum Rearward Pressure (2msec)

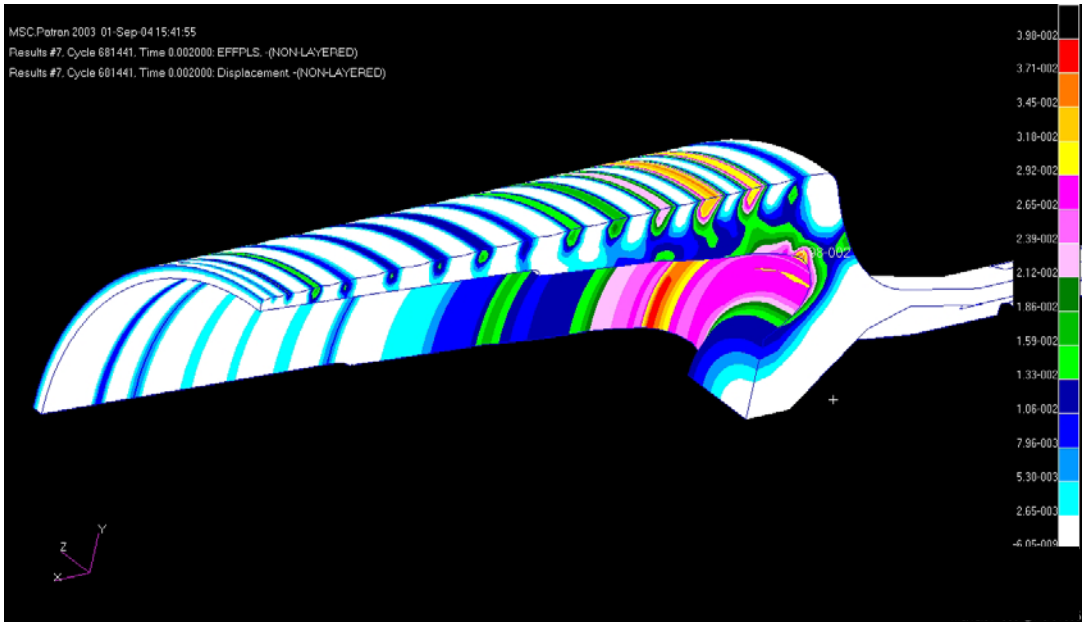

Figure 8.21: Reduced Mass Sabot Cup: Plastic Strain Results at Maximum Rearward Pressure (2msec)

The initial mass of the reduced mass sabot and supporting rod is 0.343 kg. After the rod breaks off during firing the weight of the sabot reduces to around 0.23 kg, a weight reduction of almost 1/3 of the original mass. It was stated previously that sabot mass should represent one-quarter to one half of the entire projectile weight for most modern kinetic energy projectiles [38]. The values stated above are well within this range for the assumed 1kg launch package.

It was feared that the separation of the supporting rod might have an undesired effect on the possible rate of fire of the round. This would result from the supporting rod being slower to clear the barrel as compared to the sabot cup and penetrator. Results of the analysis showed that the sabot and rod had a forward velocity of around 500 m/s when separation occurred. Assuming this speed is maintained, it was found that the rod would clear the barrel in about 10 milliseconds after firing for a barrel length of 70 calibres.

This result significantly exceeds the specified 10 rounds per second performance requirement as stipulated in Section 6.2.4. The obtained muzzle velocity for the penetrator was 1630m/s, again exceeding the required performance target stated in the design goals.

8.5.1.3 Gas Seal Assessment using FSI Modelling

Fluid Structure Interaction modelling was used to determine the gas seal effectiveness of the refined Cup Seal Design. The Lagrangian model employed in analysing the refined sabot design was slightly simplified for use in this investigation. The model can be seen in Figure 8.22. The supporting rod was removed as the axial restraint behaviour of the system was not important in this investigation. Rather, nodal constraints were applied to the rear end of the sabot to provide axial restraint.

A Eulerian mesh was embedded inside the barrel covering the entire sabot mesh and a portion of the barrel mesh. Coupling surfaces were prescribed on the exterior surfaces of both the sabot and barrel Lagrangian meshes. Generating the coupling surfaces was straight forward as both exterior surfaces formed closed volumes. The requirement for closed volumes was discussed in Chapter 3.2.4.1.

Due to restrictions described in Section 5.6 it was not possible to utilise the developed propellant combustion material sub routine as apart of this investigation due to the associated complex geometries. However, FSI could still be used to determine the integrity of the gas seal in this case by simulating a high pressure gas inside the sabot cup.

Eulerian elements were used to model this high pressure gas in front of the sabot. Pressures in the Eulerian material were transferred to the Lagrangian meshes via coupling surfaces, causing them to distort. If the seal between the sabot and barrel was not effective, then gasses would be able to pass along this interface and build up behind the sabot. Any build of gas pressure behind the sabot would imply failure of the seal. A Contact definition was imposed between the sabot and barrel with the coefficient of friction set to 0.2.

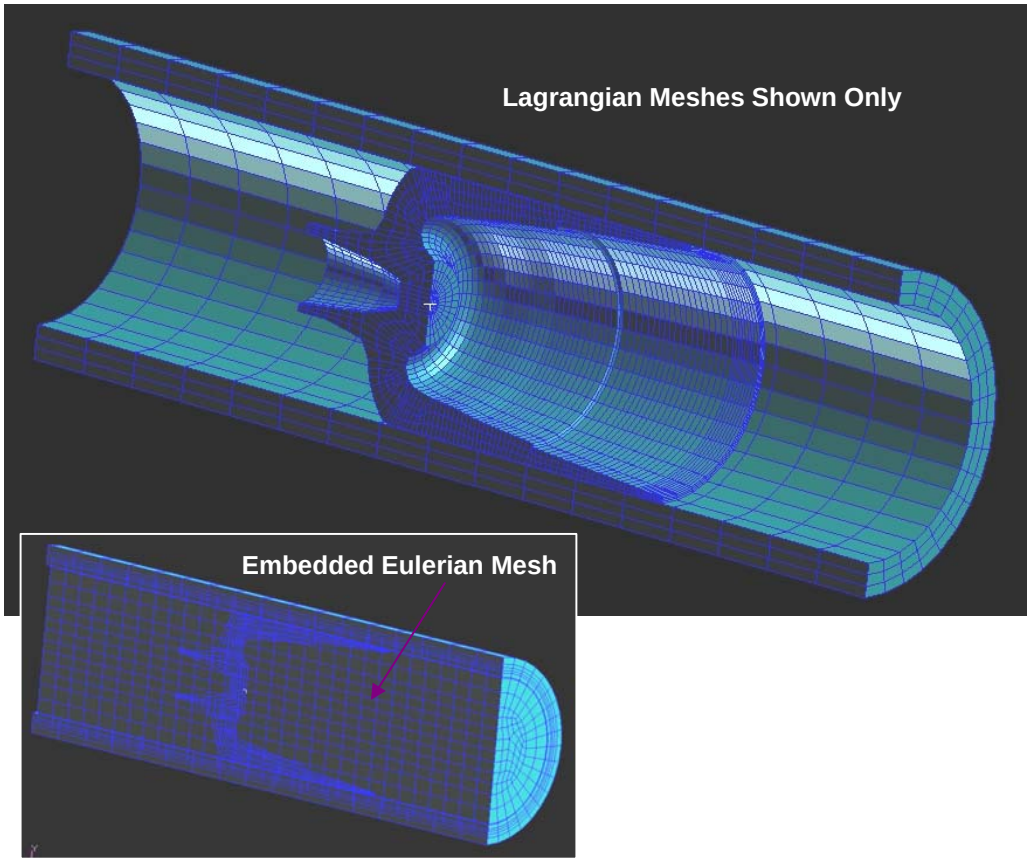

Figure 8.22 Sabot/Barrel Fluid Structure Interaction Model

Figure 8.23 contains the results which were obtained for this analysis. The plots depict the state of the sabot and barrel system at a series of increasing average pressures. The plots show that the sabot is successful in sealing the gas pressure in all instances as no build up of pressure is witnessed behind the sabot.

As the average pressure increased in the Eulerian elements, the stresses in the barrel approach the yield of the material. This result implies that the contact forces between sabot and barrel were well above that the maximum gas pressure.

Stresses in the sabot approached the material yield (532MPa), however, as the material was in compression, no significant plastic deformation was observed. Earlier in this Chapter, it was shown that this behaviour did not impact sabot ejection during the forward load case and was therefore not a concern.

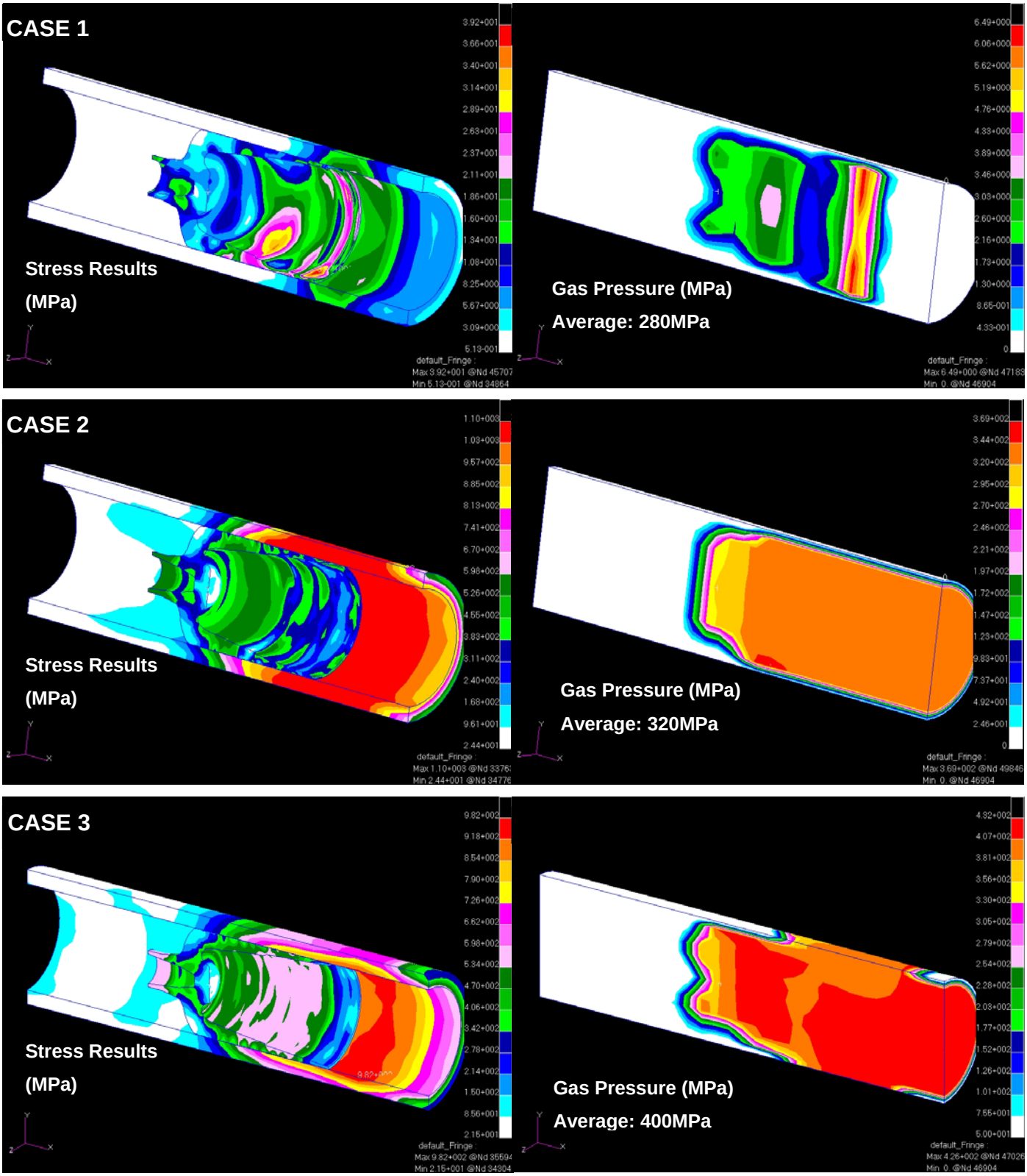

Figure 8.23 Sabot/Barrel Fluid Structure Interaction Results

8.6 Conclusion

In this chapter the results of an experimental study conducted to both validate the stacked HVFSDS round concept and the Virtual Design Process were presented. Subsequently, the entire VDP was again utilised in refining the HVFSDS round based on the results of physical testing.

The HVFSDS design concept was successfully tested using a test chamber designed and manufactured by DSTO. Only a limited amount of tests could be performed due to damage sustained by the test rig. However, these tests were able to provide enough justification to the design ideas and development methods adopted as apart of this research.

The testing results indicated that the titanium sabot was capable of sealing gas pressures up to 477MPa. This, however, did not represent a threshold value for the design. Further testing would be required to determine if the design was capable of sealing the intended gas pressure of 546MPa in order to satisfy the 30% overpressure condition.

The titanium sabots, penetrators, locating fingers and high tensile steel supporting rods were largely undamaged by the tests. Some shearing of the sabot teeth occurred when the sabot was able to slip inside the insert, however, the damage was minor and did not compromise the seal. In addition, grooving of insert walls resulted from contact with the teeth. If an interchangeable insert is not to be used in future design iterations, then this behaviour would require close attention.

Based on the results, it was decided that a hard barrel design, eliminating the requirement for an interchangeable insert, would be the best solution. However, in order to achieve this solution, it was necessary to refine the sabot design to incorporate a supporting rod. The inclusion of the rod also allowed the sabot design to revert back to using aluminium.

Explicit FEA was used to design the rod such that it could distribute a portion of the load from the sealing sabot to aft rounds and into the gun breech. This was most necessary during the early stages of the blast until the sabot was able to expand and generate friction with the barrel. It was envisaged that the supporting rod would also be used to house the primer and ignition electronics of the round.

Shape optimisation was then used to further reduce the mass of the sabot bulkhead which was shown to endure only small amounts of stress with the inclusion of the supporting rod. Results of finite element analysis showed that the optimised round was able to meet necessary performance targets while staying within material tolerances. An unexpected, yet useful design feature was also discovered with regard to the separation of the supporting rod during the forward load case

The optimised sabot design was then used in an FSI simulation in which high gas pressures were used to test the effectiveness of the gas seal. The results showed that the sabot was capable of sealing pressures of over 400MPa without any sign of gas leakage.

9 Conclusions and Future Work

9.1 Conclusions

In this research, a VDP was presented for the design and development of a novel gun system containing multiple rounds in a single barrel which could be fired at high muzzle velocities. The VDP methodology was based on the integration of models derived from disciplines such as structural mechanics, fluid dynamics and shape optimisation. Its application was demonstrated through undertaking a case study of 16th Century Cannon in which modelling techniques such as Implicit and Explicit FEA, Fluid Structure Interaction (FSI) modelling and Shape Optimisation modelling were applied to analyse the design. The integrated models provided the capability to visualise the effect of changing one variable in the analysis over the entire system.

Analysis and evaluation of the 16th Century Cannon using the VDP revealed that implicit finite element methods were able to identify the stresses experienced by the cannon during firing. Implicit methods, however, were limited in their ability to assess the dynamic interaction of barrel and munitions as well as determining vital performance parameters such as muzzle velocity.

Explicit methods were therefore used to generate Von Mises stress data over the entire interior ballistic cycle of the cannon. Regions of high stress were identified in the chamber and muzzle regions. The studies also revealed gun system vibrations that would be detrimental to weapon accuracy. In comparison with implicit finite analysis, explicit methods were found to be superior for the study of tube launched weapon systems.

FSI modelling of the cannon system identified the lack of a material model to accurately simulate propellant combustion in the FE environment. Simulating a detonation inside the gun chamber using the JWL EOS was found to be unsuitable for this application. The analysis, however, demonstrated the potential for FSI to integrate the properties of the propellant and structural system into a single analysis. The application of Shape Optimisation modelling resulted in identifying structural deficiencies in the cannon structure with the possibility of reducing its overall mass and controlling muzzle vibrations during the interior ballistic cycle.

Subsequent to the cannon case study, an interior ballistic model proposed by Krier and Adams 1979 [13] was integrated into the MSC. Dytran Explicit Solver through a user subroutine. FSI modelling was then used to study the structural behaviour of components subject to the dynamics of propellant combustion.

The subroutine was further developed in order to allow for the combustion of propellant in an expanding volume. This required the dynamic introduction of new and originally void Eulerian elements into the analysis as they were filled by the combustion products. This allowed for a more realistic simulation of projectile acceleration using a set of known system parameters.

The developed VDP techniques were then advanced for the design and development of a gun system where multiple HVFSDS KE rounds could be loaded in a single barrel. The major design challenge was to develop a gun system where one or more rounds could be loaded and fired. This required the creation of robust sealing between the rounds from propellant gas pressures and also providing axial restraint for the firing of forward rounds.

Explicit finite element methods were used to develop a wide variety of design possibilities. Push and traction type sabots were assessed in detail, with the push type sabot proving to be a likely and more robust solution. Traction sabot designs possessing identical petals were eliminated early in the design process due to difficulties encountered in developing a gas seal. This was made evident in the proposed "Segmented Sabot Design" which required a complicated overlapped petal arrangement to seal combustion gasses.

Designs for push type sabots evolved through to "Rear Seal Designs". Analysis of early push type sabots revealed some interesting behaviour in terms of the rearward movement of the sabot. The idea of the Rear Seal Design was to utilise this rear movement to activate a "buckle zone" which would seal against the barrel. Numerous Rear Seal Designs were proposed possessing various iterations of the buckle zone, penetrator support mechanisms, and sabot cup profiles.

Concerns relating to the compression of rear propellant created by the rear movement of the Rear Seal Design initiated the "Cup Seal Design". While still retaining many original features, this design no

longer relied on the action of a buckle zone. Instead, it was intended that friction on the sabot cup possessing teeth would restrain the axial load and perform the gas seal. An analysis of material properties indicated that a titanium alloy needed to be used for the fabrication of the sabot as previous aluminium designs appeared incapable of sustaining the required loads in this configuration.

The sealing and restraint behaviour of the round was tested using hard and soft barrel options. It was found that the soft barrel would yield around the sabot teeth during sealing and provide the required performance. It was also shown that minor yielding of the barrel did not impede the sabot during the forward load. The limitation of the soft barrel option was that a separate barrel insert would be required with each set of rounds due to the sustained deformation.

The hard barrel option was also capable of generating a gas seal however significant rearward movement was experienced by the sabot at maximum pressure. The sliding of the cup in the barrel also caused vibrations which further reduced the ability of this option to provide sufficient axial restraint. The potential advantage of this combination was that a removable insert within the barrel was no longer necessary as no permanent barrel deformations were created.

Shape Optimisation modelling was applied to optimise the mass of the sabot cup and increase the magnitude of contact forces within the barrel. Based on these design outcomes, the Cup Seal Design was fabricated in order to conduct preliminary testing of the axial restraint and gas sealing mechanisms. These tests were conducted using a test chamber supplied by DSTO. Various configurations, including hard and soft barrel options, were proposed for testing. The forward load case was not tested in the experiment.

The results of the experiment showed that the Cup Seal Sabot, using a hard barrel, was capable of sealing gas pressures of up to 477MPa, however, some rearward sliding was observed as predicted by FEA. The sabot components were largely undamaged by the tests. Due to damage sustained by the test chamber, only a limited amount of tests were performed. However, sufficient data was obtained to validate and justify the design and development methods employed in this research.

Further design studies were undertaken to find a possible solution for the application of hard barrel with a view to eliminate the requirement for an interchangeable insert. Results of finite element modelling and physical testing showed that the sabot was unlikely to be retained by friction alone using this configuration. A sabot supporting structure was consequently developed to complement the sabot design.

Further analysis revealed that the sabot supporting structure was able to transfer loads from propellant combustion into aft rounds and into the gun breech. This added support was able to restrain the sabot movement in the early stages of the blast until the sabot was able to expand and generate significant friction with the barrel. The inclusion of the support structure also allowed the use of aluminium for the fabrication of both the sabot cup and support.

The optimised Cup Seal Sabot design was subjected to an FSI simulation. A high pressure gas was modelled using Eulerian elements inside the sabot cup to validate the sealing behaviour of the round. Results indicated that the modified sabot structure was capable of sealing gaseous pressures of over 400MPa without any sign of leakage.

These studies highlight that the VDP is a valuable tool for the design and analysis of complex systems. The integrated model was useful in providing a quick and inexpensive means to analyse and evaluate the design options in virtual mode before they are prototyped for testing.

9.2 Recommendations for Future Work

The FSI modelling presented in Chapter 5 successfully incorporated a model of interior ballistics into the explicit finite element environment. It was identified that the developed subroutine was stable for very simple geometries. However, model instability was encountered in cases possessing more sophisticated geometry profiles, rendering unrealistic results. More advanced methods of dynamically assigning properties to originally void Eulerian elements could be attempted to improve the stability of the solution. Further work is therefore required in improving the developed subroutine which would enable it to be directly applied to the development of advanced and novel tube launched weapons concepts.

The conceptual HVFSDS KE round design developed through this research requires further testing under live fire conditions to validate its behaviour in both the forward and rearward load cases as compared to that predicted using the VDP.

The design of the test program should be staged to ensure the structural integrity of components prior to the firing of multiple stacked rounds. Figure 9.1 illustrates the order of testing which should be undertaken. The propellant shown in red is combusted during the test. For the tests where multiple rounds are to be fired, the combustion of propellants should be staged such that the round closest to the muzzle is fired first and then so on. The rate of fire at which the tests are conducted would not be crucial initially whilst trying to demonstrate the integrity of the system. The propellant shown in blue is not combusted during the test. Rather, the propellant shown in blue is included to prove that pre-mature ignition, due to compaction or flash over, does not occur.

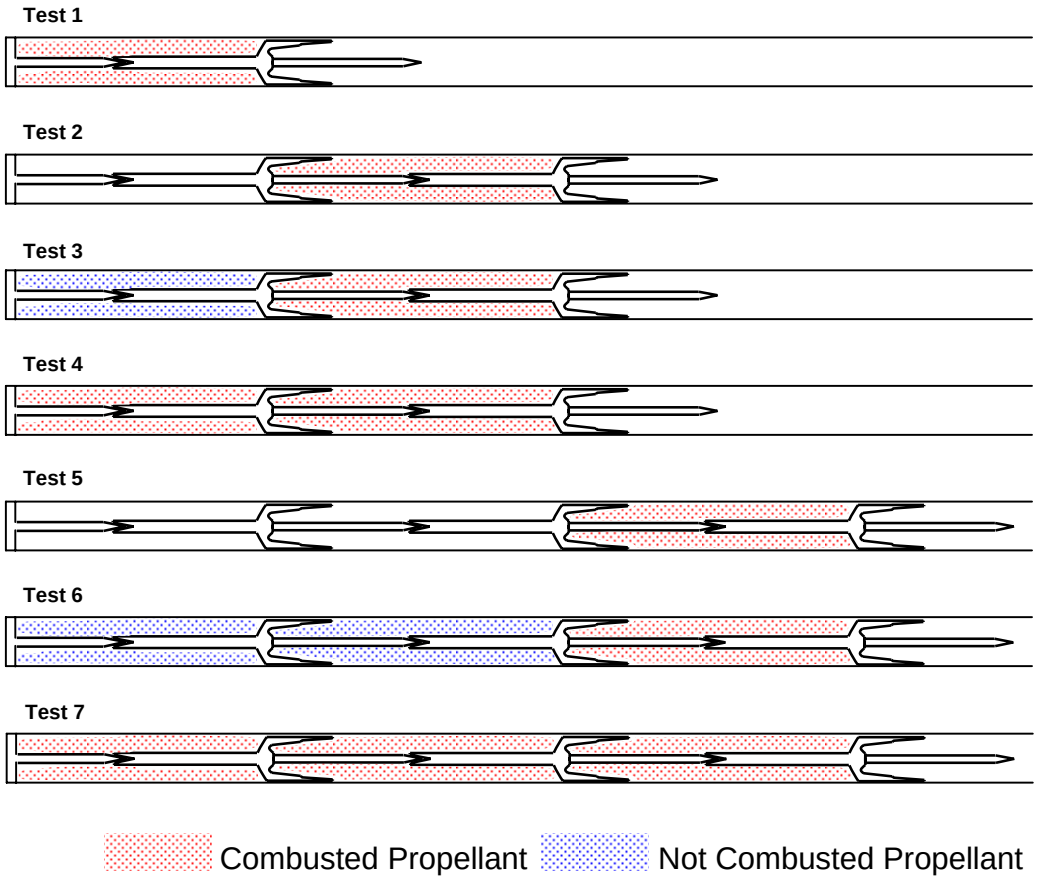

Figure 9.1: Proposed Test Plan for the Testing of Multiple Stacked Rounds inside a Gun Barrel.

It is recommended that some further design options should be considered prior to performing the live fire tests. Some of these options may include:

- Application of a combustible cartridge case (this may require minor alterations to the sabot cup for attachment).
- Detailed design studies of the supporting rod to enable insertion and protection of the primer and firing electronics.
- Detailed design of the penetrator to enable final design of supporting fingers.
- Design of the breach support for the last round.

Results of chamber testing, as presented in Chapter 8, provided reasonable confidence in the design methods. However, the more rigorous testing of firing multiple rounds from a gun barrel would result in further validation and justification of the application of VDP. This process could then be used with greater confidence in performing future design related tasks pertaining to tube launched weapons systems.

10 References

1. Su, D. and D. Qin, *Integration of numerical analysis, virtual simulation and finite element analysis for the optimum design of worm gearing.* Journal of Materials Processing Technology, 2003. **138**(1-3): p. 429-435.
2. Lye, S.W., S.G. Lee, and B.H. Chew, *Virtual design and testing of protective packaging buffers.* Computers in Industry, 2004. **54**(2): p. 209-221.
3. Queiroz, D.M., et al., *Simulation of the Dynamic of a Bean Harvester*. 2001, ASAE Paper No. 01-3148.
4. Kim, H.J., S.H. Park, and T.Y. Kwak. *Development of an Automatic Transplanter for Cabbage Cultivation*. in *Korean ADAMS User Conference*. 2001. Seoul, Korea.
5. Yan, T.Y., J.H. Chung, and Y.S. Choi, *Design of the Driving System of an Automatic Vacuum Packer using Functional Virtual Prototyping.* Biosystems Engineering, 2004. **89**(1): p. 37-46.
6. Altintas, Y. and Y. Cao, *Virtual Design and Optimization of Machine Tool Spindles.* CIRP Annals - Manufacturing Technology, 2005. **54**(1): p. 379-382.
7. Pathak, K.K. and M. Jha. *Structural Analysis of a Kinetic Energy Projectile for Medium Caliber Gun*. in *19th International Symposium of Ballistics*. 2001. Interlaken, Switzerland.
8. Pflegl, G.A., J.H. Underwood, and G.P. O'Hara, *Structural Analysis of a Kinetic Energy Projectile During Launch*. 1981, US Army Armament Research and Development Command: New York.
9. Hollis, M.S.L., *Use of finite-element stress analysis in the design of a tank-cannon-launched training projectile.* Computers in Engineering 1994. Finite Element Analysis. CAD/CAM, Fluid Mechanics and Energy Systems, Al/Feature-Based Design and Manufacturing, Computers in Engineering Education, Robotics and Controls, Multimedia Application/Interface. Proceedings. ASME. Part vol.2, 1994, 1994: p. 533-44 vol.
10. Rabern, D.A. and R.B. Parker, *Launch behavior of 60-mm pushed and traction driven saboted launch packages.* International Journal of Impact Engineering, 1995. **16**(1): p. 133-148.
11. Kloster, M.S., *Coupled Lagrangian and Eulerian approach to Detonation and Fragmentation Problems*. 2001, Naval Postgraduate School: Monterey, CA. p. 67.
12. Livermore, G. and L. Sadowski, *Barrel Weight Reduction*. 2005.

13. Krier, H. and M.J. Adams, *An Introduction to Gun Interior Ballistics and a Simplified Ballistic Code*, in *Interior Ballistics of Guns*. 1979, American Institute of Aeronautics and Astronautics: New York. p. 1-36.
14. Li, S.P., et al., *Research on the working mechanism and virtual design for a brush shape cleaning element of a sugarcane harvester.* Journal of Materials Processing Technology, 2002. **129**(1-3): p. 418-422.
15. Choi, W.C., D.C. Kim, and K.U. Kim. *Development of an Automatic Pick-up Mechanism for Plug Seedlings*. in *Korean ADAMS User Conference*. 2001. Seoul Korea.
16. Luo, J., et al., *Optimum tooling design for resin transfer molding with virtual manufacturing and artificial intelligence.* Composites Part A: Applied Science and Manufacturing, 2001. **32**(6): p. 877-888.
17. Yeh, T.-P. and J.M. Vance, *Combining MSC/NASTRAN, sensitivity methods, and virtual reality to facilitate interactive design.* Finite Elements in Analysis and Design, 1997. **26**(2): p. 161-169.
18. Whyte, J., et al., *From CAD to virtual reality: modelling approaches, data exchange and interactive 3D building design tools.* Automation in Construction, 2000. **10**(1): p. 43-55.
19. Hindman, C. and K.B. Ousterhout, *A virtual design system for sheet metal forming.* Journal of Materials Processing Technology, 1998. **84**(1-3): p. 107-116.
20. Kan, H.Y., V.G. Duffy, and C.-J. Su, *An Internet virtual reality collaborative environment for effective product design.* Computers in Industry, 2001. **45**(2): p. 197-213.
21. Lau, H.Y.K., K.L. Mak, and M.T.H. Lu, *A virtual design platform for interactive product design and visualization.* Journal of Materials Processing Technology, 2003. **139**(1-3): p. 402-407.
22. Cook, R.D., *Finite Element Modelling for Stress Analysis*. 1995, Toronto: John Wiley & Sons, Inc.
23. *MSC. Dytran Theory Manual Version 2005*. 2004, CA, USA: MSC. Software Corporation.
24. Drysdale, W.H. and B.P. Burns, *Structural Design of Projectiles*, in *Gun Propulsion Technology*, L. Stiefel, Editor. 1988, American Institute of Aeronautics and Astonautics: Washington.
25. Kim, S.-H., *Tool design for the tubular press forming of a rear suspension member with the finite element analysis.* Journal of Materials Processing Technology, 2007. **192-193**: p. 181-187.

26. Park, J., et al., *Application of FE analysis for optimal design of caulking process.* Journal of Materials Processing Technology, 2008. **198**(1-3): p. 471-477.
27. Song, J.H. and Y.T. Im, *Process design for closed-die forging of bevel gear by finite element analyses.* Journal of Materials Processing Technology, 2007. **192-193**: p. 1-7.
28. Demir, I., O. Kayabasi, and B. Ekici, *Probabilistic design of sheet-metal die by finite element method.* Materials & Design, 2008. **29**(3): p. 721-727.
29. Hur, K.D., Y. Choi, and H.T. Yeo, *A design method for cold backward extrusion using FE analysis.* Finite Elements in Analysis and Design, 2003. **40**(2): p. 173-185.
30. Koc, M. and M.A. Arslan, *Design and finite element analysis of innovative tooling elements (stress pins) to prolong die life and improve dimensional tolerances in precision forming processes.* Journal of Materials Processing Technology, 2003. **142**(3): p. 773-785.
31. Gil, B. and E. Bayo, *An alternative design for internal and external semi-rigid composite joints. Part II: Finite element modelling and analytical study.* Engineering Structures, 2008. **30**(1): p. 232-246.
32. Pokharel, N. and M. Mahendran, *Finite element analysis and design of sandwich panels subject to local buckling effects.* Thin-Walled Structures, 2004. **42**(4): p. 589-611.
33. Shuaeib, F.M., et al., *A new motorcycle helmet liner material: The finite element simulation and design of experiment optimization.* Materials & Design, 2007. **28**(1): p. 182-195.
34. Bennett, D. and T. Goswami, *Finite element analysis of hip stem designs.* Materials & Design, 2008. **29**(1): p. 45-60.
35. De Beule, M., et al., *Realistic finite element-based stent design: The impact of balloon folding.* Journal of Biomechanics, 2008. **41**(2): p. 383-389.
36. Kayabasi, O. and B. Ekici, *Probabilistic design of a newly designed cemented hip prosthesis using finite element method.* Materials & Design, 2008. **29**(5): p. 963-971.
37. Mansat, P., et al., *Evaluation of the glenoid implant survival using a biomechanical finite element analysis: Influence of the implant design, bone properties, and loading location.* Journal of Shoulder and Elbow Surgery, 2007. **16**(3, Supplement 1): p. S79-S83.
38. Drysdale, W.H., *Design of Kinetic Energy Projectiles for Structural Integrity*. 1981, US Army Armament Research and Development Command: Maryland.

39. Eches, N., N. Paugain, and C. Doffemont. *In-Bore Behaviour of Large Calibre Armour Piercing Fin Stabilised Discarding Sabot Projectiles*. in *20th International Symposium on Ballistics*. 2002. Orlando, Florida: DEStech Publications, Inc.
40. Wilkerson, S., D. Hopkins, and B. Held. *Techniques for Modelling Bullet Exit Conditions predicted by Transient Finite Element Models*. in *8th Symposium on Gun Dynamics*. 1996.
41. Gupta, A.D., *Evaluation of a fully assembled armored vehicle hull-turret model using computational and experimental modal analyses.* Computers & Structures, 1999. **72**(1-3): p. 177-183.
42. Cordes, J.A., D. Carlucci, and R. Jafar. *Dynamics of a Simplified 155-mm Projectile*. in *21st International Symposium on Ballistics*. 2004. Adelaide, South Australia.
43. Alyanak, E., et al., *Structural response and optimization of a supercavitating torpedo.* Finite Elements in Analysis and Design, 2005. **41**(6): p. 563-582.
44. Alyanak, E., R. Grandhi, and R. Penmetsa, *Optimum design of a supercavitating torpedo considering overall size, shape, and structural configuration.* International Journal of Solids and Structures, 2006. **43**(3-4): p. 642-657.
45. Yi, W., et al. *Vibration Analysis of Fin-Stabilized Sabot-Discarded Penetrator during Launching*. in *21st International Symposium on Ballistics*. 2004. Adelaide, South Australia.
46. Rabern, D.A., *Axial and lateral impulsive loading of kinetic energy projectiles during launch--part I. Experimental investigations.* International Journal of Impact Engineering, 1992. **12**(1): p. 49-64.
47. Rabern, D.A., *Axial and lateral impulsive loading of kinetic energy projectiles during launch--part II. Numerical simulations.* International Journal of Impact Engineering, 1992. **12**(1): p. 65-88.
48. Schmidt, E.M., B.J. Held, and D.S. Savick, *Hypervelocity launch dynamics.* International Journal of Impact Engineering, 1993. **14**(1-4): p. 619-630.
49. Allen, R.H., *Dynamic Responses of a Kinetic Energy Projectile under Transverse Loadings.* International Journal of Impact Engineering, 1995. **16**(1): p. 119-132.
50. Shoji, S. and K. Hino. *Transitional Motion of KE Projectiles and Governing Factors on Jump*. in *19th International Symposium of Ballistics*. 2001. Interlaken, Switzerland.
51. Tomas, J., *ReSHAPE User's Manual*. Version 98a ed. 2003, Melbourne: Advea Engineering Pty. Ltd.

52. Barbieri, R. and N. Barbieri, *Finite element acoustic simulation based shape optimization of a muffler.* Applied Acoustics, 2006. **67**(4): p. 346-357.
53. Hyun, S., et al., *An efficient shape optimization method based on FEM and B-spline curves and shaping a torque converter clutch disk.* Finite Elements in Analysis and Design, 2004. **40**(13-14): p. 1803-1815.
54. Lanzi, L., L.M.L. Castelletti, and M. Anghileri, *Multi-objective optimisation of composite absorber shape under crashworthiness requirements.* Composite Structures, 2004. **65**(3-4): p. 433-441.
55. Kayabasi, O. and B. Ekici, *The effects of static, dynamic and fatigue behavior on three-dimensional shape optimization of hip prosthesis by finite element method.* Materials & Design, 2007. **28**(8): p. 2269-2277.
56. Nicolella, D.P., et al., *The effect of three-dimensional shape optimization on the probabilistic response of a cemented femoral hip prosthesis.* Journal of Biomechanics, 2006. **39**(7): p. 1265-1278.
57. Tovar, A., et al., *Optimum design of an interbody implant for lumbar spine fixation.* Advances in Engineering Software, 2005. **36**(9): p. 634-642.
58. McLachlan, N., B.K. Nigjeh, and P. Trivailo. *Application of Modal Analysis to Musical Bell Design*. in *AAS Acoustics 2002*. 2002. Adelaide, South Australia.
59. Sorensen, B., *Design, Analysis, and Verification of a 50-mm Push/Traction Sabot*. 2000, US Army Research Laboratory: Maryland. p. 1-29.
60. Relvas, A. and A. Suleman, *Fluid-structure interaction modelling of nonlinear aeroelastic structures using the finite element corotational theory.* Journal of Fluids and Structures, 2006. **22**(1): p. 59-75.
61. Kamakoti, R. and W. Shyy, *Fluid-structure interaction for aeroelastic applications.* Progress in Aerospace Sciences, 2004. **40**(8): p. 535-558.
62. Zwaan, R.J. and B.B. Prananta, *Fluid/structure interaction in numerical aeroelastic simulation.* International Journal of Non-Linear Mechanics, 2002. **37**(4-5): p. 987-1002.
63. Ribet, H., P. Laborde, and M. Mahe, *Numerical modeling of the impact on water of a flexible structure by explicit finite element method -- Comparisons with Radioss numerical results and experiments.* Aerospace Science and Technology, 1999. **3**(2): p. 83-91.

64. Lam, K.Y., Q.X. Wang, and Z. Zong, *A Nonlinear Fluid-Structure Interaction Analysis of a Near-Bed Submarine Pipeline in a Current.* Journal of Fluids and Structures, 2002. **16**(8): p. 1177-1191.

65. McCoy, R.W. and C.T. Sun, *Fluid-structure interaction analysis of a thick-section composite cylinder subjected to underwater blast loading.* Composite Structures, 1997. **37**(1): p. 45-55.

66. Rabczuk, T., E. Samaniego, and T. Belytschko, *Simplified model for predicting impulsive loads on submerged structures to account for fluid-structure interaction.* International Journal of Impact Engineering, 2007. **34**(2): p. 163-177.

67. Anghileri, M., L.-M.L. Castelletti, and M. Tirelli, *Fluid-structure interaction of water filled tanks during the impact with the ground.* International Journal of Impact Engineering, 2005. **31**(3): p. 235-254.

68. Lu, C.H., Y.S. He, and G.X. Wu, *Coupled Analysis of Nonlinear Interaction between Fluid and Structure during Impact.* Journal of Fluids and Structures, 2000. **14**(1): p. 127-146.

69. van Loon, R. and S.J. Sherwin, *A fluid-structure interaction model of the aortic heart valve.* Journal of Biomechanics, 2006. **39**(Supplement 1): p. S293-823.

70. van Loon, R., P.D. Anderson, and F.N. van de Vosse, *A fluid-structure interaction method with solid-rigid contact for heart valve dynamics.* Journal of Computational Physics, 2006. **217**(2): p. 806-823.

71. van Loon, R., et al., *A three-dimensional fluid-structure interaction method for heart valve modelling.* Comptes Rendus Mecanique, 2005. **333**(12): p. 856-866.

72. Torii, R., et al., *Computer modeling of cardiovascular fluid-structure interactions with the deforming-spatial-domain/stabilized space-time formulation.* Computer Methods in Applied Mechanics and Engineering, 2006. **195**(13-16): p. 1885-1895.

73. Carmody, C.J., et al., *An approach to the simulation of fluid-structure interaction in the aortic valve.* Journal of Biomechanics, 2006. **39**(1): p. 158-169.

74. Canic, S., A. Mikelic, and J. Tambaca, *A two-dimensional effective model describing fluid-structure interaction in blood flow: analysis, simulation and experimental validation.* Comptes Rendus Mecanique: Fluid-solid interactions: modeling, simulation, bio-mechanical applications, 2005. **333**(12): p. 867-883.

75. Wolters, B.J.B.M., et al., *A patient-specific computational model of fluid-structure interaction in abdominal aortic aneurysms.* Medical Engineering & Physics: Advances in the finite element modelling of soft tissue deformation, 2005. **27**(10): p. 871-883.
76. Gerbeau, J.-F., M. Vidrascu, and P. Frey, *Fluid-structure interaction in blood flows on geometries based on medical imaging.* Computers & Structures: Advances in Analysis of Fluid Structure Interaction, 2005. **83**(2-3): p. 155-165.
77. De Hart, J., et al., *A computational fluid-structure interaction analysis of a fiber-reinforced stentless aortic valve.* Journal of Biomechanics: Cardiovascular Biomechanics, 2003. **36**(5): p. 699-712.
78. *LS-DYNA User's Manual - Nonlinear Dynamic Analysis of Structures*. 1999, California: Livermore Software Technology Corporation.
79. Cooper, P.W., *Explosives Engineering*. 1996, Canada: Wiley-VCH.
80. Johnston, I.A., *The Nobel-Abel Equation of State: Thermodynamic Derivations for Ballistics Modelling*. 2005, Defence Science and Technology Organisation: Edinburgh, South Australia.
81. Papliski, A., Z. Leciejewski, and Z. Surma. *About Thermodynamical Adjustment of the Nobel-Abel Equation of State*. in *21st International Symposium on Ballistics*. 2004. Adelaide, South Australia: Defence Science and Technology Organisation.
82. Heiser, R. *Predictions of the Performance of Modern Interior Ballistics Propulsion Systems by Standard Codes*. in *18th International Symposium on Ballistics*. 1999. San Antonio, Texas: Technomic Publishing Company, Inc.
83. Newill, J.F., M.J. Nusca, and A.W. Horst. *Advances in Coupled Projectile-Dynamics/Interior-Ballistics Simulations: Coupling the DYNA3D and the ARL-NGEN3 Code*. in *21st International Symposium on Ballistics*. 2004. Adelaide, South Australia: Defence Science and Technology Organisation.
84. Nusca, M.J. *Computational Fluid Dynamics Model of Multiphase Flows applied to Solid Propellant Combustion in Gun Systems*. in *18th International Symposium on Ballistics*. 1999. San Antonio, Texas: Technomic Publishing Company, Inc.
85. Ritchie, S.J., P.D. Lusk, and J.K. Domen. *Performance Prediction of 120mm Gun Propellants with a Ballistic Simulator*. in *18th International Symposium on Ballistics*. 1999. San Antonio, Texas: Technomic Publishing Company, Inc.

86. Pocock, M.D., P.M. Locking, and C.C. Guyott. *Effect of Statistical Variation in Grain Geometry on Internal Ballistics Modelling*. in *21st International Symposium on Ballistics*. 2004. Adelaide, South Australia: Defence Science and Technology Organisation.

87. Dayan, Y. and A. Pila. *Simulation of Combustion through Granulated Propellants in a 105mm Gun Barrel including Two Different Ignition Configurations*. in *21st International Symposium on Ballistics*. 2004. Adelaide, South Australia: Defence Science and Technology Organisation.

88. Woodley, C.R. *The Roles of Gun Propellant Properties in Attaining High Velocities*. in *21st International Symposium on Ballistics*. 2004. Adelaide, South Australia: Defence Science and Technology Organisation.

89. Woodley, C.R., P.S. Henning, and D.H. Walker. *Experimental and Modelling Studies of Composite Gun Propellants*. in *21st International Symposium on Ballistics*. 2004. Adelaide, South Australia: Defence Science and Technology Organisation.

90. Dupuis, A. and C. Berner. *Aerodynamic Aspects of Fin Geometries on a Lattice Finned Projectile*. in *20th International Symposium on Ballistics*. 2002. Orlando, Florida: DEStech Publications, Inc.

91. Cordes, J.A. and P.E. Reinhardt. *The Rise and Fall of Temperature in a Gun Tube due to Multiple Gun-Firings*. in *21st International Symposium on Ballistics*. 2004. Adelaide, South Australia: Defence Science and Technology Organisation.

92. Boisson, D. *Breach Heating and Cooling in a 155mm-52 Calibre Gun Barrel: Calculation and Experimental Investigation*. in *21st International Symposium on Ballistics*. 2004. Adelaide, South Australia: Defence Science and Technology Organisation.

93. Corner, J., *Theory of the Interior Ballistics of Guns*. 1950, New York: John Wiley and Sons, INC.

94. Calvert, J.B. *Cannons and Gunpowder*. [Website] 2000 18/03/2004 [cited; http://www.du.edu/~jcalvert/tech/cannon.htm]. Available from: http://www.du.edu/~jcalvert/tech/cannon.htm.

95. Sasse, R.A., *Black Powder*, in *Gun Propulsion Technology*. 1988, American institute of Aeronautics and Astronautics: USA. p. 35-58.

96. Guilmartin, J.F., *Gunpowder and Galleys*. 1974, London: Cambridge University Press.

97. Pike, J. *Big Bullets for Beginners*. [Website] 2005 27/04/2005 [cited; http://www.globalsecurity.org/military/systems/munitions/bullets2.htm]. Available from: http://www.globalsecurity.org/military/systems/munitions/bullets2.htm.

98. Varney, A.M., *Primers and Igniters*, in *Gun Propulsion Technology*, L. Stiefel, Editor. 1988, American Institute of Aeronautics and Astonautics: Washington.

99. Potapov, V. *Definitions of Soviet Ammunition*. The Russian Battlefield 1998 [cited; http://www.battlefield.ru/index.php?option=com_content&task=category&sectionid=10&id=44&Itemid=64&lang=en]. Available from: http://www.battlefield.ru/index.php?option=com_content&task=category&sectionid=10&id=44&Itemid=64&lang=en.

100. *MSC. Dytran User's Guide Version 2005*. 2004, CA, USA: MSC. Software Corporation.

101. Tomas, J., *ReSHAPE Theory Manual Version d02*. 2002, Melbourne, Australia: ADVEA Engineering Pty. Ltd.

102. Tomas, J., *Starting with ReSHAPE*. 2002, Melbourne, Australia: ADVEA Engineering Pty. Ltd.

103. Hall, B.S., *The Corning of Gunpowder and the Development of Firearms in the Renaissance*, in *Gunpowder: The History of an International Technology*. 1996, Bath University Press: UK.

104. Suceska, M., *Evaluation of Detonation Energy from EXPLO5 Computer Code Results.* Propellants, Explosives, Pyrotechnics, 1999. **24**: p. 280-285.

105. Lee, E., M. Finger, and W. Collins, *JWL Equation of State Corfficients for High Explosives UCID-16189* 1973, Lawrence Livermore Laboratory: California.

106. Tomas, J., *ReSHAPE Reference Manual Version d02*. 2002, Melbourne, Australia: ADVEA Engineering Pty. Ltd.

107. Buckmaster, J., et al., *Response of a burning heterogeneous propellant to small pressure disturbances.* Proceedings of the Combustion Institute, 2005. **30**(2): p. 2079-2086.

108. Zhou, X., T.L. Jackson, and J. Buckmaster, *Oscillations in propellant flames with edges.* Combustion and Flame, 2003. **133**: p. 157-168.

109. Massa, L., et al., *Exploring propellant science using a fully coupled combustion code (AIAA Paper No. 2003-1165)*, in *41th Aerospace Sciences Meeting & Exhibit*. 2003: Reno, Nevada.

110. Tsangalis, C., N. McLachlan, and P. Trivailo, *Fluid-Structure Interaction Modelling of Propellant Combustion.* Australian and New Zealand Industrial and Applied Mathematics Journal, 2006. **47**: p. C388-C403.

111. Guidos, B.J. and G.R. Cooper. *Model of KE Projetile Motion subjected to a Simple In-Flight Lateral Control Impulse*. in *18th International Symposium on Ballistics*. 1999. San Antonio, Texas: Technomic Publishing Company, Inc.

112. Newill, J.F., et al. *Simulation of the M865 Kinetic Energy Projectile with Experimental Validation*. in *18th International Symposium on Ballistics*. 1999. San Antonio, Texas: Technomic Publishing Company, Inc.

113. Hasslid, J.G. *Analysis and Reduction of Dispersion caused by Intermediate Ballistics Behaviour for an Optimized Medium Calibre APFSDS-T*. in *18th International Symposium on Ballistics*. 1999. San Antonio, Texas: Technomic Publishing Company, Inc.

114. Newill, J.F., et al. *Launch Dynamics of the 120-mm XM1002 Target Practice Training Multipurpose Projectile (TPMP-T)*. in *20th International Symposium on Ballistics*. 2002. Orlando, Florida: DEStech Publications, Inc.

115. Worst, D.W. *An APFSDS Kinetic Energy Practice Round*. in *21st International Symposium on Ballistics*. 2004. Adelaide, South Australia: Defence Science and Technology Organisation.

116. Bless, S., et al. *Reverse Impact Results for Yawed Long Rods Perforating Oblique Plates*. in *18th International Symposium on Ballistics*. 1999. San Antonio, Texas: Technomic Publishing Company, Inc.

117. Hohler, V. and T. Behner. *Influence of the Yaw Angle on the Performance Reduction of Long Rod Projectiles*. in *18th International Symposium on Ballistics*. 1999. San Antonio, Texas: Technomic Publishing Company, Inc.

118. Heider, N., K. Weber, and P. Weidemaier. *Experimental and Numerical Simulation Analysis of the Impact Process of Structured KE Penetrators onto Semi-Infinite and Oblique Plate Targets*. in *21st International Symposium on Ballistics*. 2004. Adelaide, South Australia: Defence Science and Technology Organisation.

119. Lundberg, P., et al. *Replica Modelling Experiments with Long Rod Penetrators Hitting Oblique Plates: Influence of Scale and Experimental Deviations*. in *21st International Symposium on Ballistics*. 2004. Adelaide, South Australia: Defence Science and Technology Organisation.

120. Borrmann, M., I. Becker, and R. Tewes. *Influence of Vibrations on the Penetration Efficiency of Long-Rod Penetrators*. in *18th International Symposium on Ballistics*. 1999. San Antonio, Texas: Technomic Publishing Company, Inc.

121. Asprey, R.J. and M.R. Edwards. *Tungsten as a Penetrator Material*. in *18th International Symposium on Ballistics*. 1999. San Antonio, Texas: Technomic Publishing Company, Inc.

122. Xu, S., et al. *Mechanism Study of the Penetration of Long Rod Projectiles of Torqued Tungsten Alloy*. in *18th International Symposium on Ballistics*. 1999. San Antonio, Texas: Technomic Publishing Company, Inc.

123. Chan, V., et al. *Resistance to Dynamic Frature of Tungsten Alloys determined by a New Test Technique*. in *18th International Symposium on Ballistics*. 1999. San Antonio, Texas: Technomic Publishing Company, Inc.

124. Gee, D.J. *Numerical Experiments with Jacketed Projectiles*. in *21st International Symposium on Ballistics*. 2004. Adelaide, South Australia: Defence Science and Technology Organisation.

125. Kaufmann, H., et al. *Ballistic Performance of Monoblock and Jacketed Medium-Caliber Penetrators against Composite Armor and Spaced Targets*. in *21st International Symposium on Ballistics*. 2004. Adelaide, South Australia: Defence Science and Technology Organisation.

126. Leeming, D.W. and M. Rigby. *An Analysis of the Penetration Performance of Long Rod Projectiles with Various Sleeving Materials*. in *20th International Symposium on Ballistics*. 2002. Orlando, Florida: DEStech Publications, Inc.

127. Lanz, W. and H. Kaufmann. *Comparison of L/D=21.5 Standard and L/D=40 Jacketed Penetrators in Composite Armour*. in *20th International Symposium on Ballistics*. 2002. Orlando, Florida: DEStech Publications, Inc.

128. Ernst, H.J., et al. *Temperature Influence on Long-Rod Penetration*. in *21st International Symposium on Ballistics*. 2004. Adelaide, South Australia: Defence Science and Technology Organisation.

129. Yaziv, D., Y. Reifen, and G. Gans. *The Penetration Process of Long Rods at Interfaces between Materials*. in *21st International Symposium on Ballistics*. 2004. Adelaide, South Australia: Defence Science and Technology Organisation.

130. Sahu, J., K.R. Heavey, and E.N. Ferry, *Computational modeling of multibody aerodynamic interference.* Advances in Engineering Software, 1998. **29**(3-6): p. 383-388.

Appendix A

MATLAB CODE: Solving Krier and Adams 1979 Ballistic Model [13]

```
E0 = [1e-2; 0; 0];                          % initial conditions

t0 = 0;
tmax  = 0.003;
tstep = 0.0001;
tspan = [t0:tstep:tmax];

[t,E]=ode45('ssp_ball_Con',tspan, E0);


ball_plot_Con;
```

File: ssp_ball_Con

```
function ydot=ssp_xdot(t,y)

x = y(1);
Vp = y(2);
s= y(3);

beta=0;
gamma=0;
Ball_Constants_Con;


%**********************************
% Calculate Fraction of Charge Burnt
%**********************************

Z=((2*((c*L)+d)*x)-(((L*(1-nperf))+(4*c))*(x^2))+(2*(1-nperf)*(x^3)))/(L*d);


%*******************************
% Calculate Total Chamber Volume
%*******************************

VCt=VCo1+(As*s)-(C*((1/rho_s)+(Z*(cvol-(1/rho_s)))))


%*******************************
% Calculate Average Gas Pressure
%*******************************

ME=Ws+((C*Z)/3);

PA=((lamda*C*Z)-((gamma-1)*(1+beta)*(ME*(Vp^2)/2)))/VCt
```

```
%********************
% Pressure Conversion
%********************

fact=(1+(((gamma-1)/2)*((Vp^2)/(gc*lamda))))^((-gamma)/(gamma-1));

PB=PA*fact;

ydot(1,1) = B*PA^n;
ydot(2,1) = (Rd*(PB*As*((cos(theta))-(Cf*(sin(theta))))-Fd))/((Ws*Rd*((cos(theta))-
      (Cf*(sin(theta)))))+(I*k*((sin(theta))+(Cf*cos(theta)))));
ydot(3,1) = Vp;
```

File: Ball_Constants_Con

```
%**********************
% Propellant Properties
%**********************

L=6.13;                                 %[mm]       Grain Length
Dgr=3.12;                               %[mm]       Grain Diameter
Rgr=Dgr/2;                              %[mm]       Grain Radius

nperf=1;                                Number of Propellant Perforations
perf_d=0.51;                            %[mm]       Perf Diameter
perf_r=perf_d/2;                        %[mm]       Perf Radius
web_d=(Dgr-(3*perf_d))/4;               %[mm]       Web Diameter

rho_s=1.45e-9;                          %[t/mm^3]   Solid Propellant Density
C=0.00005;                              %[t]        Charge Weight

%**********************************
% Gun/Projectile Physical Properties
%**********************************

bore_diam=73.46;                                %[mm]
bore_rad=bore_diam/2;                           %[mm]
barrel_length=1315;                             %[mm]


Chamb_length=(C/((rho_s/2)*pi*(bore_rad^2));    %[mm]
As=pi*((bore_rad)^2);                           %[mm^2]     Bore Cross-Sect Area
VCo1=As*Chamb_length*1.6                        %[mm^3]     Initial Chamber Volume
beta=0;                                         %           Heat Loss Adjustment

Ws=0.0004;                                      %[t]        Projectile Weight

Rd=29.96/2;                                     %[mm]       Radius of Projectile
theta=0;                                        %[deg]      Twist (of rifling)
Cf=0.2;                                         %           Sliding Friction Coef
k=0 ;                                           %[rad/mm]   Rotational Constant
I=0;                                            %           Axial Moment of Inertia
```

```
%***************
% Gas Properties
%***************

gamma=1.2582;                                   %           Specific Heat Ratio
lamda=9.41e11;                                  %[mJ/t]     Force Constant
R=364.5e6;                                      %[mJ/t/K]   Gas Constant
cvol=1.06e9;                                    %[mm^3/t]   Gas Covolume


%****************
% Burn Properties
%****************

tempF=2561;                                     %[K]        Flame Temp
B=0.732;                                        %[mm/s]     Burn Rate Coef
n=0.952;                                        %[For MPa]  Burn Rate Exponent

c=Rgr+(nperf*perf_r);
d=((Rgr^2)-(nperf*(perf_r^2)));
```

File: ball_plot_Con

```
%*************************
% Calculate Output Matrices
%*************************

Ball_Constants_Con;

Zm=((2*((c*L)+d).*(E(:,1)))-(((L*(1-nperf))+(4*c)).*((E(:,1)).^2))+(2*(1-
      nperf).*((E(:,1)).^3)))/(L*d);

VCtm=VCo1+(As.*(E(:,3)))-(C*((1/rho_s)+((Zm(:,1)).*(cvol-(1/rho_s)))));

MEm=Ws+((C.*(Zm(:,1))./3);

PAm=((lamda*C.*(Zm(:,1)))-((gamma-
      1)*(1+beta).*((MEm(:,1)).*((E(:,2)).^2)/2))./(VCtm(:,1));

factm=(1+(((gamma-1)/2).*(((E(:,2)).^2)/(gc*lamda)))).^((-gamma)/(gamma-1));

PBm=PAm.*factm;


%******
% Plots
%******

figure(1)                                       %Grain Recession Plot
plot(t, E(:,1), 'r-')
grid on
xlabel('Time, [s]');
ylabel('Linear Grain Recession, [mm]');
title('Grain Recession vs Time');
```

```
figure(2)                                          %Projectile Velocity Plot
plotyy(t, E(:,2), t, E(:,3))
grid on
xlabel('Time, [s]');
ylabel('Projectile Velocity, [mm/s]');
title('Projectile Velocity and Displacement vs Time');

figure(3)                                          %Average Pressure Plot
plot(t, PAm(:,1), 'g-')
grid on
xlabel('Time, [s]');
ylabel('Pressure, [MPa]');
title('Pressure vs Time');
hold on
                                                   %Base Pressure Plot
plot(t, PBm(:,1), 'b:')
hold off
```

Appendix B

MSC. Dytran Subroutine: EXEOS User Defined Equation of State

Combustion in a Constant Volume

```
      SUBROUTINE EXEOS(CNAME,LENNAM,ISTART,IEND,RHO,DV,DEVIS,XMASS,
     +                         FBURN,POLD,SIEOLD,PNEW,SIENEW,CLNEW,GRUNGM)
*
*     single or double defined below
      IMPLICIT DOUBLE PRECISION (A-H,O-Z)
*
*
      SAVE
*
*     declare argument as arrays and data-type here....
*
      CHARACTER*(*) CNAME
      CHARACTER*16 CVRNAM
      PARAMETER ( NENT = 128 )
*
*     local dimensions and declarations
*
      DIMENSION RHO(*),DV(*),DEVIS(*)
      DIMENSION XMASS(*),FBURN(*),POLD(*),SIEOLD(*)
      DIMENSION PNEW(*),SIENEW(*),CLNEW(*),GRUNGM(*)
      DIMENSION ZF(NENT),XL(NENT)
*
*
      COMMON /MSCD_XCYVAR/ XB0013,DLTH,DLTB,DTMIN,FRAT,
     +                      TIME,TIMB,DLTFH,DLTMAX,DTWRAP,TIMH,
     +                      TIMLIM,DZONDT,DLTE,DLTFE,DTSHL,DLEN,
     +                      XE0013
*
*
*     Variables
*
************************************************
*     Propellant Properties
************************************************
*
      GL=6.13                       !Grain Length [mm]
      Dgr=3.12                      !Grain Diameter [mm]
      Rgr=Dgr/2                     !Grain Radius [mm]
*
      nperf = 1                     !Number of Perforations
      perf_d = 0.51                 !Perf Diameter [mm]
      perf_r = perf_d/2             !Perf Radius [mm]
      web_d=(Dgr-(3*perf_d))/4      !Web Diameter [mm]
      rho_s=1.45e-9                 !Solid Propellant Density [t/mm^3]
```

```
      c=Rgr+(nperf*perf_r)
      d=((Rgr**2)-(nperf*(perf_r**2)))
*
************************************************
*     Gas Properties
************************************************
*
      gamma=1.2582                  !Specific Heat Ratio
      specf=9.41e11                 !Force Constant (Impetus) [mJ/t]
      R=364.5e6                     !Gas Constant [mJ/t/K]
      cvol=1.06e9                   !Gas Covolume [mm^3/t]
*
*
************************************************
*     Burn Properties
************************************************
*
      B=0.732                       !Burn Rate Coefficient [mm/s]
      EXP=0.952                     !Burn Rate Exponent [For MPa]
*
      RELV=2207.16
*
      TEMP=2576
*
*
************************************************
*     Loop Calculations
************************************************
*
*
      DO 100 NZ = ISTART, IEND
*
*
        IF (TIME == DLTH) THEN
          XL(NZ)=0.1
*
*
**********************
*     INITIAL LOOP
**********************
*
*
*     Calculate Burn Fraction
************************************************
*
          ZF(NZ)=((2*((c*GL)+d)*XL(NZ))-(((GL*(1-nperf))+(4*c))*
     +         ((XL(NZ))**2))+(2*(1-nperf)*((XL(NZ))**3)))/(GL*d)
*
*
*     Calculate New Pressure
************************************************
*
          PNEW(NZ)=(specf*XMASS(NZ)*ZF(NZ))/(RELV-
     +          ((XMASS(NZ)/rho_s)*(1-ZF(NZ)))-(cvol*ZF(NZ)*XMASS(NZ)))

*
*
```

```
*     Calculate New XB
*********************************************
*
          XL(NZ)=XL(NZ)+DLTH*B*(PNEW(NZ))**EXP
*
        END IF
*
*
*
*
**********************
*     MAIN LOOP
**********************
*
*
        IF (TIME > DLTH) THEN
*
*
*******************************
*      EXISTING ELEMENTS
*******************************
*
*
            IF (ZF(NZ) >= 1) THEN
*
               PNEW(NZ) = POLD(NZ)
*
            END IF
*
*
            IF (ZF(NZ) >= 1) GOTO 999

*
*
          IF (XL(NZ) > 0.1) THEN
*
*
*     Calculate Burn Fraction
*********************************************
*
            ZF(NZ)=((2*((c*GL)+d)*XL(NZ))-(((GL*(1-nperf))+(4*c))*
     +           ((XL(NZ))**2))+(2*(1-nperf)*((XL(NZ))**3)))/(GL*d)
*
*
*     Calculate New Pressure
*********************************************
*
            PNEW(NZ)=(specf*XMASS(NZ)*ZF(NZ))/(RELV-
     +            ((XMASS(NZ)/rho_s)*(1-ZF(NZ)))-(cvol*ZF(NZ)*XMASS(NZ)))
*
*
*
*     Calculate New XB
*********************************************
*
            XL(NZ)=XL(NZ)+DLTH*B*(PNEW(NZ))**EXP
*
```

```
          END IF
*
*
*********************************
*     NEW ELEMENTS
*********************************
*
*
          IF (XL(NZ) <= 0.1) THEN
            XL(NZ) = (XL(NZ-25)+XL(NZ-50))/2
*
*     Calculate Burn Fraction
*********************************************
*
            ZF(NZ)=((2*((c*GL)+d)*XL(NZ))-(((GL*(1-nperf))+(4*c))*
     +           ((XL(NZ))**2))+(2*(1-nperf)*((XL(NZ))**3)))/(GL*d)
*
*
*     Calculate New Pressure
*********************************************
*
            PNEW(NZ)=(specf*XMASS(NZ)*ZF(NZ))/(RELV-
     +            ((XMASS(NZ)/rho_s)*(1-ZF(NZ)))-(cvol*ZF(NZ)*XMASS(NZ)))
*
*
*
*     Calculate New XB
*********************************************
*
            XL(NZ)=XL(NZ)+DLTH*B*(PNEW(NZ))**EXP
*
          END IF
*
*
999   CONTINUE
*
*
        END IF
*
*
100   CONTINUE
*

      RETURN
      END
```

Appendix C

MSC. Dytran Subroutine: EXEOS User Defined Equation of State

Combustion in an Expanding Volume

```
      SUBROUTINE EXEOS(CNAME,LENNAM,ISTART,IEND,RHO,DV,DEVIS,XMASS,
     +                         FBURN,POLD,SIEOLD,PNEW,SIENEW,CLNEW,GRUNGM)
*
*     single or double defined below
      IMPLICIT DOUBLE PRECISION (A-H,O-Z)
*
*
      SAVE
*
*     declare argument as arrays and data-type here....
*
      CHARACTER*(*) CNAME
      CHARACTER*16 CVRNAM
      PARAMETER ( NENT = 128 )
*
*     local dimensions and declarations
*
      DIMENSION RHO(*),DV(*),DEVIS(*)
      DIMENSION XMASS(*),FBURN(*),POLD(*),SIEOLD(*)
      DIMENSION PNEW(*),SIENEW(*),CLNEW(*),GRUNGM(*)
      DIMENSION ZF(NENT),XL(NENT)
*
*
      COMMON /MSCD_XCYVAR/ XB0013,DLTH,DLTB,DTMIN,FRAT,
     +                      TIME,TIMB,DLTFH,DLTMAX,DTWRAP,TIMH,
     +                      TIMLIM,DZONDT,DLTE,DLTFE,DTSHL,DLEN,
     +                      XE0013
*
*
*     Variables
*
************************************************
*     Propellant Properties
************************************************
*
      GL=6.13                       !Grain Length [mm]
      Dgr=3.12                      !Grain Diameter [mm]
      Rgr=Dgr/2                     !Grain Radius [mm]
*
      nperf = 1                     !Number of Perforations
      perf_d = 0.51                 !Perf Diameter [mm]
      perf_r = perf_d/2             !Perf Radius [mm]
      web_d=(Dgr-(3*perf_d))/4      !Web Diameter [mm]
      rho_s=1.45e-9                 !Solid Propellant Density [t/mm^3]
```

```
      c=Rgr+(nperf*perf_r)
      d=((Rgr**2)-(nperf*(perf_r**2)))
*
*
************************************************
*     Gas Properties
************************************************
*
      gamma=1.2582                  !Specific Heat Ratio
      specf=9.41e11                 !Force Constant (Impetus) [mJ/t]
      R=364.5e6                     !Gas Constant [mJ/t/K]
      cvol=1.06e9                   !Gas Covolume [mm^3/t]
*
*
************************************************
*     Burn Properties
************************************************
*
      B=0.732                       !Burn Rate Coefficient [mm/s]
      EXP=0.952                     !Burn Rate Exponent [For MPa]
*
      TEMP=2576
*
      RELV=1767.15
*
*
************************************************
*     Loop Calculations
************************************************
*
*
      DO 100 NZ = ISTART, IEND
*
*
        IF (TIME == DLTH) THEN
          XL(NZ)=0.1
*
*
**********************
*     INITIAL LOOP
**********************
*
*
*     Calculate Burn Fraction
************************************************
*
          ZF(NZ)=((2*((c*GL)+d)*XL(NZ))-(((GL*(1-nperf))+(4*c))*
     +         ((XL(NZ))**2))+(2*(1-nperf)*((XL(NZ))**3)))/(GL*d)
*
*
*     Calculate New Pressure
************************************************
*
          PNEW(NZ)=(specf*XMASS(NZ)*ZF(NZ))/(RELV-
     +          ((XMASS(NZ)/rho_s)*(1-ZF(NZ)))-(cvol*ZF(NZ)*XMASS(NZ)))
*
*
```

```
*     Calculate New XB
*********************************************
*
          XL(NZ)=XL(NZ)+DLTH*B*(PNEW(NZ))**EXP
*
        END IF
*
*
*********************
*     MAIN LOOP
*********************
*
*
        IF (TIME > DLTH) THEN
*
*
*******************************
*      EXISTING ELEMENTS
*******************************
*
*
            IF (ZF(NZ) >= 1) THEN
*
               PNEW(NZ) = POLD(NZ)
*
            END IF
*
*
            IF (ZF(NZ) >= 1) GOTO 999

*
*
          IF (XL(NZ) > 0.1) THEN
*
*
*     Calculate Burn Fraction
*********************************************
*
            ZF(NZ)=((2*((c*GL)+d)*XL(NZ))-(((GL*(1-nperf))+(4*c))*
     +           ((XL(NZ))**2))+(2*(1-nperf)*((XL(NZ))**3)))/(GL*d)
*
*
*     Calculate New Pressure
*********************************************
*
            PNEW(NZ)=(specf*XMASS(NZ)*ZF(NZ))/(RELV-
     +            ((XMASS(NZ)/rho_s)*(1-ZF(NZ)))-(cvol*ZF(NZ)*XMASS(NZ)))
*
*
*     Calculate New XB
*********************************************
*
            XL(NZ)=XL(NZ)+DLTH*B*(PNEW(NZ))**EXP
*
          END IF
*
*
```

```
*********************************
*     NEW ELEMENTS
*********************************
*
*
          IF (XL(NZ) <= 0.1) THEN
            XL(NZ) = (XL(NZ-25)+XL(NZ-50))/2
*
*     Calculate Burn Fraction
***********************************************
*
            ZF(NZ)=((2*((c*GL)+d)*XL(NZ))-(((GL*(1-nperf))+(4*c))*
     +           ((XL(NZ))**2))+(2*(1-nperf)*((XL(NZ))**3)))/(GL*d)
*
*
*     Calculate New Pressure
***********************************************
*
            PNEW(NZ)=(specf*XMASS(NZ)*ZF(NZ))/(RELV-
     +            ((XMASS(NZ)/rho_s)*(1-ZF(NZ)))-(cvol*ZF(NZ)*XMASS(NZ)))
*
*
*     Calculate New XB
***********************************************
*
            XL(NZ)=XL(NZ)+DLTH*B*(PNEW(NZ))**EXP
*
          END IF
*
*
999   CONTINUE
*
*
        END IF
*
*
100   CONTINUE
*
      RETURN
      END
```